

Stefan Uhlar

Energy Consistent Time-Integration of Hybrid Multibody Systems

Herausgeber: Peter Betsch

Schriftenreihe des Lehrstuhls für
Numerische Mechanik

Band III

Impressum

Prof. Dr.-Ing. habil. Peter Betsch
Lehrstuhl für Numerische Mechanik
Universität Siegen
57068 Siegen
ISSN 1866-1203
URN urn:nbn:de:hbz:467-4086
Zugl.: Siegen, Univ., Diss., 2009

Energy Consistent Time-Integration of Hybrid Multibody Systems

dem Fachbereich Maschinenbau
der Universität Siegen
zur Erlangung des akademischen Grades

Doktor-Ingenieur (Dr.-Ing.)

vorgelegte Dissertation
von

Dipl.-Ing. Stefan Uhlar

aus
Worms

Hauptreferent:	Prof. Dr.-Ing. habil. P. Betsch
Korreferenten:	Prof. Dr.-Ing. habil. P. Eberhard Prof. Dr.-Ing. B. Schweizer
Vorsitzender:	Prof. Dr.-Ing. C.P. Fritzen
Dekan:	Prof. Dr. techn. G. Adlbrecht

Tag der Einreichung:	29.04.2009
Tag der mündl. Prüfung:	23.10.2009

Siegen, Oktober 2009
Band III

'The brick walls are there for a reason. The brick walls are not there to keep us out; the brick walls are there to give us a chance to show how badly we want something.'

Randy Pausch (1960 - 2008)

Preface



"Piled Higher and Deeper" by Jorge Cham www.phdcomics.com

The work presented in this thesis was carried out during my time as a research assistant at the Chair of Numerical Mechanics in the Department of Mechanical Engineering at the University of Siegen from July 2005 to April 2009. The support of the DFG (Deutsche Forschungsgemeinschaft) within the Project BE 2285/4 entitled 'Mechanische Integratoren für diskrete mechanische Systeme mit holonomen und nichtholonomen Zwangsbedingungen' is gratefully acknowledged.

I'd like to thank in the first instance my advisor Professor Peter Betsch, for supporting me during the whole time of my research and helping me to surmount the obstacles of the PhD-path. I would also like to express my gratitude to my reviewers Professor Peter Eberhard and Professor Bernhard Schweizer, for showing interest in my work and finding the time to act as referees. Also many thanks to Professor Horst Idelberger and the head of the committee Professor Claus-Peter Fritzen.

I thank all my colleagues at the Chair for their support and the pleasant working atmosphere.

Starting in Siegen after studying in Kaiserslautern wasn't an easy beginning, therefore I'd like to thank in the following those people who made the time a very pleasant one.

Starting with Frank ‘General’ Hanses for spending with me so many hours in the local pizza house each Tuesday and Marcus ‘Lumpy’ Langenbach for being a co-viewer for a couple of ‘youtube’ videos. Not to forget the pool playing evenings against the both of them. Also many thanks to Rolf ‘RT’ Schulte for the poker-evenings and jogging tours. I’d like to thank Professor¹ (where $i \geq 2$) Andreas ‘Andy’ Menzel for a great PhD-time with a lot of fun and inspiration during his stay in Siegen as a visiting Professor from 2006 to 2007. Finally I’d like to thank Tobias ‘W.’ a.k.a ‘Pep’ a.k.a ‘Mr. Weapon’ Waffenschmidt; gaining him as a friend was worth the effort to come to Siegen.

Furthermore I thank my friends from Kaiserslautern, Michael ‘H.’ Scherer and Johannes ‘J.’ Utzinger for having a great time during our years of study and the PhD-period. Many thanks go especially to Marina and Rouven ‘Matze’ a.k.a ‘Rauwe’ a.k.a ‘Wuzz’ Mohr for their true friendship. Rouven’s help in my first months in Siegen and our discussions throughout our university and PhD-time always supported me and contributed essentially to this thesis.

Most of all I’d like to thank my family for their unconditional support my whole life long. Without them all of this would not have been possible. I love you all!

Siegen, October 2009

Stefan Uhlar

Abstract

In the present contribution we address the design of energy-consistent time stepping schemes for hybrid multibody systems, which consist of rigid and flexible parts. First focusing on rigid body dynamics, we will present a specific rotationless formulation to describe rigid body rotations. This kinematics alleviates the design of energy-consistent integration schemes which facilitate a stable numerical integration of the corresponding set of differential algebraic equations. Furthermore we will mainly focus on vital modeling features concerning rigid bodies. In this connection we present the coordinate augmentation technique, the design of explicit null space matrices for closed loop systems, the incorporation of control constraints, the modeling of dissipation and its consistent time integration, the incorporation of kinematic constraints as well as the coupling of flexible and rigid structures. The performance of the final hybrid scheme will be demonstrated with an example incorporating all modeling features listed above.

Keywords: Differential-algebraic equations, coordinate augmentation, inverse dynamics, nonholonomic constraints, dissipation, multibody systems

Zusammenfassung

In der vorliegenden Arbeit steht die Entwicklung eines energiekonsistenten Zeitintegrationsverfahrens für hybride Mehrkörpersysteme, bestehend aus starren und flexiblen Komponenten, im Vordergrund. Dabei beschäftigen wir uns zunächst mit der Starrkörperdynamik und wählen eine rotationsfreie Formulierung als Starrkörperkinematik. Diese erleichtert die Entwicklung von energiekonsistenten Zeitintegratoren, welche ein stabiles Verhalten bei der Lösung von differential-algebraischen Gleichungssystemen aufweisen. Ein weiterer Schwerpunkt der Arbeit liegt auf Modellierungstechniken für die Starrkörperdynamik. In diesem Zusammenhang stellen wir die Koordinaten Augmentierung vor, präsentieren eine explizite Darstellung von Null-Raum Matrizen für Systeme mit geschlossenen kinematischen Schleifen, behandeln Steuerungsprobleme, beschäftigen uns mit der Modellierung von Dissipation und der zugehörigen energie-konsistenten Zeitintegration, wie auch letztendlich die Behandlung von nichtholonomen Systemen. Die Leistungsfähigkeit des neuen Zeitintegrationsverfahrens für hybride Mehrkörpersysteme wird anhand eines letzten Beispiels, welches alle oben genannten Modellierungsaspekte beinhaltet, aufgezeigt.

Schlagwörter: Differential-algebraische Gleichungen, Koordinaten Augmentierung, inverse Dynamik, nichtholonome Zwangsbedingungen, Dissipation, Mehrkörpersysteme


Contents

1. Introduction	1
2. Prolog – Motivation	13
2.1. Equations of Motion	14
2.2. Discrete Equations of Motion	15
2.2.1. The Newmark method	15
2.2.2. The HHT scheme	16
2.2.3. Variational integrator	16
2.2.4. Energy-momentum scheme	17
2.3. Results	18
3. Dynamics of Constrained Mechanical Systems	23
3.1. Continuous Equations of Motion	25
3.1.1. Size-reduction of the DAEs	26
3.2. Discrete Equations of Motion: Energy-Momentum Schemes	27
3.2.1. The basic energy-momentum scheme	28
3.2.2. The reduced energy-momentum scheme	29
3.3. Benefits of the DAE-Formulation	30
4. Rotationless Formulation of the Rigid Body	33
4.1. The Rigid Body	34
4.1.1. First size reduction	37
4.1.2. Second size reduction	39
4.2. Kinematic Pairs	40
4.2.1. The cylindrical pair	41
4.2.2. Overview of lower kinematic pairs	44
5. Modeling Techniques	51
5.1. Coordinate Augmentation Technique	52
5.1.1. Augmented planar revolute pair	52
5.1.2. The screw-pair	59
5.2. Design of Explicit Null Space Matrices for Closed Loop Systems	70
5.2.1. Description of open chains	71
5.2.2. Description of the system with tree structure	74
5.2.3. Incorporation of the loop-closure constraints	76

5.2.4.	Coordinate augmentation	82
5.2.5.	Numerical example	85
5.3.	Control of Multibody Systems	89
5.3.1.	Systems with mixed holonomic and servo constraints	89
5.3.2.	Conserving integration of the control DAEs	90
5.3.3.	Controlled motion of a closed-loop multibody system	91
5.4.	Modeling of Dissipation and its Consistent Integration	98
5.4.1.	Linear viscous joint friction	100
5.4.2.	Incorporation of dissipation	105
5.4.3.	Viscoelastic model	108
5.4.4.	Viscoelastic-element oscillator	109
5.4.5.	Double wishbone suspension	112
5.4.6.	Plasticity model	118
5.4.7.	Friction-element oscillator	119
5.4.8.	Planar physical pendulum	122
5.4.9.	Enhanced rheological model for joint-plasticity	123
5.4.10.	Planar parallel manipulator with joint friction	127
5.5.	Nonholonomic Constraints	132
5.5.1.	Systems with mixed geometric and kinematic constraints	132
5.5.2.	Conserving integration of the mixed set of DAEs	133
5.5.3.	Ball on a rotating plate	134
5.5.4.	Two wheeled robot	138
6.	Hybrid Multibody Systems	145
6.1.	Flexible Body Dynamics	146
6.1.1.	Semidiscrete equations of motion	147
6.1.2.	Discrete equations of motion	148
6.2.	Coupling of Rigid and Flexible Components	149
6.3.	Dynamics of Hybrid Multibody Systems	151
6.3.1.	Reduction by coupling constraints	152
6.4.	Numerical Examples	154
6.4.1.	3D-Helicopter rotor	154
6.4.2.	Medieval trebuchet	157
6.4.3.	Nonholonomic manipulator	164
7.	Visualization Approach for Hybrid Multibody Systems	171
7.1.	Visualization of Rigid Bodies	172
7.1.1.	Direction Cosine vs. Quaternions	172
7.1.2.	Modeling steps	174
7.2.	Visualization of Flexible Bodies	178
7.2.1.	Spatial 8-Node element	178
7.2.2.	Plotting the stress field	182

7.3. Visualization of other results obtained with EM-schemes	184
8. Epilog – Conclusions	193
A. Conservation Properties	197
A.1. Conservation of energy	197
A.2. Conservation of angular momentum	198
A.3. Algorithmic force of a viscoelastic model with linear spring characteristic	200

1. Introduction



NEWTON'S THREE LAWS OF GRADUATION

Though famous for his seminal work in Mechanics, Isaac Newton's theories on the prediction of a doctoral graduation formulated while still a grad student at Cambridge, remain his most important contribution to academia.

FIRST LAW

"A grad student in procrastination tends to stay in procrastination unless an external force is applied to it"


This postulate is known as the "Law of Inertia" and was originally discovered experimentally by Galileo four years before Newton was born when he threatened to cut his grad student's funding. This resulted in a quickening of the student's research progress.

Galileo's observations were later perfected by Descartes through the application of "Weekly Meetings."

Before Galileo's time, it was wrongfully thought that grad students would rest only as long as no work was required of them and that in the absence of external forces, they would graduate by themselves.

(From Encyclopaedia Britannica)

PHD.STANFORD.EDU
JORGE_CHAM@THE.STANFORD.DAILY



NEWTON'S THREE LAWS OF GRADUATION

First published in 1679, Isaac Newton's "Procrastinare Unnaturalis Principia Mathematica" is often considered one of the most important single works in the history of science. Its Second Law is the most powerful of the three, allowing mathematical calculation of the duration of a doctoral degree.

SECOND LAW

"The age, a, of a doctoral process is directly proportional to the flexibility, f, given by the advisor and inversely proportional to the student's motivation, m"

Mathematically, this postulate translates to:


$$a \propto \frac{f}{m}$$

$$\mathbf{a} = \mathbf{F} / \mathbf{m}$$

$$\therefore \mathbf{F} = \mathbf{m} \mathbf{a}$$

This Law is a quantitative description of the effect of the forces experienced by a grad student. A highly motivated student may still remain in grad school given enough flexibility. As motivation goes to zero, the duration of the PhD goes to infinity.

PHD.STANFORD.EDU
JORGE_CHAM@THE.STANFORD.DAILY



NEWTON'S THREE LAWS OF GRADUATION

Having postulated the first two Laws of Graduation, Isaac Newton the grad student was still perplexed by this paradox: If indeed the first two Laws accounted for the forces which delayed graduation, why doesn't explicit awareness of these forces allow a grad student to graduate?

It is believed that Newton practically abandoned his graduate research in Celestial Mechanics to pursue this paradox and develop his Third Law.

THIRD LAW

"For every action towards graduation there is an equal and opposite distraction"

This Law states that, regardless of the nature of the interaction with the advisor, every force for productivity acting on a grad student is accompanied by an equal and opposing useless activity such that the net advancement in thesis progress is zero.

Newton's Laws of Graduation were ultimately shown to be an approximation of the more complete description of Graduation Mechanics given by Einstein's Special Theory of Research Inactivity.

Einstein's theory, developed during his graduate work in Zurich, explains the general phenomena that, relative to the grad student, time slows down to nearly a standstill.

PHD.STANFORD.EDU
JORGE_CHAM@THE.STANFORD.DAILY

"Piled Higher and Deeper" by Jorge Cham www.phdcomics.com

Nowadays in engineering the simulation of real world mechanical systems has become a standard. Especially in the field of multibody dynamics, the proper modeling of real technical systems and their mathematical treatment came to the fore. In this connection two main issues need to be taken care of. The first one is to derive a mechanical / mathematical model of a real world problem and the second is to obtain a solution of the mathematical expressions. Due to the complexity of the systems which arise in common engineering problems, an analytical solution can only be found in special cases. In general one has to rely on numerical methods to approach the set of equations. Especially in the field of dynamics, where it is necessary to solve time dependent equations,

it is vital to rely on time integration schemes which guarantee a stable, accurate and fast run. This challenge was approached by several authors in the last century, yet the schemes proposed were mainly derived for linear mechanical systems. This generally leads to numerical instabilities while dealing with nonlinearities which arise specifically in the field of rigid- and elastodynamics. Therefore in recent years special emphasis was laid on the design of time integration schemes which preserve fundamental physical properties such as the balance of momentum maps or the fulfillment of the laws of thermodynamics. From an engineering point of view this approach is highly relevant since the developed schemes do not suffer from numerical dissipation, which typically deteriorates the results. Furthermore the robustness of the mechanical integration scheme allows to choose coarser step sizes, which again reduces the computational costs while maintaining the accuracy. Simultaneously modern modeling techniques demand the combination of rigid and flexible components in multibody systems, in order to capture the influence of flexibility (e.g. high oscillations, material behavior) within the global system behavior. Typically, in commercial codes, flexibility is only captured on a linear level, accounting only for small deformations and linear material behavior (modal reduction). For many practical issues, where components undergo large deformations and where the assumption of linear elastic material behavior is not valid, one has to rely on fully discretized systems. Since for dynamic simulations large scale finite element models of complete constructions are computationally inefficient and since not all parts of a construction undergo the same deformation, it is common to rely on hybrid models, where some parts are assumed to be rigid. This procedure offers to exploit all benefits from rigid body modeling, like using simple kinematic pairs instead of finite element contact. In this connection the modeling of dissipation, especially joint friction plays a major role. Furthermore we can resort to many modeling techniques from rigid body dynamics, which alleviate the assembly of complex multibody systems, relying on holonomic, nonholonomic, scleronomic or rheonomic constraints. All these modeling instruments will be emphasized in this thesis and their performance demonstrated by representative numerical examples.

Short Literature Survey: Starting with the pioneering works by Simo and co-workers [143, 142, 141], energy-momentum conserving schemes and energy-decaying variants thereof have been developed primarily in the context of nonlinear finite element methods. In this connection, representative works are due to Brank et al. [39], Bauchau and Bottasso [11], Crisfield and Jelenić [45], Ibrahimbegović et al. [80], Romero and Armero [127], Betsch and Steinmann [24], Puso [124], Laursen and Love [92] and Armero [3], see also the references cited in these works.

Problems of nonlinear elastodynamics and nonlinear structural dynamics can be characterized as stiff systems possessing high frequency contents. In the conservative case, the corresponding semi-discrete systems can be classified as finite-dimensional Hamiltonian systems with symmetry. The time integration of the associated nonlinear ODEs by

means of energy-momentum schemes has several advantages:

In addition to their appealing algorithmic conservation properties energy-momentum schemes are known to possess enhanced numerical stability properties (see Gonzalez and Simo [62]). Due to these advantageous properties energy-momentum schemes have even been successfully applied to penalty formulations of multibody dynamics, see Goicolea and Garcia Orden [56]. Indeed, the enforcement of holonomic constraints by means of penalty methods again yields stiff systems possessing high frequency contents. The associated equations of motion are characterized by ODEs containing strong constraining forces. In the limit of infinitely large penalty parameters these ODEs replicate Lagrange's equations of motion of the first kind (see Rubin and Ungar [129]), which can be identified as index-3 differential-algebraic equations (DAEs). This observation strongly supports the expectation that energy-momentum methods are also beneficial to the discretization of index-3 DAEs (see G eradin and Cardona [54, Chapter 12] and Leyendecker et al. [97]).

The specific formulation of the equations of motion strongly affects the subsequent time discretization. In the context of multibody systems the main distinguishing feature of alternative formulations is the choice of coordinates for the description of the orientation of the individual rigid bodies. For this purpose some kind of rotational variables (e.g. joint-angles, Euler angles or other 3-parameter representations of finite rotations) are often employed. In general, the equations of motion in terms of rotational variables are quite cumbersome. In the case of systems with tree structure one is typically confronted with highly-nonlinear ODEs. Further challenges arise in the case of closed-loop systems due to the presence of algebraic loop-closure constraints leading to index-3 DAEs. As a consequence of their inherent complexity, the design of energy-momentum conserving schemes is hardly conceivable for formulations of general multibody systems involving rotations.

In the present work the use of rotational variables is completely circumvented in the formulation of the equations of motion. Our formulation turns out to be especially well-suited for the energy-momentum conserving integration of both open-loop and closed-loop multibody systems. In our approach the orientation of each rigid body is characterized by the elements of the rotation matrix (or the direction cosine matrix). This leads to a set of redundant coordinates which are subject to holonomic constraints. In this connection two types of constraints may be distinguished (see also Betsch and Steinmann [27]): (i) Internal constraints which are intimately connected to the assumption of rigidity and, (ii) external constraints due to the interconnection of the bodies constituting the multibody system. Item (ii) implies that loop-closure constraints can be taken into account without any additional difficulty. The resulting DAEs exhibit a comparatively simple structure which makes possible the design of energy-momentum conserving schemes. Another advantage of the present rotationless formulation of multibody systems lies in the fact that planar motions as well as spatial motions can be treated without any conceptual differences. That is, the extension from the planar case

to the full three-dimensional case can be accomplished in a straightforward way, which is in severe contrast to formulations employing rotations, due to their non-commutative nature in the three-dimensional setting. It is worth mentioning that the present rotationless approach resembles to some degree the natural coordinates formulation advocated by García de Jalón et al. [52].

As pointed out above, the rotationless formulation of multibody systems benefits the design of energy-momentum schemes. On the other hand, the advantages for the discretization come at the expense of a comparatively large number of unknowns. In addition to that, joint-angles and associated torques are often required in practical applications, for example, if a joint is actuated. The size of the algebraic system to be solved can be systematically reduced by applying the discrete null space method developed in [15].

As mentioned above in many practical applications rotational DOF are required. In this sense we refer to a specific coordinate augmentation technique which was first introduced in the context of the rotationless formulation of rigid bodies in [28, 149, 148]. This procedure can be regarded as a pure modeling feature. Since the rotationless formulation completely circumvents rotational DOF, yet practical applications need the actuation of joint angles, the augmentation technique remedies this drawback. The basic idea of introducing additional dependent coordinates (or fields, e.g. in finite element formulations for incompressible models in nonlinear elasticity) is well-known and can be found in many previous works. In Géradin and Cardona [54] the rotation angle in a hinge joint (cf. Sect. 7.6.1) is introduced in the spirit of the augmentation technique, albeit the corresponding additional constraint is only enforced approximately. The work by Bottasso and Croce [37] is another example of the implicit use of the augmentation technique to deal with joint-angles and joint-displacements (cf. Sect. 3.3).

The beneficial structure of the DAEs makes possible the introduction of additional constraints. In this connection we will concern the implementation of control constraints. This approach makes possible to partially specify the motion of a multibody system. In particular, inverse dynamics problems can be dealt with in the present simulation framework. In contrast to common approaches to solve inverse dynamic problems (see e.g. [47, 53, 132]), the application of our scheme will solve for all unknowns in parallel. It turns out that the rotationless formulation along with the coordinate augmentation technique yields simple-structured control contributions to the DAEs.

The modeling of damping phenomena plays a central role in dynamical systems. Especially for the design of drive trains or gears in robotic applications the accurate physical modeling of friction is of major interest. The challenging task of modeling joint friction was undertaken by several authors [8, 9, 41, 75, 46, 146]. Apparently most models for friction applied in the field of multibody dynamics do not rely on thermodynamic consistency, which means that the models themselves produce energy artificially. For the intention of designing an energy consistent time integration scheme, which accounts

numerically exact for the correct amount of dissipation, we will have to apply thermodynamic consistent models. To this end we rely on rheological models originating from constitutive modeling in material mechanics. They possess the advantage of calculating the correct amount of dissipation, while retaining the ability of being augmented in such a way, that they can match experimental results by applying parameter identification [87, 102]. The ideas to this approach go back to the modeling of viscoelastic material behavior for dynamics, applying an energy consistent integration scheme by Gross et al. [67, 68, 69, 70]. For finite elasto-plasto-dynamics energy consistent schemes have been developed by Noels et al. [119, 118], Meng and Laursen [106], Mohr et al. [108, 109, 110, 111] or Armero [3, 4]. We will basically follow these ideas and break them down to the 1D case. In this connection the aforementioned coordinate augmentation technique will play a major role.

The analysis of nonholonomic systems from a mathematical point of view has been of great interest, mainly in the field of analytical mechanics (see e.g. Neimark [113, 114]). Recent publication in the field of numerical mechanics combine control issues with non-holonomic problems, refer e.g. to [32, 126, 44]. The incorporation of kinematic constraints into the rotationless formulation along with the design of energy-momentum time stepping schemes was undertaken in [16] or [148].

The coupling of rigid and flexible bodies represents another challenging task. Recent publications presented for instance by Bauchau [10, 11, 12], Borri et al. [34, 35], Imbrahimbegović et al. [80, 81], Kübler et al. [88], Göttlicher and Schweizerhof [63] or Betsch [26], Leyendecker [98] or Uhlar [151, 154] represent the state of the art formulations in this field.

The main new contributions presented in this thesis are (i) a coordinate augmentation technique which facilitates to incorporate rotational degrees of freedom along with associated torques, (ii) a systematic procedure for the construction of discrete null space matrices for closed-loop systems, (iii) the incorporation of control constraints into the multibody scheme, (iv) the modeling of dissipation and the design of a corresponding energy-consistent time stepping scheme, (v) the treatment of kinematic constraints arising under the assumption of rolling without slipping and finally, (vi) the coupling of rigid and flexible structures leading to a unified approach for hybrid multibody systems.

Outline of the Present Work

In the following we will give a short overview and summary of each chapter of the thesis. This shall guide the reader through the structure and highlight the main issues of each part.

Chapter 2: The thesis starts with a motivating example of a free floating flexible dumb-

bell. The focus of this chapter is to present a comparison of different time integration schemes concerning their accuracy and robustness for solving problems of nonlinear flexible multibody systems. In this connection we will outline the equations of motion, governed by ODEs and derive their time-discrete counterpart according to four different time stepping schemes. Here we will compare the well established schemes by Newmark and its extension by Hilber, Hughes and Taylor with the up to date time integrators like the variational integrator and the here favored energy-momentum scheme. The results will be discussed and conclusions will be drawn.

Chapter 3: The third chapter concerns the dynamics of constrained mechanical systems. Here we will derive the equations of motion and outline their numerical treatment. Hereby we focus on the aforementioned mechanical time integration schemes. In this connection we will present size reduction techniques for the system of differential algebraic equations, which lead to a minimal and well conditioned discrete set of nonlinear algebraic equations. Finally we will shortly discuss the benefits of the DAE-structure of the equations of motion and emphasize on their extension to cover vital modeling features for hybrid multibody systems.

Chapter 4: The fundament for the design of energy-momentum consistent time stepping schemes will be outlined in this chapter, dealing with rigid body rotations. We rely on the so-called rotationless formulation for rigid bodies, based on the direction cosine description for rigid body kinematics. Furthermore we will present size reduction techniques to break down the redundant set of coordinates and treat exemplarily the cylindrical pair, representative for all other basic joint connections. A brief overview of all remaining pairs closes this chapter.

Chapter 5: The main contribution of this thesis is summarized in this chapter, presenting vital modeling features for rigid body dynamics:

First we will present the coordinate augmentation technique, which incorporates rotational degrees of freedom into our rotationless formulation. To this end we will explain the procedure with a planar revolute pair. Simultaneously this forms the base for the treatment of the last kinematic pair, namely the screw joint which will be outlined in detail.

The second issue addressed, will be the design of explicit null space matrices for closed loop systems. This will be discussed with the example of a free floating parallel manipulator. A comparison of the basic and reduced scheme will clearly demonstrate the capability of the new time integration scheme for closed loop systems.

Subsequently we will address the incorporation of control constraints into our multibody framework. For this purpose we restrict ourselves to fully actuated systems, rendering a control constraint Jacobian of Boolean type. The performance of the time stepping scheme for mechanical systems with mixed geometric and control constraints will be demonstrated with the example of a radio telescope.

The treatment of dissipative effects in multibody systems represents a major issue. In this connection we will present three different approaches for modeling dissipation. The goal is to obtain an energy-consistent time stepping scheme, which does not suffer from numerical dissipation. Therefore we will rely on thermodynamic consistent models elevating from constitutive modeling. Again the performance will be proven with adequate numerical examples.

The last modeling feature outlined in this chapter will address the modeling of non-holonomic constraints. These constraints mainly arise under the assumption of rolling without slipping. We will extend our time integration schemes by new kinematic constraints and present two numerical examples dealing with a ball on a turntable and the motion of a two wheeled robot.

Chapter 6: The connection of rigid and flexible bodies will be the point of interest in this chapter. For this purpose we emphasize on the incorporation of coupling constraints, which connect rigid and elastic parts. For the modeling of flexible structures we rely on a standard finite element discretization and derive for flexible body dynamics a corresponding set of nonlinear ODEs. The treatment of these equations in the discrete sense will again be carried out by applying energy-momentum conserving schemes. The global hybrid system will then be governed by a set of DAEs. In this connection we will again devise suitable null space matrices which will reduce the number of unknowns by the number of coupling constraints. The performance of the newly introduced hybrid energy-momentum scheme will be tested with three challenging examples.

Chapter 7: The obtained results within this thesis will always be visualized using a non-commercial image rendering application. The visualization process, starting with some theory on rigid body rotations, followed by the import of the computed data and the subsequent modeling of rigid and flexible bodies, will be addressed in this chapter. For this purpose we will present the freeware rendering software POV-Ray and all necessary steps to obtain computer generated images for hybrid multibody systems. Furthermore we will present the visualization of flexible bodies according to the imported finite element data, also emphasizing on the visualization of the stress field. Finally some representative snapshots of simulations not closer described in the thesis will be summed up.

Appendix A: The appendix will cover the conservation properties of our time integration scheme. In this connection the fulfillment of the mechanical properties are studied in detail. Furthermore a proof for the algorithmic force in Chapter 5 will be highlighted in detail.

Einleitung

In der Ingenieurpraxis sind Simulationswerkzeuge heutzutage zum Standard geworden. Speziell auf dem Gebiet der Mehrkörperdynamik kommt der Modellierung von mechanischen Systemen und ihrer mathematischen Behandlung mehr Bedeutung zu. In diesem Zusammenhang stehen hauptsächlich zwei Punkte im Vordergrund. Der erste Punkt ist es aus dem realen Model ein mechanisches / mathematisches Ersatzmodel zu abstrahieren, und der zweite Punkt ist es, die mathematischen Ausdrücke entsprechend zu behandeln. Aufgrund der Komplexität heutiger ingenieur Systeme kann eine analytische Lösung der mathematischen Gleichungen nur in den seltensten Fällen gefunden werden. Im Allgemeinen muss man sich auf numerische Methoden verlassen, um das entsprechende Gleichungssystem zu lösen. Speziell im Bereich der Dynamik, wo es notwendig ist zeitabhängige Gleichungen zu lösen, ist es wichtig Zeitintegrationsverfahren zu verwenden, welche eine stabile, akurate und auch schnelle Berechnung garantieren. Diese Aufgabe wurde im letzten Jahrhundert von mehreren Autoren angegangen, jedoch waren die entwickelten Verfahren lediglich für lineare Systeme ausgelegt. Dies führt im Allgemeinen zu numerischen Instabilitäten, speziell wenn man es mit nichtlinearen Systemen der Starrkörper- oder Elastodynamik zu tun hat. Deswegen wurde in den letzten Jahren der Schwerpunkt auf die Entwicklung von Zeitintegrationsverfahren gelegt, welche den fundamentalen physikalischen Eigenschaften wie der Erhaltung des Drehimpulses oder der Erfüllung der Hauptsätze der Thermodynamik genügen. Aus ingenieurmäßiger Sicht betrachtet, ist diese Entwicklung sehr relevant, denn diese Zeitintegrationsverfahren sind frei von numerischer Dissipation, welche in den meisten Fällen die Ergebnisse stark verfälschen kann. Weiterhin erlauben die meisten robusten Verfahren größere Zeitschrittweiten, was Rechenzeit einspart bei gleichbleibender Genauigkeit. Gleichzeitig verlangen moderne Simulationstechniken die Kopplung von starren und flexiblen Körpern um den Einfluss der Flexibilität (z.B. hochfrequente Oszillationen, nichtlineares Materialverhalten) auf das Gesamtsystem abzubilden. In kommerziellen Codes wurde dieser Einfluss meist nur auf einer linearen Ebene erfasst, was die Deformation und das Materialverhalten angeht (modale Reduktion). In vielen praktischen Anwendungen, wobei Komponenten großen Deformationen unterliegen, gilt die linearisierte Annahme nicht mehr. In diesen Fällen kommen räumlich diskretisierte Komponenten zum Einsatz. Da es jedoch sehr rechenzeitintensiv ist gesamte Strukturen zu diskretisieren und zu berechnen, und da einige Komponenten einer Konstruktion nicht denselben Belastungen und Deformationen unterliegen, ist es üblich hybride Systeme zu

verwenden. Hierbei sind einige Komponenten starr modelliert, einige hingegen wieder voll elastisch. Diese Vorgehensweise bietet den Vorteil alle Modellierungsmöglichkeiten, die aus der Starrkörperdynamik bekannt sind anzuwenden, wie z.B. die Modellierung von Gelenken statt der vollständigen Diskretisierung einer Finite Elemente Kontaktzone. In diesem Zusammenhang spielt Gelenkreibung eine entscheidende Rolle. Weiterhin können wir auf alle Modellierungsaspekte zurückgreifen um komplexe Mehrköpersysteme aufzubauen, hierunter zählen u.a. holonome, rheonome oder nichtholonome Zwangsbedingungen. All diese Modellierungsinstrumente werden in dieser Arbeit angesprochen und ihre Wirkweise mit Hilfe numerischer Beispiele belegt.

Hauptaspekte der vorliegenden Arbeit

Es folgt ein kurzer Überblick und Inhaltsangabe von jedem Kapitel der vorliegenden Arbeit. Dies soll den Leser durch die Dissertation führen und die Hauptaspekte hervorheben.

Kapitel 2: Die Arbeit startet mit einem einleitenden Beispiel einer frei fliegenden flexiblen Hantel. Das Hauptaugenmerk liegt dabei auf den Vergleich von verschiedenen Zeitintegrationsverfahren und deren Vergleich hinsichtlich Genauigkeit und Robustheit. Hierbei stellen wir die Bewegungsgleichungen auf, die durch gewöhnliche Differentialgleichungen charakterisiert werden. Diese diskretisieren wir mit Hilfe vier verschiedener numerischer Verfahren. Wir vergleichen die etablierten Verfahren von Newmark und dessen Erweiterung von Hilber, Hughes und Taylor mit den aktuellen Verfahren der variationellen Integratoren und der energie- und drehimpulserhaltenden Zeitintegratoren.

Kapitel 3: Das dritte Kapitel beschäftigt sich mit der Dynamik von mechanischen Systemen mit Zwangsbedingungen. Wir stellen die Bewegungsgleichungen auf und diskretisieren diese in der Zeit. Dabei verwenden wir die bereits erwähnten mechanischen Zeitintegratoren. Gleichzeitig präsentieren wir Reduktionstechniken, um das System aus differential-algebraischen Gleichungen zu minimieren und die Kondition des zu lösenden algebraischen Gleichungssystems zu verbessern. Abschliessend heben wir die Vorteile der differential-algebraischen Struktur hervor und betonen ihre Erweiterbarkeit um wichtige Modellierungsaspekte.

Kapitel 4: Die Grundlage zur Konstruktion von energie- und drehimpulserhaltenden Zeitintegratoren wird in diesem Kapitel vorgestellt, die rotationsfreie Formulierung. Auch hier stellen wir die Reduktion der Kinematik dar und behandeln exemplarisch das zylindrische Gelenk, repräsentativ für alle Grundgelenkartarten, die am Schluß des Kapitels kurz vorgestellt werden.

Kapitel 5: Der Hauptbeitrag der Arbeit liegt in diesem Kapitel, es stellt wichtige Mode-

lierungsaspekte für die Starrkörperdynamik vor:

Zunächst stellen wir die Koordinaten Augmentierung vor, welche verwendet wird um Rotationsfreiheitsgrade in unsere rotationsfreie Formulierung zu implementieren. Dieses Verfahren stellen wir am ebenen Drehgelenk dar. Die Koordinaten Augmentierung bildet gleichzeitig die Grundlage zur Behandlung des noch fehlenden kinematischen Paares, des Schraubgelenkes. Dieses wird im Detail erläutert.

Der zweite Punkt ist die Behandlung von Nullraum Matrizen für geschlossene kinematische Schleifen. Die Generierung der Reduktionsmatrizen wird anhand eines frei fliegenden parallelen Manipulators erläutert. Der Vergleich zwischen der vollständig reduzierten Version und der ursprünglichen Version soll die Leistungsfähigkeit des vorgestellten Reduktionsverfahrens belegen.

Weiterhin beschäftigen wir uns mit Steuerungsproblemen. Dabei beschränken wir uns nur auf vollaktuierte Systeme. Dies führt auf ein Zeitintegrationsverfahren welches sowohl geometrische als auch Steuerungszwangsbedingungen beherrscht. Das Verfahren wird am Beispiel eines vollaktuierten Radioteleskops getestet.

Die Behandlung von dissipativen Effekten in der Mehrkörperdynamik spielt eine wesentliche Rolle. Deshalb widmen wir uns in diesem Kapitel ebenfalls der Modellierung von Reibung und stellen drei verschiedene Ansätze vor. Das Ziel ist es einen energiekonsistenten Zeitintegrator zu entwickeln, welcher keine numerische Dissipation aufweist. Daher berufen wir uns auf thermodynamisch konsistente Modelle, die aus der Materialmodellierung stammen. Jeder Ansatz wird durch zugehörige numerische Beispiele begleitet.

Der letzte Modellierungsaspekt in diesem Kapitel bildet die Behandlung von nicht-holonomen Zwangsbedingungen. Diese tauchen speziell dann auf, wenn es um die Beschreibung von Rollvorgängen geht, bei denen kein Schlupf auftaucht. Dabei erweitern wir erneut unser Zeitintegrationsschema um kinematische Zwangsbedingungen. Repräsentative Beispiele in Form eines Balles auf einer konstant rotierenden Platte, oder die vollaktuierte Steuerung eines nichtholonomen Roboters begleiten diesen Abschnitt.

Kapitel 6: Den Hauptaspekt dieses Kapitels bildet die Kopplung von starren und flexiblen Körpern. Daher widmen wir uns zunächst den Kopplungszwangsbedingungen. Die Modellierung flexibler Körper geschieht mittels der Finiten Elemente Methode und führt auf ein System von gewöhnlichen Differentialgleichungen. Die Diskretisierung dieser Gleichungen geschieht erneut mit Hilfe energie- und drehimpulserhaltender Integratoren. Das hybride System wird wiederum von differential-algebraischen Gleichungen geprägt. Wir zeigen erneut ein Reduktionsschema auf um die neu eingeführten Kopplungszwangsbedingungen zu eliminieren. Drei anspruchsvolle Beispiele testen das neu entwickelte hybride Zeitintegrationsverfahren.

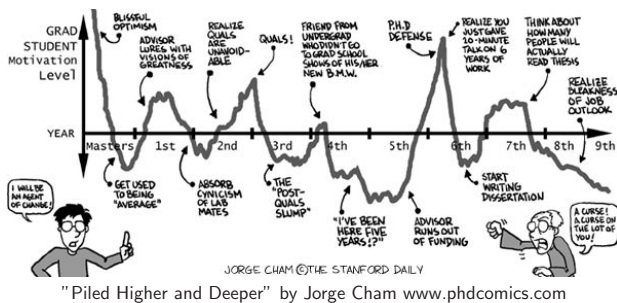
Kapitel 7: Alle in dieser Arbeit vorgestellten numerischen Beispiele werden visualisiert. Dazu benutzen wir ein nicht-kommerzielles Werkzeug zur Generierung von gerenderten Bildern. Dieser Visualisierungsprozess soll in diesem Kapitel vorgestellt werden.

1. Introduction

Dazu wird zunächst die Starrkörperrotation erläutert, gefolgt vom Import der berechneten Daten in den freeware Renderer POV-Ray. Wir sprechen die Generierung von Starrkörpern an und gehen gleichzeitig auf die Erstellung von flexiblen Strukturen ein. Dabei wird die Visualisierung von Spannungsfeldern in flexiblen Strukturen erläutert. Abschließend werden noch Bilder von Simulationen präsentiert, die nicht näher in der Arbeit vom numerischen Standpunkt aus erläutert wurden.

Anhang A: Der Anhang stellt die Erhaltungseigenschaften der Zeitintegrationsverfahren da. In diesem Zusammenhang werden die mathematischen Beweise welche die mechanischen Erhaltungsgrößen garantieren dargelegt. Gleichzeitig wird bewiesen, dass die algorithmische Kraft aus Kapitel 5 für lineare Federgesetze auf die gewöhnliche Mittelpunktauswertung runterbricht.

2. Prolog – Motivation



As a motivation for the topic of hybrid multibody systems, we deal with the exemplary motion a planar free floating flexible dumbbell, as also discussed in [23]. This can be viewed as a simplified flexible multibody system. As depicted in Fig. 2.1 it consists of two mass points which are connected via an nonlinear-elastic spring. In this case the spring represents the flexible body structure (with an nonlinear material law), one could think of a simple discretization using one finite element. Both mass points are given an initial velocity, perpendicular to the spring, with the same value, acting in opposite directions. This makes the system spin on an orbit according to the nonlinear character of the spring. The system at hand represents, due to the absence of gravity, a Hamiltonian system with symmetry; preserving the total energy and angular momentum.

In the first instance we will briefly present the equations of motion of the underlying system. Hereby we rely on the Lagrangian formalism, outlined in Chapter 3. The main issue which shall be outlined in this chapter, is the numerical treatment of the equations of motion. In this connection we will apply two common time integration schemes which are typically used in some commercial multibody codes and two up to date schemes. Specifically we will compare the well known Newmark-scheme [115] and the HHT-scheme [76] with the recently developed variational integrators [104, 85, 84, 94, 158, 99, 17] and our choice for this thesis, the energy-momentum scheme [15, 18, 28, 149, 153, 152, 151].

It is well known that the variational schemes are symplectic and therefore guarantee the conservation of angular momentum. In this connection, the simple example at hand shall demonstrate the performance of each time stepping scheme and outline the importance of mechanical conservation properties while dealing with hybrid dynamical systems.

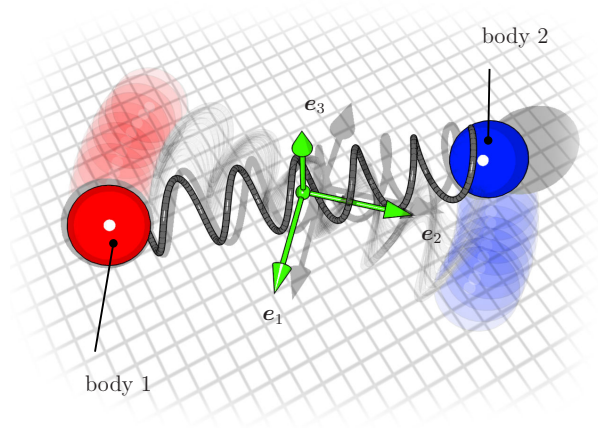


Figure 2.1.: Schematic of the flexible free flying dumbbell.

2.1. Equations of Motion

First we will derive briefly the continuous equations of motion. Thereby we rely on the Lagrange's equations, where we need to state the kinetic and potential energies. Since the system at hand is free floating, there is no potential due to gravity, yet we obtain a stored energy function for the nonlinear spring. Thereby the kinetic energy of the two-body system can be written as

$$T(\dot{\mathbf{q}}) = \frac{1}{2} \dot{\mathbf{q}} \cdot \mathbf{M} \dot{\mathbf{q}} \quad (2.1)$$

Here \mathbf{M} denotes the diagonal and constant mass matrix

$$\mathbf{M} = \begin{bmatrix} m_1 \mathbf{I} & \mathbf{0} \\ \mathbf{0} & m_2 \mathbf{I} \end{bmatrix}_{4 \times 4} \quad (2.2)$$

The potential energy of the spring is inspired by molecular dynamics simulations and is governed by a Lennard-Jones potential according to [65]

$$V(\mathbf{q}) = \alpha \varepsilon \left[\left(\frac{\bar{r}}{r} \right)^n - \left(\frac{\bar{r}}{r} \right)^m \right] \quad \text{where } m < n \quad (2.3)$$

Here $r = \| \mathbf{q}^1 - \mathbf{q}^2 \|$ is measuring the distance between the mass points. Furthermore \bar{r} denotes the zero crossing of the potential, which will be chosen here to $\bar{r} = (1/2)^{-6}$ guaranteeing a zero force at a distance of $r = 1$. The strength of the repulsive or attractive force is governed by ε , the constant value α is defined as follows (see [65])

$$\alpha = \frac{1}{n - m} \left(\frac{n^m}{m^m} \right)^{\frac{1}{n-m}} \quad (2.4)$$

In our example we choose $n = 12$ and $m = 6$, which means that the potential and thereby the force decreases rapidly with increasing distance. The nonlinear spring characteristics represents an additional challenge for the time integration schemes which will be applied later.

The configuration vector for the flexible dumbbell reads

$$\mathbf{q} = \begin{bmatrix} \mathbf{q}^1 \\ \mathbf{q}^2 \end{bmatrix}_{4 \times 1} \quad \text{with} \quad \mathbf{q}^i = \begin{bmatrix} x \\ y \end{bmatrix}_{2 \times 1} \quad (2.5)$$

Having the kinetic and potential energy at hand, the application of Lagrange's formalism finally renders the continuous nonlinear equations of ODE-type

$$M\ddot{\mathbf{q}} + \nabla V(\mathbf{q}) = \mathbf{0} \quad (2.6)$$

2.2. Discrete Equations of Motion

In the following we will derive the discrete counterparts of Equation (2.6) by applying different time integration schemes. In this sense we will outline the Newmark-scheme, the HHT-scheme, a variational integrator and the energy-momentum method.

2.2.1. The Newmark method

According to the Newmark scheme [115, 159] we obtain the following set of discrete equations of motion

$$M\ddot{\mathbf{q}}_{n+1} + \nabla V(\mathbf{q}_{n+1}) = \mathbf{0} \quad (2.7)$$

2. Prolog – Motivation

The nonlinear algebraic equation above can be stated in terms of the configuration by expressing the acceleration and velocity as (see also [160])

$$\ddot{\mathbf{q}}_{n+1} = \alpha_1 (\mathbf{q}_{n+1} - \mathbf{q}_n) - \alpha_2 \dot{\mathbf{q}}_n - \alpha_3 \ddot{\mathbf{q}}_n \quad (2.8a)$$

$$\dot{\mathbf{q}}_{n+1} = \alpha_4 (\mathbf{q}_{n+1} - \mathbf{q}_n) + \alpha_5 \dot{\mathbf{q}}_n + \alpha_6 \ddot{\mathbf{q}}_n \quad (2.8b)$$

with the abbreviations

$$\begin{aligned} \alpha_1 &= \frac{1}{\beta \Delta t^2}, & \alpha_2 &= \frac{1}{\beta \Delta t}, & \alpha_3 &= \frac{1 - 2\beta}{2\beta} \\ \alpha_4 &= \frac{\gamma}{\beta \Delta t}, & \alpha_5 &= \left(1 - \frac{\gamma}{\beta}\right), & \alpha_6 &= \left(1 - \frac{\gamma}{2\beta}\right) \Delta t \end{aligned} \quad (2.9)$$

Here β and γ are the Newmark parameters, defining a corresponding time-stepping family. A popular choice is $\gamma = 0.5$ and $\beta = 0.25$, which is the trapezoidal rule, known to be energy conserving for linear dynamical systems [159].

2.2.2. The HHT scheme

The Hilber, Hughes and Taylor algorithm [76], also known as the α -method, represents a slight modification of the Newmark scheme outlined above. The scheme at hand incorporates numerical dissipation into the system without losing accuracy. This is governed by a newly introduced constant α which typically ranges from $\alpha \in [-0.3, 0]$. The modification of the scheme in Equation (2.7) concerns the evaluation of the positions, which yields

$$M \ddot{\mathbf{q}}_{n+1} + \nabla V(\mathbf{q}_{n+1+\alpha}) = \mathbf{0} \quad (2.10)$$

whereby the modified configuration vector reads

$$\mathbf{q}_{n+1+\alpha} = (1 + \alpha) \mathbf{q}_{n+1} - \alpha \mathbf{q}_n \quad (2.11)$$

The Equations (2.8) are still valid, so that the whole scheme can be rewritten in terms of \mathbf{q} . The Newmark values change according to

$$\beta = (1 - \alpha)^2 / 4 \quad (2.12a)$$

$$\gamma = (1 - 2\alpha) / 2 \quad (2.12b)$$

2.2.3. Variational integrator

The discrete equations of motion for the variational scheme, must be derived from the discrete Lagrangian (see e.g. [158, 99])

$$L_d(\mathbf{q}_n, \mathbf{q}_{n+1}) = \Delta t L \left(\frac{\mathbf{q}_n + \mathbf{q}_{n+1}}{2}, \frac{\mathbf{q}_{n+1} - \mathbf{q}_n}{\Delta t} \right) \quad (2.13)$$

The discrete Euler-Lagrange equations directly yield

$$D_2 L_d(\mathbf{q}_{n-1}, \mathbf{q}_n) + D_1 L_d(\mathbf{q}_n, \mathbf{q}_{n+1}) = \mathbf{0} \quad (2.14)$$

Having the continuous Lagrangian function at hand,

$$L(\mathbf{q}, \dot{\mathbf{q}}) = \frac{1}{2} \dot{\mathbf{q}} \cdot \mathbf{M} \dot{\mathbf{q}} - V(\mathbf{q}) \quad (2.15)$$

we can write the discrete Lagrangian according to

$$L_d(\mathbf{q}_n, \mathbf{q}_{n+1}) = \frac{1}{2\Delta t} (\mathbf{q}_{n+1} - \mathbf{q}_n) \cdot \mathbf{M} (\mathbf{q}_{n+1} - \mathbf{q}_n) - \Delta t \nabla V \left(\frac{\mathbf{q}_n + \mathbf{q}_{n+1}}{2} \right) \quad (2.16)$$

For the discrete Euler-Lagrange equations we directly obtain

$$D_1 L_d = \nabla_{\mathbf{q}_n} L_d = -\frac{1}{\Delta t} \mathbf{M} (\mathbf{q}_{n+1} - \mathbf{q}_n) - \frac{\Delta t}{2} \nabla V \left(\frac{\mathbf{q}_n + \mathbf{q}_{n+1}}{2} \right) \quad (2.17a)$$

$$D_2 L_d = \nabla_{\mathbf{q}_{n+1}} L_d = \frac{1}{\Delta t} \mathbf{M} (\mathbf{q}_{n+1} - \mathbf{q}_n) - \frac{\Delta t}{2} \nabla V \left(\frac{\mathbf{q}_n + \mathbf{q}_{n+1}}{2} \right) \quad (2.17b)$$

By inserting the expression above in Equation (2.14), we obtain the following set of nonlinear algebraic equations, governing the motion of the system

$$\frac{1}{\Delta t} \mathbf{M} (\mathbf{q}_{n+1} - 2\mathbf{q}_n + \mathbf{q}_{n-1}) + \frac{\Delta t}{2} \left[\nabla V \left(\frac{\mathbf{q}_{n-1} + \mathbf{q}_n}{2} \right) + \nabla V \left(\frac{\mathbf{q}_n + \mathbf{q}_{n+1}}{2} \right) \right] = \mathbf{0} \quad (2.18)$$

Further details concerning the implementation can also be found in [17].

2.2.4. Energy-momentum scheme

The implementation of the energy momentum scheme relies in general on the introduction of a so called discrete derivative (as will be outlined in detail in Chapter 3). In this special case, treating the free flying flexible dumbbell, the construction of an energy-momentum consistent time stepping scheme relies on the so-called G-equivariant discrete derivative due to Gonzalez [59, 58] (see also Section 5.1.1). This procedure guarantees the conservation of linear as well as angular momentum, while the total energy is also preserved. The discrete set of equations of motion reads

$$\frac{2}{\Delta t} \mathbf{M} (\mathbf{q}_{n+1} - \mathbf{q}_n) - 2\mathbf{M} \mathbf{v}_n + \bar{\nabla} V(\mathbf{q}_{n+1}, \mathbf{q}_n) = \mathbf{0} \quad (2.19)$$

The vital part is to evaluate the internal spring force algorithmically correct. Hence we rely on the G-equivariant discrete derivate which yields

$$\bar{\nabla}V(\mathbf{q}_{n+1}, \mathbf{q}_n) = \bar{\nabla}V(\mathbf{\Pi}_{n+1}, \mathbf{\Pi}_n) \left(\frac{\partial \mathbf{\Pi}}{\partial \mathbf{q}} \right)_{n+1/2} \quad (2.20)$$

where the gradient of the potential energy is expressed in invariants according to¹ (see [58])

$$\bar{\nabla}V(\mathbf{\Pi}_{n+1}, \mathbf{\Pi}_n) = \nabla V(\mathbf{\Pi})_{1/2} + \frac{V(\mathbf{\Pi}_2) - V(\mathbf{\Pi}_1) - \nabla V(\mathbf{\Pi}_{1/2}) \cdot (\mathbf{\Pi}_2 - \mathbf{\Pi}_1)}{\|\mathbf{\Pi}_2 - \mathbf{\Pi}_1\|^2} (\mathbf{\Pi}_2 - \mathbf{\Pi}_1) \quad (2.21)$$

The invariant can be found straightforwardly and yields for this example

$$\Pi = (\mathbf{q}^1 - \mathbf{q}^2) \cdot (\mathbf{q}^1 - \mathbf{q}^2) \quad (2.22)$$

A detailed description of the application of energy-momentum schemes for constrained mechanical systems will be given in the subsequent chapters of this thesis.

2.3. Results

For our numerical experiment we choose the following initial conditions

$$\mathbf{q}_0 = \begin{bmatrix} 0 \\ 1 \\ 0 \\ 0 \end{bmatrix}, \quad \mathbf{v}_0 = \begin{bmatrix} 5 \\ 0 \\ -5 \\ 0 \end{bmatrix} \quad (2.23)$$

Both mass points have the same value of $m_1 = m_2 = 1$. The Lennard-Jones potential is governed by $\varepsilon = 16.2$, $n = 12$ and $m = 6$. The system at hand can be classified as a Hamiltonian system with symmetry, i.e. the total system energy as well as the angular momentum represent conserved quantities. In the following we will compare all time integration schemes based upon the total energy, the angular momentum and the position of the masses at different step sizes.

The first Fig. 2.2 shows the comparison of the Newmark (NM) algorithm with the energy-momentum (EM) scheme. Obviously from Fig. 2.2a, the total system energy obtained with the NM-scheme is oscillating, whereby the amplitude of the oscillation is time-step dependent, decreasing by lowering the step size. The same characteristics is revealed in Fig. 2.2b, where the angular momentum of the Newmark scheme is compared with the constant value of the EM-method. In conclusion one can say, that the

¹Here $(\bullet)_{1/2} = \frac{(\bullet)_{n+1} + (\bullet)_n}{2}$ denotes the mid-point evaluation, while $(\bullet)_2$ stands for the evaluation at t_{n+1} , accordingly $(\bullet)_1$ gives the expression at t_n .

Newmark scheme is neither energy- nor angular momentum preserving, but gives qualitatively good results by lowering the time step size. The energy-momentum scheme is inherently energy and angular momentum conserving. Additionally the scheme does not show the same robustness as the favored EM-scheme, i.e. no convergence for coarse step sizes. For the simulation we choose $\gamma = 1/2$ and $\beta = 1/4$.

A comparable result can be achieved with the HHT-scheme with the parameter $\alpha = -0.1$.

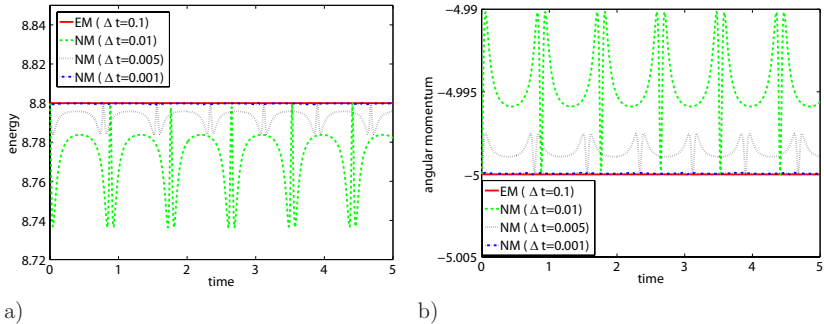


Figure 2.2.: Newmark scheme: a) Comparison of total system energy with the EM-scheme, b) comparison of angular momentum.

In contrast to the Newmark method, it incorporates numerical dissipation into the system, without losing accuracy. The dissipative character is shown in Fig. 2.3a, where for the coarse step size a decrease in the energy is obvious. Similarly this decrease is reflected in the angular momentum as well (see Fig. 2.3b). Again a step size refinement leads to results which converge towards the exact solution.

We next compare the variational integrator with the results of the EM-scheme. Obviously due to its symplecticity, the variational scheme is angular momentum preserving. This is indeed verified in Fig. 2.4b. For an arbitrary step size the solution of both schemes is equal. In contrast to that, the variational scheme typically is not energy conserving. This is shown in Fig. 2.4a where again a step size refinement leads to a convergence towards the real solution. The evolution of the system energy for the variational scheme is oscillating in character, yet it should be noted that the amplitude is higher than the one of the Newmark or HHT-scheme.

Finally a comparison of the relative configuration error is depicted in Fig. 2.5. To this end, the position vector of the second mass \mathbf{q}^2 has been used to calculate the relative error $e = \|\mathbf{q}^2 - \mathbf{q}_{ref}^2\| / \|\mathbf{q}_{ref}^2\|$ at time $t = 5s$. In this connection the reference solution \mathbf{q}_{ref}^2 has been obtained with $\Delta t = 10^{-4}$. Obviously all time integration schemes are second order accurate. Significantly the Newmark method, the HHT-scheme and

2. Prolog – Motivation

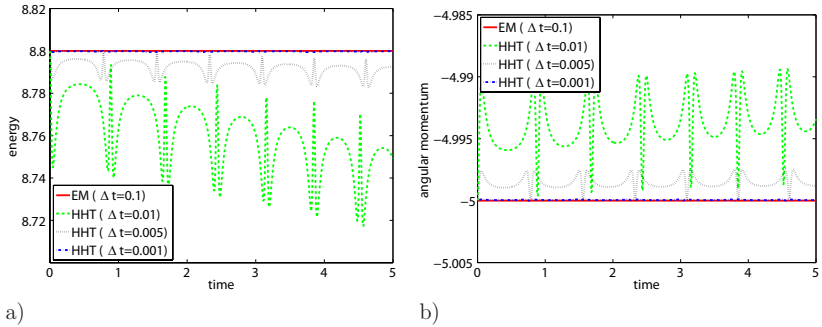


Figure 2.3: HHT scheme: a) Comparison of total system energy with the EM-scheme, b) comparison of angular momentum ($\alpha = -0.1$).

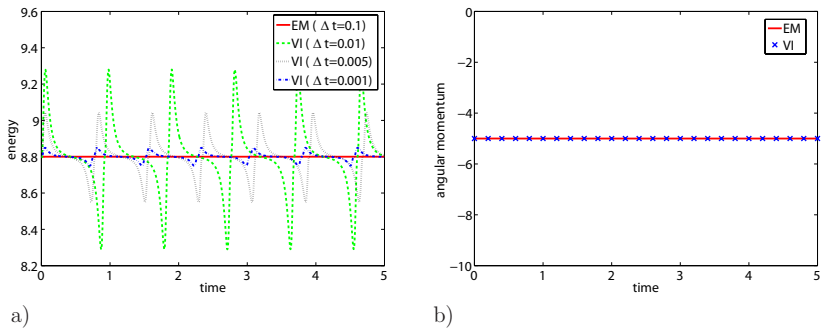


Figure 2.4: Variational scheme: a) Comparison of total system energy with the EM-scheme, b) comparison of angular momentum.

the variational integrator give comparable accurate results, while the energy-momentum scheme exhibits the best performance. Finally we see in Fig. 2.6 some snapshots of the

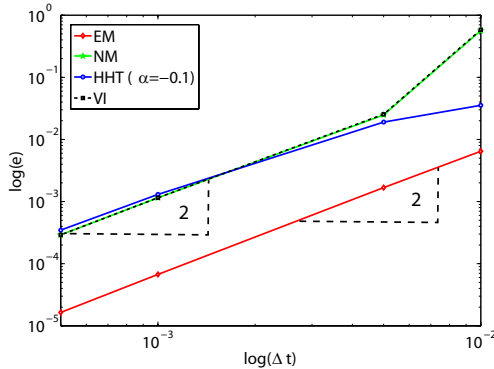


Figure 2.5.: Relative configuration error of the second mass point q^2 .

motion of the flexible dumbbell.

Essentially this simple example clearly demonstrated the influence of a proper time integration scheme for nonlinear dynamical systems. While the well-established schemes from the late 70s perform well with small step sizes, the variational and energy-momentum scheme exhibit a robust and mainly structure preserving integration. Especially the conservation of angular momentum turns out to be of major importance in this example, since it turns the schemes to be especially robust, i.e. that they can handle coarse time step sizes, while the NM and HHT scheme only performed well with an initial step size of $\Delta t = 0.01$. According to the comparison carried out with the example of the flexible dumbbell, we have to conclude that the energy-momentum consistent time stepping scheme offers superior qualities in comparison to common and also recently developed time stepping schemes. Hence this scheme will be the time integrator of choice for the subsequent chapters of this thesis.

Although we dealt in this introductory example with a system consisting of ODEs, all presented schemes can be extended straightforwardly for constrained systems governed by DAEs. The extension of the energy-momentum scheme will be outlined in detail in the following chapters. For the variational scheme we refer e.g. to [99, 17]. The Newmark and HHT scheme have been extended for DAE-systems in [83, 82, 112].

2. Prolog – Motivation

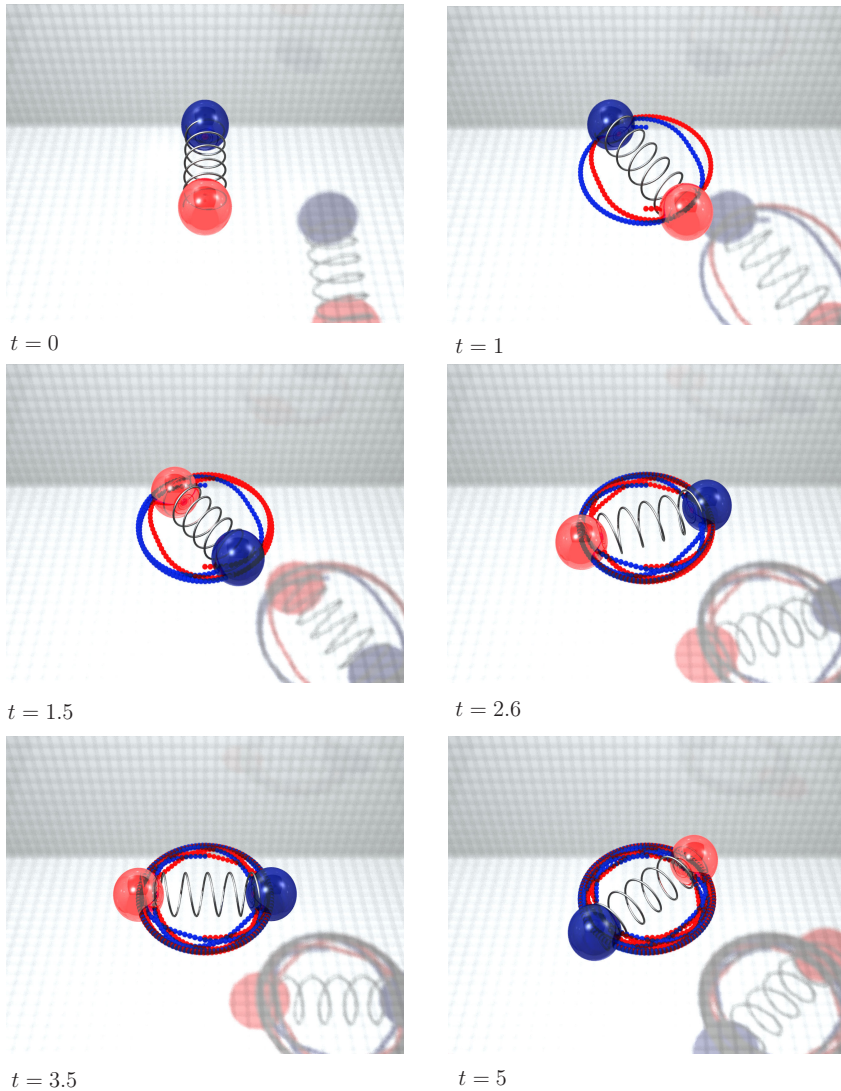
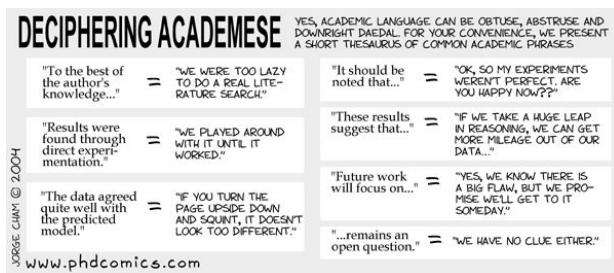


Figure 2.6.: Snapshots of the motion at $t \in \{0, 1, 1.5, 2.6, 3.5, 5\}$, obtained with $\Delta t = 0.01$ using the EM-scheme. The red and blue traces represent the motion of the mass points.

3. Dynamics of Constrained Mechanical Systems



"Piled Higher and Deeper" by Jorge Cham www.phdcomics.com

In this chapter we will present the fundamental equations of motion for rigid multibody systems. The derivation of the equations of motion relies on the variational principles of mechanics and will be carried out by applying Hamilton's principle (see e.g. [91, 57]). Obviously the form of the equations of motion is strongly influenced by the underlying choice of coordinates for the description of the orientation of the individual rigid bodies. Since we choose a redundant coordinate formulation – as will be outlined in Chapter 4 – we apply Hamilton's variational principle with side conditions in order to derive the equations of motion¹. These side conditions are represented here as a number of m constraint equations which generally constrain the mechanical system to a lower dimensional manifold

$$\Phi : [t_1, t_2] \times Q \rightarrow \mathbb{R}^m \quad \text{where} \quad Q \in \mathbb{R}^n \quad (3.1)$$

The constraints of the form above are called holonomic, if their temporal differentiated form $d\Phi/dt$ is integrable. If the constraints are not integrable, they are called

¹In contrast to generalized coordinates, redundancy always leads to additional algebraic equations, which means that the system of equations will always be of DAE-type.

3. Dynamics of Constrained Mechanical Systems

nonholonomic. A treatment of nonholonomic constraints is given in Section 5.5. Furthermore one distinguishes between scleronomic and rheonomic constraints. The latter are time dependent constraints as they will be outlined in Section 5.3, describing control problems. A classification of constraints is also given in Goldstein, Török or Marsden [57, 147, 103].

Hamilton's principle of stationary action for constrained mechanical systems reads

$$\delta S = \int_{t_1}^{t_2} \delta \tilde{L} dt \stackrel{!}{=} 0 \quad (3.2)$$

which means that the variation in time of the modified Lagrange-function must be minimized. The modified Lagrange function for constrained systems reads

$$\tilde{L}(\mathbf{v}, \mathbf{q}) = T(\mathbf{v}, \mathbf{q}) - V(\mathbf{q}) - \Phi(\mathbf{q})\boldsymbol{\lambda} \quad (3.3)$$

Here $\mathbf{q} \in \mathbb{R}^n$ represents the configuration vector, $T(\mathbf{v}, \mathbf{q})$ is the kinetic energy and $V(\mathbf{q})$ the potential energy. The incorporation of redundant coordinates is carried out by using so called Lagrange multipliers $\boldsymbol{\lambda}$.

Exploiting Equation (3.2) means to perform a variation with respect to each coordinate, leading to the following expression

$$\delta S = \int_{t_1}^{t_2} \left(\frac{\partial T}{\partial \mathbf{v}} \delta \mathbf{v} + \frac{\partial T}{\partial \mathbf{q}} \delta \mathbf{q} - \frac{\partial V}{\partial \mathbf{q}} \delta \mathbf{q} - \frac{\partial \Phi}{\partial \mathbf{q}} \cdot \boldsymbol{\lambda} \delta \mathbf{q} - \Phi \delta \boldsymbol{\lambda} \right) dt \stackrel{!}{=} 0 \quad (3.4)$$

Taking into account the relationship between displacement and velocity

$$\dot{\mathbf{q}} = \mathbf{v} \quad (3.5)$$

we now perform a partial integration of the first term inside Equation (3.4), which leads to

$$\int_{t_1}^{t_2} \frac{\partial T}{\partial \mathbf{v}} \delta \mathbf{v} dt = \left[\frac{\partial T}{\partial \mathbf{v}} \delta \mathbf{q} \right]_{t_1}^{t_2} - \int_{t_1}^{t_2} \frac{d}{dt} \left(\frac{\partial T}{\partial \mathbf{v}} \right) \delta \mathbf{q} dt \quad (3.6)$$

The first term of the right hand side is neglected since there is no variation along the borders. Inserting the expression above back into Equation (3.4), while recalling the definition of the Lagrange function $L = T - V$, we finally obtain the first variation

$$\int_{t_1}^{t_2} \left(-\frac{d}{dt} \left(\frac{\partial L}{\partial \mathbf{v}} \right) + \frac{\partial L}{\partial \mathbf{q}} - \frac{\partial \Phi}{\partial \mathbf{q}} \cdot \boldsymbol{\lambda} \right) \delta \mathbf{q} dt - \int_{t_1}^{t_2} \Phi(\mathbf{q}) \delta \boldsymbol{\lambda} dt \stackrel{!}{=} 0 \quad (3.7)$$

Applying the fundamental lemma of variational calculus [130], saying that the expressions inside the brackets in Equation (3.7) must be zero for all times $t \in \mathbb{R}_+$, leads to the Lagrange equations of first kind, also known as the Euler-Lagrange equations [120, 91]

$$\frac{d}{dt} \left(\frac{\partial L}{\partial \mathbf{v}} \right) - \frac{\partial L}{\partial \mathbf{q}} + \frac{\partial \Phi}{\partial \mathbf{q}} \cdot \boldsymbol{\lambda} = \mathbf{Q} \quad (3.8a)$$

$$\Phi(\mathbf{q}) = 0 \quad (3.8b)$$

Here \mathbf{Q} accounts for external loads which cannot be derived from a potential. The equations above obviously represent a $n + m$ -dimensional set of Differential-Algebraic-Equations (DAEs) of index three (see [40, 123, 90]). In the following we will present the continuous equations of motion for constrained rigid multibody systems, accompanied with size reduction techniques. A temporal discretization will be performed, leading to energy-momentum schemes for holonomic-scleronomous mechanical systems.

3.1. Continuous Equations of Motion

Due to the specific choice of coordinates (see Chapter 4) we obtain a *constant* and symmetric mass matrix $\mathbf{M} \in \mathbb{R}^{n \times n}$. Hence the kinetic energy can be expressed as

$$T(\mathbf{v}) = \frac{1}{2} \mathbf{v} \cdot \mathbf{M} \mathbf{v} \quad (3.9)$$

According to that, we can directly identify the terms of Equation (3.8a) as

$$\frac{d}{dt} \left(\frac{\partial L}{\partial \mathbf{v}} \right) = \mathbf{M} \dot{\mathbf{v}} \quad \text{and} \quad \frac{\partial L}{\partial \mathbf{q}} = \nabla V(\mathbf{q}) \quad (3.10)$$

Reformulating Equations (3.8) in first order form using Equation (3.5), we finally obtain the continuous DAE-set for rigid multibody systems

$$\dot{\mathbf{q}} - \mathbf{v} = 0 \quad (3.11a)$$

$$\mathbf{M} \dot{\mathbf{v}} - \mathbf{f} + \mathbf{G}^T \boldsymbol{\lambda} = 0 \quad (3.11b)$$

$$\boldsymbol{\Phi}(\mathbf{q}) = 0 \quad (3.11c)$$

Here $\mathbf{q}(t) \in \mathbb{R}^n$ specifies the configuration of the mechanical system at time t , where $\mathbf{v}(t) \in \mathbb{R}^n$ is the velocity vector. Together (\mathbf{q}, \mathbf{v}) form the vector of state space coordinates (see, for example, Rosenberg [128]), where a superposed dot denotes differentiation with respect to time. Moreover, $\mathbf{f} \in \mathbb{R}^n$ is a load vector which in the present work is decomposed according to

$$\mathbf{f} = \mathbf{Q} - \nabla V(\mathbf{q}) \quad (3.12)$$

Recapitulating, $V(\mathbf{q}) \in \mathbb{R}$ represents the potential energy function, while $\mathbf{Q} \in \mathbb{R}^n$ accounts for loads which can not be derived from a potential. Moreover, the constraints reducing the mechanical system to a smaller manifold are given by $\boldsymbol{\Phi}(\mathbf{q}) \in \mathbb{R}^m$. The derivation of the constraint equations with respect to the configuration $\mathbf{G} = D\boldsymbol{\Phi}(\mathbf{q}) \in \mathbb{R}^{m \times n}$ is labeled as the constraint Jacobian. The vector of Lagrange multipliers $\boldsymbol{\lambda} \in \mathbb{R}^m$ specifies the relative magnitude of the constraint forces. In the description above, it is tacitly assumed that the m constraints are independent.

Due to the presence of holonomic constraints (3.11c), the configuration space of the system is given by

$$\mathbf{Q} = \{\mathbf{q}(t) \in \mathbb{R}^n \mid \boldsymbol{\Phi}(\mathbf{q}) = \mathbf{0}\} \quad (3.13)$$

As outlined above, Equations (3.11) presently concern only holonomic-scleronomic constraints. An extension to rheonomic and nonholonomic constraints will be given in the following chapters.

3.1.1. Size-reduction of the DAEs

Obviously the set of DAEs (3.11) is comparatively large, i.e. one has to solve for the redundant coordinates \mathbf{q} as well as for the corresponding Lagrange multipliers $\boldsymbol{\lambda}$. Therefore a size reduction to a minimal size is aspired.

The DAEs can be reformulated in various ways. Here we follow the concept of null space methods for saddle point problems (see, for example, Benzi et al. [14] or Strang [145]), accompanied with a reparametrization of the configuration manifold. Null space methods rely on the introduction of a properly designed matrix, which in the present work will be called the null space matrix. This procedure relies on the works of Betsch (see [15, 18]).

The geometric constraints give rise to kinematic (or hidden) constraints which follow from the consistency condition $d\boldsymbol{\Phi}/dt = 0$. Accordingly, the kinematic constraints assume the form

$$\mathbf{G}\mathbf{v} = \mathbf{0} \quad (3.14)$$

Suppose that the columns of $\mathbf{P} \in \mathbb{R}^{n \times (n-m)}$ span the null space of $\mathbf{G} \in \mathbb{R}^{m \times n}$ and call \mathbf{P} the null space matrix. Thus

$$\mathbf{G}\mathbf{P} = \mathbf{0} \quad (3.15)$$

and, consistent with (3.14), admissible velocities² $\mathbf{v} \in T_{\mathbf{q}}\mathbf{Q} = \ker \mathbf{G}(\mathbf{q})$ may be written in the form

$$\mathbf{v} = \mathbf{P}\boldsymbol{\nu} \quad (3.16)$$

with independent velocities $\boldsymbol{\nu} \in \mathbb{R}^{n-m}$. Using (3.16), the reduced form of the kinetic energy \tilde{T} is defined by

$$\tilde{T}(\mathbf{q}, \boldsymbol{\nu}) = \frac{1}{2} \boldsymbol{\nu} \cdot \tilde{\mathbf{M}} \boldsymbol{\nu} \quad (3.17)$$

²hereby \ker denotes the kernel of a matrix, see Strang [145].

with the reduced mass matrix

$$\widetilde{\mathbf{M}} = \mathbf{P}^T \mathbf{M} \mathbf{P} \quad (3.18)$$

Note that $\widetilde{\mathbf{M}}$ is generally configuration-dependent and assumed to be positive-definite. The null space matrix can be employed to eliminate the forces of constraint. Specifically, pre-multiplying (3.11b) by \mathbf{P}^T and making use of (3.15) and (3.16) yields the alternative reduced formulation

$$\dot{\mathbf{q}} - \mathbf{P}\boldsymbol{\nu} = \mathbf{0} \quad (3.19a)$$

$$\widetilde{\mathbf{M}}\dot{\boldsymbol{\nu}} + \mathbf{P}^T \mathbf{M} \dot{\mathbf{P}}\boldsymbol{\nu} - \mathbf{P}^T \mathbf{f} = \mathbf{0} \quad (3.19b)$$

$$\boldsymbol{\Phi}(\mathbf{q}) = \mathbf{0} \quad (3.19c)$$

which governs the motion of the constrained mechanical system. A further size-reduction may be achieved by expressing the redundant coordinates $\mathbf{q} \in \mathbb{R}^n$ in terms of local coordinates for the parametrization of the configuration manifold \mathbf{Q} :

$$\mathbf{F} : U \subset \mathbb{R}^{n-m} \mapsto \mathbf{Q} \quad \text{i.e.} \quad \boldsymbol{\Phi}(\mathbf{q}) = \boldsymbol{\Phi}(\mathbf{F}(\mathbf{u})) = \mathbf{0} \quad (3.20)$$

Remark 3.1.1 *The notion of the null space matrix is closely related to the natural orthogonal complement introduced by Angeles and co-workers, see [2] and the references cited therein. However, in contrast to these works, the present formulation of multibody dynamics does neither rely on the classical Newton-Euler equations for rigid bodies nor does the following discretization start from (3.19).*

3.2. Discrete Equations of Motion: Energy-Momentum Schemes

'Experience indicates that the best results can generally be obtained using a direct discretization of the equations of motion.' Leimkuhler & Reich [93, Sec. 7.2.1]

The quote above characterizes the procedure we will apply in order to obtain a time discretized set of equations of motion. The presented approach aims at the design of time-stepping schemes which inherit key characteristic features from the underlying continuous formulation, such as conservation of total energy and momentum maps. Hence, we will apply the discrete null space method developed in [15, 18, 96] for the time integration of the equations of motion. In essence, this method relies on the direct discretization of the DAEs (3.11) and a subsequent size-reduction of the discrete system. In this sense in the following we will present two schemes which render the desired conservation properties for arbitrary time step sizes. These schemes represent the fundament for the extension to the rheonomic or nonholonomic case (see Sections 5.3 and 5.5) as well as for the treatment of hybrid multibody systems in Chapter 6.

3.2.1. The basic energy-momentum scheme

Concerning the direct discretization of the DAEs (3.11), we employ the methodology developed by Gonzalez [60], see also Betsch and Steinmann [26]. Consider a representative time interval $[t_n, t_{n+1}]$ with time step $\Delta t = t_{n+1} - t_n$, and given state space coordinates $\mathbf{q}_n \in \mathbf{Q}$, $\mathbf{v}_n \in \mathbb{R}^n$ at t_n . The discretized version of (3.11) is given by

$$\mathbf{q}_{n+1} - \mathbf{q}_n = \frac{\Delta t}{2} (\mathbf{v}_n + \mathbf{v}_{n+1}) \quad (3.21a)$$

$$\mathbf{M} (\mathbf{v}_{n+1} - \mathbf{v}_n) = \Delta t \mathbf{f}(\mathbf{q}_n, \mathbf{q}_{n+1}) - \Delta t \mathbf{G}(\mathbf{q}_n, \mathbf{q}_{n+1})^T \bar{\boldsymbol{\lambda}} \quad (3.21b)$$

$$\boldsymbol{\Phi}(\mathbf{q}_{n+1}) = \mathbf{0} \quad (3.21c)$$

with

$$\mathbf{f}(\mathbf{q}_n, \mathbf{q}_{n+1}) = \mathbf{Q}(\mathbf{q}_n, \mathbf{q}_{n+1}) - \bar{\nabla} V(\mathbf{q}_n, \mathbf{q}_{n+1}) \quad (3.22)$$

In the following, the algorithm (3.21) will be called the basic energy-momentum (**BEM**) scheme (see [28]). The advantageous algorithmic conservation properties (see Remark 3.2.1 below) of the **BEM** scheme are linked to the notion of a discrete gradient (or derivative) of a function $f : \mathbb{R}^n \mapsto \mathbb{R}$ according to Gonzalez [59, 58, 60]. In the present work $\bar{\nabla} f(\mathbf{q}_n, \mathbf{q}_{n+1})$ denotes the discrete gradient of f . It is worth mentioning, that if f is at most quadratic then the discrete gradient coincides with the standard gradient evaluated in the mid-point configuration $\mathbf{q}_{n+\frac{1}{2}} = (\mathbf{q}_n + \mathbf{q}_{n+1})/2$, that is, in this case $\bar{\nabla} f(\mathbf{q}_n, \mathbf{q}_{n+1}) = \nabla f(\mathbf{q}_{n+\frac{1}{2}})$. In (3.21b) the discrete gradient is applied to the potential energy function V as well as to the constraint functions Φ_i . In particular, the discrete constraint Jacobian is given by

$$\mathbf{G}(\mathbf{q}_n, \mathbf{q}_{n+1})^T = [\bar{\nabla} \Phi_1(\mathbf{q}_n, \mathbf{q}_{n+1}), \dots, \bar{\nabla} \Phi_m(\mathbf{q}_n, \mathbf{q}_{n+1})] \quad (3.23)$$

Concerning (3.22), for the present purposes it suffices to set $\mathbf{Q}(\mathbf{q}_n, \mathbf{q}_{n+1}) = \mathbf{Q}(\mathbf{q}_{n+\frac{1}{2}})$. The **BEM** scheme can be used to determine $\mathbf{q}_{n+1} \in \mathbf{Q}$, $\mathbf{v}_{n+1} \in \mathbb{R}^n$ and $\bar{\boldsymbol{\lambda}} \in \mathbb{R}^m$. To this end, one may substitute for \mathbf{v}_{n+1} from (3.21a) into (3.21b) and then solve the remaining system of nonlinear algebraic equations for the $n + m$ unknowns $(\mathbf{q}_{n+1}, \bar{\boldsymbol{\lambda}})$. We refer to [15] for further details of the implementation.

Remark 3.2.1 *The algorithm (3.21) inherits fundamental mechanical properties from the underlying continuous formulation such as (i) conservation of energy, and (ii) conservation of momentum maps that are at most quadratic in (\mathbf{q}, \mathbf{v}) . While algorithmic conservation of linear momentum is a trivial matter, algorithmic conservation of angular momentum is made possible by the specific formulation of rigid bodies and multibody systems proposed in the present work. Indeed, it is shown in Appendix A.2 that the present description of multibody systems yields quadratic expressions for the angular momentum. Moreover, Appendix A.1 contains a verification of the aforementioned conservation properties.*

As already mentioned in Section 3.1.1, besides the relatively large number of unknowns, a second drawback of the **BEM**-scheme lies in the condition number of the iteration matrix for the solution of the nonlinear system of Equations (3.21). According to Petzold [123] the condition number is of the order $\mathcal{O}(h^{-3})$, which implies that for decreasing time-steps, the iteration matrix becomes more and more ill-conditioned (for a proof see Leyendecker [95]). Therefore the following section proposes a modified scheme, which remedies both drawbacks of the **BEM**-scheme.

3.2.2. The reduced energy-momentum scheme

To reduce the computational costs and improve the conditioning of the algebraic system to be solved, we perform a size-reduction of the **BEM** scheme. Similar to the continuous case treated in Section 3.1.1, we have to devise a discrete null space matrix $\mathbf{P}(\mathbf{q}_n, \mathbf{q}_{n+1})$, the columns of which span the null space of the discrete constraint Jacobian (3.23). In particular, as proposed in [18], we seek a discrete null space matrix which satisfies the following properties:

- (a) In the limit of vanishing time steps, $\Delta t \rightarrow 0$, the discrete version has to coincide with the continuous one. That is,

$$\mathbf{P}(\mathbf{q}_n, \mathbf{q}_{n+1}) \rightarrow \mathbf{P}(\mathbf{q}_n) \quad \text{as} \quad \mathbf{q}_{n+1} \rightarrow \mathbf{q}_n \quad (3.24)$$

- (b) The $n \times (n - m)$ matrix $\mathbf{P}(\mathbf{q}_n, \mathbf{q}_{n+1})$ has full rank and satisfies

$$\mathbf{G}(\mathbf{q}_n, \mathbf{q}_{n+1})\mathbf{P}(\mathbf{q}_n, \mathbf{q}_{n+1}) = \mathbf{0} \quad (3.25)$$

This condition should be fulfilled at least for $\mathbf{q}_n, \mathbf{q}_{n+1} \in \mathcal{Q}$.

In the following chapters we will outline in detail the construction of viable null space matrices for open-loop multibody systems (i.e. for basic kinematic pairs) as well as for closed-loop systems (i.e. the elimination of loop closure constraints). Once a discrete null space matrix is at hand, the discrete constraint forces can be eliminated from the **BEM** scheme. To this end, pre-multiplication of (3.21b) by $\mathbf{P}(\mathbf{q}_n, \mathbf{q}_{n+1})^T$ and use of property (b) yields the reduced scheme

$$\mathbf{q}_{n+1} - \mathbf{q}_n = \frac{\Delta t}{2} (\mathbf{v}_n + \mathbf{v}_{n+1}) \quad (3.26a)$$

$$\mathbf{P}(\mathbf{q}_n, \mathbf{q}_{n+1})^T \mathbf{M} (\mathbf{v}_{n+1} - \mathbf{v}_n) = \Delta t \mathbf{P}(\mathbf{q}_n, \mathbf{q}_{n+1})^T \mathbf{f}(\mathbf{q}_n, \mathbf{q}_{n+1}) \quad (3.26b)$$

$$\Phi(\mathbf{q}_{n+1}) = \mathbf{0} \quad (3.26c)$$

A further size-reduction can be accomplished by a reparametrization of the remaining unknowns. For open-loop multibody systems it is generally feasible to choose $n - m$

local coordinates (e.g. joint variables) for the parametrization of the configuration space (see Sections 5.2.1 and 5.2.2). Accordingly, use can be made of a mapping $\mathbf{F} : \mathbb{R}^{n-m} \mapsto \mathbb{Q} \subset \mathbb{R}^n$, such that

$$\mathbf{q}_{n+1} = \mathbf{F}(\mathbf{u}) \quad (3.27)$$

Substitution from (3.27) into (3.26) yields $n - m$ algebraic equations for the determination of the new unknowns $\mathbf{u} \in \mathbb{R}^{n-m}$. The case of closed-loop multibody systems can be dealt with in a similar way by taking into account the loop-closure constraints (see Section 5.2.3). Further details of the size-reduction along with the corresponding implementation can be found in [15]. Application of the two size-reduction steps outlined above yields a scheme which will be referred to as the reduced energy-momentum (**REM**) scheme in the following.

3.3. Benefits of the DAE-Formulation

The choice of redundant coordinates, which will be outlined in the next Section, leads to a set of Differential-Algebraic-Equations. As outlined before, the two drawbacks (i) a high number of unknowns and (ii) possible conditioning problems were treated by applying specific reduction techniques. In contrast to different common coordinates which describe rigid body rotation, e.g. joint-angles, Euler angles, Quaternions (see e.g. [22]) or other 3-parameter representations of finite rotations, the benefit of our approach is the very simple extension of the basic scheme by different modeling techniques³. As will be outlined in detail in Chapter 5, it will become obvious how features like the coordinate augmentation, the modeling of dissipation, the implementation of rheonomic, nonholonomic or coupling constraints for hybrid systems can be implemented in a straightforward way. In general, all these features will be appended to the **BEM**-scheme as additional constraints, accompanied by a corresponding constraint Jacobian. In this sense the **BEM**-scheme forms the base for the extension by modeling features. In general the system of DAEs can be written as

$$\dot{\mathbf{q}} - \mathbf{v} = 0 \quad (3.28a)$$

$$M\dot{\mathbf{v}} - \mathbf{f} + \mathbf{G}^T\boldsymbol{\lambda} + \mathbf{A}^T\boldsymbol{\mu} = 0 \quad (3.28b)$$

$$\boldsymbol{\Phi}(\mathbf{q}) = 0 \quad (3.28c)$$

$$\boldsymbol{\Phi}_{\text{add}}(\mathbf{q}, \mathbf{v}, t) = 0 \quad (3.28d)$$

where $\boldsymbol{\Phi}_{\text{add}}(\mathbf{q}, \mathbf{v}, t)$ accounts for arbitrary constraint equations. As already known, the incorporation is accompanied with a corresponding constraint Jacobian, in general labeled here as \mathbf{A} and Lagrange multipliers $\boldsymbol{\mu}$. A specific format of these new expressions

³This advantage is strictly linked to the application of the rotationless formulation for the description of rigid body rotations, as presented in Chapter 4.

will be given in Section 5.3, which will introduce control constraints, Section 5.5 incorporates nonholonomic constraints and finally introducing coupling constraints as outlined in Chapter 6. These sections will also provide a detailed presentation of the discrete counterparts of the continuous formulation. In this sense we will always aim at the design of energy-momentum schemes, which again needs a proper evaluation of the discrete constraint Jacobians.

The incorporation of dissipative effects can also be done in a straightforward manner. Nonconservative systems will be modeled by simply adding an internal load vector to the equations of motion according to

$$\dot{\mathbf{q}} - \mathbf{v} = \mathbf{0} \quad (3.29a)$$

$$\mathbf{M}\dot{\mathbf{v}} - \mathbf{f} + \mathbf{G}^T \boldsymbol{\lambda} + \mathbf{F}_{\text{int}} = \mathbf{0} \quad (3.29b)$$

$$\boldsymbol{\Phi}(\mathbf{q}) = \mathbf{0} \quad (3.29c)$$

The internal load vector \mathbf{F}_{int} , which will be the object of interest in Section 5.4, needs a proper treatment in the time discrete case as well, similar to the constraint Jacobians mentioned above. In this case we aim at the design of so-called energy-consistent schemes, which do not suffer from artificial numerical dissipation or an unphysical energy blow-up respectively.

All features can be combined to a global system, rendering an energy-consistent time integration scheme for hybrid multibody systems as will be outlined with the examples in Chapter 6.

The extension of the **BEM**-scheme by all of these features does not influence the reduction techniques outlined in Section 3.1.1. The procedures can still be applied to reduce the number of unknowns, e.g. it will be demonstrated in Section 5.1 how augmented coordinates can be eliminated as well. The second size reduction, which was the reparametrization of the configuration manifold, is also still applicable, as will be demonstrated with the example of a radio telescope in Section 5.3.3.

4. Rotationless Formulation of the Rigid Body

'...in the author's personal opinion, Euler angles are a necessary evil. Not being frame-invariant, their manipulation tends to become extremely cumbersome...' Angeles [2, Preface to the Second Edition]

This chapter introduces the rotationless formulation for the description of rigid body rotation. This formulation, which relies on the so-called direction cosine description, forms the base for the design of energy-momentum conserving schemes as they were outlined in the chapter before. The treatment of open, as well as closed loop multibody systems, can be done in the same straightforward way. In this approach the orientation of each rigid body is characterized by the elements of the rotation matrix (or the direction cosine matrix). This leads to a set of redundant coordinates which are subject to holonomic constraints. In this connection two types of constraints may be distinguished (see also Betsch and Steinmann [27]): (i) Internal constraints which are intimately connected to the assumption of rigidity and, (ii) external constraints due to the interconnection of the bodies constituting the multibody system. Item (ii) implies that loop-closure constraints can be taken into account without any additional difficulty. The resulting DAEs exhibit a comparatively simple structure. Another advantage of the present rotationless formulation of multibody systems lies in the fact that planar motions as well as spatial motions can be treated without any conceptual differences. That is, the extension from the planar case to the full three-dimensional case can be accomplished in a straightforward way, which is in severe contrast to formulations employing rotations, due to their non-commutative nature in the three-dimensional setting. It is worth mentioning, that the present rotationless approach is closely related to the natural coordinates formulation advocated by García de Jalón et al. [52, 50], which will be shown in Remark 4.1.1 of the following section.

4.1. The Rigid Body

Let $\mathbf{X} = X^i \mathbf{e}_i$ ¹ be a material point which belongs to the reference configuration $V \subset \mathbb{R}^3$ of the rigid body. The spatial position of $\mathbf{X} \in V$ at time t relative to an inertial Cartesian basis $\{\mathbf{e}_I\}$ is given by

$$\mathbf{x}(\mathbf{X}, t) = \boldsymbol{\varphi}(t) + X_i \mathbf{d}_i(t) \quad (4.1)$$

where $\boldsymbol{\varphi}(t) \in \mathbb{R}^3$ denotes the position of the center of mass, $\{\mathbf{d}_i\}$, $\mathbf{d}_i(t) \in \mathbb{R}^3$ ($i = 1, 2, 3$) is a body fixed director frame, and t denotes the time. The director frame is assumed to coincide with the principal axes of the body. It is obvious from Figure (4.1) that the configuration of the rigid body is specified by the vector of coordinates

$$\mathbf{q} = [\boldsymbol{\varphi}^T \quad \mathbf{d}_1^T \quad \mathbf{d}_2^T \quad \mathbf{d}_3^T]^T \quad (4.2)$$

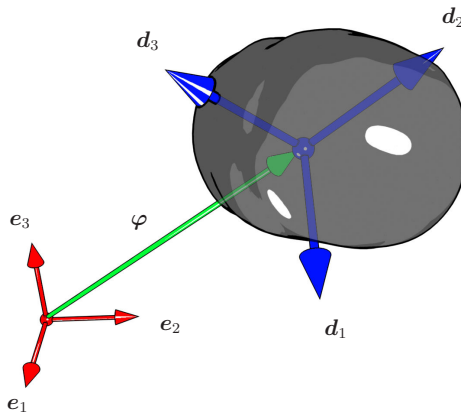


Figure 4.1.: The rigid body – rotationless description.

Since the directors are fixed in the body and moving with it, they have to stay orthonormal for all times $t \in \mathbb{R}_+$. This fact gives rise to six independent geometric (or holonomic) constraints $\Phi_{\text{int}}^i(\mathbf{q}) = 0$, which will be termed internal constraints, since they are intimately connected with the assumption of rigidity. The functions $\Phi_{\text{int}}^i : \mathbb{R}^{12} \rightarrow \mathbb{R}$

¹In this work the summation convention applies to repeated lower case Roman indices.

may be arranged in the vector of internal constraint functions

$$\Phi_{\text{int}}(\mathbf{q}) = \begin{bmatrix} \mathbf{d}_1 \cdot \mathbf{d}_1 - 1 \\ \mathbf{d}_2 \cdot \mathbf{d}_2 - 1 \\ \mathbf{d}_3 \cdot \mathbf{d}_3 - 1 \\ \mathbf{d}_1 \cdot \mathbf{d}_2 \\ \mathbf{d}_1 \cdot \mathbf{d}_3 \\ \mathbf{d}_2 \cdot \mathbf{d}_3 \end{bmatrix} \quad (4.3)$$

In the following we distinguish between *internal* constraints associated with the assumption of rigidity and *external* constraints, which account for the connection between contiguous bodies in a multibody system.

With regard to the internal constraints, the configuration space of the free rigid body may be now written in the form

$$\mathbb{Q}_{\text{free}} = \{\mathbf{q}(t) \in \mathbb{R}^{12} \mid \Phi(\mathbf{q}) = \mathbf{0}, (\mathbf{d}_1 \times \mathbf{d}_2) \cdot \mathbf{d}_3 = +1\} \quad (4.4)$$

Note that the director frame $\{\mathbf{d}_1, \mathbf{d}_2, \mathbf{d}_3\}$ can be connected with a rotation matrix $\mathbf{R} \in \text{SO}(3)$ through the relationship $\mathbf{d}_\alpha = \mathbf{R}\mathbf{e}_\alpha$. In this connection,

$$\text{SO}(3) = \{\mathbf{R} \in \mathbb{R}^{3 \times 3} \mid \mathbf{R}^T \mathbf{R} = \mathbf{I}_3, \det \mathbf{R} = +1\} \quad (4.5)$$

is the special orthogonal group of \mathbb{R}^3 . Accordingly, $R_{\alpha\beta} = \mathbf{e}_\alpha \cdot \mathbf{d}_\beta$, such that the directors coincide with the columns of the rotation matrix. Alternatively, the configuration space of the free rigid body may be written as

$$\mathbb{Q}_{\text{free}} = \mathbb{R}^3 \times \text{SO}(3) \subset \mathbb{R}^{12}$$

The motion of the free rigid body can now be described by means of the DAEs (3.11). The kinetic energy of the rigid body can be written as $T = \frac{1}{2} \dot{\mathbf{q}} \cdot \mathbf{M} \dot{\mathbf{q}}$, where a superposed dot denotes differentiation with respect to time and \mathbf{M} is a 12×12 mass matrix. One of the main distinguishing features of the rotationless rigid body formulation is the fact that the mass matrix is *constant* and *diagonal*. Specifically,

$$\mathbf{M} = \begin{bmatrix} \mathcal{M}\mathbf{I} & \mathbf{0} & \mathbf{0} & \mathbf{0} \\ \mathbf{0} & \mathcal{E}_1\mathbf{I} & \mathbf{0} & \mathbf{0} \\ \mathbf{0} & \mathbf{0} & \mathcal{E}_2\mathbf{I} & \mathbf{0} \\ \mathbf{0} & \mathbf{0} & \mathbf{0} & \mathcal{E}_3\mathbf{I} \end{bmatrix} \quad (4.6)$$

where \mathbf{I} and $\mathbf{0}$ are the 3×3 identity and zeros matrices, \mathcal{M} denotes the total mass of the rigid body and \mathcal{E}_I ($I = 1, 2, 3$) are the principal values of the Euler tensor relative to the center of mass. The connection with the principal values of the convected inertia tensor is given by

$$\mathcal{E}_I = \frac{1}{2} [\mathcal{J}_J + \mathcal{J}_K - \mathcal{J}_I] \quad (4.7)$$

4. Rotationless Formulation of the Rigid Body

for even permutations of the indices (I, J, K) .

Furthermore, in view of the constraint functions (4.3), the constraint Jacobian pertaining to the free rigid body is given by $\mathbf{G}_{int} = D\boldsymbol{\Phi}_{int}(\mathbf{q})$. Thus

$$\mathbf{G}_{int}(\mathbf{q}) = \begin{bmatrix} \mathbf{0}^T & 2\mathbf{d}_1^T & \mathbf{0}^T & \mathbf{0}^T \\ \mathbf{0}^T & \mathbf{0}^T & 2\mathbf{d}_2^T & \mathbf{0}^T \\ \mathbf{0}^T & \mathbf{0}^T & \mathbf{0}^T & 2\mathbf{d}_3^T \\ \mathbf{0}^T & \mathbf{d}_2^T & \mathbf{d}_1^T & \mathbf{0}^T \\ \mathbf{0}^T & \mathbf{d}_3^T & \mathbf{0}^T & \mathbf{d}_1^T \\ \mathbf{0}^T & \mathbf{0}^T & \mathbf{d}_3^T & \mathbf{d}_2^T \end{bmatrix} \quad (4.8)$$

To summarize, the motion of the spatial free rigid body is governed by the DAEs (3.11), with $n = 12$ and $m = 6$. This rigid body formulation is the cornerstone of the present approach to the energy-momentum integration of arbitrary multibody systems. Additional details about the present rigid body formulation may be found in [25, 18, 28]. As mentioned before, the remark below shall illustrate the similarity to the natural coordinate formulation favoured by García de Jalón.

Remark 4.1.1 *The present rotationless formulation of rigid bodies is closely related to the notion of natural coordinates advocated by García de Jalón and co-workers. This can be easily shown by considering the connection between the present coordinates in (4.2) and the natural coordinates associated with the most general element, see [51]. The configuration of the most general element is specified by*

$$\mathbf{q}^e = [\mathbf{r}_A^T \quad \mathbf{r}_B^T \quad \mathbf{u}^T \quad \mathbf{v}^T]^T \quad (4.9)$$

where $\mathbf{r}_A, \mathbf{r}_B$ denote the position vectors of two basic points A, B , and \mathbf{u}, \mathbf{v} denote two non-coplanar unit vectors (Fig. 4.2). The natural coordinates in (4.9) can now be expressed in terms of the present coordinates

$$\begin{aligned} \mathbf{r}_A &= \boldsymbol{\varphi} + X_A^i \mathbf{d}_i & \mathbf{u} &= U^i \mathbf{d}_i \\ \mathbf{r}_B &= \boldsymbol{\varphi} + X_B^i \mathbf{d}_i & \mathbf{v} &= V^i \mathbf{d}_i \end{aligned} \quad (4.10)$$

Here X_A^i, X_B^i are the material coordinates of points A, B , and U^i, V^i are the components of the unit vectors \mathbf{u}, \mathbf{v} relative to the body frame. Alternatively, we may write

$$\mathbf{q}^e = \mathbf{T}\mathbf{q} \quad (4.11)$$

where \mathbf{T} is a 12×12 transformation matrix of the form

$$\mathbf{T} = \begin{bmatrix} \mathbf{I} & X_A^1 \mathbf{I} & X_A^2 \mathbf{I} & X_A^3 \mathbf{I} \\ \mathbf{I} & X_B^1 \mathbf{I} & X_B^2 \mathbf{I} & X_B^3 \mathbf{I} \\ \mathbf{0} & U^1 \mathbf{I} & U^2 \mathbf{I} & U^3 \mathbf{I} \\ \mathbf{0} & V^1 \mathbf{I} & V^2 \mathbf{I} & V^3 \mathbf{I} \end{bmatrix} \quad (4.12)$$

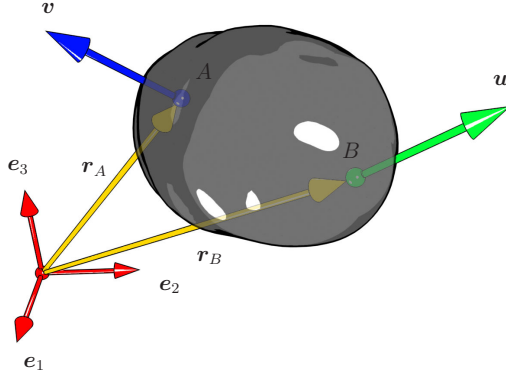


Figure 4.2.: The rigid body – natural coordinates.

The mass matrix pertaining to the most general element is given by $\mathbf{M}^e = \mathbf{T}^T \mathbf{M} \mathbf{T}$. Since \mathbf{T} is constant, \mathbf{M}^e is constant too. The connection between further rigid body elements belonging to the family of elements provided by the natural coordinates approach can be found in [51, Section 4.2.2].

We next apply the size-reduction outlined in Section 3.1.1 to the present rigid body formulation. In particular, in the wake of the size-reduction procedure, we illustrate the design of an appropriate null space matrix along with the use of local coordinates for the parametrization of \mathbf{Q}_{free} .

4.1.1. First size reduction

For the free rigid body the tangent space $T\mathbf{q}\mathbf{Q}_{\text{free}} = \ker \mathbf{G}_{\text{int}}(\mathbf{q})$ can be easily constructed by resorting to the twist (see also [2])

$$\mathbf{t} = \begin{bmatrix} \mathbf{v}_\varphi \\ \boldsymbol{\omega} \end{bmatrix} \quad (4.13)$$

Here, $\mathbf{v}_\varphi = \dot{\boldsymbol{\varphi}}$ is the velocity of the center of mass and $\boldsymbol{\omega} \in \mathbb{R}^3$ is the angular velocity. The director velocities $\mathbf{v}_\alpha = \dot{\mathbf{d}}_\alpha$ can be written as

$$\mathbf{v}_\alpha = \boldsymbol{\omega} \times \mathbf{d}_\alpha = -\widehat{\mathbf{d}}_\alpha \boldsymbol{\omega} \quad (4.14)$$

Here, $\widehat{\mathbf{a}}$ denotes the skew-symmetric matrix associated with $\mathbf{a} \in \mathbb{R}^3$, such that $\widehat{\mathbf{a}}\mathbf{b} = \mathbf{a} \times \mathbf{b}$, for any $\mathbf{b} \in \mathbb{R}^3$. The three independent components of the twist can now be used

4. Rotationless Formulation of the Rigid Body

to specify admissible velocities $\mathbf{v} \in T\mathbf{q}\mathbf{Q}_{\text{free}}$ through the relationship

$$\mathbf{v} = \mathbf{P}_{\text{int}}(\mathbf{q})\mathbf{t} \quad (4.15)$$

where, in view of (4.14), the 12×6 matrix \mathbf{P}_{int} assumes the form

$$\mathbf{P}_{\text{int}}(\mathbf{q}) = \begin{bmatrix} \mathbf{I} & \mathbf{0} \\ \mathbf{0} & -\widehat{\mathbf{d}}_1 \\ \mathbf{0} & -\widehat{\mathbf{d}}_2 \\ \mathbf{0} & -\widehat{\mathbf{d}}_3 \end{bmatrix} \quad (4.16)$$

The last relationship can be used to calculate the reduced mass matrix $\widetilde{\mathbf{M}} = \mathbf{P}_{\text{int}}^T \mathbf{M} \mathbf{P}_{\text{int}}$. A straightforward calculation yields

$$\widetilde{\mathbf{M}} = \begin{bmatrix} \mathcal{M}\mathbf{I} & \mathbf{0} \\ \mathbf{0} & -\sum_{\alpha=1}^3 \mathcal{E}_{\alpha} (\widehat{\mathbf{d}}_{\alpha})^2 \end{bmatrix} \quad (4.17)$$

Accordingly, if $\mathbf{q} \in \mathbf{Q}_{\text{free}}$, then

$$\widetilde{\mathbf{M}} = \begin{bmatrix} \mathcal{M}\mathbf{I} & \mathbf{0} \\ \mathbf{0} & \mathbf{J} \end{bmatrix} \quad (4.18)$$

where \mathbf{J} is the classical Euler inertia tensor. Similarly, a further calculation yields

$$\mathbf{P}_{\text{int}}^T \mathbf{M} \dot{\mathbf{P}}_{\text{int}} \mathbf{t} = \begin{bmatrix} \mathbf{0} \\ -\boldsymbol{\omega} \times (\sum_{\alpha=1}^3 \mathcal{E}_{\alpha} \mathbf{d}_{\alpha} \otimes \mathbf{d}_{\alpha}) \boldsymbol{\omega} \end{bmatrix} = \begin{bmatrix} \mathbf{0} \\ \boldsymbol{\omega} \times \mathbf{J} \boldsymbol{\omega} \end{bmatrix} \quad (4.19)$$

Finally, the last term in (3.19b) can be written as

$$\mathbf{P}_{\text{int}}^T \mathbf{f} = \begin{bmatrix} \mathbf{f}_{\varphi} \\ \sum_{\alpha=1}^3 \mathbf{d}_{\alpha} \times \mathbf{f}_{\alpha} \end{bmatrix} =: - \begin{bmatrix} \bar{\mathbf{f}} \\ \bar{\mathbf{m}} \end{bmatrix} \quad (4.20)$$

where $\bar{\mathbf{f}}$ and $\bar{\mathbf{m}}$ is the resultant external force and torque relative to the center of mass, respectively. To summarize, in the case of the free rigid body, the reduced equations of motion in (3.19) read

$$\dot{\mathbf{q}} = \mathbf{P}_{\text{int}}(\mathbf{q})\mathbf{t} \quad (4.21a)$$

$$\mathcal{M}\dot{\mathbf{v}}_{\varphi} = \bar{\mathbf{f}} \quad (4.21b)$$

$$\mathbf{J}\dot{\boldsymbol{\omega}} + \boldsymbol{\omega} \times \mathbf{J}\boldsymbol{\omega} = \bar{\mathbf{m}} \quad (4.21c)$$

$$\Phi_{\text{int}}(\mathbf{q}) = \mathbf{0} \quad (4.21d)$$

4.1.2. Second size reduction

For the spatial free rigid body a minimal set of three coordinates for the parametrization of the configuration space can be easily found. Consider the mapping

$$\mathbf{q} = \mathbf{F}(\varphi, \boldsymbol{\theta}) = \begin{bmatrix} \varphi \\ \mathbf{d}_1(\boldsymbol{\theta}) \\ \mathbf{d}_2(\boldsymbol{\theta}) \\ \mathbf{d}_3(\boldsymbol{\theta}) \end{bmatrix} \quad (4.22)$$

where the directors can be expressed by

$$\mathbf{d}_I(\boldsymbol{\theta}) = \exp(\widehat{\boldsymbol{\theta}}) \mathbf{d}_I^0 \quad \text{with } I = 1, 2, 3 \quad (4.23)$$

In the equation above, \mathbf{d}_I^0 marks the director at time $t = 0$, which is the initial value. The operator \exp represents the exponential map which, in the present case, coincides with the well-known Rodrigues formula [2, 103]

$$\exp(\widehat{\boldsymbol{\theta}}) = \mathbf{I} + \frac{\sin \|\boldsymbol{\theta}\|}{\|\boldsymbol{\theta}\|} \widehat{\boldsymbol{\theta}} + \frac{1}{2} \left(\frac{\sin(\|\boldsymbol{\theta}\|/2)}{\|\boldsymbol{\theta}\|/2} \right)^2 (\widehat{\boldsymbol{\theta}})^2 \quad (4.24)$$

Then admissible velocities $\mathbf{v} \in T\mathbf{q}\mathbf{Q}_{\text{free}}$ can be obtained from

$$\mathbf{v} = \frac{d}{dt} \mathbf{F}(\varphi, \boldsymbol{\theta}) = D\mathbf{F}(\varphi, \boldsymbol{\theta}) \begin{bmatrix} \dot{\varphi} \\ \dot{\boldsymbol{\theta}} \end{bmatrix} \quad (4.25)$$

Comparison of the last equation with (4.15) leads to the identifications $\mathbf{P}_{\text{int}}(\mathbf{q}) = D\mathbf{F}(\varphi, \boldsymbol{\theta})$, with $\mathbf{q} = \mathbf{F}(\varphi, \boldsymbol{\theta})$, and $\boldsymbol{\omega} = \mathbf{N}(\boldsymbol{\theta})\dot{\boldsymbol{\theta}}$. Where $\mathbf{N}(\boldsymbol{\theta})$ can be extracted from $D\mathbf{F}(\varphi, \boldsymbol{\theta})$ in Equation (4.25). In conclusion, the size-reduction procedure yields the familiar form of the equations of motion

$$\dot{\varphi} = v_\varphi \quad (4.26a)$$

$$\mathbf{N}(\boldsymbol{\theta})\dot{\boldsymbol{\theta}} = \boldsymbol{\omega} \quad (4.26b)$$

$$\mathcal{M}\dot{v}_\varphi = \bar{\mathbf{f}} \quad (4.26c)$$

$$\mathbf{J}\dot{\boldsymbol{\omega}} + \boldsymbol{\omega} \times \mathbf{J}\boldsymbol{\omega} = \bar{\mathbf{m}} \quad (4.26d)$$

pertaining to the free rigid body.

Remark 4.1.2 *Although, within this chapter all formulations were presented for the general three dimensional case, they can be directly broken down to the two dimensional case. Betsch and Uhlar [28] contains a detailed description of the treatment for the two dimensional case. Use will be made of this notation in Section 5.2, where we will present the construction of null space matrices for closed loop systems with the example of a planar parallel manipulator.*

Discrete reduced equations for the free rigid body

Now we will illustrate the application of the **REM** scheme (Equations (3.26)) to describe the rotational motion of a free rigid body. The rotationless formulation relies on $n = 9$ redundant coordinates $\mathbf{q}^{\text{red}} = [\mathbf{d}_1^T, \mathbf{d}_2^T, \mathbf{d}_3^T]^T$, subject to 6 holonomic constraints $\boldsymbol{\Phi}_{\text{int}}(\mathbf{q}^{\text{red}}) = \mathbf{0}$, where $\boldsymbol{\Phi}_{\text{int}}$ is given by (4.3). With regard to (4.6), the mass matrix is given by

$$\mathbf{M} = \begin{bmatrix} \mathcal{E}_1 & 0 & 0 \\ 0 & \mathcal{E}_2 & 0 \\ 0 & 0 & \mathcal{E}_3 \end{bmatrix} \otimes \mathbf{I} \quad (4.27)$$

where \otimes denotes the Kronecker (or tensor) product. Since the internal constraints $\boldsymbol{\Phi}_{\text{int}}(\mathbf{q}^{\text{red}})$ are only quadratic, the discrete constraint Jacobian is given by² $\mathbf{G}(\mathbf{q}_n^{\text{red}}, \mathbf{q}_{n+1}^{\text{red}}) = D\boldsymbol{\Phi}_{\text{int}}(\mathbf{q}_{n+\frac{1}{2}}^{\text{red}})$. An explicit representation of the discrete null space matrix can be shown to be (see Betsch & Leyendecker [18])

$$\mathbf{P}(\mathbf{q}_n^{\text{red}}, \mathbf{q}_{n+1}^{\text{red}}) = \begin{bmatrix} (\widehat{\mathbf{d}}_1)_{n+\frac{1}{2}} \\ (\widehat{\mathbf{d}}_2)_{n+\frac{1}{2}} \\ (\widehat{\mathbf{d}}_3)_{n+\frac{1}{2}} \end{bmatrix} \quad (4.28)$$

Concerning the mapping (3.27), in the present example, the incremental rotation of the rigid body can be characterized by a rotation vector $\boldsymbol{\theta} \in \mathbb{R}^3$. Accordingly, $\mathbf{F}_{q_n^{\text{red}}} : \mathbb{R}^3 \mapsto \mathbb{Q} \subset \mathbb{R}^9$ assumes the form

$$\mathbf{F}_{q_n^{\text{red}}}(\boldsymbol{\mu}) = \begin{bmatrix} \exp(\widehat{\boldsymbol{\theta}})(\mathbf{d}_1)_n \\ \exp(\widehat{\boldsymbol{\theta}})(\mathbf{d}_2)_n \\ \exp(\widehat{\boldsymbol{\theta}})(\mathbf{d}_3)_n \end{bmatrix} \quad (4.29)$$

Note that $\exp(\widehat{\boldsymbol{\theta}}) \in \text{SO}(3)$ plays the role of an incremental rotation matrix, the use of which is restricted to a single time step. Accordingly, singularities of the Rodrigues formula are not an issue in practical applications.

4.2. Kinematic Pairs

This section covers the basic kinematic pairs, which are necessary to build complex multibody systems. Within this section we will present the necessary external constraint equations which connect rigid bodies. Along with the coupling constraints, we will provide their corresponding constraint Jacobians in their continuous fashion, as well as the time discrete version. In order to apply the reduction techniques outlined in Section

²Remind that $(\bullet)_{n+\frac{1}{2}} = \frac{(\bullet)_{n+1} + (\bullet)_n}{2}$ denotes the mid-point evaluation of a respective term.

3.2.2, viable discrete null space matrices which eliminate the external constraints will also be presented. Since the treatment of these pairs has already been presented in detail in several papers by Betsch et al. [18, 28, 95, 149] we only recapitulate exemplarily the cylindrical pair, since it sets the stage for the treatment of the screw pair which was not yet treated in the citations above. This issue will be dealt with in detail in Section 5.1.2. The screw pair couples the relative displacement along a predefined axis with the relative rotation about the same axis. This necessitates the explicit treatment of the relative rotations in the underlying rotationless formulation. This task can only be accomplished by applying a specific coordinate augmentation technique which will be presented in Section 5.1. Therefore we will present the missing kinematic pair based upon [153], namely the screw joint in detail, closing the gap to [18, 95].

4.2.1. The cylindrical pair

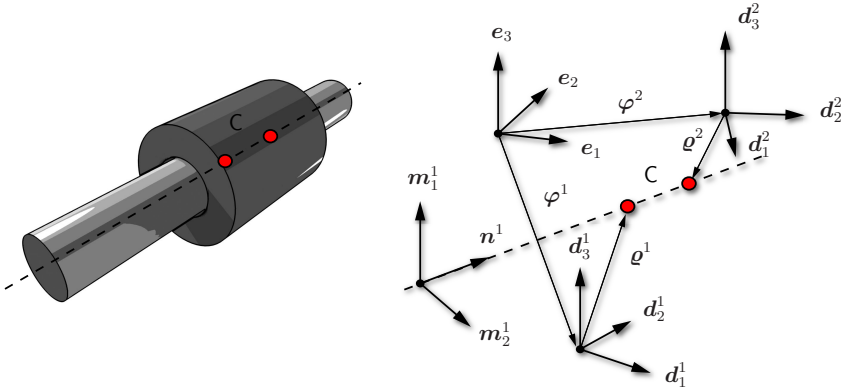


Figure 4.3.: Cylindrical pair.

To set the stage for the treatment of the screw pair, we next outline the rotationless framework for the cylindrical pair (Fig. 4.3). To this end, we proceed along the lines of Betsch and Leyendecker [18]. The configuration of the C pair can be characterized by $n^{(C)} = 24$ redundant coordinates

$$\mathbf{q}^{(C)} = \begin{bmatrix} \mathbf{q}^1 \\ \mathbf{q}^2 \end{bmatrix} \quad \text{with} \quad \mathbf{q}^\alpha = \begin{bmatrix} \varphi^\alpha \\ d_1^\alpha \\ d_2^\alpha \\ d_3^\alpha \end{bmatrix} \quad (\alpha = 1, 2) \quad (4.30)$$

Accordingly, the configuration of each rigid body is again characterized by 12 redundant coordinates of the form (4.2). As before, each individual rigid body is subject to six

4. Rotationless Formulation of the Rigid Body

independent constraints of rigidity. For the 2-body system under consideration we thus get the following vector of internal constraint functions

$$\boldsymbol{\Phi}_{\text{int}}^{(C)}(\mathbf{q}^{(C)}) = \begin{bmatrix} \boldsymbol{\Phi}_{\text{int}}^1(\mathbf{q}^1) \\ \boldsymbol{\Phi}_{\text{int}}^2(\mathbf{q}^2) \end{bmatrix} \quad (4.31)$$

where $\boldsymbol{\Phi}_{\text{int}}^\alpha$ is given by (4.3). In addition to the internal constraints we get four external constraints due to the coupling of the two bodies. In this connection, we introduce a right-handed orthonormal frame $\{\mathbf{m}_1^1, \mathbf{m}_2^1, \mathbf{n}^1\}$ fixed to the first body. In particular, with respect to the director frame $\{\mathbf{d}_1^1, \mathbf{d}_2^1, \mathbf{d}_3^1\}$,

$$\mathbf{n}^1 = n_i^1 \mathbf{d}_i^1 \quad \mathbf{m}_\alpha^1 = (m_\alpha^1)_i \mathbf{d}_i^1 \quad (4.32)$$

The motion of the second body relative to the first one is restricted to a rotation about \mathbf{n}^1 and a translation along \mathbf{n}^1 . The corresponding external constraint functions can be written as

$$\boldsymbol{\Phi}_{\text{ext}}^{(C)}(\mathbf{q}^{(C)}) = \begin{bmatrix} \mathbf{m}_1^1 \cdot (\mathbf{p}^2 - \mathbf{p}^1) \\ \mathbf{m}_2^1 \cdot (\mathbf{p}^2 - \mathbf{p}^1) \\ \mathbf{n}^1 \cdot \mathbf{d}_1^2 - \eta_1 \\ \mathbf{n}^1 \cdot \mathbf{d}_2^2 - \eta_2 \end{bmatrix} \quad (4.33)$$

where

$$\mathbf{p}^\alpha = \boldsymbol{\varphi}^\alpha + \boldsymbol{\varrho}^\alpha \quad \text{and} \quad \boldsymbol{\varrho}^\alpha = \varrho_k \mathbf{d}_k^\alpha \quad (4.34)$$

($\alpha = 1, 2$) and η_1, η_2 are constant and need to be consistent with the initial conditions. In conclusion, the $n^{(C)} = 24$ coordinates are subject to $m^{(C)} = 16$ constraints which may be arranged in the vector of geometric constraint functions

$$\boldsymbol{\Phi}^{(C)}(\mathbf{q}^{(C)}) = \begin{bmatrix} \boldsymbol{\Phi}_{\text{int}}^{(C)}(\mathbf{q}^{(C)}) \\ \boldsymbol{\Phi}_{\text{ext}}^{(C)}(\mathbf{q}^{(C)}) \end{bmatrix} \quad (4.35)$$

Accordingly, the C pair has $n^{(C)} - m^{(C)} = 8$ degrees of freedom. Its configuration space is given by

$$\mathbf{Q}^{(C)} = \{\mathbf{q}(t) \in \mathbb{R}^{24} \mid \boldsymbol{\Phi}^{(C)}(\mathbf{q}) = \mathbf{0}\} \quad (4.36)$$

The constraint Jacobian can be directly calculated from (4.35), such that

$$\mathbf{G}^{(C)}(\mathbf{q}^{(C)}) = D \boldsymbol{\Phi}^{(C)}(\mathbf{q}^{(C)}) \quad (4.37)$$

Since all the constraint functions in (4.35) are only quadratic, the discrete constraint Jacobian is given by $\mathbf{G}^{(C)}(\mathbf{q}_{n+\frac{1}{2}}^{(C)})$.

Null space matrix

It is shown in [18], that a velocity analysis can be applied to devise an explicit representation of the null space matrix. To this end, the vector of independent velocities $\boldsymbol{\nu}^{(C)} \in \mathbb{R}^{n^{(C)}-m^{(C)}}$ is introduced in the form

$$\boldsymbol{\nu}^{(C)} = \begin{bmatrix} \dot{\varphi}^1 \\ \boldsymbol{\omega}^1 \\ \dot{u} \\ \dot{\Theta} \end{bmatrix} \quad (4.38)$$

where $\boldsymbol{\omega}^1 \in \mathbb{R}^3$ is the angular velocity of the first body. Furthermore, $u \in \mathbb{R}$ and $\Theta \in \mathbb{R}$ account for the displacement (along \mathbf{n}^1) and rotation (about \mathbf{n}^1) of the second body relative to the first one. Now the redundant velocities $\dot{\mathbf{q}}^{(C)} \in \mathbb{R}^{24}$ can be expressed in terms of the independent velocities $\boldsymbol{\nu}^{(C)} \in \mathbb{R}^8$ according to

$$\dot{\mathbf{q}}^{(C)} = \mathbf{P}^{(C)} \boldsymbol{\nu}^{(C)} \quad (4.39)$$

where $\mathbf{P}^{(C)}$ is a null space matrix pertaining to the C pair. In particular, an explicit representation of $\mathbf{P}^{(C)}$ is given by³

$$\mathbf{P}^{(C)}(\mathbf{q}^{(C)}) = \begin{bmatrix} \mathbf{I} & \mathbf{0} & \mathbf{0} & \mathbf{0} \\ \mathbf{0} & -\widehat{\mathbf{d}}_1^1 & \mathbf{0} & \mathbf{0} \\ \mathbf{0} & -\widehat{\mathbf{d}}_2^1 & \mathbf{0} & \mathbf{0} \\ \mathbf{0} & -\widehat{\mathbf{d}}_3^1 & \mathbf{0} & \mathbf{0} \\ \mathbf{I} & \widehat{\boldsymbol{\varphi}}^1 - \boldsymbol{\varphi}^2 & \mathbf{m}_1^1 \times \mathbf{m}_2^1 & \boldsymbol{\rho}^2 \times \mathbf{n}^1 \\ \mathbf{0} & -\widehat{\mathbf{d}}_1^2 & \mathbf{0} & \mathbf{n}^1 \times \mathbf{d}_1^2 \\ \mathbf{0} & -\widehat{\mathbf{d}}_2^2 & \mathbf{0} & \mathbf{n}^1 \times \mathbf{d}_2^2 \\ \mathbf{0} & -\widehat{\mathbf{d}}_3^2 & \mathbf{0} & \mathbf{n}^1 \times \mathbf{d}_3^2 \end{bmatrix} \quad (4.40)$$

It can be easily verified that the discrete counterpart of the null space matrix (4.40) is given by

$$\mathbf{P}^{(C)}(\mathbf{q}_n^{(C)}, \mathbf{q}_{n+1}^{(C)}) = \mathbf{P}^{(C)}(\mathbf{q}_{n+\frac{1}{2}}^{(C)}) \quad (4.41)$$

In this connection, we remark that, although in the continuous case $\mathbf{m}_1^1 \times \mathbf{m}_2^1 = \mathbf{n}^1$, in general, this relationship is not valid in the mid-point configuration $\mathbf{q}_{n+\frac{1}{2}}^{(C)} \in \mathbb{R}^{24}$. This is due to the fact that, in the discrete setting outlined in Section 3.2, the orthonormality of the director frame $\{\mathbf{d}_1^1, \mathbf{d}_2^1, \mathbf{d}_3^1\}$ is only enforced at the end-point of each time step.

³Note that the $\mathbf{0}$ -matrices have different dimensions, ranging from 3×3 to 3×1 , depending in which row or column they are placed.

Reparametrization of unknowns

For each time step the number of unknowns can be reduced to the least possible by introducing local coordinates $\boldsymbol{\mu}^{(C)} \in U^{(C)} \subset \mathbb{R}^8$ for the parametrization of $\mathbf{Q}^{(C)}$ in a neighborhood of $\mathbf{q}_n^{(C)} \in \mathbf{Q}^{(C)}$. That is, the unknown redundant coordinates $\mathbf{q}_{n+1}^{(C)} \in \mathbf{Q}^{(C)}$ can be calculated from the new incremental unknowns $\boldsymbol{\mu}^{(C)} \in U^{(C)}$ via

$$\mathbf{q}_{n+1}^{(C)} = \mathbf{F}_{q_n}^{(C)}(\boldsymbol{\mu}^{(C)}) \quad (4.42)$$

where

$$\boldsymbol{\mu}^{(C)} = \begin{bmatrix} \mathbf{u}_\varphi^1 \\ \boldsymbol{\theta}^1 \\ \mu \\ \Theta \end{bmatrix} \quad (4.43)$$

Here, $\mathbf{u}_\varphi^1 \in \mathbb{R}^3$ is the incremental displacement of the center of mass of the first body, $\boldsymbol{\theta}^1 \in \mathbb{R}^3$ contains three parameters which characterize the incremental rotation of the first body, $\mu \in \mathbb{R}$ and $\Theta \in \mathbb{R}$ specify the incremental displacement and rotation of the second body relative to the first one, respectively. In particular, the mapping $\mathbf{F}_{q_n}^{(C)} : U^{(C)} \rightarrow \mathbf{Q}^{(C)}$ follows from the following incremental update formulas

$$\begin{aligned} \varphi_{n+1}^1 &= \varphi_n^1 + \mathbf{u}_\varphi^1 \\ (\mathbf{d}_I^1)_{n+1} &= \exp(\widehat{\boldsymbol{\theta}^1})(\mathbf{d}_I^1)_n \\ (\mathbf{d}_I^2)_{n+1} &= \exp(\widehat{\boldsymbol{\theta}^1}) \exp(\Theta(\widehat{\mathbf{n}}^1)_n)(\mathbf{d}_I^2)_n \\ \boldsymbol{\varrho}_{n+1}^2 &= \boldsymbol{\varrho}_{n+1}^1 + \boldsymbol{\varrho}_{n+1}^1 - \boldsymbol{\varrho}_{n+1}^2 + (\mu_n + \mu)\mathbf{n}_{n+1}^1 \end{aligned} \quad (4.44)$$

A corresponding numerical example treating the cylindrical pair was given in [18, 95], therefore we refer to the works cited above and focus on the new contributions within this thesis.

4.2.2. Overview of lower kinematic pairs

This section summarizes all necessary formulas pertaining to the remaining kinematic pairs. For details of derivation and additional information see [18, 95]. We now conclude the results from the works cited before and present the constraint equations, the corresponding constraint Jacobians as well as viable continuous and discrete null space matrices. As already mentioned above, we will provide a detailed description of the newly introduced screw-pair in Section 5.1.2.

Spherical pair

- Vector of independent velocities

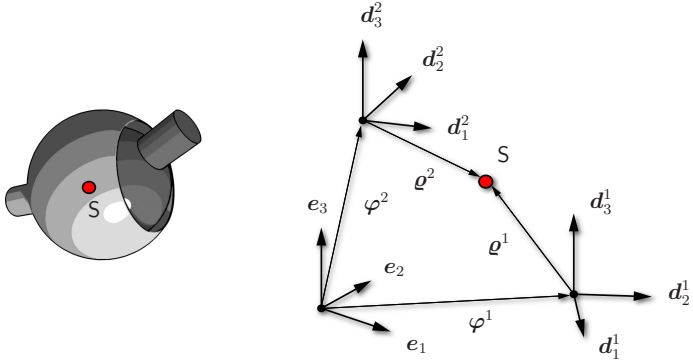


Figure 4.4.: Spherical pair.

$$\boldsymbol{\nu}^{(S)} = \begin{bmatrix} \dot{\varphi}^1 \\ \boldsymbol{\omega}^1 \\ \dot{\varphi}^2 \\ \boldsymbol{\omega}^2 \end{bmatrix} \quad (4.45)$$

- Constraint equations

$$\boldsymbol{\Phi}_{\text{ext}}^{(S)}(\mathbf{q}^{(S)}) = \varphi^2 - \varphi^1 + \varrho^2 - \varrho^1 \quad (4.46)$$

- Continuous constraint Jacobian

$$\mathbf{G}_{\text{ext}}^{(S)}(\mathbf{q}^{(S)}) = [-\mathbf{I} \quad -\varrho_1^1 \mathbf{I} \quad -\varrho_2^1 \mathbf{I} \quad -\varrho_3^1 \mathbf{I} \quad \mathbf{I} \quad \varrho_1^2 \mathbf{I} \quad \varrho_2^2 \mathbf{I} \quad \varrho_3^2 \mathbf{I}] \quad (4.47)$$

- Discrete constraint Jacobian

$$\mathbf{G}_{\text{ext}}^{(S)}(\mathbf{q}_n^{(S)}, \mathbf{q}_{n+1}^{(S)}) = \mathbf{G}_{\text{ext}}^{(S)}(\mathbf{q}_{n+\frac{1}{2}}^{(S)}) \quad (4.48)$$

- Continuous null space matrix

$$\mathbf{P}^{(S)}(\mathbf{q}^{(S)}) = \begin{bmatrix} \mathbf{I} & \mathbf{0} & \mathbf{0} \\ \mathbf{0} & -\widehat{d_1^1} & \mathbf{0} \\ \mathbf{0} & -\widehat{d_2^1} & \mathbf{0} \\ \mathbf{0} & -\widehat{d_3^1} & \mathbf{0} \\ \mathbf{I} & -\widehat{\varrho^1} & \widehat{\varrho^2} \\ \mathbf{0} & \mathbf{0} & -\widehat{d_1^2} \\ \mathbf{0} & \mathbf{0} & -\widehat{d_2^2} \\ \mathbf{0} & \mathbf{0} & -\widehat{d_3^2} \end{bmatrix} \quad (4.49)$$

4. Rotationless Formulation of the Rigid Body

- Discrete null space matrix

$$\mathbf{P}^{(S)}(\mathbf{q}_n^{(S)}, \mathbf{q}_{n+1}^{(S)}) = \mathbf{P}^{(S)}(\mathbf{q}_{n+\frac{1}{2}}^{(S)}) \quad (4.50)$$

Revolute pair

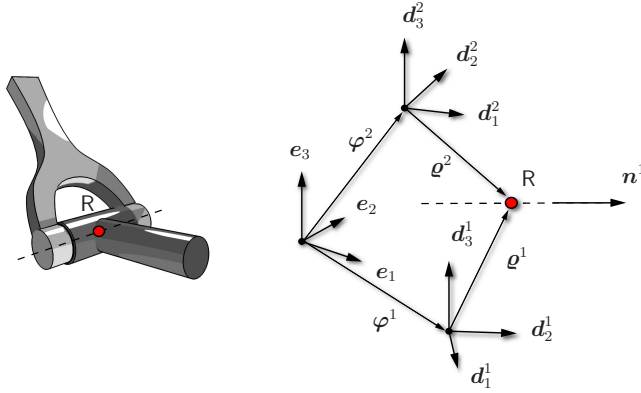


Figure 4.5: Revolute pair.

- Vector of independent velocities

$$\boldsymbol{\nu}^{(R)} = \begin{bmatrix} \dot{\varphi}^1 \\ \dot{\omega}^1 \\ \dot{\theta} \end{bmatrix} \quad (4.51)$$

- Constraint equations

$$\boldsymbol{\Phi}_{\text{ext}}^{(R)}(\mathbf{q}^{(R)}) = \begin{bmatrix} \varphi^2 - \varphi^1 + \varrho^2 - \varrho^1 \\ \mathbf{n}^1 \cdot \mathbf{d}_1^2 - \eta_1 \\ \mathbf{n}^1 \cdot \mathbf{d}_2^2 - \eta_2 \end{bmatrix} \quad (4.52)$$

- Continuous constraint Jacobian

$$\mathbf{G}_{\text{ext}}^{(R)}(\mathbf{q}^{(R)}) = \begin{bmatrix} -\mathbf{I} & -\varrho_1^1 \mathbf{I} & -\varrho_2^1 \mathbf{I} & -\varrho_3^1 \mathbf{I} & \mathbf{I} & \varrho_1^2 \mathbf{I} & \varrho_2^2 \mathbf{I} & \varrho_3^2 \mathbf{I} \\ \mathbf{0}^T & n_1^1 (\mathbf{d}_1^2)^T & n_2^1 (\mathbf{d}_1^2)^T & n_3^1 (\mathbf{d}_1^2)^T & \mathbf{0}^T & (\mathbf{n}^1)^T & \mathbf{0}^T & \mathbf{0}^T \\ \mathbf{0}^T & n_1^1 (\mathbf{d}_2^2)^T & n_2^1 (\mathbf{d}_2^2)^T & n_3^1 (\mathbf{d}_2^2)^T & \mathbf{0}^T & \mathbf{0}^T & (\mathbf{n}^1)^T & \mathbf{0}^T \end{bmatrix} \quad (4.53)$$

- Discrete constraint Jacobian

$$\mathbf{G}_{\text{ext}}^{(R)}(\mathbf{q}_n^{(R)}, \mathbf{q}_{n+1}^{(R)}) = \mathbf{G}_{\text{ext}}^{(R)}(\mathbf{q}_{n+\frac{1}{2}}^{(R)}) \quad (4.54)$$

- Continuous null space matrix

$$\mathbf{P}^{(R)}(\mathbf{q}^{(R)}) = \begin{bmatrix} \mathbf{I} & \mathbf{0} & \mathbf{0} \\ \mathbf{0} & -\widehat{\mathbf{d}}_1^1 & \mathbf{0} \\ \mathbf{0} & -\widehat{\mathbf{d}}_2^1 & \mathbf{0} \\ \mathbf{0} & -\widehat{\mathbf{d}}_3^1 & \mathbf{0} \\ \mathbf{I} & \widehat{\boldsymbol{\varrho}}^1 - \widehat{\boldsymbol{\varrho}}^2 & \boldsymbol{\varrho}^2 \times \mathbf{n}^1 \\ \mathbf{0} & -\widehat{\mathbf{d}}_1^2 & \mathbf{n}^1 \times \mathbf{d}_1^2 \\ \mathbf{0} & -\widehat{\mathbf{d}}_2^2 & \mathbf{n}^1 \times \mathbf{d}_2^2 \\ \mathbf{0} & -\widehat{\mathbf{d}}_3^2 & \mathbf{n}^1 \times \mathbf{d}_3^2 \end{bmatrix} \quad (4.55)$$

- Discrete null space matrix

$$\mathbf{P}^{(R)}(\mathbf{q}_n^{(R)}, \mathbf{q}_{n+1}^{(R)}) = \mathbf{P}^{(R)}(\mathbf{q}_{n+\frac{1}{2}}^{(R)}) \quad (4.56)$$

Prismatic pair

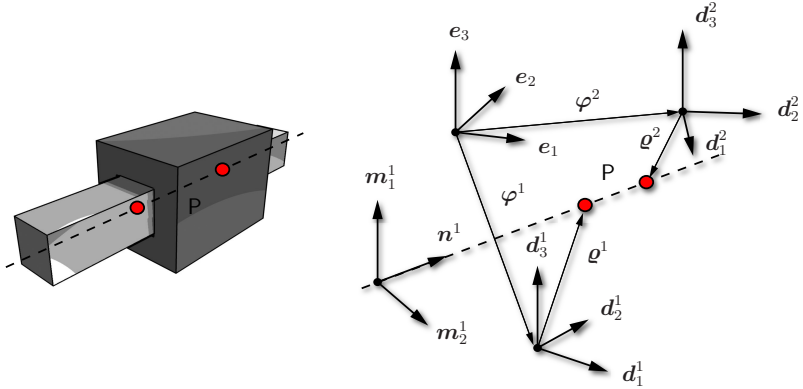


Figure 4.6.: Prismatic pair.

- Vector of independent velocities

$$\boldsymbol{\nu}^{(P)} = \begin{bmatrix} \dot{\varphi}^1 \\ \boldsymbol{\omega}^1 \\ \dot{i} \end{bmatrix} \quad (4.57)$$

4. Rotationless Formulation of the Rigid Body

- Constraint equations

$$\Phi_{\text{ext}}^{(P)}(\mathbf{q}^{(P)}) = \begin{bmatrix} \mathbf{m}_1^1 \cdot (\mathbf{p}^2 - \mathbf{p}^1) \\ \mathbf{m}_2^1 \cdot (\mathbf{p}^2 - \mathbf{p}^1) \\ \mathbf{d}_1^1 \cdot \mathbf{d}_2^2 - \eta_1 \\ \mathbf{d}_2^1 \cdot \mathbf{d}_3^2 - \eta_2 \\ \mathbf{d}_3^1 \cdot \mathbf{d}_1^2 - \eta_3 \end{bmatrix} \quad (4.58)$$

- Continuous constraint Jacobian

$$\mathbf{G}_{\text{ext}}^{(P)}(\mathbf{q}^{(P)}) = \begin{bmatrix} -(\mathbf{m}_1^1)^T & \mathbf{G}_{11}^T & \mathbf{G}_{12}^T & \mathbf{G}_{13}^T & (\mathbf{m}_1^1)^T & \varrho_1^2(\mathbf{m}_1^1)^T & \varrho_2^2(\mathbf{m}_1^1)^T & \varrho_3^2(\mathbf{m}_1^1)^T \\ -(\mathbf{m}_2^1)^T & \mathbf{G}_{21}^T & \mathbf{G}_{22}^T & \mathbf{G}_{23}^T & (\mathbf{m}_2^1)^T & \varrho_1^2(\mathbf{m}_2^1)^T & \varrho_2^2(\mathbf{m}_2^1)^T & \varrho_3^2(\mathbf{m}_2^1)^T \\ \mathbf{0}^T & (\mathbf{d}_2^2)^T & \mathbf{0}^T & \mathbf{0}^T & \mathbf{0}^T & \mathbf{0}^T & (\mathbf{d}_1^1)^T & \mathbf{0}^T \\ \mathbf{0}^T & \mathbf{0}^T & (\mathbf{d}_3^2)^T & \mathbf{0}^T & \mathbf{0}^T & \mathbf{0}^T & \mathbf{0}^T & (\mathbf{d}_2^1)^T \\ \mathbf{0}^T & \mathbf{0}^T & \mathbf{0}^T & (\mathbf{d}_1^2)^T & \mathbf{0}^T & (\mathbf{d}_3^1)^T & \mathbf{0}^T & \mathbf{0}^T \end{bmatrix} \quad (4.59)$$

with

$$\mathbf{G}_{\kappa i} = (m_{\kappa}^i)_i (\mathbf{p}^2 - \mathbf{p}^1) - \varrho_i^1 \mathbf{m}_{\kappa}^1 \quad (4.60)$$

for $\kappa = 1, 2$ and $i = 1, 2, 3$.

- Discrete constraint Jacobian

$$\mathbf{G}_{\text{ext}}^{(P)}(\mathbf{q}_n^{(P)}, \mathbf{q}_{n+1}^{(P)}) = \mathbf{G}_{\text{ext}}^{(P)}(\mathbf{q}_{n+\frac{1}{2}}^{(P)}) \quad (4.61)$$

- Continuous null space matrix

$$\mathbf{P}^{(P)}(\mathbf{q}^{(P)}) = \begin{bmatrix} \mathbf{I} & \mathbf{0} & \mathbf{0} \\ \mathbf{0} & -\widehat{\mathbf{d}}_1^1 & \mathbf{0} \\ \mathbf{0} & -\widehat{\mathbf{d}}_2^1 & \mathbf{0} \\ \mathbf{0} & -\widehat{\mathbf{d}}_3^1 & \mathbf{0} \\ \mathbf{I} & \widehat{\boldsymbol{\varphi}}^1 - \widehat{\boldsymbol{\varphi}}^2 & \mathbf{n}^1 \\ \mathbf{0} & -\widehat{\mathbf{d}}_1^2 & \mathbf{0} \\ \mathbf{0} & -\widehat{\mathbf{d}}_2^2 & \mathbf{0} \\ \mathbf{0} & -\widehat{\mathbf{d}}_3^2 & \mathbf{0} \end{bmatrix} \quad (4.62)$$

- Discrete null space matrix

$$\mathbf{P}^{(P)}(\mathbf{q}_n^{(P)}, \mathbf{q}_{n+1}^{(P)}) = \mathbf{P}^{(P)}(\mathbf{q}_{n+\frac{1}{2}}^{(P)}) \quad (4.63)$$

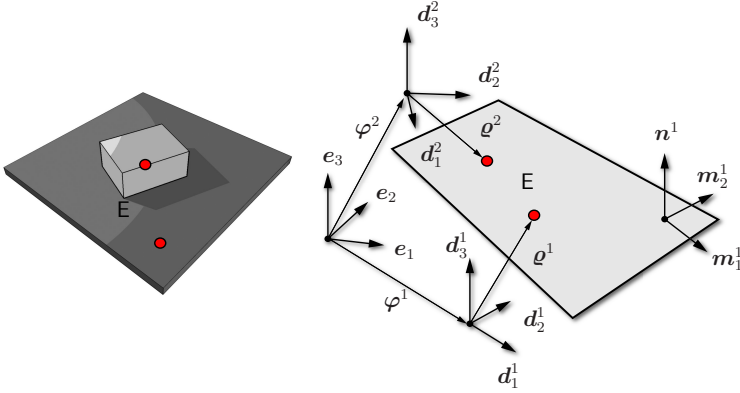


Figure 4.7.: Planar pair.

Planar pair

- Vector of independent velocities

$$\boldsymbol{\nu}^{(E)} = \begin{bmatrix} \dot{\varphi}^1 \\ \boldsymbol{\omega}^1 \\ \dot{\boldsymbol{u}} \\ \dot{\Theta} \end{bmatrix} \quad (4.64)$$

where $\dot{\boldsymbol{u}} \in \mathbb{R}^2$

- Constraint equations

$$\boldsymbol{\Phi}_{\text{ext}}^{(E)}(\boldsymbol{q}^{(E)}) = \begin{bmatrix} \boldsymbol{n}^1 \cdot (\boldsymbol{p}^2 - \boldsymbol{p}^1) \\ \boldsymbol{n}^1 \cdot \boldsymbol{d}_1^2 - \eta_1 \\ \boldsymbol{n}^1 \cdot \boldsymbol{d}_2^2 - \eta_2 \end{bmatrix} \quad (4.65)$$

- Continuous constraint Jacobian

$$\boldsymbol{G}_{\text{ext}}^{(E)}(\boldsymbol{q}^{(E)}) = \begin{bmatrix} -(\boldsymbol{n}^1)^T & \boldsymbol{G}_1^T & \boldsymbol{G}_2^T & \boldsymbol{G}_3^T & (\boldsymbol{n}^1)^T & \varrho_1^2(\boldsymbol{n}^1)^T & \varrho_2^2(\boldsymbol{n}^1)^T & \varrho_3^2(\boldsymbol{n}^1)^T \\ \mathbf{0}^T & n_1^1(\boldsymbol{d}_1^2)^T & n_2^1(\boldsymbol{d}_1^2)^T & n_3^1(\boldsymbol{d}_1^2)^T & \mathbf{0}^T & (\boldsymbol{n}^1)^T & \mathbf{0}^T & \mathbf{0}^T \\ \mathbf{0}^T & n_1^1(\boldsymbol{d}_2^2)^T & n_2^1(\boldsymbol{d}_2^2)^T & n_3^1(\boldsymbol{d}_2^2)^T & \mathbf{0}^T & \mathbf{0}^T & (\boldsymbol{n}^1)^T & \mathbf{0}^T \end{bmatrix} \quad (4.66)$$

with

$$\boldsymbol{G}_i = n_i^1 (\boldsymbol{p}^2 - \boldsymbol{p}^1) - \varrho_i^1 \boldsymbol{n}^1 \quad (4.67)$$

4. Rotationless Formulation of the Rigid Body

for $i = 1, 2, 3$.

- Discrete constraint Jacobian

$$\mathbf{G}_{\text{ext}}^{(E)}(\mathbf{q}_n^{(E)}, \mathbf{q}_{n+1}^{(E)}) = \mathbf{G}_{\text{ext}}^{(E)}(\mathbf{q}_{n+\frac{1}{2}}^{(E)}) \quad (4.68)$$

- Continuous null space matrix

$$\mathbf{P}^{(E)}(\mathbf{q}^{(E)}) = \begin{bmatrix} \mathbf{I} & \mathbf{0} & \mathbf{0} & \mathbf{0} & \mathbf{0} \\ \mathbf{0} & -\widehat{\mathbf{d}}_1^1 & \mathbf{0} & \mathbf{0} & \mathbf{0} \\ \mathbf{0} & -\widehat{\mathbf{d}}_2^1 & \mathbf{0} & \mathbf{0} & \mathbf{0} \\ \mathbf{0} & -\widehat{\mathbf{d}}_3^1 & \mathbf{0} & \mathbf{0} & \mathbf{0} \\ \mathbf{I} & \widehat{\boldsymbol{\varphi}}^1 - \widehat{\boldsymbol{\varphi}}^2 & m_1^1 & m_2^1 & \boldsymbol{\varrho}^2 \times \mathbf{n}^1 \\ \mathbf{0} & -\widehat{\mathbf{d}}_1^2 & \mathbf{0} & \mathbf{0} & \mathbf{n}^1 \times \mathbf{d}_1^2 \\ \mathbf{0} & -\widehat{\mathbf{d}}_2^2 & \mathbf{0} & \mathbf{0} & \mathbf{n}^1 \times \mathbf{d}_2^2 \\ \mathbf{0} & -\widehat{\mathbf{d}}_3^2 & \mathbf{0} & \mathbf{0} & \mathbf{n}^1 \times \mathbf{d}_3^2 \end{bmatrix} \quad (4.69)$$

- Discrete null space matrix

$$\mathbf{P}^{(E)}(\mathbf{q}_n^{(E)}, \mathbf{q}_{n+1}^{(E)}) = \mathbf{P}^{(E)}(\mathbf{q}_{n+\frac{1}{2}}^{(E)}) \quad (4.70)$$

5. Modeling Techniques

This chapter presents most of the modeling features which are necessary in order to describe common real world problems arising in multibody dynamics. For each modeling feature our goal will be to establish a consistent time stepping scheme which will be based upon the basic set of Equations (3.11), maintaining the mechanical properties of the underlying system. The chapter is divided in multiple sections treating each individual modeling feature:

The first section starts with the coordinate augmentation technique which is necessary in order to introduce rotational degrees of freedom into our rotationless formulation of rigid bodies as outlined in Chapter 4. This modeling feature is a necessity, since in practical applications it is often required to model joint-angles and their associated torques. An energy-momentum consistent scheme for handling the nonlinear character of the augmentation constraints will be discussed.

The second section will present the explicit design of null space matrices for closed loop systems. Although a numerical solution to this problem was already given in [18, 95], a systematic procedure for the construction of explicit discrete null space matrices was lacking. This will be presented with the example of a planar parallel manipulator.

The third modeling technique is the incorporation of rheonomic or control (servo) constraints. Typically this question arises when one is interested in gathering necessary driving inputs for a prescribed motion. In other words, an inverse dynamics problem must be solved. Hence the DAE-scheme will be extended by appending servo constraints, reflecting the benefits of the DAE-formulation (see Section 3.3).

In the fourth section, we will outline the modeling of dissipative effects under the aspect of designing an energy consistent time integration scheme. We will focus on the modeling of joint friction, presenting three different approaches, two of them will rely on rheological models. Corresponding examples will verify the performance of the consistent integration scheme.

The final section covers the introduction of nonholonomic constraints. Similar to Section 5.3, they can be appended in the same straightforward way. Nonholonomic constraints are non-integrable constraints, commonly describing rolling without slipping. The goal will once again be to establish a time integration scheme with mixed geometric and

kinematic constraints.

5.1. Coordinate Augmentation Technique

The coordinate augmentation technique introduced in the context of the rotationless formulation of rigid bodies in [28, 149, 148] can be regarded as a pure modeling feature. Although it might seem to be peculiar to introduce variables we tried to avoid by choosing the direction cosine description as coordinates, it is worth to remember that the rotationless formulation forms the base for the construction of energy-momentum schemes as outlined in Chapter 3. Having the rotationless formulation at hand, we still need, in order to actuate the system, a corresponding value where the torque can be applied. For this purpose we introduce the coordinate augmentation technique. The basic idea of introducing additional dependent coordinates (or fields, e.g. in finite element formulations for incompressible models in nonlinear elasticity) is well-known and can be found in many previous works. In G eradin and Cardona [54] the rotation angle in a hinge joint (cf. Sect. 7.6.1) is introduced in the spirit of the augmentation technique, albeit the corresponding additional constraint is only enforced approximately. The work by Bottasso and Croce [37] is another example of the implicit use of the augmentation technique to deal with joint-angles and joint-displacements (cf. Sect. 3.3). In order to present all necessary steps for the augmentation technique, we will outline the procedure with the simple example of a planar revolute pair (see also [28] for a similar example with a torsional spring). The augmentation technique facilitates the treatment of the last kinematic pair not presented yet, namely the screw pair.

5.1.1. Augmented planar revolute pair

The simplest way of introducing the augmentation technique is by augmenting the joint coordinate in a planar revolute pair according to Fig. 5.1. Please keep in mind, that all expression labeled $(\bullet)_{\text{ori}}$ refer to the original set of coordinates and can, if not declared here, be found in the overview of basic kinematics pairs (see Section 4.2.2)¹.

The intention is to measure the angle Θ characterizing the rotation of the second body relative to the first one. The coordinate augmentation is based on the introduction of an extended configuration vector

$$\mathbf{q} = \begin{bmatrix} \mathbf{q}^1 \\ \mathbf{q}^2 \\ \Theta \end{bmatrix} \quad (5.1)$$

¹Note that the rotationless formulation summarized before, deals with the three dimensional case. However, the two dimensional case can be treated without any conceptual differences (see also [28]).

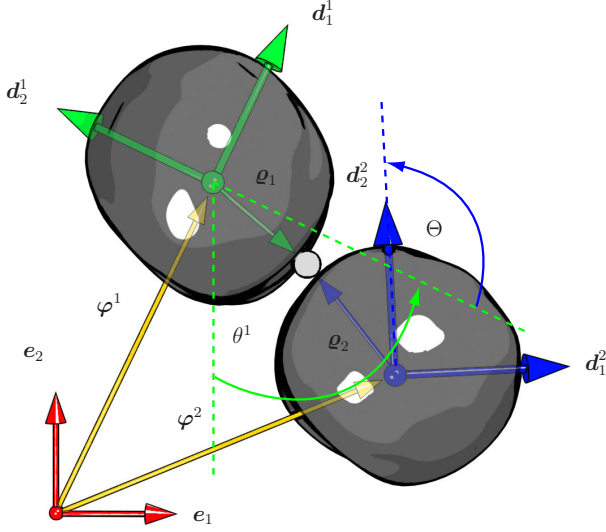


Figure 5.1.: The planar revolute pair.

Note that in the 2D-case the rotationless formulation of a rigid body relies on 6 redundant coordinates of the form

$$\mathbf{q}^\alpha = \begin{bmatrix} \varphi^\alpha \\ \mathbf{d}_1^\alpha \\ \mathbf{d}_2^\alpha \end{bmatrix} \quad (5.2)$$

The new coordinate Θ is connected with the original ones by introducing an additional constraint function of the form

$$\Phi_{\text{aug}}(\mathbf{q}) = \mathbf{d}_2^2 \cdot \mathbf{d}_1^1 + \sin \Theta + \mathbf{d}_2^2 \cdot \mathbf{d}_2^1 - \cos \Theta \quad (5.3)$$

In anticipation of the subsequent treatment of the discretization we write (5.3) in partitioned form

$$\Phi_{\text{aug}}(\mathbf{q}) = \Phi_{\text{aug}}^1(\mathbf{q}_{\text{ori}}) + \Phi_{\text{aug}}^2(\Theta) \quad (5.4)$$

with the original coordinates

$$\mathbf{q}_{\text{ori}} = \begin{bmatrix} \mathbf{q}^1 \\ \mathbf{q}^2 \end{bmatrix} \quad (5.5)$$

5. Modeling Techniques

and

$$\Phi_{\text{aug}}^1(\mathbf{q}_{\text{ori}}) = \mathbf{d}_2^2 \cdot \mathbf{d}_1^1 + \mathbf{d}_2^2 \cdot \mathbf{d}_2^1 \quad (5.6a)$$

$$\Phi_{\text{aug}}^2(\Theta) = \sin \Theta - \cos \Theta \quad (5.6b)$$

Additionally, we get the Jacobian

$$\mathbf{G}_{\text{aug}}(\mathbf{q}) = D\Phi_{\text{aug}}(\mathbf{q}) = \begin{bmatrix} \mathbf{0}^T & \mathbf{d}_2^{2T} & \mathbf{d}_2^{2T} & \mathbf{0}^T & \mathbf{0}^T & (\mathbf{d}_1^1 + \mathbf{d}_2^1)^T & (\sin \Theta + \cos \Theta) \end{bmatrix} \quad (5.7)$$

With regard to (5.4), we decompose (5.7) according to

$$\mathbf{G}_{\text{aug}}(\mathbf{q}) = [\mathbf{G}_{\text{aug}}^1(\mathbf{q}_{\text{ori}}) \quad \mathbf{G}_{\text{aug}}^2(\Theta)] \quad (5.8)$$

with

$$\mathbf{G}_{\text{aug}}^1(\mathbf{q}_{\text{ori}}) = \begin{bmatrix} \mathbf{0}^T & \mathbf{d}_2^{2T} & \mathbf{d}_2^{2T} & \mathbf{0}^T & \mathbf{0}^T & (\mathbf{d}_1^1 + \mathbf{d}_2^1)^T \end{bmatrix} \quad (5.9a)$$

$$\mathbf{G}_{\text{aug}}^2(\Theta) = \sin \Theta + \cos \Theta \quad (5.9b)$$

In conclusion, we have $n = 13$ coordinates subject to $m = 9$ geometric constraints. In order to completely specify the DAEs (3.11) for the augmented system at hand one simply has to extend the relevant matrices of the revolute pair in Section 4.2.2. Accordingly, the mass matrix of the augmented system is given by

$$\mathbf{M} = \begin{bmatrix} \mathbf{M}^1 & \mathbf{0}_{6 \times 6} & \mathbf{0}_{6 \times 1} \\ \mathbf{0}_{6 \times 6} & \mathbf{M}^2 & \mathbf{0}_{6 \times 1} \\ \mathbf{0}_{1 \times 6} & \mathbf{0}_{1 \times 6} & 0 \end{bmatrix} \quad (5.10)$$

In view of (5.3), the augmentation gives rise to an extended vector of constraint functions of the form

$$\Phi(\mathbf{q}) = \begin{bmatrix} \Phi_{\text{ori}}(\mathbf{q}_{\text{ori}}) \\ \Phi_{\text{aug}}(\mathbf{q}) \end{bmatrix} \quad (5.11)$$

where Φ_{ori} stands for the original constraints pertaining to the planar revolute pair. The augmented constraint Jacobian assumes the form

$$\mathbf{G}(\mathbf{q}) = \begin{bmatrix} \mathbf{G}_{\text{ori}}(\mathbf{q}_{\text{ori}}) & \mathbf{0}_{8 \times 1} \\ \mathbf{G}_{\text{aug}}^1(\mathbf{q}_{\text{ori}}) & \mathbf{G}_{\text{aug}}^2(\Theta) \end{bmatrix} \quad (5.12)$$

where \mathbf{G}_{ori} represents the original constraint Jacobian.

Continuous null space matrix

With regard to (5.1), the augmented vector of redundant velocities can be written as

$$\mathbf{v} = \begin{bmatrix} \mathbf{v}^1 \\ \mathbf{v}^2 \\ \dot{\Theta} \end{bmatrix} \quad (5.13)$$

Admissible velocities $\mathbf{v} \in T\mathbf{q}\mathbf{Q}_{\text{revolute}}$ can be written in the form

$$\mathbf{v} = \mathbf{P}(\mathbf{q})\boldsymbol{\nu} \quad (5.14)$$

where $\boldsymbol{\nu} \in \mathbb{R}^4$ is again given similarly to (4.51) and \mathbf{P} is now a 13×4 null space matrix of the form

$$\mathbf{P}(\mathbf{q}) = \begin{bmatrix} \mathbf{P}_{\text{ori}}(\mathbf{q}_{\text{ori}}) \\ \mathbf{P}_{\text{aug}} \end{bmatrix} \quad (5.15)$$

where \mathbf{P}_{ori} stands for the original 12×4 null space matrix. It is obvious that the 1×4 matrix \mathbf{P}_{aug} assumes the form

$$\mathbf{P}_{\text{aug}} = [\mathbf{0}_{1 \times 2} \quad 0 \quad 1] \quad (5.16)$$

In view of the subsequent deduction of an appropriate discrete version of (5.16) it is illustrative to verify the property $\mathbf{G}\mathbf{P} = \mathbf{0}$, which, of course, is satisfied by design. Accordingly, with regard to (5.12) and (5.15) we get

$$\mathbf{G}(\mathbf{q})\mathbf{P}(\mathbf{q}) = \begin{bmatrix} \mathbf{G}_{\text{ori}}(\mathbf{q}_{\text{ori}})\mathbf{P}_{\text{ori}}(\mathbf{q}_{\text{ori}}) \\ \mathbf{G}_{\text{aug}}^1(\mathbf{q}_{\text{ori}})\mathbf{P}_{\text{ori}}(\mathbf{q}_{\text{ori}}) + \mathbf{G}_{\text{aug}}^2(\Theta)\mathbf{P}_{\text{aug}} \end{bmatrix} \quad (5.17)$$

By construction, $\mathbf{G}_{\text{ori}}\mathbf{P}_{\text{ori}} = \mathbf{0}$. Furthermore, a straightforward calculation yields

$$\mathbf{G}_{\text{aug}}^1(\mathbf{q}_{\text{ori}})\mathbf{P}_{\text{ori}}(\mathbf{q}_{\text{ori}}) = [\mathbf{0}_{1 \times 2} \quad 0 \quad (\mathbf{d}_1^1 + \mathbf{d}_2^1) \cdot \mathbf{E}^T \mathbf{d}_2^1] \quad (5.18)$$

with the constant matrix

$$\mathbf{E} = \begin{bmatrix} 0 & 1 \\ -1 & 0 \end{bmatrix} \quad \text{with} \quad \mathbf{E}^T = -\mathbf{E} = \mathbf{E}^{-1} \quad \text{and} \quad \mathbf{E}^2 = -\mathbf{I}_2 \quad (5.19)$$

On the other hand the augmented part yields

$$\mathbf{G}_{\text{aug}}^2(\Theta)\mathbf{P}_{\text{aug}} = [\mathbf{0}_{1 \times 2} \quad 0 \quad (\sin \Theta + \cos \Theta)] \quad (5.20)$$

Since

$$(\mathbf{d}_1^1 + \mathbf{d}_2^1) \cdot \mathbf{E}^T \mathbf{d}_2^1 = (\mathbf{d}_1^1 + \mathbf{d}_2^1) \cdot (-\mathbf{d}_1^1) = -(\mathbf{d}_1^1 \cdot \mathbf{d}_1^1 + \mathbf{d}_2^1 \cdot \mathbf{d}_1^1) = -(\cos \Theta + \sin \Theta) \quad (5.21)$$

we obtain the desired result $\mathbf{G}_{\text{aug}}^1\mathbf{P}_{\text{ori}} + \mathbf{G}_{\text{aug}}^2\mathbf{P}_{\text{aug}} = \mathbf{0}$.

Discrete constraint Jacobian

The discrete version of (5.12) can be written as

$$\mathbf{G}(\mathbf{q}_n, \mathbf{q}_{n+1}) = \begin{bmatrix} \mathbf{G}_{\text{ori}}((\mathbf{q}_{\text{ori}})_{n+\frac{1}{2}}) & \mathbf{0}_{8 \times 1} \\ \mathbf{G}_{\text{aug}}^1((\mathbf{q}_{\text{ori}})_{n+\frac{1}{2}}) & \mathbf{G}_{\text{aug}}^2(\Theta_n, \Theta_{n+1}) \end{bmatrix} \quad (5.22)$$

Since the constraint functions $\Phi_{\text{ori}}(\mathbf{q}_{\text{ori}})$ and $\Phi_{\text{aug}}^1(\mathbf{q}_{\text{ori}})$ (cf. (4.52) and (5.6a), respectively) are at most quadratic, the associated discrete gradient coincides with the mid-point evaluation of the respective continuous constraint Jacobians. This is in contrast to the constraint function $\Phi_{\text{aug}}^2(\Theta)$, see (5.6b). In this case we choose

$$\mathbf{G}_{\text{aug}}^2(\Theta_n, \Theta_{n+1}) = \frac{\Phi_{\text{aug}}^2(\Theta_{n+1}) - \Phi_{\text{aug}}^2(\Theta_n)}{\Theta_{n+1} - \Theta_n} \quad (5.23)$$

If $\Theta_{n+1} \rightarrow \Theta_n$, then $\mathbf{G}_{\text{aug}}^2(\Theta_n, \Theta_{n+1}) \rightarrow (\Phi_{\text{aug}}^2)'(\Theta_n)$.

Remark 5.1.1 *Formula (5.23) can be interpreted as a G -equivariant discrete derivative of the corresponding constraint function in the sense of Gonzalez [59]. In this connection G represents the group acting by translations and rotations, respectively. In the present case (5.23) coincides with Greenspan's formula [64].*

Discrete null space matrix

The discrete version of the null space matrix (5.15) can be written in the form

$$\mathbf{P}(\mathbf{q}_n, \mathbf{q}_{n+1}) = \begin{bmatrix} \mathbf{P}_{\text{ori}}((\mathbf{q}_{\text{ori}})_{n+\frac{1}{2}}) \\ \mathbf{P}_{\text{aug}}(\mathbf{q}_n, \mathbf{q}_{n+1}) \end{bmatrix} \quad (5.24)$$

where we choose

$$\mathbf{P}_{\text{aug}}(\mathbf{q}_n, \mathbf{q}_{n+1}) = \begin{bmatrix} \mathbf{0}_{1 \times 2} & 0 \\ 0 & \frac{(\mathbf{d}_1^1 + \mathbf{d}_2^1)_{n+\frac{1}{2}} \cdot \mathbf{E} (\mathbf{d}_2^2)_{n+\frac{1}{2}}^T}{\mathbf{G}_{\text{aug}}^2(\Theta_n, \Theta_{n+1})} \end{bmatrix} \quad (5.25)$$

as discrete version of (5.16). That (5.24) is indeed a viable choice for the discrete null space matrix, can be easily verified by a calculation along the lines of the continuous case.

Numerical example

To demonstrate the numerical performance of the present formulation we investigate the free flight of our institute logo NM (Numerical Mechanics). Both letters are modeled as

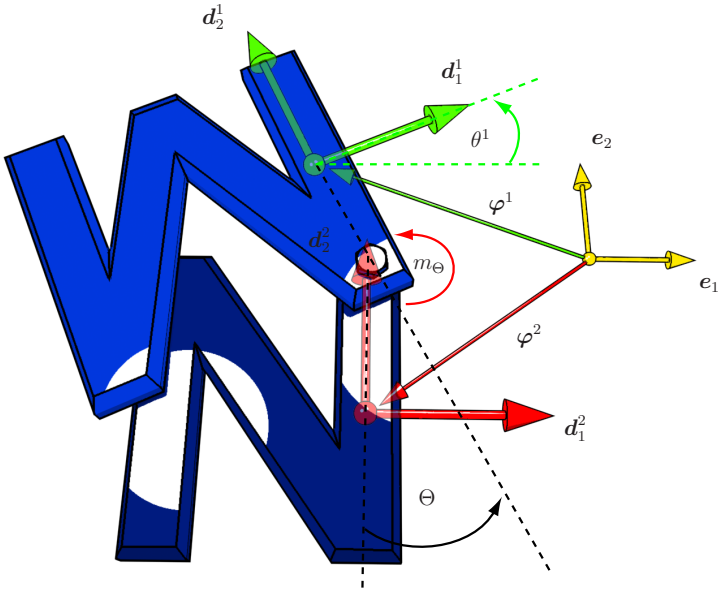


Figure 5.2.: The NM-logo as 2-body system. Arbitrary configuration of both connected letters.

rigid bodies which are connected by a revolute joint (Fig. 5.2). The inertial parameters for the numerical example are summarized in Table 5.1. The location of the joint relative to the center of mass of each body is specified by

$$\mathbf{e}^A = \sum_{\alpha=1}^2 \varrho_{\alpha}^A \mathbf{d}_{\alpha}^A \quad \text{where} \quad [\varrho_{\alpha}^1] = \begin{bmatrix} 0 \\ -0.4 \end{bmatrix} \quad \text{and} \quad [\varrho_{\alpha}^2] = \begin{bmatrix} 0 \\ 0.4 \end{bmatrix} \quad (5.26)$$

The initial configuration of the system is given by the following generalized coordinates (see Fig. 5.2)

$$\mathbf{u}_0 = \begin{bmatrix} \varphi_0^1 \\ \theta_0^1 \\ \Theta_0 \end{bmatrix} = \begin{bmatrix} \mathbf{0} \\ 0 \\ \pi \end{bmatrix} \quad (5.27)$$

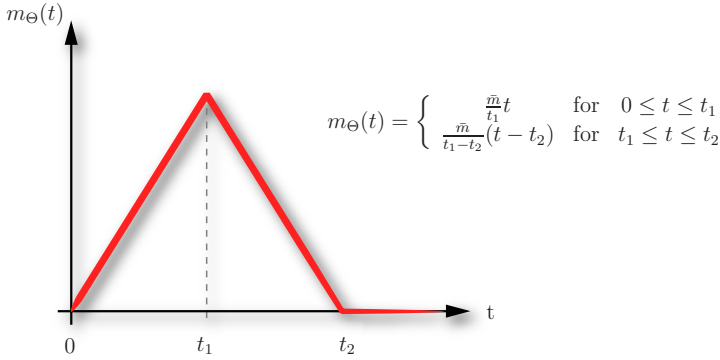


Figure 5.3.: Magnitude of the torque during the initial load period.

Initial generalized velocities can be written as

$$\boldsymbol{\nu}_0 = \begin{bmatrix} \mathbf{e}_1 \cdot (\mathbf{v}_{\varphi}^1)_0 \\ \mathbf{e}_2 \cdot (\mathbf{v}_{\varphi}^1)_0 \\ \omega_0^1 \\ \dot{\Theta}_0 \end{bmatrix} \quad (5.28)$$

In the present example the system is initially at rest, i.e. $\boldsymbol{\nu}_0 = \mathbf{0}$. Since it is a free

body	\mathcal{M}	\mathcal{E}_1	\mathcal{E}_2
1	1.1	0.004	0.0917
2	2	0.0073	0.1667

Table 5.1.: Inertial parameters for the 2-body system.

flight, we neglect the gravitational forces, having no potential energy in the system. To initialize the motion, external loads $\mathbf{Q} \in \mathbb{R}^{13}$ are acting on the system. Specifically,

$$\mathbf{Q} = \begin{bmatrix} \mathbf{0}_{12 \times 1} \\ m_{\Theta}(t) \end{bmatrix} \quad (5.29)$$

This means that we only apply a joint torque m_{Θ} , which is directly acting on the newly introduced rotational component Θ . The torque itself is applied in the form of a hat function over time (cf. Fig. 5.3), where $t_1 = 0.25$, $t_2 = 0.5$, $\bar{m} = 5$. Accordingly, for $t > t_2$, $m_{\Theta} = 0$. The system can thus be classified as an autonomous Hamiltonian system with symmetry. Consequently, the Hamiltonian (or the total energy) represents

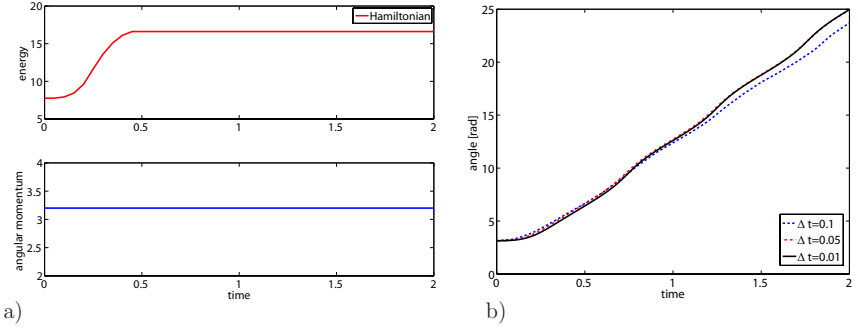


Figure 5.4.: Free flying NM-logo: a) conservation properties $\Delta t = 0.05$, b) angle $\Theta(t)$ over time.

a conserved quantity for $t > t_2$. The angular momentum remains equal for all times, since it is an internal joint torque acting on the system. The present energy-momentum scheme does indeed satisfy these conservation properties for any time step size Δt , see Fig. 5.4a. The simulated motion is illustrated with some snapshots at discrete times in Fig. 5.5 for the exemplary choice of $\Delta t = 0.05$. Moreover, the evolution of the angle $\Theta(t)$, calculated with different time steps $\Delta t \in \{0.1, 0.05, 0.01\}$, is depicted in Fig. 5.4b.

5.1.2. The screw-pair

Here we deal with the screw (H) pair within the rotationless framework of multibody dynamics. As mentioned before, in the previous treatments [18, 95] of lower kinematic pairs, the (H) pair has been excluded due to the absence of rotational variables within the rotationless formulation. To remedy this drawback, we make use of a specific coordinate augmentation technique which makes possible the design of a new energy-momentum conserving integrator for the (H) pair.

In the (H) pair, the relative displacement u along the screw axis \mathbf{n}^1 is related to the relative rotation Θ about \mathbf{n}^1 by $u = p\Theta$, where p is the pitch of the screw. To describe the kinematics of the (H) pair we introduce the vector of redundant coordinates

$$\mathbf{q}^{(H)} = \begin{bmatrix} \mathbf{q}^{(C)} \\ u \\ \Theta \end{bmatrix} \quad (5.30)$$

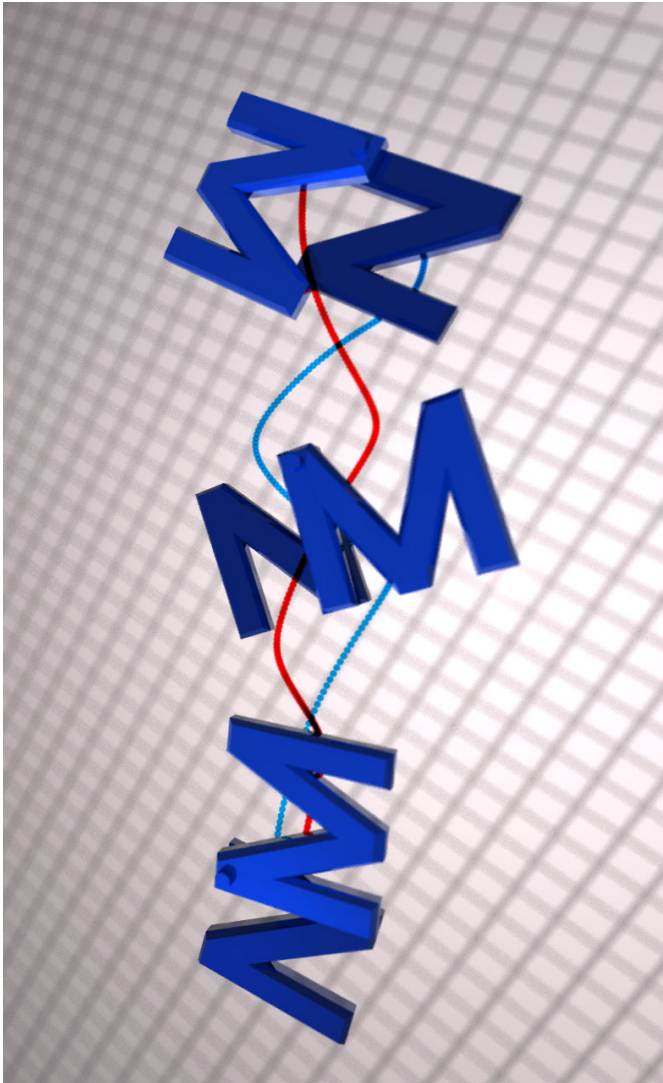


Figure 5.5.: Snapshots of the free flying NM-logo. The two curves correspond to the trajectories of the mass centers of the individual bodies constituting the present multibody system ($t \in \{0, 1, 2\}$).

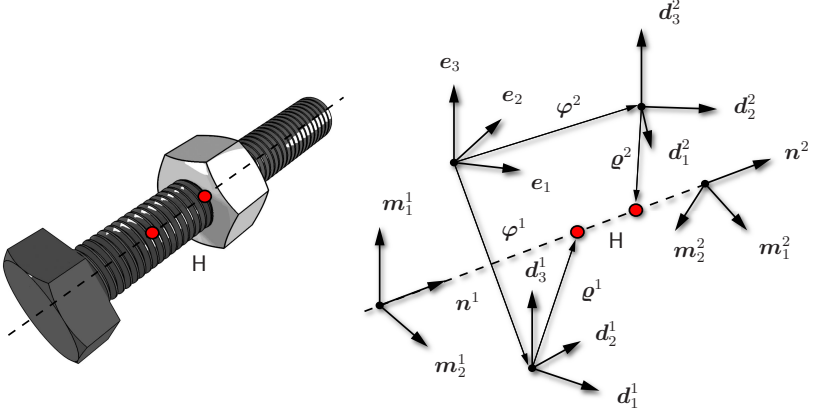


Figure 5.6.: Screw pair.

along with the vector of constraint functions

$$\Phi^{(H)}(\mathbf{q}^{(H)}) = \begin{bmatrix} \Phi^{(C)}(\mathbf{q}^{(C)}) \\ \Phi_u(\mathbf{q}^{(H)}) \\ \Phi_\Theta(\mathbf{q}^{(H)}) \\ u - p\Theta \end{bmatrix} \quad (5.31)$$

With regard to (5.30), the original coordinates of the (C) pair have been augmented with the relative displacement u and rotation Θ , respectively. The new coordinates u and Θ are linked to the original ones through the additional constraint functions

$$\Phi_u(\mathbf{q}^{(H)}) = \Phi_u^1(\mathbf{q}^{(C)}) + \Phi_u^2(u) \quad (5.32a)$$

$$\Phi_\Theta(\mathbf{q}^{(H)}) = \Phi_\Theta^1(\mathbf{q}^{(C)}) + \Phi_\Theta^2(\Theta) \quad (5.32b)$$

with

$$\begin{aligned} \Phi_u^1(\mathbf{q}^{(C)}) &= \mathbf{n}^1 \cdot (\mathbf{p}^2 - \mathbf{p}^1) & \Phi_u^2(u) &= -u \\ \Phi_\Theta^1(\mathbf{q}^{(C)}) &= \mathbf{m}_2^2 \cdot \mathbf{m}_1^1 + \mathbf{m}_2^2 \cdot \mathbf{m}_2^1 & \Phi_\Theta^2(\Theta) &= \sin \Theta - \cos \Theta \end{aligned} \quad (5.33)$$

In this connection, $\{\mathbf{m}_1^2, \mathbf{m}_2^2, \mathbf{n}^2\}$ is a right-handed orthonormal frame fixed to the second body with $\mathbf{n}^2 = \mathbf{n}^1$ (cf. Fig. 5.6). Similar to (4.32),

$$\mathbf{n}^2 = n_i^2 \mathbf{d}_i^2 \quad \mathbf{m}_\alpha^2 = (m_\alpha^2)_i \mathbf{d}_i^2 \quad (5.34)$$

Note, that the purpose of the two constraint functions Φ_u and Φ_Θ is to link the newly introduced relative coordinates u and Θ to the original coordinates $\mathbf{q}^{(C)}$, leading to the

5. Modeling Techniques

augmented configuration vector (5.30). In contrast to that, the last component of the vector (5.31) yields the additional screw constraint $u = p\Theta$.

Remark 5.1.2 *The screw constraint can also be enforced directly on the original coordinates $\mathbf{q}^{(C)}$, i.e. without applying the coordinate augmentation technique. Since $\Phi_u = 0$ is equivalent to $u = \mathbf{n}^1 \cdot (\mathbf{p}^2 - \mathbf{p}^1)$, and $\Phi_\Theta = 0$ implies $\sin \Theta = -\mathbf{m}_2^2 \cdot \mathbf{m}_1^1$ and $\cos \Theta = \mathbf{m}_2^2 \cdot \mathbf{m}_2^1$, the screw joint can be written in the alternative form*

$$\mathbf{n}^1 \cdot (\mathbf{p}^2 - \mathbf{p}^1) + p \arctan \frac{\mathbf{m}_2^2 \cdot \mathbf{m}_1^1}{\mathbf{m}_2^2 \cdot \mathbf{m}_2^1} = 0$$

Note, however, that due to the presence of the tangent function singularities are introduced which are not present in the above treatment relying on the coordinate augmentation technique. Moreover, the introduction of relative joint-coordinates via the coordinate augmentation technique is accompanied by associated joint-forces, which can be used as control inputs (see also Section 5.3).

Constraint Jacobian

The constraint Jacobian pertaining to the (H) pair, $\mathbf{G}^{(H)}(\mathbf{q}^{(H)}) = D\Phi^{(H)}(\mathbf{q}^{(H)})$, can be easily calculated from (5.31) to obtain

$$\mathbf{G}^{(H)}(\mathbf{q}^{(H)}) = \begin{bmatrix} \mathbf{G}^{(C)}(\mathbf{q}^{(C)}) & \mathbf{0} & \mathbf{0} \\ D\Phi_u^1(\mathbf{q}^{(C)}) & -1 & 0 \\ D\Phi_\Theta^1(\mathbf{q}^{(C)}) & 0 & D\Phi_\Theta^2(\Theta) \\ \mathbf{0}^T & 1 & -p \end{bmatrix} \quad (5.35)$$

with

$$D\Phi_u^1(\mathbf{q}^{(C)}) = [-(\mathbf{n}^1)^T \quad \tilde{\mathbf{n}}_1^T \quad \tilde{\mathbf{n}}_2^T \quad \tilde{\mathbf{n}}_3^T \quad (\mathbf{n}^1)^T \quad \varrho_1^2(\mathbf{n}^1)^T \quad \varrho_2^2(\mathbf{n}^1)^T \quad \varrho_3^2(\mathbf{n}^1)^T] \quad (5.36a)$$

$$D\Phi_\Theta^1(\mathbf{q}^{(C)}) = [\mathbf{0}^T \quad \tilde{\mathbf{m}}_1^T \quad \tilde{\mathbf{m}}_2^T \quad \tilde{\mathbf{m}}_3^T \quad \mathbf{0}^T \quad \tilde{\mathbf{m}}_1^T \quad \tilde{\mathbf{m}}_2^T \quad \tilde{\mathbf{m}}_3^T] \quad (5.36b)$$

$$D\Phi_\Theta^2(\Theta) = \sin \Theta + \cos \Theta \quad (5.36c)$$

and

$$\tilde{\mathbf{n}}_i = n_i^1(\mathbf{p}^2 - \mathbf{p}^1) - \varrho_i^1 \mathbf{n}^1 \quad (5.37a)$$

$$\tilde{\mathbf{m}}_i = ((m_1^1)_i + (m_2^1)_i) \mathbf{m}_2^2 \quad (5.37b)$$

$$\tilde{\mathbf{m}}_i = (m_2^2)_i (\mathbf{m}_1^1 + \mathbf{m}_2^1) \quad (5.37c)$$

for $i = 1, 2, 3$.

Discrete constraint Jacobian

Except for $\Phi_{\Theta}^2(\Theta)$, all constraint functions in (5.31) are at most quadratic. Consequently, to devise an energy-momentum conserving scheme, the discrete constraint Jacobian can be chosen in the form

$$\mathbf{G}^{(H)}(\mathbf{q}_n^{(H)}, \mathbf{q}_{n+1}^{(H)}) = \begin{bmatrix} \mathbf{G}^{(C)}(\mathbf{q}_{n+\frac{1}{2}}^{(C)}) & \mathbf{0} & \mathbf{0} \\ D\Phi_u^1(\mathbf{q}_{n+\frac{1}{2}}^{(C)}) & -1 & 0 \\ D\Phi_{\Theta}^1(\mathbf{q}_{n+\frac{1}{2}}^{(C)}) & 0 & D\Phi_{\Theta}^2(\Theta_n, \Theta_{n+1}) \\ \mathbf{0}^T & 1 & -p \end{bmatrix} \quad (5.38)$$

where the discrete derivative of $\Phi_{\Theta}^2(\Theta)$ is given by Equation (5.23).

Null space matrix

We next aim at the design of a null space matrix for the (H) pair. To this end we start from (4.39), i.e. $\dot{\mathbf{q}}^{(C)} = \mathbf{P}^{(C)}\boldsymbol{\nu}^{(C)}$ and account for the additional constraints due to (i) the coordinate augmentation and (ii) the relation $u = p\Theta$. The second item implies

$$\boldsymbol{\nu}^{(C)} = \mathbf{P}^{(C,H)}\boldsymbol{\nu}^{(H)} \quad \text{with} \quad \boldsymbol{\nu}^{(H)} = \begin{bmatrix} \dot{\varphi}^1 \\ \dot{\omega}^1 \\ \dot{\Theta} \end{bmatrix} \quad (5.39)$$

With regard to (4.38), the coupling matrix $\mathbf{P}^{(C,H)}$ can be written as

$$\mathbf{P}^{(C,H)} = \begin{bmatrix} \mathbf{I} & \mathbf{0} & \mathbf{0} \\ \mathbf{0} & \mathbf{I} & \mathbf{0} \\ \mathbf{0}^T & \mathbf{0}^T & p \\ \mathbf{0}^T & \mathbf{0}^T & 1 \end{bmatrix} \quad (5.40)$$

Accounting for the aforementioned two items, the demanded relationship

$$\dot{\mathbf{q}}^{(H)} = \mathbf{P}^{(H)}\boldsymbol{\nu}^{(H)} \quad \text{with} \quad \dot{\mathbf{q}}^{(H)} = \begin{bmatrix} \dot{\mathbf{q}}^{(C)} \\ \dot{u} \\ \dot{\Theta} \end{bmatrix} \quad (5.41)$$

implies, that the null space matrix $\mathbf{P}^{(H)}$ pertaining to the (H) pair can be written in the form

$$\mathbf{P}^{(H)} = \mathbf{P}^{(C,\text{aug})}\mathbf{P}^{(C,H)} \quad (5.42)$$

where $\mathbf{P}^{(C,\text{aug})}$ takes into account the coordinate augmentation and thus can be written as

$$\mathbf{P}^{(C,\text{aug})} = \begin{bmatrix} \mathbf{P}^{(C)} \\ \mathbf{P}_u \\ \mathbf{P}_{\Theta} \end{bmatrix} \quad (5.43)$$

5. Modeling Techniques

Here, $\mathbf{P}^{(C)}$ is given by (4.40), and the coordinate augmentation yields

$$\mathbf{P}_u = [\mathbf{0}^T \quad \mathbf{0}^T \quad 1 \quad 0] \quad (5.44a)$$

$$\mathbf{P}_\Theta = [\mathbf{0}^T \quad \mathbf{0}^T \quad 0 \quad 1] \quad (5.44b)$$

The present design procedure warrants that matrix $\mathbf{P}^{(H)}$ in (5.42) is indeed a null space matrix for the (H) pair. In particular, making use of (5.35), a straightforward calculation yields

$$\mathbf{G}^{(H)} \mathbf{P}^{(H)} = \begin{bmatrix} \left\{ \mathbf{G}^{(C)} \mathbf{P}^{(C)} \right\} \mathbf{P}^{(C,H)} \\ \left\{ D \Phi_u^1(\mathbf{q}^{(C)}) \mathbf{P}^{(C)} - \mathbf{P}_u \right\} \mathbf{P}^{(C,H)} \\ \left\{ D \Phi_\Theta^1(\mathbf{q}^{(C)}) \mathbf{P}^{(C)} + D \Phi_\Theta^2(\Theta) \mathbf{P}_\Theta \right\} \mathbf{P}^{(C,H)} \\ (\mathbf{P}_u - p \mathbf{P}_\Theta) \mathbf{P}^{(C,H)} \end{bmatrix} \quad (5.45)$$

By design, the expressions in the curly brackets as well as the last row vanish, so that $\mathbf{G}^{(H)} \mathbf{P}^{(H)} = \mathbf{0}$, as desired.

Discrete null space matrix

To set up a discrete version of the null space matrix $\mathbf{P}^{(H)}$, we closely follow the lines of the continuous case outlined above (see also the guidelines for the design of discrete null space matrices in Betsch & Leyendecker [18, Section 4.3.]). Accordingly, similar to (5.42), the discrete null space matrix pertaining to the (H) pair follows from

$$\mathbf{P}^{(H)}(\mathbf{q}_n^{(H)}, \mathbf{q}_{n+1}^{(H)}) = \mathbf{P}^{(C,\text{aug})}(\mathbf{q}_n^{(H)}, \mathbf{q}_{n+1}^{(H)}) \mathbf{P}^{(C,H)}(\mathbf{q}_n^{(H)}, \mathbf{q}_{n+1}^{(H)}) \quad (5.46)$$

with

$$\mathbf{P}^{(C,\text{aug})}(\mathbf{q}_n^{(H)}, \mathbf{q}_{n+1}^{(H)}) = \begin{bmatrix} \mathbf{P}^{(C)}(\mathbf{q}_{n+\frac{1}{2}}) \\ \mathbf{P}_u(\mathbf{q}_n^{(H)}, \mathbf{q}_{n+1}^{(H)}) \\ \mathbf{P}_\Theta(\mathbf{q}_n^{(H)}, \mathbf{q}_{n+1}^{(H)}) \end{bmatrix} \quad (5.47)$$

In (5.47), we choose

$$\mathbf{P}_u(\mathbf{q}_n^{(H)}, \mathbf{q}_{n+1}^{(H)}) = [\mathbf{0}^T \quad \mathbf{0}^T \quad \Xi(\mathbf{q}_n^{(H)}, \mathbf{q}_{n+1}^{(H)}) \quad 0] \quad (5.48a)$$

$$\mathbf{P}_\Theta(\mathbf{q}_n^{(H)}, \mathbf{q}_{n+1}^{(H)}) = [\mathbf{0}^T \quad \mathbf{0}^T \quad 0 \quad \Gamma(\mathbf{q}_n^{(H)}, \mathbf{q}_{n+1}^{(H)})] \quad (5.48b)$$

as discrete versions of the matrices in (5.44), where

$$\Xi(\mathbf{q}_n^{(H)}, \mathbf{q}_{n+1}^{(H)}) = \{ \mathbf{n}^1 \cdot (\mathbf{m}_1^1 \times \mathbf{m}_2^1) \}_{n+\frac{1}{2}} \quad (5.49a)$$

$$\Gamma(\mathbf{q}_n^{(H)}, \mathbf{q}_{n+1}^{(H)}) = \frac{\{ \mathbf{m}_2^2 \cdot (\mathbf{n}^1 \times (\mathbf{m}_1^1 + \mathbf{m}_2^1)) \}_{n+\frac{1}{2}}}{D \Phi_\Theta^2(\Theta_n, \Theta_{n+1})} \quad (5.49b)$$

Moreover, in (5.46), we choose

$$\mathbf{P}^{(C,H)}(\mathbf{q}_n^{(H)}, \mathbf{q}_{n+1}^{(H)}) = \begin{bmatrix} \mathbf{I} & \mathbf{0} & \mathbf{0} \\ \mathbf{0} & \mathbf{I} & \mathbf{0} \\ \mathbf{0}^T & \mathbf{0}^T & \tilde{p}(\mathbf{q}_n^{(H)}, \mathbf{q}_{n+1}^{(H)}) \\ \mathbf{0}^T & \mathbf{0}^T & 1 \end{bmatrix} \quad (5.50)$$

as the discrete version of the coupling matrix (5.40). In (5.50), \tilde{p} is given by

$$\tilde{p}(\mathbf{q}_n^{(H)}, \mathbf{q}_{n+1}^{(H)}) = \frac{\Gamma(\mathbf{q}_n^{(H)}, \mathbf{q}_{n+1}^{(H)})}{\Xi(\mathbf{q}_n^{(H)}, \mathbf{q}_{n+1}^{(H)})} p \quad (5.51)$$

and can be interpreted as an algorithmic pitch. It is worth noting that for $\Delta t \rightarrow 0$, it can be easily verified that $\Xi(\mathbf{q}_n^{(H)}, \mathbf{q}_{n+1}^{(H)}) \rightarrow 1$ and $\Gamma(\mathbf{q}_n^{(H)}, \mathbf{q}_{n+1}^{(H)}) \rightarrow 1$, such that $\tilde{p}(\mathbf{q}_n^{(H)}, \mathbf{q}_{n+1}^{(H)}) \rightarrow p$. That is, the continuous case is recovered in the limit of vanishing step sizes. Eventually, application of (5.46) yields the following explicit representation of the discrete null space matrix

$$\mathbf{P}^{(H)}(\mathbf{q}_n^{(H)}, \mathbf{q}_{n+1}^{(H)}) = \begin{bmatrix} \mathbf{I} & \mathbf{0} & \mathbf{0} \\ \mathbf{0} & -(\widehat{\mathbf{d}}_1^1)_{n+\frac{1}{2}} & \mathbf{0} \\ \mathbf{0} & -(\widehat{\mathbf{d}}_2^1)_{n+\frac{1}{2}} & \mathbf{0} \\ \mathbf{0} & -(\widehat{\mathbf{d}}_3^1)_{n+\frac{1}{2}} & \mathbf{0} \\ \mathbf{I} & (\varphi^1 - \varphi^2)_{n+\frac{1}{2}} & \tilde{p}(\mathbf{q}_n^{(H)}, \mathbf{q}_{n+1}^{(H)}) (\widehat{\mathbf{m}}_1^1 \mathbf{m}_2^1)_{n+\frac{1}{2}} + (\widehat{\varrho}^2 \mathbf{n}^1)_{n+\frac{1}{2}} \\ \mathbf{0} & -(\widehat{\mathbf{d}}_1^2)_{n+\frac{1}{2}} & (\mathbf{n}^1 \times \mathbf{d}_1^2)_{n+\frac{1}{2}} \\ \mathbf{0} & -(\widehat{\mathbf{d}}_2^2)_{n+\frac{1}{2}} & (\mathbf{n}^1 \times \mathbf{d}_2^2)_{n+\frac{1}{2}} \\ \mathbf{0} & -(\widehat{\mathbf{d}}_3^2)_{n+\frac{1}{2}} & (\mathbf{n}^1 \times \mathbf{d}_3^2)_{n+\frac{1}{2}} \\ \mathbf{0}^T & \mathbf{0}^T & p \Gamma(\mathbf{q}_n^{(H)}, \mathbf{q}_{n+1}^{(H)}) \\ \mathbf{0}^T & \mathbf{0}^T & \Gamma(\mathbf{q}_n^{(H)}, \mathbf{q}_{n+1}^{(H)}) \end{bmatrix} \quad (5.52)$$

It is worth mentioning that for $p = 0$, the discrete null space matrix pertaining to the revolute pair is recovered (see 4.2.2).

Reparametrization of unknowns

As already known, for each time step the number of unknowns can be reduced to a minimum by introducing local coordinates $\boldsymbol{\mu}^{(H)} \in U^{(H)} \subset \mathbb{R}^7$ for the parametrization of $\mathbf{Q}^{(H)}$ in a neighborhood of $\mathbf{q}_n \in \mathbf{Q}^{(H)}$. That is, the unknown redundant coordinates $\mathbf{q}_{n+1} \in \mathbf{Q}^{(H)}$ can be calculated from the new incremental unknowns $\boldsymbol{\mu}^{(H)} \in U^{(H)}$ via

$$\mathbf{q}_{n+1}^{(H)} = \mathbf{F}_{\mathbf{q}_n}^{(H)}(\boldsymbol{\mu}^{(H)}) \quad (5.53)$$

where

$$\boldsymbol{\mu}^{(H)} = \begin{bmatrix} \mathbf{u}_\varphi^1 \\ \boldsymbol{\theta}^1 \\ \Theta \end{bmatrix} \quad (5.54)$$

As before, $\Theta \in \mathbb{R}$ specifies the incremental relative rotation. The mapping $\mathbf{F}_{q_n}^{(H)} : U^{(H)} \rightarrow \mathbb{Q}^{(H)}$ follows from the incremental update formulas

$$\boldsymbol{\varphi}_{n+1}^1 = \boldsymbol{\varphi}_n^1 + \mathbf{u}_\varphi^1 \quad (5.55a)$$

$$(\mathbf{d}_I^1)_{n+1} = \exp(\widehat{\boldsymbol{\theta}^1})(\mathbf{d}_I^1)_n \quad (5.55b)$$

$$(\mathbf{d}_I^2)_{n+1} = \exp(\widehat{\boldsymbol{\theta}^1}) \exp(\Theta \widehat{\mathbf{n}}_n)(\mathbf{d}_I^2)_n \quad (5.55c)$$

$$u_{n+1} = u_n + p\Theta \quad (5.55d)$$

$$\Theta_{n+1} = \Theta_n + \Theta \quad (5.55e)$$

$$\boldsymbol{\varphi}_{n+1}^2 = \boldsymbol{\varphi}_{n+1}^1 + \boldsymbol{\varrho}_{n+1}^1 - \boldsymbol{\varrho}_{n+1}^2 + u_{n+1} \mathbf{n}_{n+1}^1 \quad (5.55f)$$

Numerical example

To check the algorithmic conservation properties of the newly developed energy-momentum scheme for the screw pair, we consider the example of a free flying (H) pair. With respect to an orthogonal frame $\{\mathbf{e}_1, \mathbf{e}_2, \mathbf{e}_3\}$, the initial configuration of the (H) pair is specified by

$$\boldsymbol{\varphi}^1 = \mathbf{0}, \quad \boldsymbol{\varphi}^2 = -30\mathbf{e}_3, \quad \mathbf{d}_i^\alpha = \mathbf{e}_i, \quad \mathbf{n}^1 = \mathbf{d}_3^1, \quad \boldsymbol{\varrho}_i^\alpha = 0 \quad (5.56)$$

The pitch is chosen to be $p = 20$ and the initial independent velocities in (5.39) are given by

$$\boldsymbol{\nu}^{(H)} = \begin{bmatrix} \dot{\boldsymbol{\varphi}}^1 \\ \dot{\boldsymbol{\omega}}^1 \\ \dot{\Theta} \end{bmatrix} = \begin{bmatrix} 150 \\ 10 \\ 0 \\ 2\pi \cdot 0.2 \\ 2\pi \cdot 0.2 \\ 0 \\ 2\pi \cdot 3.5 \end{bmatrix} \quad (5.57)$$

Note that (5.57) together with (5.41) determine the redundant velocities of the underlying rotationless formulation. The inertia data for the present 2-body system is summarized in Table 5.2. Snapshots of the motion of the screw pair are depicted in Fig. 5.9. Since no external forces or torques are acting on the system, the total energy as well as the total angular momentum vector are first integrals of the motion. These conservation properties are indeed exactly reproduced for any time step size by the applied **BEM/REM** scheme (Fig. 5.8a). Additionally, Fig. 5.8b depicts the relative angle

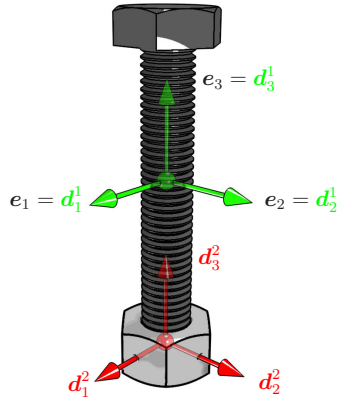
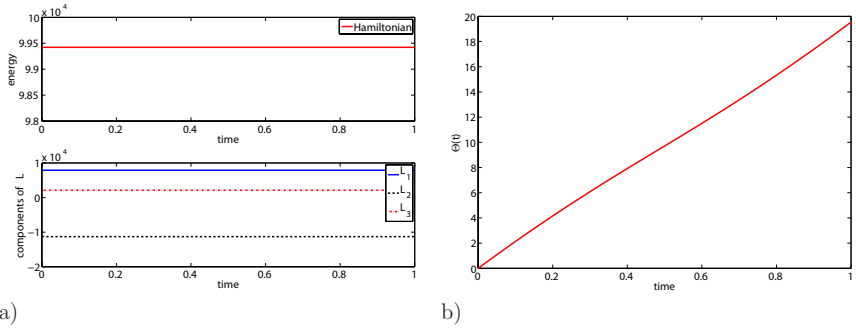


Figure 5.7.: Initial configuration of the screw pair.


 Figure 5.8.: Free flying screw pair: a) conservation of energy and angular momenta, b) relative angle $\Theta(t)$. ($\Delta t = 0.02$)

body	\mathcal{M}	\mathcal{E}_1	\mathcal{E}_2	\mathcal{E}_3
1	3	36	36	1600
2	4	48	48	48

Table 5.2.: Inertia data for the screw pair.

Θ versus time, which has been introduced through the coordinate augmentation technique described in this section. Eventually, the two alternative implementations (i.e. the **BEM** and the **REM** scheme) of the conserving time discretization described in Chapter 3 are compared. It can be observed from Table 5.3 that the **REM** scheme is about 5 times faster than the **BEM** scheme. Moreover, in contrast to the **BEM** scheme, the conditioning of the **REM** scheme does not deteriorate with the time step refinement.

	BEM scheme	REM scheme
number of unknowns	45	7
CPU-Time ($\Delta t = 2 \cdot 10^{-2}$)	5	1
condition $\Delta t = 10^{-2}$	$\mathcal{O}(10^{12})$	$\mathcal{O}(10^3)$
number $\Delta t = 10^{-3}$	$\mathcal{O}(10^{15})$	$\mathcal{O}(10^3)$
$\Delta t = 10^{-4}$	$\mathcal{O}(10^{18})$	$\mathcal{O}(10^3)$

Table 5.3.: Screw pair: comparison of the **BEM** scheme with the **REM** scheme.

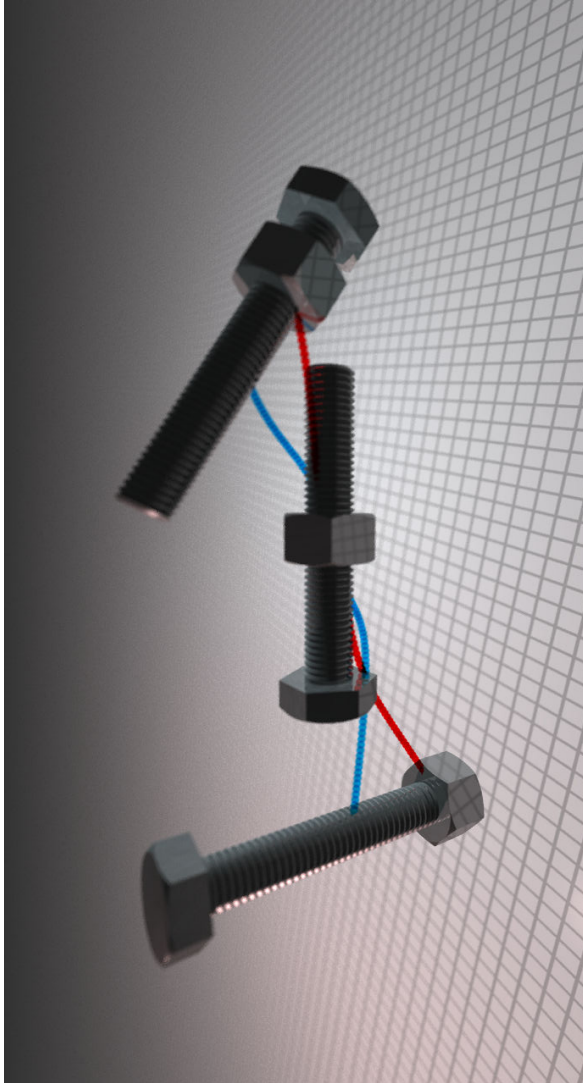


Figure 5.9.: Snapshots of the motion at $t \in \{0, 0.6, 1\}$. The two curves depict the trajectories of the center of mass of the respective body.

5.2. Design of Explicit Null Space Matrices for Closed Loop Systems

In this section we illustrate the treatment of closed-loop systems with the example of a free floating planar parallel manipulator (Fig. 5.10). The simulation of a similar planar parallel manipulator has been treated by Khan et al. [86], see also the references cited therein.

For simplicity of exposition we convert the closed-loop system at hand into an associated open-loop system with tree structure by cutting suitably selected joints. Each of the three branches of the system with tree structure can be regarded as an open chain (Fig. 5.11).

We first present a systematic derivation of the null space matrix for open chains. After this we assemble the contributions of the individual branches to get the null space matrix of the system with tree structure. Eventually, the assembly is completed by taking into account the closure constraints which yields the complete null space matrix of the closed-loop system.

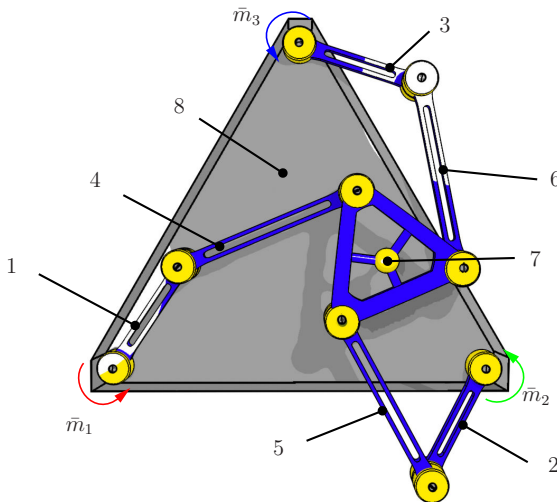


Figure 5.10.: Free floating planar parallel manipulator.

5.2.1. Description of open chains

As outlined above, the description of the closed-loop multibody system under consideration can be based on the three open chains depicted in Fig. 5.11. We next show that the treatment of the revolute pair in Section 4.2.2 can be easily extended to the description of open chains. To this end, we consider the open chain depicted in Fig. 5.12b along with the revolute pair in Fig. 5.12a.

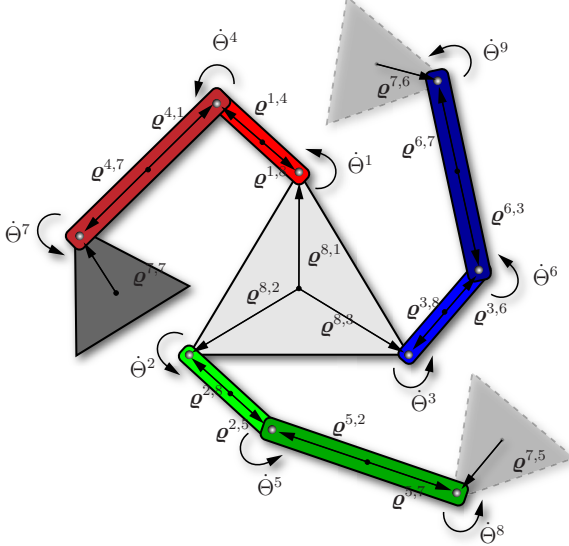


Figure 5.11.: Three open chains corresponding to the system with tree structure (branch 1: red, branch 2: green and branch 3: blue).

Design of the null space matrix

Revolute pair in an open chain Let body i_2 be connected to body i_1 and Θ^{j_1} measure the rotation of body i_2 relative to body i_1 . We obtain for the velocities

$$\mathbf{v}_\varphi^{i_2} = \mathbf{v}_\varphi^{i_1} + \mathbf{E}(\mathbf{q}^{i_2,j_1} - \mathbf{q}^{i_1,j_1})\omega^{i_1} + \mathbf{E}\mathbf{q}^{i_2,j_1}\dot{\Theta}^{j_1} \quad (5.58a)$$

$$\omega^{i_2} = \omega^{i_1} + \dot{\Theta}^{j_1} \quad (5.58b)$$

5. Modeling Techniques

whereby \mathbf{E} has been defined in Equation 5.19. Taking into account the relationship

$$\mathbf{q}^{i_2, j_1} - \mathbf{q}^{i_1, j_1} = -(\boldsymbol{\varphi}^{i_2} - \boldsymbol{\varphi}^{i_1}) \quad (5.59)$$

Equation (5.58) can be rewritten in the form

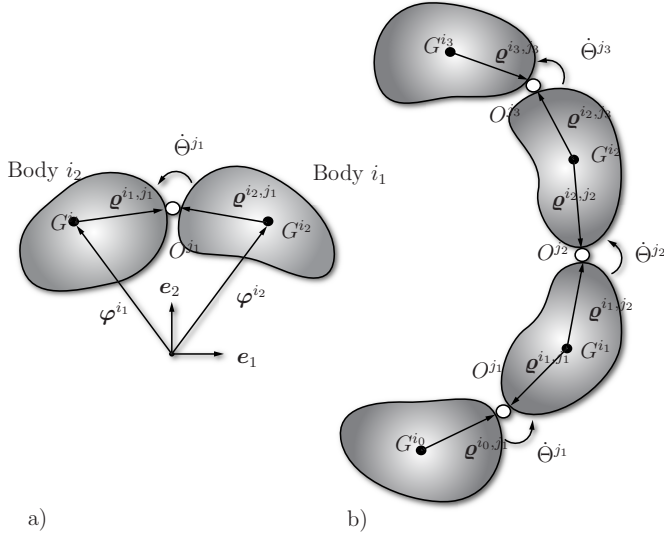


Figure 5.12.: a) Revolute pair in an open chain, b) schematic illustration of an open chain.

$$\mathbf{t}^{i_2} = \mathbf{B}^{i_2, i_1} \mathbf{t}^{i_1} + \mathbf{b}^{i_2, j_1} \dot{\theta}^{j_1} \quad (5.60)$$

with

$$\mathbf{B}^{i_2, i_1} = \begin{bmatrix} \mathbf{I}_{2 \times 2} & -\mathbf{E}(\boldsymbol{\varphi}^{i_2} - \boldsymbol{\varphi}^{i_1}) \\ \mathbf{0}_{1 \times 2} & 1 \end{bmatrix} \quad (5.61)$$

and

$$\mathbf{b}^{i_2, j_1} = \begin{bmatrix} \mathbf{E} \mathbf{q}^{i_2, j_1} \\ 1 \end{bmatrix} \quad (5.62)$$

It can be easily verified that the matrices $\mathbf{B}^{I, J}$ possess the following properties:

1. $\mathbf{B}^{I,J} \mathbf{B}^{J,K} = \mathbf{B}^{I,K}$
2. $(\mathbf{B}^{I,J})^{-1} = \mathbf{B}^{J,I}$

The first property is of paramount importance for the kinematic description of open chains.

Open chains The twist of each body pertaining to an open chain can be expressed in terms of the base twist \mathbf{t}^{i_0} together with the joint rates by applying (5.60) recursively. For example, the twist of body i_2 belonging to the chain depicted in Fig. 5.12b can be written as

$$\mathbf{t}^{i_2} = \mathbf{B}^{i_2, i_1} \mathbf{t}^{i_1} + \mathbf{b}^{i_2, j_2} \dot{\Theta}^{j_2} \quad (5.63a)$$

$$\mathbf{t}^{i_2} = \mathbf{B}^{i_2, i_1} \mathbf{B}^{i_1, i_0} \mathbf{t}^{i_0} + \mathbf{B}^{i_2, i_1} \mathbf{b}^{i_1, j_1} \dot{\Theta}^{j_1} + \mathbf{b}^{i_2, j_2} \dot{\Theta}^{j_2} \quad (5.63b)$$

$$\mathbf{t}^{i_2} = \mathbf{B}^{i_2, i_0} \mathbf{t}^{i_0} + \mathbf{B}^{i_2, i_1} \mathbf{b}^{i_1, j_1} \dot{\Theta}^{j_1} + \mathbf{b}^{i_2, j_2} \dot{\Theta}^{j_2} \quad (5.63c)$$

To summarize, the twist of the chain under consideration can be written in the form

$$\mathbf{t}^{chain} = \mathbf{P}_{ext}^{chain} \mathbf{v}^{chain} \quad (5.64)$$

or, more explicitly,

$$\begin{bmatrix} \mathbf{t}^{i_0} \\ \mathbf{t}^{i_1} \\ \mathbf{t}^{i_2} \\ \mathbf{t}^{i_3} \end{bmatrix} = \begin{bmatrix} \mathbf{I} & \mathbf{0} & \mathbf{0} & \mathbf{0} \\ \mathbf{P}^{i_1, i_0} & \mathbf{P}^{i_1, j_1} & \mathbf{0} & \mathbf{0} \\ \mathbf{P}^{i_2, i_0} & \mathbf{P}^{i_2, j_1} & \mathbf{P}^{i_2, j_2} & \mathbf{0} \\ \mathbf{P}^{i_3, i_0} & \mathbf{P}^{i_3, j_1} & \mathbf{P}^{i_3, j_2} & \mathbf{P}^{i_3, j_3} \end{bmatrix} \begin{bmatrix} \mathbf{t}^{i_0} \\ \dot{\Theta}^{j_1} \\ \dot{\Theta}^{j_2} \\ \dot{\Theta}^{j_3} \end{bmatrix} \quad (5.65)$$

It is obvious from the previous considerations that the external null space matrix of the open chain can be decomposed multiplicatively

$$\mathbf{P}_{ext}^{chain} = \mathbf{P}_L^{chain} \mathbf{P}_D^{chain} \quad (5.66)$$

Here, the lower block triangular matrix \mathbf{P}_L^{chain} is given by

$$\mathbf{P}_L^{chain} = \begin{bmatrix} \mathbf{I} & \mathbf{0} & \mathbf{0} & \mathbf{0} \\ \mathbf{B}^{i_1, i_0} & \mathbf{I} & \mathbf{0} & \mathbf{0} \\ \mathbf{B}^{i_2, i_0} & \mathbf{B}^{i_2, i_1} & \mathbf{I} & \mathbf{0} \\ \mathbf{B}^{i_3, i_0} & \mathbf{B}^{i_3, i_1} & \mathbf{B}^{i_3, i_2} & \mathbf{I} \end{bmatrix} \quad (5.67)$$

and \mathbf{P}_D^{chain} is a block diagonal matrix of the form

$$\mathbf{P}_D^{chain} = \begin{bmatrix} \mathbf{I} & \mathbf{0} & \mathbf{0} & \mathbf{0} \\ \mathbf{0} & \mathbf{b}^{i_1, j_1} & \mathbf{0} & \mathbf{0} \\ \mathbf{0} & \mathbf{0} & \mathbf{b}^{i_2, j_2} & \mathbf{0} \\ \mathbf{0} & \mathbf{0} & \mathbf{0} & \mathbf{b}^{i_3, j_3} \end{bmatrix} \quad (5.68)$$

Eventually, application of (3.16) yields the complete null space matrix $\mathbf{P}^{\text{chain}}$ of the present open-loop system

$$\mathbf{P}^{\text{chain}} = \mathbf{P}_{\text{int}}^{\text{chain}} \mathbf{P}_{\text{ext}}^{\text{chain}} \quad (5.69)$$

with

$$\mathbf{P}_{\text{int}}^{\text{chain}} = \begin{bmatrix} \mathbf{P}_{\text{int}}^{i_0} & \mathbf{0} & \mathbf{0} & \mathbf{0} \\ \mathbf{0} & \mathbf{P}_{\text{int}}^{i_1} & \mathbf{0} & \mathbf{0} \\ \mathbf{0} & \mathbf{0} & \mathbf{P}_{\text{int}}^{i_2} & \mathbf{0} \\ \mathbf{0} & \mathbf{0} & \mathbf{0} & \mathbf{P}_{\text{int}}^{i_3} \end{bmatrix} \quad (5.70)$$

where $\mathbf{P}_{\text{int}}^i$ is given by (4.16). The discrete version of the null space matrix pertaining to open chains coincides with the mid-point evaluation of (5.69).

Remark 5.2.1 *The decomposition (5.66) corresponds to the ‘Decoupled Natural Orthogonal Complement’ introduced by Saha [131], see also [132]. Moreover, in these works, (5.61) is referred to as the ‘twist propagation matrix’, whereas (5.62) is called the ‘joint-rate propagation vector’.*

Parametrization of the configuration space

The choice of coordinates for the description of open chains follows closely the previous treatment of the revolute pair (see Section 5.1.1). Accordingly, if the open chain consists of N bodies, we have $n = 6N$ redundant coordinates. For each body we have to account for three internal constraints of the form (4.3)². In addition to that, each joint yields two external constraints of the form (4.52). To summarize, we have $m = 3N + 2(N - 1)$ constraints. Accordingly, the **BEM** scheme relies on $n + m = 11N - 2$ unknowns.

In contrast to that, the chain has only $n - m = N + 2$ degrees of freedom. The $N + 2$ coordinates can be used to characterize the configuration space of the chain. Concerning the map (3.27), we now have

$$\mathbf{F} : \mathbb{R}^2 \times \underbrace{\mathbb{R}^1 \times \cdots \times \mathbb{R}^1}_{N\text{-times}} \mapsto \mathbf{Q}_{\text{chain}} \subset \mathbb{R}^{6N} \quad (5.71)$$

Accordingly, the reduced scheme makes use of $N + 2$ unknowns.

5.2.2. Description of the system with tree structure

Assembly of the null space matrix

As outlined above the null space matrix pertaining to the open-loop system with tree structure can be obtained by assembling the contributions stemming from the chains

²Again broken down to the 2D-case, see also [28, 149].

associated with the three branches (Fig. 5.11). Taking into account the selected numbering of the bodies the first chain consists of bodies $\{8, 1, 4, 7\}$, whereas the second and third chain consist of bodies $\{8, 2, 5\}$ and $\{8, 3, 6\}$, respectively. Accordingly, the twist and the generalized velocities pertaining to the system with tree structure may be written as

$$\mathbf{t}^{\text{tree}} = \begin{bmatrix} \mathbf{t}^8 \\ \mathbf{t}^1 \\ \mathbf{t}^4 \\ \mathbf{t}^7 \\ \mathbf{t}^2 \\ \mathbf{t}^5 \\ \mathbf{t}^3 \\ \mathbf{t}^6 \end{bmatrix} \quad \text{and} \quad \boldsymbol{\nu}^{\text{tree}} = \begin{bmatrix} \mathbf{t}^8 \\ \dot{\theta}^1 \\ \dot{\theta}^4 \\ \dot{\theta}^7 \\ \dot{\theta}^2 \\ \dot{\theta}^5 \\ \dot{\theta}^3 \\ \dot{\theta}^6 \end{bmatrix} \quad (5.72)$$

Since the null space matrix of each chain assumes the form (5.69), it can be easily verified that the assembly yields the following null space matrix pertaining to the system with tree structure

$$\mathbf{P}^{\text{tree}} = \mathbf{P}_{\text{int}}^{\text{tree}} \mathbf{P}_L^{\text{tree}} \mathbf{P}_D^{\text{tree}} \quad (5.73)$$

Here, the lower block triangular matrix $\mathbf{P}_L^{\text{tree}}$ is given by

$$\mathbf{P}_L^{\text{tree}} = \begin{bmatrix} \mathbf{I} & \mathbf{0} & \mathbf{0} & \mathbf{0} & \mathbf{0} & \mathbf{0} & \mathbf{0} & \mathbf{0} \\ \mathbf{B}^{1,8} & \mathbf{I} & \mathbf{0} & \mathbf{0} & \mathbf{0} & \mathbf{0} & \mathbf{0} & \mathbf{0} \\ \mathbf{B}^{4,8} & \mathbf{B}^{4,1} & \mathbf{I} & \mathbf{0} & \mathbf{0} & \mathbf{0} & \mathbf{0} & \mathbf{0} \\ \mathbf{B}^{7,8} & \mathbf{B}^{7,1} & \mathbf{B}^{7,4} & \mathbf{I} & \mathbf{0} & \mathbf{0} & \mathbf{0} & \mathbf{0} \\ \mathbf{B}^{2,8} & \mathbf{0} & \mathbf{0} & \mathbf{0} & \mathbf{I} & \mathbf{0} & \mathbf{0} & \mathbf{0} \\ \mathbf{B}^{5,8} & \mathbf{0} & \mathbf{0} & \mathbf{0} & \mathbf{B}^{5,2} & \mathbf{I} & \mathbf{0} & \mathbf{0} \\ \mathbf{B}^{3,8} & \mathbf{0} & \mathbf{0} & \mathbf{0} & \mathbf{0} & \mathbf{0} & \mathbf{I} & \mathbf{0} \\ \mathbf{B}^{6,8} & \mathbf{0} & \mathbf{0} & \mathbf{0} & \mathbf{0} & \mathbf{0} & \mathbf{B}^{6,3} & \mathbf{I} \end{bmatrix} \quad (5.74)$$

where again the matrices $\mathbf{B}^{I,K}$ are given by (5.61). Moreover, in (5.73), $\mathbf{P}_D^{\text{tree}}$ is a block diagonal matrix of the form

$$\mathbf{P}_D^{\text{tree}} = \begin{bmatrix} \mathbf{I} & \mathbf{0} & \mathbf{0} & \mathbf{0} & \mathbf{0} & \mathbf{0} & \mathbf{0} & \mathbf{0} \\ \mathbf{0} & \mathbf{b}^{1,1} & \mathbf{0} & \mathbf{0} & \mathbf{0} & \mathbf{0} & \mathbf{0} & \mathbf{0} \\ \mathbf{0} & \mathbf{0} & \mathbf{b}^{4,4} & \mathbf{0} & \mathbf{0} & \mathbf{0} & \mathbf{0} & \mathbf{0} \\ \mathbf{0} & \mathbf{0} & \mathbf{0} & \mathbf{b}^{7,7} & \mathbf{0} & \mathbf{0} & \mathbf{0} & \mathbf{0} \\ \mathbf{0} & \mathbf{0} & \mathbf{0} & \mathbf{0} & \mathbf{b}^{2,2} & \mathbf{0} & \mathbf{0} & \mathbf{0} \\ \mathbf{0} & \mathbf{0} & \mathbf{0} & \mathbf{0} & \mathbf{0} & \mathbf{b}^{5,5} & \mathbf{0} & \mathbf{0} \\ \mathbf{0} & \mathbf{0} & \mathbf{0} & \mathbf{0} & \mathbf{0} & \mathbf{0} & \mathbf{b}^{3,3} & \mathbf{0} \\ \mathbf{0} & \mathbf{0} & \mathbf{0} & \mathbf{0} & \mathbf{0} & \mathbf{0} & \mathbf{0} & \mathbf{b}^{6,6} \end{bmatrix} \quad (5.75)$$

where, as before, $\mathbf{b}^{i,j}$ is given by (5.62). In addition to that, again taking into account the selected numbering of the bodies, the internal null space matrix pertaining to the system with tree structure is given by

$$\mathbf{P}_{\text{int}}^{\text{tree}} = \begin{bmatrix} \mathbf{P}_{\text{int}}^8 & \mathbf{0} & \mathbf{0} & \mathbf{0} & \mathbf{0} & \mathbf{0} & \mathbf{0} & \mathbf{0} \\ \mathbf{0} & \mathbf{P}_{\text{int}}^1 & \mathbf{0} & \mathbf{0} & \mathbf{0} & \mathbf{0} & \mathbf{0} & \mathbf{0} \\ \mathbf{0} & \mathbf{0} & \mathbf{P}_{\text{int}}^4 & \mathbf{0} & \mathbf{0} & \mathbf{0} & \mathbf{0} & \mathbf{0} \\ \mathbf{0} & \mathbf{0} & \mathbf{0} & \mathbf{P}_{\text{int}}^7 & \mathbf{0} & \mathbf{0} & \mathbf{0} & \mathbf{0} \\ \mathbf{0} & \mathbf{0} & \mathbf{0} & \mathbf{0} & \mathbf{P}_{\text{int}}^2 & \mathbf{0} & \mathbf{0} & \mathbf{0} \\ \mathbf{0} & \mathbf{0} & \mathbf{0} & \mathbf{0} & \mathbf{0} & \mathbf{P}_{\text{int}}^5 & \mathbf{0} & \mathbf{0} \\ \mathbf{0} & \mathbf{0} & \mathbf{0} & \mathbf{0} & \mathbf{0} & \mathbf{0} & \mathbf{P}_{\text{int}}^3 & \mathbf{0} \\ \mathbf{0} & \mathbf{0} & \mathbf{0} & \mathbf{0} & \mathbf{0} & \mathbf{0} & \mathbf{0} & \mathbf{P}_{\text{int}}^6 \end{bmatrix} \quad (5.76)$$

where $\mathbf{P}_{\text{int}}^i$ assumes the form (4.16). Moreover, the discrete null space matrix follows from the mid-point evaluation of (5.73).

Parametrization of the configuration space

The extension of the parametrization of chains (see Section 5.2.1) to systems with tree structure can be performed in a straightforward way. The present system is comprised of 8 rigid bodies and 7 joints. Accordingly, we have $n = 6 \cdot 8 = 48$ redundant coordinates subject to $m = 3 \cdot 8 + 2 \cdot 7 = 38$ constraints. Consequently, the **BEM** scheme entails $n + m = 86$ unknowns.

On the other hand, the **REM** scheme involves $n - m = 10$ unknowns which play the role of coordinates for the parametrization of the present configuration manifold. Consequently, concerning the map (3.27), we now have

$$\mathbf{F} : \mathbb{R}^2 \times \underbrace{\mathbb{R}^1 \times \cdots \times \mathbb{R}^1}_{\text{8-times}} \mapsto \mathbf{Q}_{\text{tree}} \subset \mathbb{R}^{48} \quad (5.77)$$

5.2.3. Incorporation of the loop-closure constraints

Eventually, we incorporate the loop-closure constraints into the description of the system with tree structure to reach the description of the free floating parallel manipulator.

Design of the null space matrix

In this section we demonstrate that the null space matrix of the closed-loop system at hand can be written in the form

$$\mathbf{P}^{\text{close}} = \mathbf{P}^{\text{tree}} \mathbf{P}^{\text{oc}} \quad (5.78)$$

where \mathbf{P}^{tree} is given by (5.73) and \mathbf{P}^{oc} links the open-loop system (or the system with tree structure) to the closed-loop system. In particular, \mathbf{P}^{oc} accounts for the loop-closure

constraints.

In the following we devise viable forms of \mathbf{P}^{oc} along with discrete counterparts. In essence, our approach is closely related to a classical variable-reduction method (see, for example, Gill et al. [55] and Remark 5.2.2 later). In particular, we seek to express the velocities of the underlying system with tree-structure, $\mathbf{v}^{tree} \in \mathbb{R}^{10}$ in terms of independent velocities $\mathbf{v} \in \mathbb{R}^6$ associated with the free-floating manipulator, that is,

$$\mathbf{v}^{tree} = \mathbf{P}^{oc} \mathbf{v} \quad (5.79)$$

To this end, we consider a representative leg of the parallel manipulator depicted in Fig. 5.13. Additionally, Table 5.4 contains the connection between the representative leg and the parallel manipulator. For each leg of the parallel manipulator we have (cf. the last

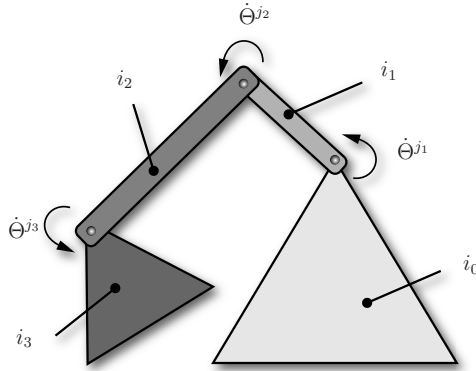


Figure 5.13.: Open chain associated with each leg of the parallel manipulator.

Table 5.4.: Connection between the numbering of the chain (Fig. 5.13) and the parallel manipulator (Fig. 5.11).

body #	i_0	i_1	i_2	i_3	joint #	j_1	j_2	j_3
leg 1	8	1	4	7	leg 1	1	4	7
leg 2	8	2	5	7	leg 2	2	5	8
leg 3	8	3	6	7	leg 3	3	6	9

5. Modeling Techniques

equation in (5.65))

$$\mathbf{t}^{i_3} = \mathbf{P}^{i_3, i_0} \mathbf{t}^{i_0} + \mathbf{P}^{i_3, j_1} \dot{\Theta}^{j_1} + \mathbf{P}^{i_3, j_2} \dot{\Theta}^{j_2} + \mathbf{P}^{i_3, j_3} \dot{\Theta}^{j_3} \quad (5.80)$$

Due to the presence of the loop-closure constraints the following conditions have to be satisfied for each leg:

$$\begin{aligned} \mathbf{t}^{i_3} &= \mathbf{t}^7 \\ \mathbf{t}^{i_0} &= \mathbf{t}^8 \end{aligned} \quad (5.81)$$

Accordingly, (5.80) yields

$$\mathbf{t}^7 = \mathbf{P}^{7,8} \mathbf{t}^8 + \mathbf{P}^{7, j_1} \dot{\Theta}^{j_1} + \mathbf{P}^{7, j_2} \dot{\Theta}^{j_2} + \mathbf{P}^{7, j_3} \dot{\Theta}^{j_3} \quad (5.82)$$

For each of the three legs the last equation can be used to establish a relationship between the individual joint velocities $\dot{\Theta}^I$, $I \in \{j_1, j_2, j_3\}$ and the twists $(\mathbf{t}^7, \mathbf{t}^8)$. Our approach is based on the introduction of projection matrices. Let the indices (I, J, K) be permutations of (j_1, j_2, j_3) and define

$$\Xi_I = \Phi_K - \frac{1}{\|\mathbf{p}_{K,J}\|^2} \mathbf{p}_{K,J} \otimes \mathbf{p}_{K,J} \quad (5.83)$$

with

$$\Phi_K = \mathbf{I} - \frac{1}{\|\mathbf{P}^{7,K}\|^2} \mathbf{P}^{7,K} \otimes \mathbf{P}^{7,K} \quad (5.84)$$

and

$$\mathbf{p}_{K,J} = \Phi_K \mathbf{P}^{7,J} \quad (5.85)$$

It can be easily verified that the projection matrices possess the following properties:

1. Ξ_I is symmetric ($\Xi_I^T = \Xi_I$)
2. Ξ_I is idempotent ($\Xi_I^2 = \Xi_I$)
3. $\Xi_I \mathbf{P}^{7,L} = \mathbf{0}$ for $I \neq L$ ($I, L \in \{j_1, j_2, j_3\}$)

Pre-multiplying both sides of (5.82) by Ξ_I yields

$$\Xi_I \mathbf{t}^7 = \Xi_I \mathbf{P}^{7,8} \mathbf{t}^8 + \Xi_I \mathbf{P}^{7,I} \dot{\Theta}^I \quad (5.86)$$

Accordingly, for each leg the last equation can be used to express the corresponding joint velocities $\dot{\theta}^I$ ($I \in \{j_1, j_2, j_3\}$) as

$$\dot{\theta}^I = \frac{1}{\xi_I} \mathbf{P}^{7,I} \cdot \Xi_I (\mathbf{t}^7 - \mathbf{P}^{7,8} \mathbf{t}^8) \quad (5.87)$$

with

$$\xi_I = \mathbf{P}^{7,I} \cdot \Xi_I \mathbf{P}^{7,I} \quad (5.88)$$

Now the redundant velocities $\boldsymbol{\nu}^{\text{tree}} \in \mathbb{R}^{10}$ associated with the underlying description of the system with tree structure can be expressed in terms of six pre-selected independent velocities $\boldsymbol{\nu} \in \mathbb{R}^6$. For this purpose we have at our disposal both the constraint twists $(\mathbf{t}^7, \mathbf{t}^8)$ and the joint velocities $(\dot{\theta}^1, \dots, \dot{\theta}^9)$ from which we can select 6 independent quantities.

Example 5.2.1 *We may choose*

$$\boldsymbol{\nu} = \begin{bmatrix} \mathbf{t}^7 \\ \mathbf{t}^8 \end{bmatrix} \quad (5.89)$$

as independent velocities. Making use of (5.87) directly yields

$$\mathbf{P}^{\text{oc}} = \begin{bmatrix} \mathbf{0}_3 & \mathbf{I}_3 \\ \mathbf{g}_1^T & -\mathbf{g}_1^T \mathbf{P}^{7,8} \\ \mathbf{g}_4^T & -\mathbf{g}_4^T \mathbf{P}^{7,8} \\ \mathbf{g}_7^T & -\mathbf{g}_7^T \mathbf{P}^{7,8} \\ \mathbf{g}_2^T & -\mathbf{g}_2^T \mathbf{P}^{7,8} \\ \mathbf{g}_5^T & -\mathbf{g}_5^T \mathbf{P}^{7,8} \\ \mathbf{g}_3^T & -\mathbf{g}_3^T \mathbf{P}^{7,8} \\ \mathbf{g}_6^T & -\mathbf{g}_6^T \mathbf{P}^{7,8} \end{bmatrix} \quad (5.90)$$

with

$$\mathbf{g}_I = \frac{1}{\xi_I} \Xi_I \mathbf{P}^{7,I} \quad (5.91)$$

The discrete version of \mathbf{P}^{oc} coincides with the mid-point evaluation of (5.90). It can be used as long as none of the values of the ξ_I 's associated with the dependent joint-rates ($I \in \{1, 4, 7, 2, 5, 3, 6\}$) reaches zero.

Example 5.2.2 *Choose*

$$\boldsymbol{\nu} = \begin{bmatrix} \mathbf{t}^8 \\ \dot{\theta}^{k_1} \\ \dot{\theta}^{k_2} \\ \dot{\theta}^{k_3} \end{bmatrix} \quad (5.92)$$

5. Modeling Techniques

as independent velocities, with $\eta := \{k_1, k_2, k_3\} \subset \{1, \dots, 9\}$. In principle, the independent joint-rates $\dot{\Theta}^J$ ($J \in \eta$) can be chosen arbitrarily. However, to prevent singularities of the type identified in Example 5.2.1, we choose to select the three joint-rates associated with one leg as independent quantities, i.e. $\eta = \{j_1, j_2, j_3\}$ (cf. Table 5.4). A singularity analysis along the lines of Mohammadi Daniiali et al. [107] shows that if one leg is either fully extended or fully folded, then the related ξ_I 's are zero (and thus the joint-rates of the respective leg would be selected as the independent ones). The remaining dependent joint-rates can then be easily determined. From (5.82) we have

$$\mathbf{t}^7 - \mathbf{P}^{7,8}\mathbf{t}^8 = \mathbf{G} \begin{bmatrix} \dot{\Theta}^{j_1} \\ \dot{\Theta}^{j_2} \\ \dot{\Theta}^{j_3} \end{bmatrix} \quad (5.93)$$

with

$$\mathbf{G} = [\mathbf{P}^{7,j_1} \quad \mathbf{P}^{7,j_2} \quad \mathbf{P}^{7,j_3}] \quad (5.94)$$

Substitution from (5.93) into (5.87) yields the dependent joint-rates. For example, if we choose the joints-rates of leg 2 as the independent ones (i.e. $\eta = \{2, 5, 8\}$), so that the independent velocities are given by

$$\boldsymbol{\nu} = \begin{bmatrix} \mathbf{t}^8 \\ \dot{\Theta}^2 \\ \dot{\Theta}^5 \\ \dot{\Theta}^8 \end{bmatrix} \quad (5.95)$$

we obtain

$$\mathbf{P}^{\text{oc}} = \begin{bmatrix} \mathbf{I}_3 & \mathbf{0}^T \\ \mathbf{0}^T & \mathbf{g}_1^T \mathbf{G} \\ \mathbf{0}^T & \mathbf{g}_4^T \mathbf{G} \\ \mathbf{0}^T & \mathbf{g}_7^T \mathbf{G} \\ \mathbf{0}^T & \mathbf{e}_1^T \\ \mathbf{0}^T & \mathbf{e}_2^T \\ \mathbf{0}^T & \mathbf{g}_3^T \mathbf{G} \\ \mathbf{0}^T & \mathbf{g}_3^T \mathbf{G} \end{bmatrix} \quad (5.96)$$

where the \mathbf{g}_I 's are given by (5.91) and

$$\mathbf{G} = [\mathbf{P}^{7,2} \quad \mathbf{P}^{7,5} \quad \mathbf{P}^{7,8}], \quad \mathbf{e}_1 = \begin{bmatrix} 1 \\ 0 \\ 0 \end{bmatrix} \quad \text{and} \quad \mathbf{e}_2 = \begin{bmatrix} 0 \\ 1 \\ 0 \end{bmatrix} \quad (5.97)$$

It is obvious from the above treatment that the ξ_I 's ($I \in \{1, 4, 7, 2, 5, 3, 6\}$) serve the purpose of selecting appropriate versions of \mathbf{P}^{oc} . In all cases the discrete counterpart of the \mathbf{P}^{oc} 's coincides with their mid-point evaluation.

Remark 5.2.2 Our approach for devising discrete null space matrices for closed-loop systems by means of the introduction of matrix \mathbf{P}^{oc} can be related to a classical variable-reduction method (see, for example, Gill et al. [55]). In the context of Example 5.2.2, the variable-reduction method relies on the partition of the joint-rates $\dot{\Theta}^J$, $J \in \eta_{\text{tree}} = \{1, \dots, 7\}$, belonging to the system with tree structure, into three independent and four dependent joint-rates. Accordingly, after a possible reordering of the components of $\boldsymbol{\nu}^{\text{tree}}$ in (5.72), the aforementioned partitioning yields

$$\boldsymbol{\nu}^{\text{tree}} = [\boldsymbol{\nu}^I \quad \boldsymbol{\nu}^D] \quad \text{with} \quad \boldsymbol{\nu}^I = \begin{bmatrix} \boldsymbol{t}^8 \\ \dot{\Theta}^{l_1} \\ \dot{\Theta}^{l_2} \\ \dot{\Theta}^{l_3} \end{bmatrix} \quad \text{and} \quad \boldsymbol{\nu}^D = \begin{bmatrix} \dot{\Theta}^{d_1} \\ \dot{\Theta}^{d_2} \\ \dot{\Theta}^{d_3} \\ \dot{\Theta}^{d_4} \end{bmatrix} \quad (5.98)$$

where $\eta_I = \{l_1, l_2, l_3\} \subset \eta_{\text{tree}}$ and $\eta_D = \eta_{\text{tree}} - \eta_I$ is the set of joint numbers corresponding to the independent and dependent joint-rates, respectively. Differentiating the loop-closure constraints (5.105) with respect to time yields

$$\frac{d}{dt} \boldsymbol{\Phi}_{\text{ext}}^{\text{close}}(\mathbf{q}) = \mathbf{G}_{\text{ext}}^{\text{close}}(\mathbf{q}) \mathbf{v} = \mathbf{0} \quad (5.99)$$

with $\mathbf{G}_{\text{ext}}^{\text{close}}(\mathbf{q}) = D \boldsymbol{\Phi}_{\text{ext}}^{\text{close}}(\mathbf{q})$. Substituting the relationship $\mathbf{v} = \mathbf{P}^{\text{tree}} \boldsymbol{\nu}^{\text{tree}}$, where \mathbf{P}^{tree} is given by (5.73), into (5.99) gives

$$\mathbf{G}_{\text{ext}}^{\text{close}} \mathbf{P}^{\text{tree}} \boldsymbol{\nu}^{\text{tree}} = \mathbf{0} \quad (5.100)$$

If \mathbf{P}^{tree} is partitioned according to (5.98), the last equation can be written as

$$\mathbf{G}_{\text{ext}}^{\text{close}} \mathbf{P}_I^{\text{tree}} \boldsymbol{\nu}^I + \mathbf{G}_{\text{ext}}^{\text{close}} \mathbf{P}_D^{\text{tree}} \boldsymbol{\nu}^D = \mathbf{0} \quad (5.101)$$

so that

$$\boldsymbol{\nu}^D = -\mathbf{B}(\mathbf{q}) \boldsymbol{\nu}^I \quad \text{with} \quad \mathbf{B}(\mathbf{q}) = (\mathbf{G}_{\text{ext}}^{\text{close}} \mathbf{P}_D^{\text{tree}})^{-1} \mathbf{G}_{\text{ext}}^{\text{close}} \mathbf{P}_I^{\text{tree}} \quad (5.102)$$

Accordingly, in view of (5.98), we have

$$\boldsymbol{\nu}^{\text{tree}} = \begin{bmatrix} \mathbf{I}_6 \\ -\mathbf{B}(\mathbf{q}) \end{bmatrix} \boldsymbol{\nu}^I \quad (5.103)$$

such that

$$\mathbf{P}^{\text{oc}}(\mathbf{q}) = \begin{bmatrix} \mathbf{I}_6 \\ -\mathbf{B}(\mathbf{q}) \end{bmatrix} \quad (5.104)$$

As before, the discrete version of (5.104) is given by $\mathbf{P}^{\text{oc}}(\mathbf{q}_{n+\frac{1}{2}})$

Parametrization of the configuration space

Starting with the system with tree structure (see Section 5.2.2), we have to incorporate four additional external constraints. In particular, the loop-closure constraints correspond to the incorporation of two additional joints (see joints 8 and 9 in Fig. 5.11), with corresponding constraint functions. Accordingly,

$$\Phi_{\text{ext}}^{\text{close}} = \begin{bmatrix} \varphi^7 - \varphi^5 + \varrho^{7,5} - \varrho^{5,7} \\ \varphi^7 - \varphi^6 + \varrho^{7,6} - \varrho^{6,7} \end{bmatrix} \quad (5.105)$$

Thus the original $n = 48$ coordinates are now subject to $m = 42$ constraints and the number of unknowns of the **BEM** scheme amounts to $n + m = 90$. On the other hand, using the map (5.71) of the underlying system with tree-structure, (cf. Section 5.2.3), the original 48 coordinates are expressed in terms of $\mathbf{u} \in \mathbb{R}^{10}$. Due to the presence of the loop-closure constraints (5.105), only $n - m = 6$ degrees of freedom remain.

5.2.4. Coordinate augmentation

As indicated in Fig. 5.10, the first three joints of the parallel manipulator (with corresponding joint-rates $\dot{\Theta}^1$, $\dot{\Theta}^2$ and $\dot{\Theta}^3$, cf. Fig. 5.11) are actuated. To incorporate into the underlying rotationless formulation the possibility of imposing the joint-torques $(\bar{m}_1, \bar{m}_2, \bar{m}_3)$, we apply the coordinate augmentation technique proposed in Section 5.1. Indeed, the application of the coordinate augmentation technique to the present closed-loop system follows from a straight-forward extension of the treatment of the revolute pair in Section 5.1.1.

In the following, the subscript *ori* again refers to quantities originally used for the description of the above-treated closed-loop system. Similar to (5.1), we augment the originally used redundant coordinates $\mathbf{q}_{\text{ori}} \in \mathbb{R}^{48}$ with the joint-angles

$$\Theta = \begin{bmatrix} \Theta^1 \\ \Theta^2 \\ \Theta^3 \end{bmatrix} \quad (5.106)$$

such that the augmented configuration vector reads

$$\mathbf{q} = \begin{bmatrix} \mathbf{q}_{\text{ori}} \\ \Theta \end{bmatrix} \quad (5.107)$$

Accordingly, we now have $n = 51$ redundant coordinates. The three additional coordinates (5.106) are linked to the original ones through the introduction of three additional constraint functions. Similar to (5.11), the extended vector of constraint functions reads

$$\Phi(\mathbf{q}) = \begin{bmatrix} \Phi_{\text{ori}}(\mathbf{q}) \\ \Phi_{\text{aug}}(\mathbf{q}) \end{bmatrix} \quad (5.108)$$

where, similar to (5.4), the additional constraints are specified by

$$\boldsymbol{\Phi}_{\text{aug}}(\mathbf{q}) = \boldsymbol{\Phi}_{\text{aug}}^I(\mathbf{q}_{\text{ori}}) + \boldsymbol{\Phi}_{\text{aug}}^{II}(\boldsymbol{\Theta}) \quad (5.109)$$

where

$$\boldsymbol{\Phi}_{\text{aug}}^I(\mathbf{q}_{\text{ori}}) = \begin{bmatrix} (\Phi_{\text{aug}}^I)_1 \\ (\Phi_{\text{aug}}^I)_2 \\ (\Phi_{\text{aug}}^I)_3 \end{bmatrix} \quad \text{with} \quad (\Phi_{\text{aug}}^I)_j = \mathbf{d}_2^j \cdot (\mathbf{d}_1^s + \mathbf{d}_2^s) \quad (5.110)$$

and

$$\boldsymbol{\Phi}_{\text{aug}}^{II}(\boldsymbol{\Theta}) = \begin{bmatrix} \Phi_{\text{aug}}^{II}(\Theta^1) \\ \Phi_{\text{aug}}^{II}(\Theta^2) \\ \Phi_{\text{aug}}^{II}(\Theta^3) \end{bmatrix} \quad \text{with} \quad \Phi_{\text{aug}}^{II}(\Theta^j) = \sin \Theta^j - \cos \Theta^j \quad (5.111)$$

Thus we have a total of $m = 45$ constraints. Consequently, the **BEM** scheme relies on $n + m = 96$ unknowns. Similar to (5.12), the augmented constraint Jacobian is given by

$$\mathbf{G}(\mathbf{q}) = \begin{bmatrix} \mathbf{G}_{\text{ori}}(\mathbf{q}_{\text{ori}}) & \mathbf{0}_{48 \times 3} \\ \mathbf{G}_{\text{aug}}^I(\mathbf{q}_{\text{ori}}) & \mathbf{G}_{\text{aug}}^{II}(\boldsymbol{\Theta}) \end{bmatrix} \quad (5.112)$$

The 3×48 matrix $\mathbf{G}_{\text{aug}}^I(\mathbf{q}_{\text{ori}})$ has the same structure as (5.9a), and $\mathbf{G}_{\text{aug}}^{II}(\boldsymbol{\Theta})$ is given by

$$\mathbf{G}_{\text{aug}}^{II} = \begin{bmatrix} \sin \Theta^1 + \cos \Theta^1 & 0 & 0 \\ 0 & \sin \Theta^2 + \cos \Theta^2 & 0 \\ 0 & 0 & \sin \Theta^3 + \cos \Theta^3 \end{bmatrix} \quad (5.113)$$

Similar to (5.22) the discrete counterpart of (5.112) can be written in the form

$$\mathbf{G}(\mathbf{q}_n, \mathbf{q}_{n+1}) = \begin{bmatrix} \mathbf{G}_{\text{ori}}((\mathbf{q}_{\text{ori}})_{n+\frac{1}{2}}) & \mathbf{0}_{48 \times 3} \\ \mathbf{G}_{\text{aug}}^I((\mathbf{q}_{\text{ori}})_{n+\frac{1}{2}}) & \mathbf{G}_{\text{aug}}^{II}(\boldsymbol{\Theta}_n, \boldsymbol{\Theta}_{n+1}) \end{bmatrix} \quad (5.114)$$

Here, the discrete version of (5.113) assumes the form

$$\mathbf{G}_{\text{aug}}^{II}(\boldsymbol{\Theta}_n, \boldsymbol{\Theta}_{n+1}) = \begin{bmatrix} G_{\text{aug}}^{II}(\Theta_n^1, \Theta_{n+1}^1) & 0 & 0 \\ 0 & G_{\text{aug}}^{II}(\Theta_n^2, \Theta_{n+1}^2) & 0 \\ 0 & 0 & G_{\text{aug}}^{II}(\Theta_n^3, \Theta_{n+1}^3) \end{bmatrix} \quad (5.115)$$

with

$$G_{\text{aug}}^{II}(\alpha, \beta) = \begin{cases} \frac{(\Phi_{\text{aug}}^{II})(\beta) - (\Phi_{\text{aug}}^{II})(\alpha)}{\beta - \alpha} & \text{if } \alpha \neq \beta \\ (\Phi_{\text{aug}}^{II})'(\alpha) & \text{if } \alpha = \beta \end{cases} \quad (5.116)$$

5. Modeling Techniques

Due to the coordinate augmentation the original null space matrix (5.73) pertaining to the system with tree structure needs to be enlarged. Accordingly, similar to (5.15), we write

$$\mathbf{P}^{\text{tree}}(\mathbf{q}) = \begin{bmatrix} \mathbf{P}_{\text{ori}}^{\text{tree}}(\mathbf{q}_{\text{ori}}) \\ \mathbf{P}_{\text{aug}}^{\text{tree}} \end{bmatrix} \quad (5.117)$$

such that again the relationship

$$\mathbf{v} = \mathbf{P}^{\text{tree}} \boldsymbol{\nu}^{\text{tree}} \quad (5.118)$$

holds. Obviously, with regard to $\boldsymbol{\nu}^{\text{tree}}$ in (5.72), the 3×10 matrix $\mathbf{P}_{\text{aug}}^{\text{tree}}$ in (5.117) assumes the form

$$\mathbf{P}_{\text{aug}}^{\text{tree}} = \begin{bmatrix} \mathbf{0}_{1 \times 3} & 1 & 0 & 0 & 0 & 0 & 0 & 0 & 0 \\ \mathbf{0}_{1 \times 3} & 0 & 0 & 0 & 1 & 0 & 0 & 0 & 0 \\ \mathbf{0}_{1 \times 3} & 0 & 0 & 0 & 0 & 0 & 1 & 0 & 0 \end{bmatrix} \quad (5.119)$$

Similar to (5.24), a viable discrete version of (5.117) is given by

$$\mathbf{P}^{\text{tree}}(\mathbf{q}_n, \mathbf{q}_{n+1}) = \begin{bmatrix} \mathbf{P}_{\text{ori}}^{\text{tree}}((\mathbf{q}_{\text{ori}})_{n+\frac{1}{2}}) \\ \mathbf{P}_{\text{aug}}^{\text{tree}}(\mathbf{q}_n, \mathbf{q}_{n+1}) \end{bmatrix} \quad (5.120)$$

with

$$\mathbf{P}_{\text{aug}}^{\text{tree}}(\mathbf{q}_n, \mathbf{q}_{n+1}) = \begin{bmatrix} \mathbf{0}_{1 \times 3} & \pi_1 & 0 & 0 & 0 & 0 & 0 & 0 & 0 \\ \mathbf{0}_{1 \times 3} & 0 & 0 & 0 & \pi_2 & 0 & 0 & 0 & 0 \\ \mathbf{0}_{1 \times 3} & 0 & 0 & 0 & 0 & 0 & \pi_3 & 0 & 0 \end{bmatrix} \quad (5.121)$$

and

$$\pi_j = \frac{(\mathbf{d}_1^{\text{s}} + \mathbf{d}_2^{\text{s}})_{n+\frac{1}{2}} \cdot \mathbf{E}(\mathbf{d}_2^j)_{n+\frac{1}{2}}}{G_{\text{aug}}^{\text{II}}(\Theta_n^j, \Theta_{n+1}^j)} \quad (5.122)$$

The loop-closure constraints can be taken into account as proposed in Section 5.2.3. Accordingly, the augmented null space matrix of the closed-loop system can be written again in the form (5.78). The corresponding discrete null space matrix is given by

$$\mathbf{P}^{\text{close}}(\mathbf{q}_n, \mathbf{q}_{n+1}) = \mathbf{P}^{\text{tree}}(\mathbf{q}_n, \mathbf{q}_{n+1}) \mathbf{P}^{\text{oc}}(\mathbf{q}_{n+\frac{1}{2}}) \quad (5.123)$$

where $\mathbf{P}^{\text{tree}}(\mathbf{q}_n, \mathbf{q}_{n+1})$ coincides with (5.120).

5.2.5. Numerical example

Our numerical example deals with the free floating parallel manipulator depicted in Fig. 5.10. This example is especially well-suited for checking the algorithmic conservation properties. Since no external forces act on the system, its center of mass does not have to move. Moreover, since no external torques act on the system, the total angular momentum has to be conserved.

Starting from rest, joint-torques $(\bar{m}_1(t), \bar{m}_2(t), \bar{m}_3(t))$ act on the system. The joint-torques are applied in form of a hat function over time (Fig. 5.3). The corresponding potential energy function may be written as

$$V(\mathbf{q}, t) = - \sum_{j=1}^3 \bar{m}_j(t) \Theta^j \quad (5.124)$$

where $\mathbf{q} \in \mathbb{R}^{51}$ corresponds to the augmented configuration vector (5.132). Accordingly, the load vector (3.12) assumes the form

$$\mathbf{f}(t) = -\nabla V(\mathbf{q}, t) = \begin{bmatrix} \mathbf{0}_{48 \times 1} \\ \bar{m}_1(t) \\ \bar{m}_2(t) \\ \bar{m}_3(t) \end{bmatrix} \quad (5.125)$$

After $t = t_2$, the joint-torques vanish and the total energy of the multibody system has to be a conserved quantity. Inertial and geometric properties of the rigid bodies constituting the parallel manipulator are summarized in Tables 5.5 and 5.6. In this connection, the two platforms (bodies 7 and 8) coincide with isosceles triangles of side-length L (Table 5.6). The initial configuration of the closed-loop system is completely specified by the redundant coordinates corresponding to the associated system with tree structure (see (5.77) and Fig. 5.13). Accordingly,

$$\mathbf{u}_0 = \begin{bmatrix} \varphi^8(0) \cdot \mathbf{e}_1 \\ \varphi^8(0) \cdot \mathbf{e}_2 \\ \theta^8(0) \\ \Theta^1(0) \\ \Theta^2(0) \\ \Theta^3(0) \\ \Theta^4(0) \\ \Theta^5(0) \\ \Theta^6(0) \\ \Theta^7(0) \end{bmatrix} = \begin{bmatrix} 0 \\ 0 \\ 0 \\ \frac{\pi}{3} \\ \frac{2}{3}\pi \\ -\frac{\pi}{6} \\ 2.277 \\ 1.039 \\ 0.975 \\ 1.115 \end{bmatrix} \quad (5.126)$$

where the values of the initial joint-angles $\Theta^4(0)$ through $\Theta^7(0)$ have been rounded for simplicity of exposition. According to Fig. 5.3, we choose the driving torques to $\bar{m}_1 =$

5. Modeling Techniques

body	\mathcal{M}	\mathcal{E}_1	\mathcal{E}_2	length	width
1	3	0.02	0.02	0.4	0.05
2	3	0.02	0.02	0.4	0.05
3	3	0.02	0.02	0.4	0.05
4	4	0.06	0.06	0.6	0.05
5	4	0.06	0.06	0.6	0.05
6	4	0.06	0.06	0.6	0.05

Table 5.5.: Inertial and geometric properties pertaining to the six legs of the manipulator.

body	\mathcal{M}	\mathcal{E}_1	\mathcal{E}_2	L
7	8	0.0408	0.0408	0.4
8	4	0.06	0.06	1.0

Table 5.6.: Inertial and geometric properties pertaining to the two platforms of the manipulator.

-36 , $\bar{m}_2 = -24$ and $\bar{m}_3 = 20$, while the time values are set to $t_1 = 0.25$ and $t_2 = 0.5$. As expected, the present energy-momentum schemes indeed satisfy the above-mentioned conservation properties for any time step size Δt , see Fig. 5.14a. The simulated motion of the manipulator is illustrated in Fig. 5.15 by showing snapshots of the multibody system at subsequent points of time. In this connection the green cross indicates the position of the center of mass, which indeed does not move. The red curve corresponds to the trajectory of the mass center of the small platform (body 7). Moreover, the evolution of the joint-angles $\Theta^1(t)$, $\Theta^2(t)$ and $\Theta^3(t)$, calculated with a time step size of $\Delta t = 0.01$, is depicted in Fig. 5.14b. Table 5.7 contains a comparison of the **BEM** scheme and the **REM** scheme. Accordingly, our implementation of the **REM** scheme is about three times faster than that of the **BEM** scheme. Moreover, the conditioning of the **REM** scheme is much better than that of the **BEM** scheme.

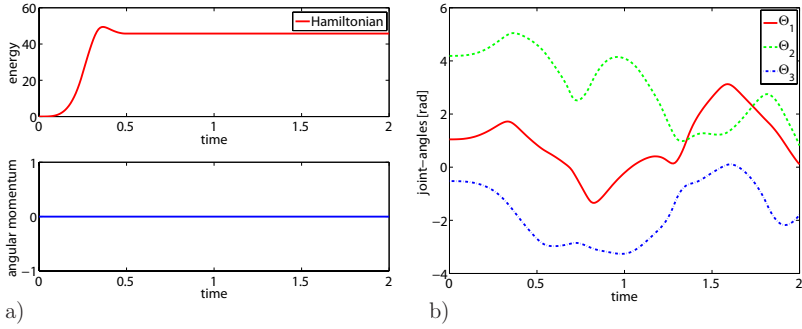
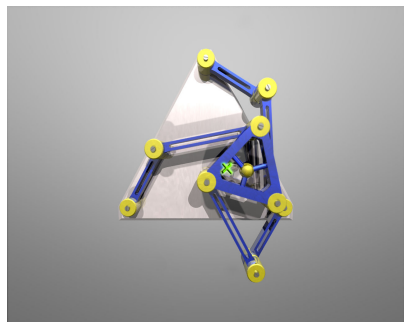


Figure 5.14.: Free floating RRR-structure: a) conservation of energy and angular momentum, b) joint-angles over time. ($\Delta t = 0.01$)

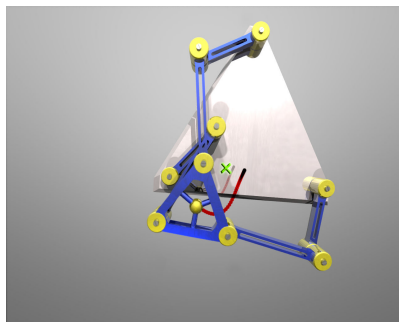
	BEM scheme	REM scheme
number of unknowns	96	10
CPU-Time ($\Delta t = 10^{-2}$)	3	1
condition		
$\Delta t = 10^{-2}$	$\mathcal{O}(10^9)$	$\mathcal{O}(10^2)$
$\Delta t = 10^{-3}$	$\mathcal{O}(10^{12})$	$\mathcal{O}(10^2)$
number		
$\Delta t = 10^{-4}$	$\mathcal{O}(10^{15})$	$\mathcal{O}(10^2)$

Table 5.7.: Comparison of the **BEM** scheme with the **REM** scheme.

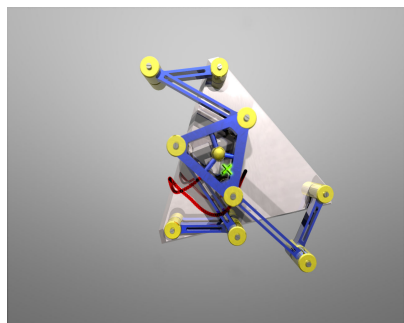
5. Modeling Techniques



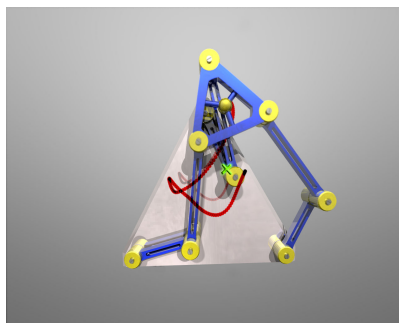
$t = 0$



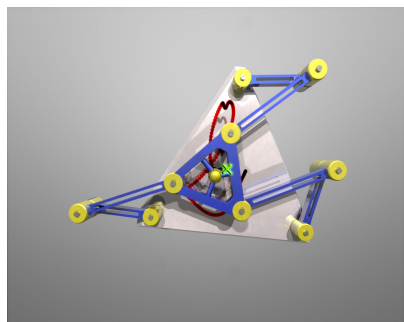
$t = 0.5$



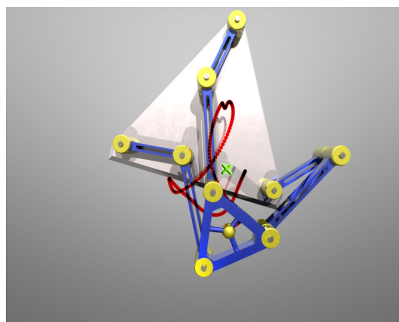
$t = 1$



$t = 1.3$



$t = 1.6$



$t = 2$

Figure 5.15.: Snapshots of the motion of the free floating RRR-structure. The trace depicts the trajectory of the center of mass of body 7.

5.3. Control of Multibody Systems

In this section we will show, that the present approach to the simulation of multibody dynamics can easily accommodate control (servo) constraints, as mentioned with the beneficial DAE form (see Section 3.3). It will be demonstrated that these constraints can be directly appended to the original DAE-set (see Equations (3.11)). This approach makes possible to partially specify the motion of a multibody system. In particular, inverse dynamics problems can be dealt within the present simulation framework. In contrast to common approaches to solve inverse dynamic problems (see e.g. [47, 53, 132]), the application of our scheme will solve for all unknowns in parallel. It turns out that the rotationless formulation along with the coordinate augmentation technique yields simple-structured control contributions to the DAEs. Specifically, the Jacobian associated with the control constraints is typically of Boolean type (see also [153, 152]).

In this thesis we will focus on fully actuated control problems, which means that the number of degrees of freedom matches the number of control inputs. In this connection we will outline the modified **BEM** and **REM** scheme for control problems and demonstrate the performance with a fully actuated motion of a closed loop system. For the treatment of some specific underactuated systems along with representative examples we refer to [29, 19].

5.3.1. Systems with mixed holonomic and servo constraints

Relying on the set of DAEs outlined in Section 3.1, we now append the new control constraints to the continuous DAEs accompanied with a corresponding constraint Jacobian according to

$$\dot{\mathbf{q}} = \mathbf{v} \quad (5.127a)$$

$$\mathbf{M}\dot{\mathbf{v}} = -\nabla V(\mathbf{q}) - \mathbf{G}^T(\mathbf{q})\boldsymbol{\lambda} - \mathbf{B}^T\mathbf{u} \quad (5.127b)$$

$$\mathbf{0} = \mathbf{b}(\mathbf{q}) - \boldsymbol{\gamma}(t) \quad (5.127c)$$

$$\mathbf{0} = \boldsymbol{\Phi}(\mathbf{q}) \quad (5.127d)$$

The algebraic constraints in (5.127c), play the role of control (or servo) constraints. In the rotationless formulation $\mathbf{b} : \mathbb{R}^n \mapsto \mathbb{R}^{m_c}$ is typically linear (m_c denotes the number of control constraints). Since we confine our attention to standard rheonomic constraints, the input transformation matrix $\mathbf{B} = D\mathbf{b}(\mathbf{q}) \in \mathbb{R}^{m_c \times n}$ is constant. The associated Lagrange multipliers $\mathbf{u} \in \mathbb{R}^{m_c}$ play the role of control inputs. The corresponding actuator forces are determined by the control inputs \mathbf{u} in conjunction with the input transformation matrix \mathbf{B} . For a more general framework of control constraints, we refer to Blajer and Kołodziejczyk [30].

5.3.2. Conserving integration of the control DAEs

To accomplish the design of an energy-momentum (EM) conserving time-stepping scheme for control problems, we perform a direct discretization of the above set of DAEs

$$\mathbf{q}_{n+1} - \mathbf{q}_n = \frac{\Delta t}{2} (\mathbf{v}_n + \mathbf{v}_{n+1}) \quad (5.128a)$$

$$\mathbf{M} (\mathbf{v}_{n+1} - \mathbf{v}_n) = -\Delta t [\bar{\nabla} V(\mathbf{q}_n, \mathbf{q}_{n+1}) + \mathbf{G}(\mathbf{q}_n, \mathbf{q}_{n+1})^T \bar{\boldsymbol{\lambda}} + \mathbf{B}^T \bar{\mathbf{u}}] \quad (5.128b)$$

$$\mathbf{0} = \mathbf{b}(\mathbf{q}_{n+1}) - \boldsymbol{\gamma}(t_{n+1}) \quad (5.128c)$$

$$\mathbf{0} = \bar{\boldsymbol{\Phi}}(\mathbf{q}_{n+1}) \quad (5.128d)$$

The scheme above represents an extension of the **BEM** scheme (3.21) and will be termed the **C-BEM** scheme in the following. It is worth mentioning that all advantages of the original **BEM**-scheme are transferred to the **C-BEM** scheme. As also addressed in Section 3.3, we can still apply the reduction procedures outlined in Section 3.2.2 to minimize the set of equations above. This will again treat the conditioning issue as well as reduce the number of unknowns. In the following we proceed along the lines of Chapter 3 and outline again the two reduction steps for the scheme with appended control constraints.

The first size-reduction again eliminates the discrete Lagrange multipliers. The **C-BEM** scheme can be rewritten in the form

$$\mathbf{q}_{n+1} - \mathbf{q}_n = \frac{\Delta t}{2} (\mathbf{v}_n + \mathbf{v}_{n+1}) \quad (5.129a)$$

$$\mathbf{P}(\mathbf{q}_n, \mathbf{q}_{n+1})^T \mathbf{M} (\mathbf{v}_{n+1} - \mathbf{v}_n) = -\Delta t \mathbf{P}(\mathbf{q}_n, \mathbf{q}_{n+1})^T [\bar{\nabla} V(\mathbf{q}_n, \mathbf{q}_{n+1}) + \mathbf{B}^T \bar{\mathbf{u}}] \quad (5.129b)$$

$$\mathbf{0} = \mathbf{b}(\mathbf{q}_{n+1}) - \boldsymbol{\gamma}(t_{n+1}) \quad (5.129c)$$

$$\mathbf{0} = \bar{\boldsymbol{\Phi}}(\mathbf{q}_{n+1}) \quad (5.129d)$$

The second size reduction again relies on the introduction of a mapping $\mathbf{F}_{q_n} : \mathbb{R}^{n-m} \mapsto \mathbf{Q} \subset \mathbb{R}^n$. Substituting now from (5.129a) into (5.129b) for \mathbf{v}_{n+1} , the algorithm (5.129) can be written in the form

$$\mathbf{P}(\mathbf{q}_n, \mathbf{q}_{n+1})^T \left[\frac{2}{\Delta t} \mathbf{M} \mathbf{q}_{n+1} + \Delta t \bar{\nabla} V(\mathbf{q}_n, \mathbf{q}_{n+1}) + \Delta t \mathbf{B}^T \bar{\mathbf{u}} - 2\mathbf{M} \left(\mathbf{v}_n + \frac{\mathbf{q}_n}{\Delta t} \right) \right] = \mathbf{0} \quad (5.130a)$$

$$\mathbf{b}(\mathbf{q}_{n+1}) - \boldsymbol{\gamma}(t_{n+1}) = \mathbf{0} \quad (5.130b)$$

where $\mathbf{q}_{n+1} \in \mathbf{Q}$ is given by (3.27). In the following the reduced scheme (5.130) will be called the **C-REM** scheme. The **C-REM** scheme provides $n - m + m_c$ algebraic

equations for the determination of $\boldsymbol{\mu} \in \mathbb{R}^{n-m}$ and $\boldsymbol{u} \in \mathbb{R}^{m_c}$. Once $\boldsymbol{q}_{n+1} \in \mathbb{Q}$ has been calculated from (3.27), the redundant velocities follow from

$$\boldsymbol{v}_{n+1} = \frac{2}{\Delta t} (\boldsymbol{q}_{n+1} - \boldsymbol{q}_n) - \boldsymbol{v}_n \quad (5.131)$$

5.3.3. Controlled motion of a closed-loop multibody system

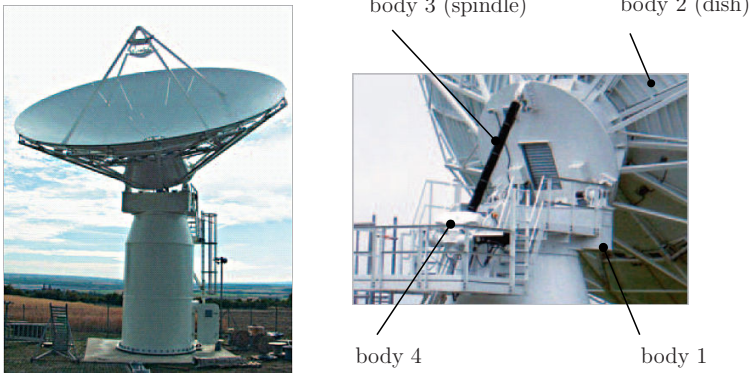


Figure 5.16.: The radio telescope.

In this section we will apply the **C-BEM** and the **C-REM** scheme to a closed loop multibody system, rendering the fully actuated motion of a radio telescope depicted in Fig. 5.16². In this connection the augmentation technique will again play a crucial role, on one hand for the implementation of a screw joint and on the other for the application of the control inputs.

The present closed-loop system consists of four rigid bodies (Fig. 5.17). Body 1 is connected via a revolute joint to the ground. Furthermore body 1 and 2 as well as body 2 and 3 are connected via revolute joints, while body 3 and 4 are connected via a screw joint. Finally, body 4 is coupled to body 1 through a spherical joint. The multibody system at hand has two degrees of freedom.

Two control constraints are applied to prescribe the rotation of the platform (body 1) and the angle of the drive mechanism (body 4). Correspondingly, the angles Θ_G and Θ_H are controlled (Fig. 5.17). The associated work-conjugate control torques are denoted by u_G and u_H .

²Courtesy of Pfaff-silberblau, www.pfaff-silberblau.com.

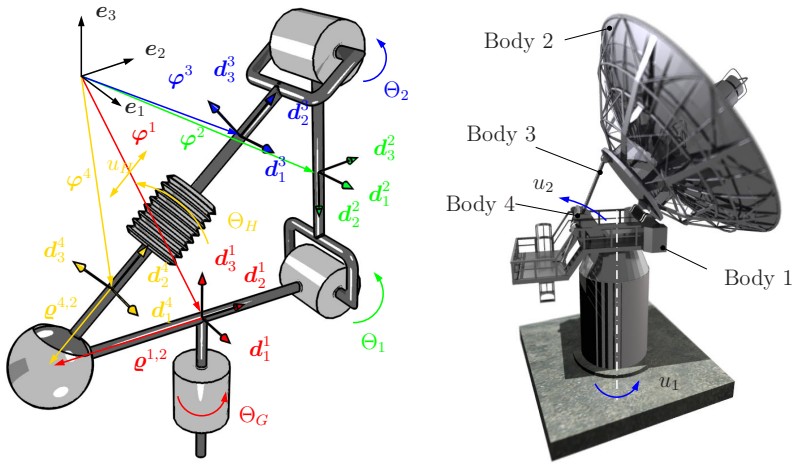


Figure 5.17.: Mechanical model of the radio telescope.

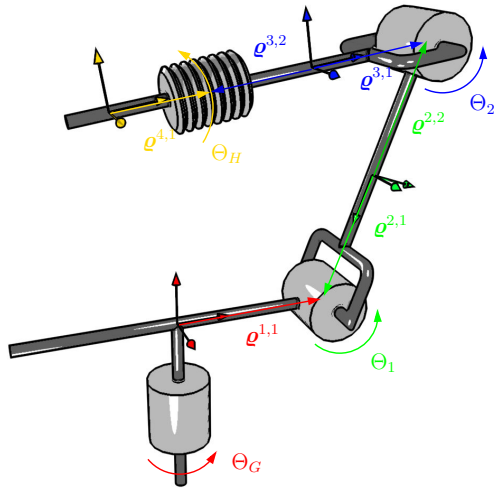


Figure 5.18.: Associated open-loop system for the radio telescope.

In complete analogy to the description of the screw joint in Section 5.1.2, the relative angles Θ_G and Θ_H are appended to the underlying rotationless formulation via the coordinate augmentation technique. For the modeling of the screw joint the relative displacement μ_H is augmented as well. In addition to the $4 \cdot 12 = 48$ redundant coordinates, $\mathbf{q}_{ori} \in \mathbb{R}^{48}$, associated with the underlying rotationless formulation of the present 4-body system, three relative coordinates are employed. Consequently, the **BEM** scheme relies on 51 redundant coordinates which may be arranged in the configuration vector

$$\mathbf{q} = \begin{bmatrix} \mathbf{q}_{ori} \\ \mu_H \\ \Theta_H \\ \Theta_G \end{bmatrix} \quad (5.132)$$

Two control constraints are used to prescribe the motion of the system. In particular, the two control constraints assume the form

$$\begin{aligned} \Theta_H &= \gamma_H(t) \\ \Theta_G &= \gamma_G(t) \end{aligned} \quad (5.133)$$

so that the corresponding control contributions to the DAEs (5.128) are given by

$$\mathbf{b}(\mathbf{q}) = \begin{bmatrix} \Theta_H \\ \Theta_G \end{bmatrix} \quad \text{and} \quad \boldsymbol{\gamma}(t) = \begin{bmatrix} \gamma_H(t) \\ \gamma_G(t) \end{bmatrix} \quad (5.134)$$

Here, $\gamma_G(t)$ and $\gamma_H(t)$ are prescribed functions. Accordingly, the input transformation matrix $\mathbf{B} = D\mathbf{b}(\mathbf{q})$ is given by

$$\mathbf{B} = \begin{bmatrix} \mathbf{0}_{1 \times 49} & 1 & 0 \\ \mathbf{0}_{1 \times 49} & 0 & 1 \end{bmatrix} \quad (5.135)$$

Gravity is acting on the present 4-body system such that the potential energy function in the DAEs (5.128,5.130) assumes the form

$$V(\mathbf{q}) = - \sum_{I=1}^4 \mathcal{M}^I \boldsymbol{\varphi}^I \cdot \mathbf{g} \quad (5.136)$$

where $\mathbf{g} = -g\mathbf{e}_3$, and g denotes the gravitational acceleration.

While the implementation of the **C-BEM** scheme is straightforward, the **C-REM** scheme requires further information to perform the two size-reduction steps outlined before. In this connection, to treat the closed-loop system at hand, we proceed along the lines of Section 5.2. Accordingly, we consider the open-loop system associated with the closed-loop system at hand (Fig. 5.18). The configuration of the associated open-loop system is specified by the four relative coordinates Θ_G , Θ_1 , Θ_2 and Θ_H . Thus the

5. Modeling Techniques

redundant coordinates $(\mathbf{q}_{\text{ori}})_{n+1} \in \mathbb{R}^{48}$ of the underlying rotationless formulation can be expressed as

$$(\mathbf{q}_{\text{ori}})_{n+1} = \mathbf{F}_{q_n}(\boldsymbol{\mu}) \quad \text{where} \quad \boldsymbol{\mu} = \begin{bmatrix} \Theta_G \\ \Theta_1 \\ \Theta_2 \\ \Theta_H \end{bmatrix} \quad (5.137)$$

The mapping \mathbf{F}_{q_n} is composed of the following contributions

$$\boldsymbol{\varphi}_{n+1}^1 = \boldsymbol{\varphi}_n^1 \quad (5.138a)$$

$$(\mathbf{d}_I^1)_{n+1} = \exp(\Theta_G \widehat{\mathbf{e}}_3) (\mathbf{d}_I^1)_n \quad (5.138b)$$

$$\boldsymbol{\varphi}_{n+1}^2 = \boldsymbol{\varphi}_{n+1}^1 + \boldsymbol{\rho}_{n+1}^{1,1} - \exp(\Theta_G \widehat{\mathbf{e}}_3) \exp(\Theta_1 \widehat{(\mathbf{d}_1^1)_n}) \boldsymbol{\rho}_n^{2,1} \quad (5.138c)$$

$$(\mathbf{d}_I^2)_{n+1} = \exp(\Theta_G \widehat{\mathbf{e}}_3) \exp(\Theta_1 \widehat{(\mathbf{d}_1^1)_n}) (\mathbf{d}_I^2)_n \quad (5.138d)$$

$$\boldsymbol{\varphi}_{n+1}^3 = \boldsymbol{\varphi}_{n+1}^2 + \boldsymbol{\rho}_{n+1}^{2,2} - \exp(\Theta_G \widehat{\mathbf{e}}_3) \exp(\Theta_1 \widehat{(\mathbf{d}_1^1)_n}) \exp(\Theta_2 \widehat{(\mathbf{d}_1^2)_n}) \boldsymbol{\rho}_n^{3,1} \quad (5.138e)$$

$$(\mathbf{d}_I^3)_{n+1} = \exp(\Theta_G \widehat{\mathbf{e}}_3) \exp(\Theta_1 \widehat{(\mathbf{d}_1^1)_n}) \exp(\Theta_2 \widehat{(\mathbf{d}_1^2)_n}) (\mathbf{d}_I^3)_n \quad (5.138f)$$

$$u_{n+1} = u_n + p \Theta_H \quad (5.138g)$$

$$(\Theta_H)_{n+1} = (\Theta_H)_n + \Theta_H \quad (5.138h)$$

$$(\Theta_G)_{n+1} = (\Theta_G)_n + \Theta_G \quad (5.138i)$$

$$\boldsymbol{\varphi}_{n+1}^4 = \boldsymbol{\varphi}_{n+1}^3 + \boldsymbol{\rho}_{n+1}^{3,2} + u_{n+1} (\mathbf{d}_2^3)_{n+1} \quad (5.138j)$$

$$(\mathbf{d}_I^4)_{n+1} = \exp(\Theta_G \widehat{\mathbf{e}}_3) \exp(\Theta_1 \widehat{(\mathbf{d}_1^1)_n}) \exp(\Theta_2 \widehat{(\mathbf{d}_1^2)_n}) \exp(\Theta_H \widehat{(\mathbf{d}_2^3)_n}) (\mathbf{d}_I^4)_n \quad (5.138k)$$

The discrete null space matrix of the associated open-loop system can be systematically assembled as described in detail in Section 5.2. In this connection, the contribution of the screw joint follows from the treatment in Section 5.1.2. In order to close the loop, the associated open-loop system is subjected to the following two loop-closure constraints (Figs. 5.18 and 5.17)

$$\mathbf{d}_2^1 \cdot (\boldsymbol{\varphi}^4 + \boldsymbol{\rho}^{4,2} - \boldsymbol{\rho}^{1,2} - \boldsymbol{\varphi}^1) = 0 \quad (5.139a)$$

$$\mathbf{d}_3^1 \cdot (\boldsymbol{\varphi}^4 + \boldsymbol{\rho}^{4,2} - \boldsymbol{\rho}^{1,2} - \boldsymbol{\varphi}^1) = 0 \quad (5.139b)$$

Note that the remaining loop-closure constraint $\mathbf{d}_1^1 \cdot (\boldsymbol{\varphi}^4 + \boldsymbol{\rho}^{4,2} - \boldsymbol{\rho}^{1,2} - \boldsymbol{\varphi}^1) = 0$ does not need to be enforced explicitly, since this constraint is already satisfied due to the topology of the corresponding open-loop system (see Fig. 5.18).

Results

The inverse dynamics problem is solved by applying the present simulation approach. Inertial and geometric properties of the 4-body system are summarized in Table 5.8.

body	\mathcal{M}	\mathcal{E}_1	\mathcal{E}_2	\mathcal{E}_3	length	width	depth
1	3	306.25	0.25	306.25	35	35	1
2	4	408. $\bar{3}$	0. $\bar{3}$	408. $\bar{3}$	35	35	1
3	1	300	0.8 $\bar{3}$	0.8 $\bar{3}$	1	60	1
4	1	8. $\bar{3}$	8. $\bar{3}$	8. $\bar{3}$	10	10	10

Table 5.8.: Inertial and geometric properties pertaining to the radio telescope.

The initial configuration of the radio telescope is specified by the following values for the vector of relative coordinates (5.137), see Fig. 5.17

$$\boldsymbol{\mu}_0 = \begin{bmatrix} \Theta_G(0) \\ \Theta_1(0) \\ \Theta_2(0) \\ \Theta_H(0) \end{bmatrix} = \begin{bmatrix} 0 \\ \frac{\pi}{12} \\ 0.2706 \\ 0 \end{bmatrix} \quad (5.140)$$

To control the motion of the radio telescope, the two control constraints (5.133) are applied. In particular, to prescribe Θ_G , the following function is used

$$\gamma_G(t) = \begin{cases} s_0(t) & \text{for } 0 \leq t \leq t_1 \\ 2\pi & \text{for } t > t_1 \end{cases} \quad (5.141)$$

where $s_0(t)$ is given by

$$s_0(t) = \left[126 \left(\frac{t}{t_1} \right)^5 - 420 \left(\frac{t}{t_1} \right)^6 + 540 \left(\frac{t}{t_1} \right)^7 - 315 \left(\frac{t}{t_1} \right)^8 + 70 \left(\frac{t}{t_1} \right)^9 \right] 2\pi \quad (5.142)$$

To prescribe Θ_H , use is made of

$$\gamma_H(t) = \begin{cases} s_1(t) & \text{for } 0 \leq t \leq t_1 \\ s_2(t) & \text{for } t_1 < t \leq t_2 \\ s_3(t) & \text{for } t_2 < t \leq t_3 \end{cases} \quad (5.143)$$

where

$$\begin{aligned}
 s_1(t) &= \left[\frac{126}{6} t_1 \left(\frac{t}{t_1} \right)^6 - \frac{420}{7} t_1 \left(\frac{t}{t_1} \right)^7 + \frac{540}{8} t_1 \left(\frac{t}{t_1} \right)^8 - \frac{315}{9} t_1 \left(\frac{t}{t_1} \right)^9 + \frac{70}{10} t_1 \left(\frac{t}{t_1} \right)^{10} \right] \omega_0 \\
 s_2(t) &= s_1(t_1) + \omega_0(t - t_1) \\
 s_3(t) &= s_2(t) - (t_3 - t_2) \left[\frac{126}{6} \left(\frac{t - t_2}{t_3 - t_2} \right)^6 - \frac{420}{7} \left(\frac{t - t_2}{t_3 - t_2} \right)^7 + \frac{540}{8} \left(\frac{t - t_2}{t_3 - t_2} \right)^8 \right. \\
 &\quad \left. - \frac{315}{9} \left(\frac{t - t_2}{t_3 - t_2} \right)^9 + \frac{70}{10} \left(\frac{t - t_2}{t_3 - t_2} \right)^{10} \right] \omega_0
 \end{aligned} \tag{5.144}$$

The polynomial function above was inspired by [30]. It is well suited for control problems due to its steady and continuous character. For the simulation we employ the following parameters

$$\begin{aligned}
 t_1 &= 2 \\
 t_2 &= 3 \quad \text{and} \quad \omega_0 = 2\pi \cdot 0.22, \quad p = 20 \quad (\text{pitch}) \\
 t_3 &= 4
 \end{aligned}$$

The time evolution of the control outputs Θ_H and Θ_G is illustrated with the two diagrams in Fig. 5.19a. Accordingly, for $t \in [0, t_1]$, the dish of the radio telescope is elevated, while the angular velocity $\dot{\Theta}_G$ of the whole telescope about the vertical axis \mathbf{e}_3 is increased. For $t \in [t_1, t_2]$, the whole radio telescope rotates with constant angular velocity $\dot{\Theta}_G = \omega_0$. Note that, since no damping effects are present, the total energy as well as the 3-component of the angular momentum are conserved quantities for $t \in [t_1, t_2]$. For $t \in [t_2, t_3]$ the system is decelerated until it comes to rest. The simulation results summarized below have been obtained with a time step of $\Delta t = 0.01$. The calculated control inputs (or joint-torques) u_G and u_H are depicted in Fig. 5.20. The numerical results for the total energy and angular momentum (component about axis \mathbf{e}_3) are shown in Fig. 5.19b. Due to the energy-momentum conserving discretization approach, energy and angular momentum are properly conserved for $t \in [t_1, t_2]$. The two alternative implementations of the energy-momentum conserving formulation are compared in Table 5.9. Accordingly, the computational effort demanded by the **C-REM** scheme is much less than that required by the **C-BEM** scheme. This can be traced back to the significant reduction of the number of unknowns in the **C-REM** scheme (4 angles Θ_G , Θ_1 , Θ_2 , and Θ_H in (5.137), and 2 control inputs u_G and u_H). In contrast to that, the **C-BEM** scheme yields 102 unknowns (51 coordinates in (5.132), 49 Lagrange multipliers and 2 control inputs u_G and u_H). Furthermore, it can be observed from Table 5.9 that the **C-REM** scheme

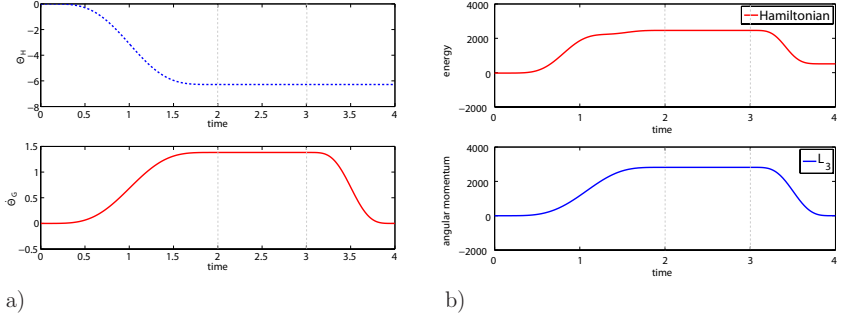


Figure 5.19.: Radio telescope: a) control outputs. Top: prescribed screw-angle $\Theta_H(t)$. Bottom: prescribed angular velocity $\dot{\Theta}_G$ b) total energy and 3-component of the angular momentum calculated with $\Delta t = 0.01$.

leads to an improvement in the condition number of the iteration matrix. Eventually, snapshots of the motion are shown in Fig. 5.21.

	C-BEM scheme	C-REM scheme
number of unknowns	100 + 2	4 + 2
CPU-Time ($\Delta t = 10^{-2}$)	26	1
condition number	$\mathcal{O}(10^{13})$	$\mathcal{O}(10^4)$
	$\Delta t = 10^{-3}$	$\mathcal{O}(10^4)$
	$\Delta t = 10^{-4}$	$\mathcal{O}(10^4)$

Table 5.9.: Comparison of the C-BEM scheme with the C-REM scheme.

Remark 5.3.1 *In the following sections we will also present some examples dealing with underactuated control problems. In this case the number of control inputs is less than the number of DOF. In some cases which are outlined in [29, 19] it is important to perform a projection of the C-BEM or C-REM scheme in order to simulate these systems. This is connected with the concept of differential flatness, see e.g. Fliess [48, 49]. Within this contribution, we will only apply the two schemes outlined in this section, since the examples presented herein are not subject to the projection technique, mentioned in the references cited above.*

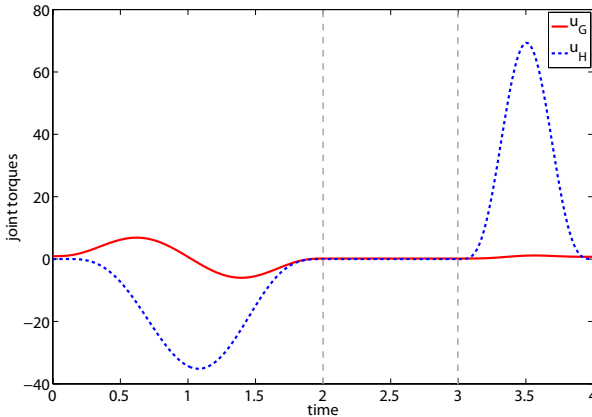
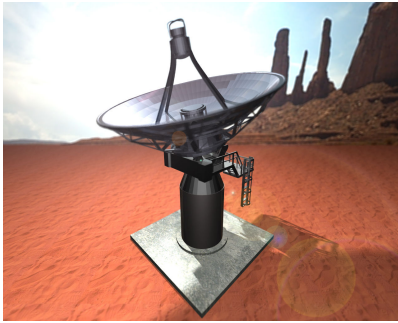


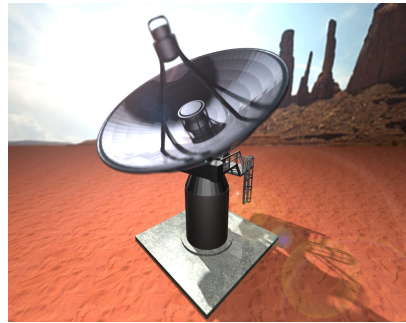
Figure 5.20: Radio telescope: control inputs calculated with $\Delta t = 0.01$.

5.4. Modeling of Dissipation and its Consistent Integration

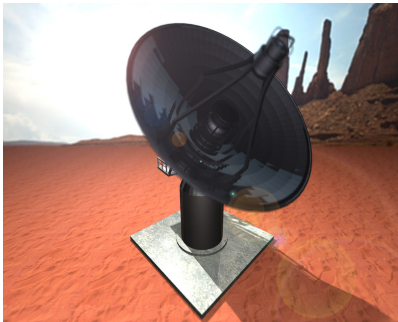
This section outlines the modeling of dissipation in multibody dynamics. Damping phenomena play a central role in the modeling of dynamical systems. On one hand they have desired effects, e.g. like shock-absorbers in a car, limiting the elongation and providing a comfortable ride. On the other hand they can excite systems to undergo self-excited oscillations e.g. a swinging string [137], or they influence dramatically the stability behavior of high speed exhaust turbochargers (see e.g. [135, 133, 134]). In short, this phenomenon influences the stability behavior of dynamical systems. Especially in multibody dynamics, modeling of joint friction is of major importance. The design of drive trains or gears in robotic applications depends on accurate physical models of friction. Especially for positioning problems, like control issues, joint friction phenomena play a crucial role. The task of modeling joint friction was undertaken by several authors [8, 9, 41, 75, 46, 146]. Typically joint friction is modeled as a combination of several phases: first there is stiction, no motion as long as the actuation torque / force is lower than the breakaway value. Once this value is surmounted, a transition phase follows accompanied with a relaxation, turning then into a linear-viscous dominated phase. The event itself is transient, discontinuous and highly nonlinear. It represents a challenging task to develop a corresponding model to capture a physically correct behavior. Ob-



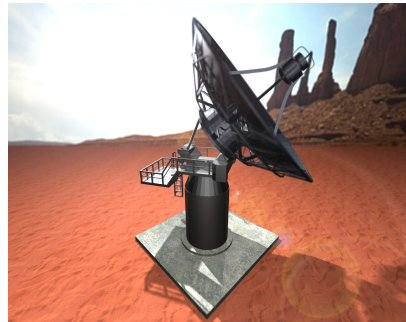
$t = 0$



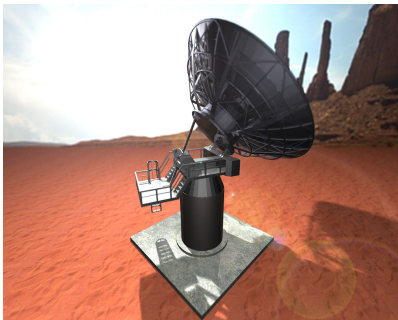
$t = 1$



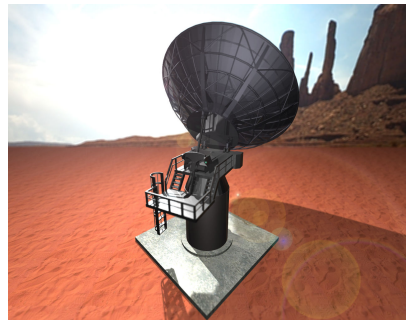
$t = 2$



$t = 2.5$



$t = 3$



$t = 4$

Figure 5.21.: Snapshots of the motion of the radio telescope.

viously even though one has obtained such a model, in order to simulate a mechanical system one has to rely on numerical methods. Typically ‘standard’ time integration procedures such as Newmark or HHT etc. [76, 115] are used, which provide a stable and robust integration based upon the introduction of numerical dissipation, namely artificial dissipation. These effects commonly deteriorate the correct amount of dissipation and in the worst case yield physically not meaningful results, which destroy the even most sophisticated dissipative model. Besides, numerical dissipation is also used as a modeling feature in order to damp high frequency oscillations see, for example, Armero and Romero [5, 6]. In addition to that, many dissipative models do not rely on thermodynamic consistency, which means that the models themselves produce artificially energy. Therefore the intention of this section is to design an energy consistent time integration scheme, which accounts numerically exact for the correct amount of dissipation. This represents an extension of the basic energy-momentum scheme outlined in Chapter 3.

Since for this purpose we need to apply thermodynamically consistent models, we rely on rheological models originating from constitutive modeling in material mechanics. They possess the advantage of calculating the correct amount of dissipation, while retaining the ability of being augmented in such a way, that they can match experimental results by applying parameter identification [87, 102]. The ideas to this approach go back to the modeling of viscoelastic material behavior for dynamics, applying an energy consistent integration scheme by Gross et al. [67, 68, 69, 70]. For finite elasto-plasto-dynamics energy consistent schemes have been developed by Noels et al. [119, 118], Meng and Laursen [106], Mohr et al. [108, 109, 110, 111] or Armero [3, 4]. We will basically follow these ideas and break them down to the 1D case, since joint friction acts only on corresponding scalar values. For the modeling of multibody systems we rely on the procedures outlined in Chapter 4. Especially for joint friction modeling, the application of the coordinate augmentation technique, presented in Section 5.1 will play a major role. It will enable us to apply internal forces which account for the dissipative effects directly on the corresponding values.

In the subsequent sections we will present an ad hoc friction model, dealing with linear viscous joint friction. Here we introduce all basic notation concerning dissipation and present a simple example of a spring-damper element. Then we will outline the incorporation of dissipative effects into our multibody scheme, deriving a consistent time stepping scheme. More sophisticated models will be rendered through the introduction of rheological models. First with a viscoelastic friction element and secondly with an enhanced plasticity model to render joint stiction and sliding.

5.4.1. Linear viscous joint friction

As an introduction to energy consistent time integration of dissipative systems, we deal in this section with a simple system consisting of a mass point attached to a spring-

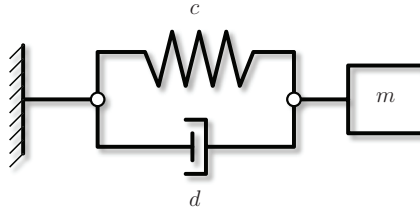


Figure 5.22.: Ad hoc model for friction (Kelvin-Voigt).

damper unit (see Fig. 5.22). This is also an introductory example in many textbooks of basic mechanics, dealing with damped oscillations. In contrast to these books, we focus on the numerical treatment of this example. In this case we emphasize on the design of time-integration schemes, which render an energy consistent behavior (see also [150]), i.e. no numerical damping distorts the results. The continuous equation of motion for this one DOF system is given by

$$m \ddot{q} + d \dot{q} + c q = 0 \quad (5.145)$$

As obvious, the damping term is velocity dependent, representing a viscous damping element. This is in contrast to other damping models, see e.g. [155], where a transient damping is modeled. For the numerical treatment of the equation above, we choose the second order accurate mid-point rule to perform a time integration

$$q_{n+1} - q_n = \frac{\Delta t}{2} (v_{n+1} + v_n) \quad (5.146a)$$

$$m (v_{n+1} - v_n) + \Delta t d v_{n+1/2} + \Delta t c q_{n+1/2} = 0 \quad (5.146b)$$

with

$$v_{n+1} = \frac{2}{\Delta t} (q_{n+1} - q_n) - v_n \quad (5.147)$$

A discrete version in terms of the configuration can be expressed as

$$\frac{2m}{\Delta t} (q_{n+1} - q_n) - 2m v_n + d (q_{n+1} - q_n) + \Delta t c q_{n+1/2} = 0 \quad (5.148)$$

For non-conservative systems the following relationship can be stated, according to the first law of thermodynamics

$$\dot{H} = -\mathcal{D} \quad (5.149)$$

5. Modeling Techniques

where $H = T + V$ is the well known Hamiltonian function, representing the conservative part as a sum of the kinetic and potential energy. The continuous equation above states that the time derivation of the Hamiltonian equals a negative dissipation³ \mathcal{D} , which according to the second law of thermodynamics must satisfy $\mathcal{D} \geq 0$ for all times $t \in \mathbb{R}_+$. To check the algorithmic consistency of a time integration scheme, we now perform an integration in time of Equation (5.149), leading to

$$R := H_{n+1} - H_n + \Delta \mathcal{D} = 0 \quad (5.150)$$

Equation (5.150) represents the residual equation which must be fulfilled for all times in order to obtain a consistent scheme⁴. Therefore we need to state the dissipation, which can be derived as follows:

Multiplying (5.145) with \dot{q}

$$m \ddot{q} \dot{q} + d \dot{q} \dot{q} + c q \dot{q} = 0 \quad (5.151)$$

and performing a time integration

$$\int m \ddot{q} \dot{q} \, dt + \int d \dot{q} \dot{q} \, dt + \int c q \dot{q} \, dt = \mathcal{H} \quad (5.152a)$$

$$\underbrace{\int m \dot{q} \frac{d\dot{q}}{dt} \, dt}_T + \underbrace{\int d \dot{q} \dot{q} \, dt}_{\mathbb{A}_D = \Delta \mathcal{D}} + \underbrace{\int c q \frac{dq}{dt} \, dt}_V = \mathcal{H} \quad (5.152b)$$

leads to the following equivalence in the continuous case

$$\mathcal{H} = H + \mathbb{A}_D \quad (5.153)$$

Here \mathcal{H} represents the augmented Hamiltonian which consists of the conservative part H and the non-conservative part \mathbb{A}_D . A consistent integration yields $\mathcal{H} = \text{const.}$ for all times $t \in \mathbb{R}_+$. Thereby \mathbb{A}_D stands for the accumulated dissipation, obtained by summation of the incremental dissipation \mathcal{D}

$$\mathbb{A}_D = \int_{t_0}^T \mathcal{D} \, dt = \sum_{k=0}^n \int_{t_k}^{t_{k+1}} \mathcal{D} \, dt = \sum_{k=0}^n \int_{t_k}^{t_{k+1}} d \dot{q} \dot{q} \, dt \quad (5.154)$$

For a discrete treatment of the equations above, we choose a mid-point evaluation leading to

$$\mathbb{A}_D^{n+1} = \underbrace{\sum_{k=0}^{n-1} \Delta \mathcal{D}}_{\mathbb{A}_D^n} + \underbrace{\Delta t d \dot{q}_{n+1/2} \dot{q}_{n+1/2}}_{\Delta \mathcal{D}} \quad (5.155)$$

³In contrast to conservative systems, where $\dot{H} = 0$ for all times $t \in \mathbb{R}_+$.

⁴Some plots in the following refer to the residual equation to show consistency, in all cases we relate to Equation (5.150).

Since the term inside the time integral in Equation (5.154) is at most quadratic, the dissipation is calculated without any numerical errors, we obtain a thermodynamic consistent integrator.

Remark 5.4.1 *We obtain a consistent integration only if the quadrature rule calculates integral (5.154) exactly. This comes with the requirement of integrating the internal damping force $F_{\text{int}} = d\dot{q}$ also in an exact sense. In the case considered above, where the integrand is a quadratic function, the second order accurate mid-point rule satisfies this condition for both cases.*

Numerical example

Here we will present the results from the ad hoc model above. We choose a mass of $m = 5$, a spring stiffness of $c = 50$ and a viscous damping coefficient of $d = 1.5$, the time step size is $\Delta t = 0.05$. Figure 5.23 shows the displacement q of the mass, significantly the system is under-damped. The phase-space is displayed in Fig. 5.24a, showing a convergence towards its attractor (time is color-coded). In order to proof consistency of the integration scheme presented above, we check the energy rate \dot{H} displayed in Fig. 5.24b. Obviously the second law of thermodynamics is fulfilled. Additionally we check the residual equation (5.150) which must lie within the range of the iteration tolerance ε for all times, here $\varepsilon = 1 \cdot 10^{-12}$ (Fig. 5.25b). Finally the energy components are plotted in Fig. 5.25a, split into the kinetic and potential energy and their sum, the Hamiltonian. The sum of the accumulated dissipation and the Hamiltonian renders a straight line ($\mathcal{H} = \text{const.}$), verifying the consistency of the time integration scheme for the ad hoc dissipative model.

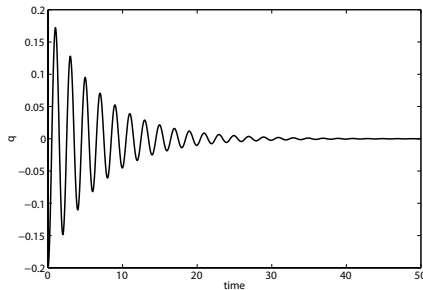


Figure 5.23.: Ad hoc model: displacement $q(t)$.

5. Modeling Techniques

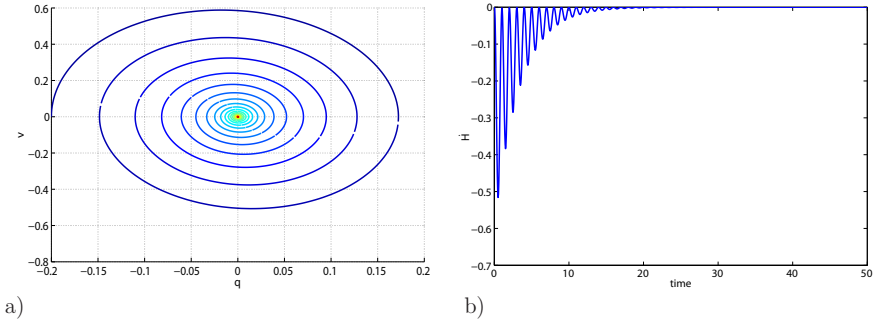


Figure 5.24.: Ad hoc model: a) phase-space plot, b) negative dissipation rate of the system.

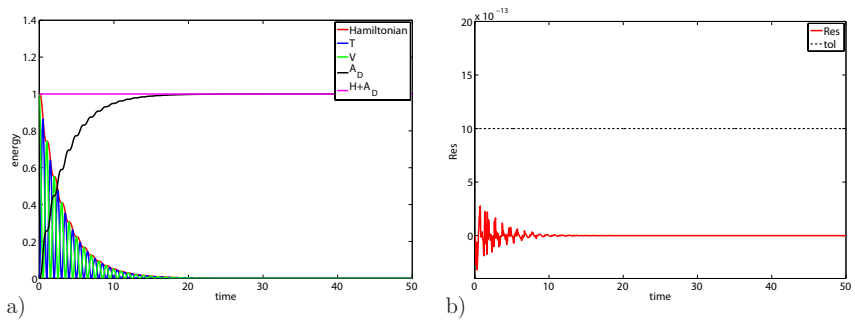


Figure 5.25.: Ad hoc model: a) energy components for spring mass system, b) fulfillment of the residual.

In the following we will extend the application from mass points to multibody systems. In this connection the coordinate augmentation technique will play a major role for the implementation of friction.

5.4.2. Incorporation of dissipation

Here we outline the implementation of dissipative effects into the multibody framework presented in Chapter 3, while relying on the coordinate augmentation technique. Since all models for dissipation within this contribution are one dimensional, acting on original or augmented coordinates, the incorporation is performed by adding an internal force to the equations of motion in the continuous case. This internal force vector has only entries at the corresponding coordinates the dissipation is acting on, therefore in general the continuous equations of motion can be written as (equivalent to Equation (3.29))

$$\dot{\mathbf{q}} - \mathbf{v} = \mathbf{0} \quad (5.156a)$$

$$\mathbf{M}\dot{\mathbf{v}} + \nabla V(\mathbf{q}) + \mathbf{G}^T(\mathbf{q})\boldsymbol{\lambda} + \mathbf{F}_{\text{int}} = \mathbf{0} \quad (5.156b)$$

$$\tilde{\boldsymbol{\Phi}}(\mathbf{q}) = \mathbf{0} \quad (5.156c)$$

To obtain a consistent time stepping scheme for dissipative multibody systems, we need to discretize the set of equations above. In a first instance we apply the **BEM**-scheme presented in Section 3.2.1, thereby we seek an algorithmic force evaluation which satisfies the consistency condition (see Equation (5.150)). In general we receive the following set of discretized algebraic equations

$$\mathbf{q}_{n+1} - \mathbf{q}_n = \frac{\Delta t}{2} (\mathbf{v}_n + \mathbf{v}_{n+1}) \quad (5.157a)$$

$$\mathbf{M}(\mathbf{v}_{n+1} - \mathbf{v}_n) = -\Delta t \bar{\nabla} V(\mathbf{q}_n, \mathbf{q}_{n+1}) - \Delta t \bar{\mathbf{G}}(\mathbf{q}_n, \mathbf{q}_{n+1})^T \boldsymbol{\lambda} + \Delta t \mathbf{F}_{\text{int}}^{\text{alg}} \quad (5.157b)$$

$$\tilde{\boldsymbol{\Phi}}(\mathbf{q}_{n+1}) = \mathbf{0} \quad (5.157c)$$

The scheme above represents an extension of the **BEM**-scheme (3.21) and will be referred to as the **Energy-Momentum-Consistent (EMC)** scheme. The character of $\mathbf{F}_{\text{int}}^{\text{alg}}$ will be revealed in detail within the following sections, since it depends on a respective dissipative model.

Rigid body with linear viscous friction

Here we want to apply the linear viscous joint friction model presented in Section 5.4.1 to a simple two dimensional pendulum, depicted in Fig. 5.26. Thereby we will use the coordinate augmentation technique in order to apply the damping force on the joint coordinate. The director dyad is situated at the center of mass. The augmented coordinate is labeled as Θ , friction is acting in the revolute joint. First we will introduce

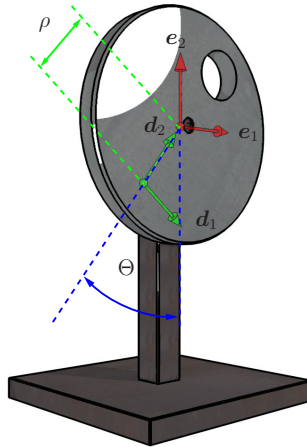


Figure 5.26.: Physical pendulum with joint friction.

the augmented coordinate by formulating its constraint, again relying on the steps outlined in Section 5.1. The intention is to measure the relative angle of the pendulum with respect to the inertial coordinate system e_i . We obtain the following augmented constraint equation

$$\Phi_{\text{aug}}(\mathbf{q}) = \mathbf{d}_2 \cdot \mathbf{e}_1 + \mathbf{d}_2 \cdot \mathbf{e}_2 + \sin \Theta - \cos \Theta \quad (5.158)$$

This leads to an augmented configuration vector

$$\mathbf{q} = \begin{bmatrix} \varphi \\ \mathbf{d}_1 \\ \mathbf{d}_2 \\ \Theta \end{bmatrix}_{7 \times 1} \quad (5.159)$$

Since joint friction only influences the augmented coordinate, we formulate the internal force \mathbf{F}_{int} , which depends on the relative joint velocity $\dot{\Theta}$

$$\mathbf{F}_{\text{int}}(\dot{\theta}) = \begin{bmatrix} \mathbf{0}_{6 \times 1} \\ d \dot{\Theta} \end{bmatrix} \quad (5.160)$$

For this dissipative model, a simple mid-point evaluation renders the **EMC** scheme, where the internal force in the discrete case yields

$$\mathbf{F}_{\text{int}}^{\text{alg}} = \begin{bmatrix} \mathbf{0}_{6 \times 1} \\ d \dot{\Theta}_{n+1/2} \end{bmatrix} = \begin{bmatrix} \mathbf{0}_{6 \times 1} \\ \frac{d}{\Delta t} (\Theta_{n+1} - \Theta_n) \end{bmatrix} \quad (5.161)$$

Concerning the energetic consistency, we calculate the dissipation (as specified in Section 5.4.1). In the continuous case we obtain

$$\mathbb{A}_D = \sum_{k=0}^n \int_{t_k}^{t_{k+1}} \mathcal{D} \, dt = \sum_{k=0}^n \int_{t_k}^{t_{k+1}} d \dot{\Theta}^2 \, dt \quad (5.162)$$

The application of the mid-point rule leads to the incremental dissipation according to

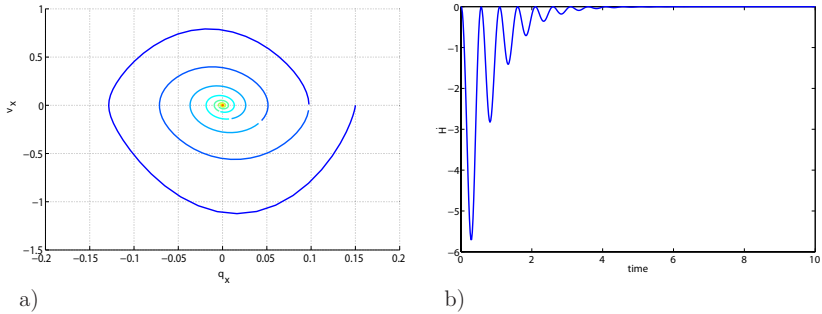


Figure 5.27.: Physical pendulum: a) phase-space portrait, b) negative dissipation rate for the physical pendulum.

$$\Delta \mathcal{D} = d \dot{\Theta}_{n+1/2}^2 \quad (5.163)$$

The accumulated dissipation is given by

$$\mathbb{A}_D^{n+1} = \mathbb{A}_D^n + \Delta t d \dot{\Theta}_{n+1/2}^2 \quad (5.164)$$

For the present example we choose the following values and initial conditions

$$\mathbf{q} = \begin{bmatrix} \rho \sin(\Theta) \\ -\rho \cos(\Theta) \\ \cos(\Theta) \\ \sin(\Theta) \\ -\sin(\Theta) \\ \cos(\Theta) \\ \Theta \end{bmatrix}, \quad \mathbf{v} = \mathbf{0} \quad (5.165)$$

where $\Theta = \frac{\pi}{2}$, the mass is set to $m = 2$ and $\rho = 0.15$. With a time step size of $\Delta t = 0.02$ and a damping ratio of $d = 0.1$ we obtain the following results: In Fig. 5.27a we see the

phase-space trajectory of the pendulum. The fulfillment of the residual condition (5.150) is depicted in Fig. 5.28b. Except for one peak, which is based upon the solution driven convergence criterion, we obtain a consistent time-integration. The residual lies within the range of the chosen computational tolerance ($\varepsilon = 1 \cdot 10^{-12}$). Fig. 5.28b renders the energy rate which remains below zero for all times. All energy components within the system are displayed in Fig. 5.28a.

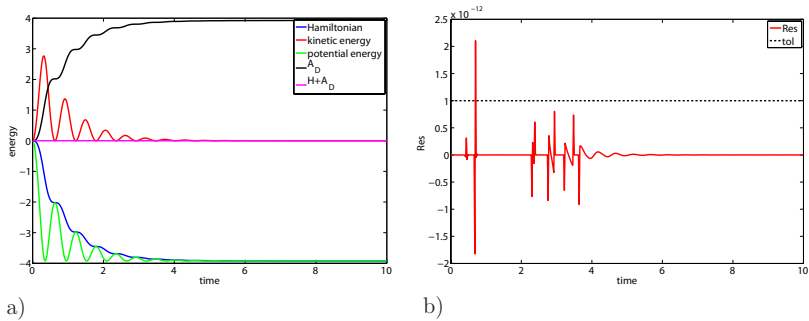


Figure 5.28: Physical pendulum: a) energy components of physical pendulum, b) fulfillment of the residual.

5.4.3. Viscoelastic model

This section introduces dissipation based upon rheological models, introducing viscoelasticity. The main distinguishing feature of rheological models is their character of inherent thermodynamic consistency, while the dissipation is always related to the rate of a free energy function.

Viscoelasticity is typically used to model damping effects in materials, e.g. rubber-like materials. Behind many viscoelastic models, we find a set of rheological models which go back to the considered Kelvin-Voigt model or the Maxwell model [140]. Generalized forms of these models can be found in many textbooks about constitutive modeling [33, 77, 122]. A theoretical framework which has been investigating viscoelastic materials in the context of energy consistent time-integration was studied by Gross et al. [67, 68, 69, 70]. In this contribution, we will focus on the one dimensional case, since the dissipation will always be acting on augmented coordinates. Therefore we break the formulations down and state a generalized non-conservative model based upon the ideas of viscoelasticity. This will enable us to model any arbitrary damping characteristic, while designing an **EMC** scheme for 1D viscoelasticity.

Based upon Simo and Hughes [140] we will introduce a dynamic viscoelastic model with the example of a viscoelastic-element oscillator followed by the adaptation of the model to a complex multibody model of a car suspension.

5.4.4. Viscoelastic-element oscillator

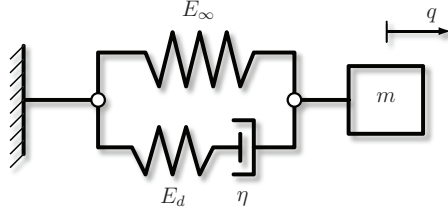


Figure 5.29.: Viscoelastic-element oscillator.

The introductory example for the viscoelastic model for a dynamic simulation is given by the viscoelastic-element oscillator. This model problem consists of a rheological element and a mass point. The system itself has one DOF (see Fig. 5.29). In contrast to Section 5.4.1, parallel to the main spring we find a spring-dashpot unit, hence the implementation differs; it relies on an internal evolution equation. Assuming a linear relationship between force and elongation, we formulate the following continuous equations of motion

$$\dot{q} = v \quad (5.166a)$$

$$m\dot{v} + F_{\text{int}} = 0 \quad (5.166b)$$

In this case, an internal force is now governing the elastic and dissipative forces. The internal force can be derived from the free energy function, maintaining the stored energy in the springs

$$\Psi(q, \alpha) = \frac{1}{2}E_{\infty}q^2 + \frac{1}{2}E_d(q - \alpha)^2 \quad (5.167)$$

Here α denotes the internal variable of the viscoelastic model and can be obtained by solving the following evolution equation (see [140] for further details)

$$\dot{\alpha} = \frac{1}{\tau}(q - \alpha) \quad (5.168)$$

with $\tau = \eta/E_d$. The internal force can be obtained by deriving the free energy function with respect to the displacement q . We obtain

$$F_{\text{int}} = \partial_q \Psi(q, \alpha) = (E_{\infty} + E_d)q - E_d\alpha \quad (5.169)$$

5. Modeling Techniques

The dissipation in the dashpot can also be directly derived from the free energy function as a derivation with respect to the internal variable α

$$\mathcal{D}(q, \alpha) = \partial_\alpha \Psi(q, \alpha) \dot{\alpha} = -E_d (q - \alpha) \dot{\alpha} \geq 0 \quad (5.170)$$

Energy-consistent discretization

Our goal is to perform a consistent time integration of Equations (5.166). In a first approach we apply the second order accurate mid-point rule

$$q_{n+1} - q_n = \frac{\Delta t}{2} (v_{n+1} + v_n) \quad (5.171a)$$

$$m (v_{n+1} - v_n) + \Delta t F_{\text{int}}(1/2) = 0 \quad (5.171b)$$

In general, the simple mid-point evaluation of the internal force does not fulfill the consistency condition (5.150). Therefore we need to introduce an algorithmic force evaluation similar to the argument given in [108]:

Starting with the first law of thermodynamics, we obtain

$$\dot{H} \equiv \dot{T} + \dot{\Psi} = -\mathcal{D} \quad (5.172)$$

A time integration yields

$$\Delta T + \Delta \Psi = -\Delta \mathcal{D} \quad (5.173)$$

For the difference of the kinetic energy we obtain

$$\Delta T = \frac{1}{2} m (v_{n+1}^2 - v_n^2) = \frac{1}{2} m (v_{n+1} + v_n) (v_{n+1} - v_n) \quad (5.174)$$

using (5.171) we extract

$$v_{n+1} + v_n = \frac{2}{\Delta t} (q_{n+1} - q_n) \quad (5.175a)$$

$$v_{n+1} - v_n = -\frac{1}{m} \Delta t F_{\text{int}}(1/2) \quad (5.175b)$$

Inserting both into the expression for ΔT we obtain

$$\Delta T = -F_{\text{int}}(1/2) (q_{n+1} - q_n) \quad (5.176)$$

This leads to

$$-\Delta T = \Delta \Psi + \Delta \mathcal{D} \quad (5.177a)$$

$$F_{\text{int}}(1/2) (q_{n+1} - q_n) = \Delta \Psi + \Delta \mathcal{D} \quad (5.177b)$$

To meet condition (5.177b) means to fulfill the consistency condition numerically exact. Therefore we need to state the algorithmic internal force by relying on an enhanced mid-point evaluation⁵

$$F_{\text{int}}^{\text{alg}} = F_{\text{int}}(1/2) + \Omega(q_2 - q_1) \quad (5.178)$$

In the equation above, the scaling factor Ω can be calculated in a straightforward way [68, 108], leading to

$$\Omega(q_2 - q_1) = \frac{\Psi_2 - \Psi_1 + \Delta\mathcal{D} - F_{\text{int}}(1/2)(q_2 - q_1)}{|q_2 - q_1|^2} \quad (5.179)$$

which then leads to the algorithmic internal force

$$F_{\text{int}}^{\text{alg}} = \frac{\Psi_2 - \Psi_1}{q_2 - q_1} + \frac{\Delta\mathcal{D}}{q_2 - q_1} \quad (5.180)$$

The expression above satisfies consistency property (5.172) for arbitrary spring characteristics used within the rheological model and inserted into (5.157) the expression completes the **EMC** scheme⁶. It is worth to note the resemblance of the equation above to Equation (5.23) which introduced the constraint Jacobian for additional scalar non-linear values.

Finally the incremental dissipation for the viscoelastic element can be obtained by a mid-point evaluation of (5.170) rendering

$$\Delta\mathcal{D} = E_d (q - \alpha)_{n+1/2} (\alpha_2 - \alpha_1) \quad (5.181)$$

Besides, the evolution equation in (5.168) needs an adequate numerical treatment as well. To maintain the accuracy order, we apply again the mid-point rule, which leads to the discrete evolution equation

$$\alpha_{n+1} - \alpha_n + \frac{1}{\tau} \Delta t \alpha_{n+1/2} = \Delta t \frac{1}{\tau} q_{n+1/2} \quad (5.182)$$

The linear algebraic equation above can directly be solved for α_{n+1} locally, within the global iteration process to acquire q_{n+1}

$$\alpha_{n+1} = \frac{1}{1 + \frac{\Delta t}{2\tau}} \left[\alpha_n \left(1 - \frac{\Delta t}{2\tau} \right) + \frac{\Delta t}{\tau} (q_{n+1} + q_n) \right] \quad (5.183)$$

The accumulated dissipation yields

$$\mathbb{A}_D^{n+1} = \mathbb{A}_D^n + \Delta t \Delta\mathcal{D} \quad (5.184)$$

⁵Please note that for reasons of simplicity, in the following $(\bullet)_2$ indicates the evaluation at time t_{n+1} , correspondingly $(\bullet)_1$ indicates the evaluation at time t_n .

⁶See the Appendix A.3 for a proof that for linear spring characteristics, the algorithmic force coincides with the mid-point evaluation of the internal force.

Numerical example

Here we investigate the nonlinear viscoelastic oscillator depicted in Fig. 5.29. As exposed in Appendix A.3, the mid-point evaluation of the internal force is only valid for linear spring characteristics, therefore we now focus on the nonlinear character. Following the modeling lines discussed above, we choose a mass of $m = 5$, spring stiffness $E_\infty = 100$, $E_d = 50$ and a damping value of $\eta = 35$. The free energy function for this example is chosen to

$$\Psi(\varepsilon, \alpha) = \frac{1}{2}E_\infty q^4 + \frac{1}{2}E_d (q - \alpha)^4 \quad (5.185)$$

The system oscillates freely under the influence of gravity. In the following we summarize the results: Fig. 5.30a represents the displacement of the mass. One clearly observes the nonlinear character according to the time-dependent frequency and the damped motion due to the decreasing amplitude. Fig. 5.30b shows the corresponding phase-space plot. The consistency is displayed in Fig. 5.31a, divided into the respective energy components, while the fulfillment of the consistency is displayed in Fig. 5.31b (which lies again within the tolerance of the iteration scheme). A time step size of $\Delta t = 0.02$ is chosen.

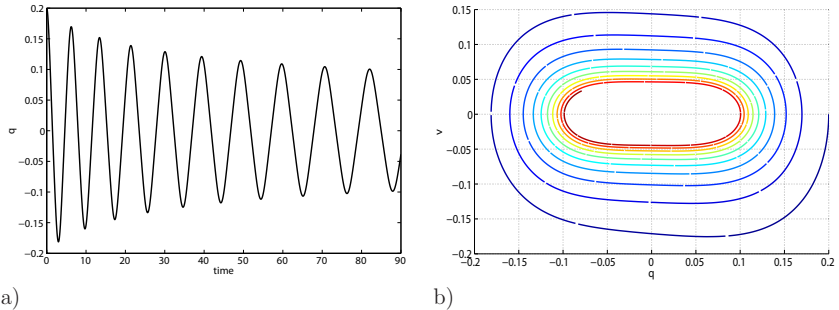


Figure 5.30.: Viscoelastic oscillator: a) displacement of mass, b) phase-space portrait.

5.4.5. Double wishbone suspension

As a practical application of the viscoelastic model, we examine a double wishbone suspension of a sports car (see Fig. 5.32). It consists of four rigid bodies, namely the lower handlebar (body 1), the wheel carrier (body 2), the wheel (body 4) and the upper handlebar (body 3), see Fig. 5.32b. The double wishbone suspension represents a

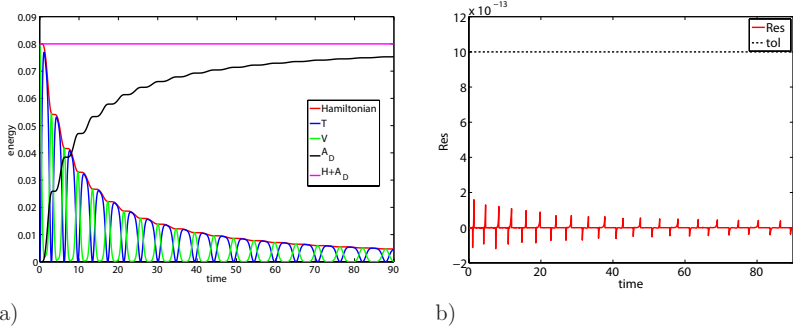


Figure 5.31.: Viscoelastic oscillator: a) energetic consistency, b) fulfillment of the residual.

closed loop system. The shock absorber will be modeled using the viscoelastic dissipative model. Vital for this purpose is once again the coordinate augmentation technique, in this case, used to introduce a translational DOF. First we will present the modeling of the system, followed by the incorporation of the damping unit. Finally we will present the obtained results.

As already mentioned before, the system at hand consists of four rigid bodies, correspondingly the configuration vector can be written as

$$\mathbf{q}_{\text{ori}} = \begin{bmatrix} \mathbf{q}^1 \\ \mathbf{q}^2 \\ \mathbf{q}^3 \\ \mathbf{q}^4 \end{bmatrix}_{48 \times 1} \quad \text{with} \quad \mathbf{q}^i = \begin{bmatrix} \varphi^i \\ \mathbf{d}_1^i \\ \mathbf{d}_2^i \\ \mathbf{d}_3^i \end{bmatrix}_{6 \times 1} \quad (5.186)$$

An important modeling feature is the incorporation of an augmented value, where the internal force of the viscoelastic element can be applied to. Therefore the augmentation technique is applied in order to measure the shock absorber elongation. The new value is simply appended to the configuration vector

$$\mathbf{q} = \begin{bmatrix} \mathbf{q}_{\text{ori}} \\ \varepsilon \end{bmatrix} \quad (5.187)$$

Again the extension of the configuration vector leads to the introduction of an additional constraint equation

$$\Phi_{\text{aug}}(\mathbf{q}) = (\mathbf{q}_0 - \varphi^1) \cdot (\mathbf{q}_0 - \varphi^1) - (u_0 - \varepsilon)^2 \quad (5.188)$$

where u_0 stands for the initial length.

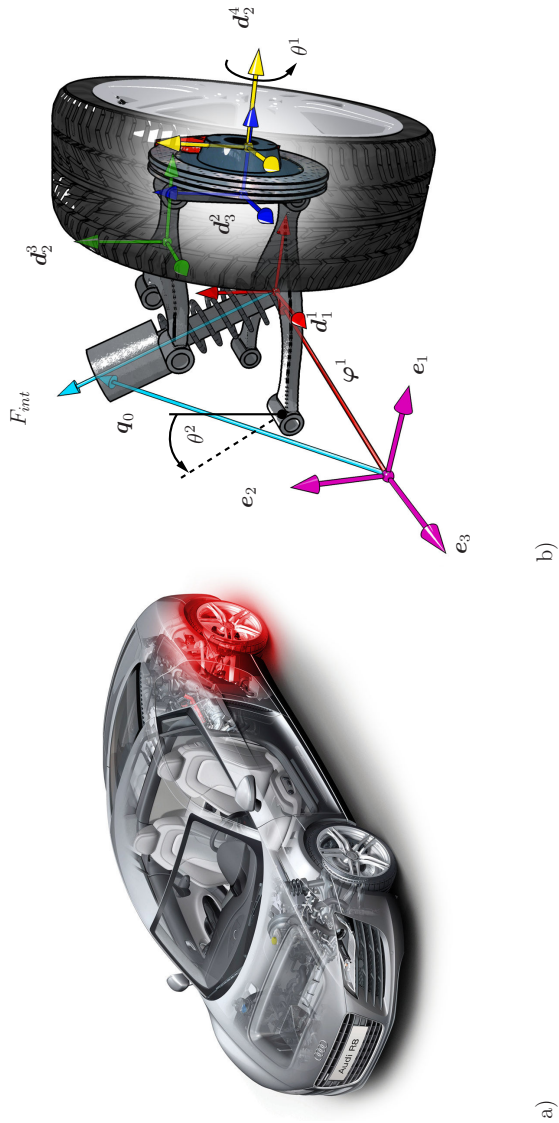


Figure 5.32.: a) Cutaway of an Audi R8 (courtesy of Audi AG), b) schematic of a double wishbone suspension.

The implementation is carried out by applying the algorithmic internal force $F_{\text{int}}^{\text{alg}}$ from Equation (5.180)⁷ to the augmented coordinate, resulting in the discrete force vector

$$\mathbf{F}_{\text{int}}^{\text{alg}} = \begin{bmatrix} \mathbf{0}_{48 \times 1} \\ F_{\text{int}}^{\text{alg}} \end{bmatrix} \quad (5.189)$$

To verify our model, we perform a free fall simulation, using a linear spring characteristic. In this case the algorithmic force $F_{\text{int}}^{\text{alg}}$ coincides with the mid-point evaluation $F_{\text{int}}(1/2)$. Starting from rest, the closed loop system falls under the action of gravity. The free energy function has the form of Equation (5.167).

body	\mathcal{M}	\mathcal{E}_1	\mathcal{E}_2	\mathcal{E}_3
1	2	0.0004	0.0417	0.1067
2	2.5	0.0521	0.0521	0.0021
3	2	0.0004	0.0417	0.0417
4	10	2.133	2.133	0.2083

Table 5.10.: Inertia data for the double wishbone suspension.

The system at hand exhibits two DOF, namely the rotation of the wheel (θ^1) and second the rotation of the closed loop linkage (θ^2), both values are initially set to zero (see Fig. 5.32b). The inertia properties are summarized in Table 5.10. For the free fall simulation, we obtain the following results: The consistency of the time-integrator

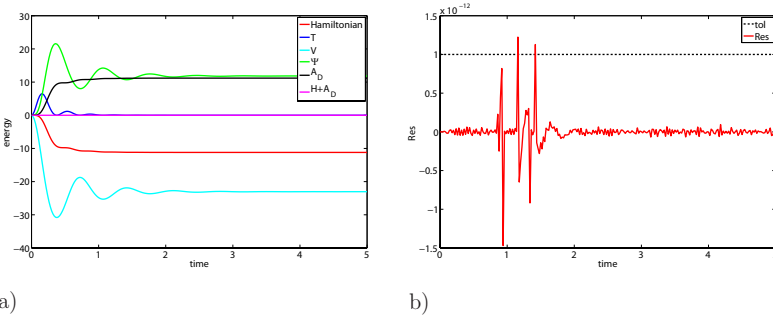


Figure 5.33.: Double wishbone: a) energetic consistency, b) fulfillment of the residual condition.

⁷For this example q coincides with the augmented value ε .

is verified in Fig. 5.33a, showing the kinetic, potential and free energy function as well as the accumulated dissipation and the augmented Hamiltonian \mathcal{H} (see Equation (5.153)). In Fig. 5.33b we find displayed the fulfillment of the residual equation, followed by the internal force in Fig. 5.34. Obviously the rheological model used, captures a physically meaningful behavior. The system reaches after a few damped oscillations its new equilibrium position, while the consistency properties are preserved. The initial and end configuration of the system is depicted in Fig. 5.35.

In practical applications, one is interested in the damping forces while a car passes over

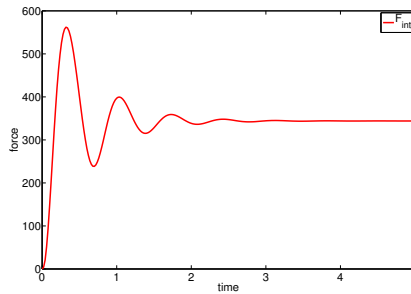


Figure 5.34.: Double wishbone: Internal force.

a stochastic road, which is essential in order to adjust the parameters for a comfortable ride. Therefore in a second test we focus on an underactuated⁸ motion of the double wishbone suspension, where we partially prescribe the motion of the tyre, namely by controlling its vertical motion. The control constraint applied yields

$$\Phi_c(\mathbf{q}, t) = \varphi_y^4 - f_{\text{random}} \quad (5.190)$$

Where f_{random} is a stochastic function with an arbitrary amplitude. The constraint above is moving the tyre (body 4) up and down according to a prescribed random function. This can be viewed as a very simple simulation of a road profile. In this case we are interested in the force of the shock-absorber as well as in the accumulated dissipation within the shock absorber. The accumulated dissipation, combined with a thermomechanical law, would yield a corresponding temperature evolution in the damping unit. Displayed in Fig. 5.36a we see the time history of the internal force followed by the accumulated dissipation, depicted in Fig. 5.36b.

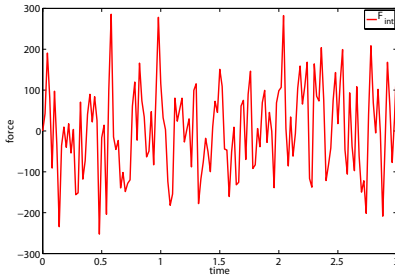
⁸Underactuated because we only prescribe one of the two DOF.



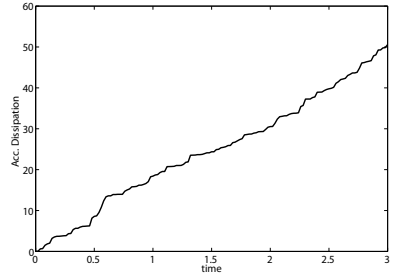
a)

b)

Figure 5.35.: Double wishbone: a) initial configuration $t = 0$, b) final configuration $t = 5$.



a)



b)

Figure 5.36.: Controlled double wishbone: a) internal force for partially controlled movement, b) accumulated dissipation in the dashpot ($\Delta t = 0.02$).

Remark 5.4.2 *A more realistic modeling of a shock absorber can be established by using a generalized Maxwell model, where e.g. all parameters could be obtained by a parameter identification within an experiment. This yields a more realistic model while maintaining all consistency properties of the dynamic model.*

5.4.6. Plasticity model

Our goal in this section is to establish a more adequate model for joint friction, than the one presented in Section 5.4.1. Typically joint friction is not only dominated by a viscous behavior but consists of different phases, i.e. stiction, transition phase and sliding. The transition between stiction (no motion, due to a force / torque smaller than the breakaway amount) and sliding (motion under the action of dissipation) is normally accompanied with a sort of relaxation of the force, while the sliding phase is dominated by a linear viscous friction for high relative velocities. This is the typical joint-friction phenomenon as described e.g. by Waiboer et al. [155]. The modeling of the complete behavior is a challenging task, and was approached by several authors see [8, 9, 41, 75, 46, 146]. Most literature concerning this phenomenon does not rely on thermodynamically consistent models, therefore these modeling approaches fail for the case of designing a consistent time-stepping scheme. In this connection we keep the concept of rheological models and focus on an augmented plasticity model to reproduce the desired effects. The benefit of the rheological model lies within its thermodynamic consistency, as well as in the opportunity to fit the model according to real world behavior⁹.

For modeling the characteristics of stiction and sliding, we choose in the first instance a rheological model of perfect plasticity as depicted in the Figure 5.37. It is obvious that

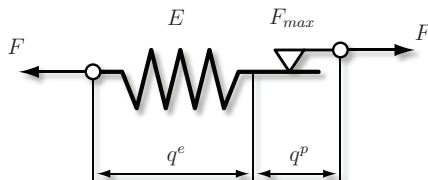


Figure 5.37.: Rheological model for plasticity.

as long as the external force is less than the break away amount, we obtain pure elastic motion, with no dissipation. As soon as the external load is higher than the break away force, plastic slip occurs, dissipation is active. Applied to a joint, this means we need a certain torque to initiate a dissipative motion. Below the break away torque, the joint undergoes small deflections, acting elastically, which leads to conservative oscillations. In

⁹The approach is similar to the constitutive modeling in material mechanics.

a first instance we start with a perfect plasticity model and demonstrate its performance on a friction-element oscillator [108], all required basic notations of perfect plasticity can be found in [140].

5.4.7. Friction-element oscillator

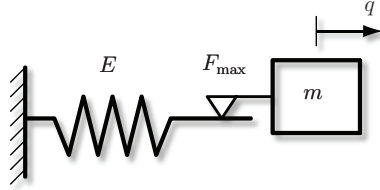


Figure 5.38.: Friction-element oscillator.

To familiarize with the 1D model we start again with a simple friction-element oscillator (Fig. 5.38). The rheological model chosen is the one of perfect plasticity. Following the lines of [108], we derive the equations of motion, show how to implement our plasticity model and how to perform a consistent integration. Starting with the additive split of the displacement

$$q = q^e + q^p \quad \Rightarrow \quad q^e = q - q^p \quad (5.191)$$

The equations of motion can directly be written as

$$m \ddot{q} + F_{\text{int}} + F_{\text{ext}} = 0 \quad (5.192)$$

Assuming a linear spring characteristic for the pure elastic case, the free energy function yields

$$\Psi(q^e) = \frac{1}{2} E (q^e)^2 = \frac{1}{2} E (q - q^p)^2 \quad (5.193)$$

A derivation of the free energy function with respect to q^e yields the internal force

$$F_{\text{int}} = \partial_{q^e} \Psi = E q^e = E (q - q^p) \quad (5.194)$$

The determination when plastic slip occurs can be stated by defining the yield condition

$$\Phi(F_{\text{int}}) = |F_{\text{int}}| - F_{\max} \leq 0 \quad (5.195)$$

5. Modeling Techniques

It is obvious from the equation above that plastic deformation only occurs if $|F_{\text{int}}| \geq F_{\text{max}}$, leading to the following evolution equation

$$\dot{q}^p = \dot{\lambda} \frac{F_{\text{int}}}{|F_{\text{int}}|} = \dot{\lambda} \text{sign } F_{\text{int}} \quad (5.196)$$

While the loading and unloading conditions can directly be written as

$$\Phi(F_{\text{int}}) < 0 \quad \dot{\lambda} = 0 \quad (5.197)$$

and

$$\Phi(F_{\text{int}}) = 0 \quad \dot{\lambda} > 0 \quad (5.198)$$

leading to the Kuhn-Tucker complementary condition

$$\dot{\lambda} \Phi(F_{\text{int}}) = 0 \quad (5.199)$$

Energy-consistent discretization

The discretization of the equations of motion in (5.192) relies again on the mid-point rule

$$q_{n+1} - q_n = \frac{\Delta t}{2} (v_{n+1} + v_n) \quad (5.200a)$$

$$m(v_{n+1} - v_n) + \Delta t F_{\text{int}}(1/2) + \Delta t F_{\text{ext}}(1/2) = 0 \quad (5.200b)$$

The rheological model is reflected by the internal force F_{int} , similar to Section 5.4.4 a mid-point evaluation of F_{int} does not yield a consistent integration. The algorithmic force evaluation must be applied, therefore we need to determine all necessary values following Table 5.4.7.

For the plasticity model we obtain the dissipation

$$\mathcal{D} = F_{\text{int}} \dot{q}^p \quad (5.201)$$

or incrementally

$$\Delta \mathcal{D} = \Delta \lambda F_{\text{max}} \quad (5.202)$$

The algorithmic force equals the expression already presented in Equation (5.180), recapitulating

$$F_{\text{int}}^{\text{alg}} = \frac{\Psi_2 - \Psi_1}{q_2 - q_1} + \frac{\Delta \mathcal{D}}{q_2 - q_1} \quad (5.203)$$

Substituting $F_{\text{int}}(1/2)$ in Equation (5.200b) by the upper expression of the algorithmic force, yields a consistent integration scheme for the friction element oscillator.

<ul style="list-style-type: none"> • Calculate F_n, obtain trial force and trial yield function $F_n = E (q_n - q_n^p)$ $F_{n+1}^{trial} = E (q_{n+1} - q_n^p)$ • Check yield condition $\Phi_{n+1}^{trial} = F_{n+1} ^{trial} - F_{max}$ IF $\Phi_{n+1}^{trial} < 0$: pure elastic step $F_{n+1} = F_{n+1}^{trial}$ $q_{n+1}^p = q_n^p$ $\Delta \lambda = 0$ ELSE: plastic step $\Delta \lambda = \frac{\Phi_{n+1}^{trial}}{E}$ $F_{n+1} = \left[1 - \frac{\Delta \lambda E}{ F_{n+1}^{trial} } \right] F_{n+1}^{trial}$ $q_{n+1}^p = q_n^p + \Delta \lambda \frac{F_{n+1}^{trial}}{ F_{n+1}^{trial} }$
--

Table 5.11.: Numerical implementation of the plasticity model; application of Euler backward scheme to solve the evolution equation.

Remark 5.4.3 For the determination of q_{n+1}^p we used a common approach in plasticity, to integrate the evolution Equation (5.196) by means of an Euler-backward integration. This yields a reduction of the accuracy order once plastic slip occurs (in contrast to the global scheme), but represents a common approach as stated in [108, 140].

Numerical example

To verify our model of the friction-element oscillator, we choose the following values: $m = 100$, $E = 20000$ and a break-away force of $F_{\max} = 100$. The excitation force of $F_{\text{ext}} = 300$ which is applied in form of a hat function (see Fig. 5.3) in time vanishes after $t = 2$. The displacement of the mass is depicted in Fig. 5.39a. After the plastic slip vanishes (approx. 3.65), the mass-point undergoes pure elastic oscillations. Fig. 5.39b shows the internal force over the displacement, revealing the character of the perfect plasticity model (time is color coded). Finally in Fig. 5.40a we see the energetic consistency. Again the sum of the Hamiltonian and the accumulated dissipation yields a straight line, the fulfillment of the residual is also displayed in Fig. 5.40b. All results were obtained using a time step size of $\Delta t = 0.02$.

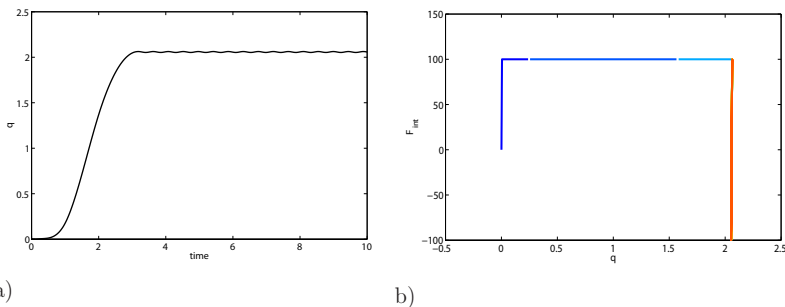


Figure 5.39.: Friction-element oscillator: a) displacement of the friction element oscillator, b) internal force over displacement.

5.4.8. Planar physical pendulum

Following the modeling steps of Section 5.4.2, we now apply our plasticity model to the planar physical pendulum. Friction is acting in the joint, the corresponding augmented coordinate is again θ . Geometric and inertia properties are now set according to Table 5.12. For the plasticity model we choose the following parameters: $E = 50000$ and a break away force of $F_{\max} = 45$. The initial configuration is given by $\theta = \frac{\pi}{2}$ while the

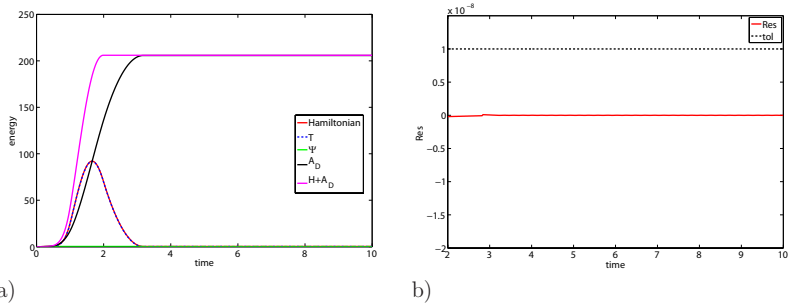


Figure 5.40.: Friction-element oscillator: a) energetic consistency, b) fulfillment of the residual.

initial velocity is set to zero. Due to the rheological model and the gravitational force, the algorithm checks for elastic or plastic behavior at each discrete time t_n . If the external force is less than the break-away force, the system oscillates about its new equilibrium. Figure 5.41 shows the expected behavior. First the sliding phase starts, at the reversal point the pendulum comes to a rest since the break-away torque is higher than the retraction torque. Obviously the system then performs pure elastic oscillations about its new equilibrium position (see zoom of displacement Fig. 5.41). Again we investigate the energetic consistency in Fig. 5.42a and check the fulfillment of the residual in Fig. 5.42b. All simulations have been performed with a time step size of $\Delta t = 0.02$.

\mathcal{M}	\mathcal{E}_1	\mathcal{E}_2
50	0.0104	1.0417

Table 5.12.: Inertia data for the physical pendulum.

Remark 5.4.4 *The plasticity model renders qualitatively good results which also fulfill the desired consistency conditions, but the model itself behaves unrealistically due to the elastic oscillations once an equilibrium state is reached. Therefore in the following we will modify the rheological model to remedy this fact.*

5.4.9. Enhanced rheological model for joint-plasticity

As mentioned above, the goal in this section is to damp the unrealistic high frequency oscillations of the plasticity model in the elastic state. Therefore we slightly augment the

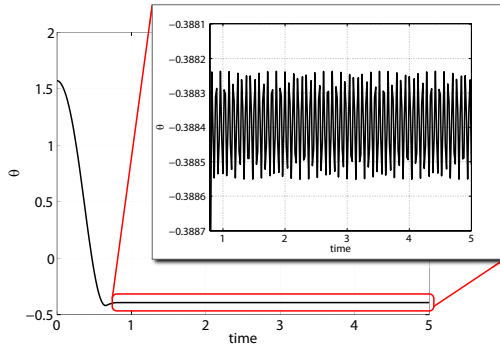


Figure 5.41.: Physical pendulum with joint plasticity: displacement of the physical pendulum (zoom shows the oscillations in the elastic state).

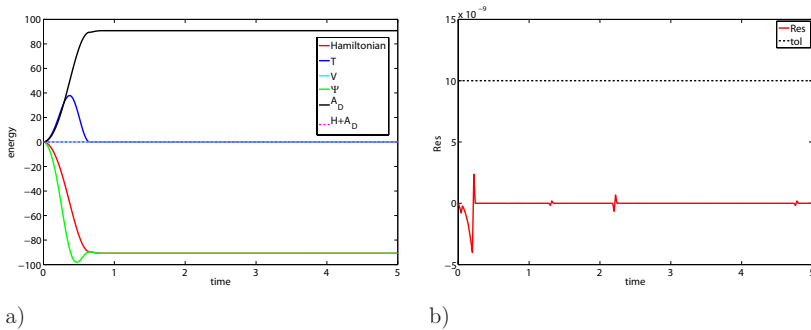


Figure 5.42.: Physical pendulum with joint plasticity: a) energetic consistency for the planar pendulum, b) fulfillment of the residual.

rheological model presented in Section 5.4.6, by adding a viscous damping unit parallel to the elastic spring, according to Fig. 5.43. Due to the installed damping element, the

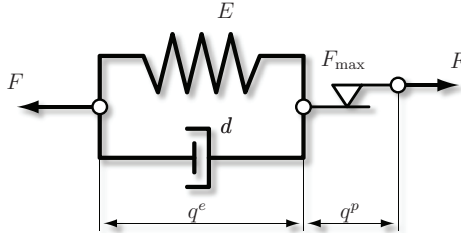


Figure 5.43.: Augmented rheological model for plasticity.

internal force of the rheological model changes to

$$F_{\text{int}} = E (q - q^p) + d (\dot{q} - \dot{q}^p) \quad (5.204)$$

The discrete internal force must again be obtained using the algorithmic force evaluation (5.203) where now the incremental dissipation consists of two parts

$$\Delta \mathcal{D} = \Delta \mathcal{D}^1 + \Delta \mathcal{D}^2 \quad (5.205)$$

split into a plastic (upper index 1) and viscous (upper index 2) contribution

$$\begin{aligned} \Delta \mathcal{D}^1 &= \Delta \lambda F_{\text{max}} \\ \Delta \mathcal{D}^2 &= \frac{d}{\Delta t} (q_{n+1} - q_n - q_{n+1}^p + q_n^p)^2 \end{aligned} \quad (5.206)$$

By inserting Equation (5.205) into the expression of the algorithmic force (Equation 5.203), we obtain a consistent scheme for the enhanced rheological model.

Again we verify the augmented model with the example of the planar physical pendulum in order to compare the results. All initial and geometric values coincide with the values from Section 5.4.8. The damping ratio of the parallel dashpot unit is chosen to $d = 150$. Fig. 5.44 shows again the angle θ and also the zoomed region, where we clearly see that in the stiction phase the high frequency oscillations are damped. Again we check the consistency in Fig. 5.45a and the fulfillment of the residual in Fig. 5.45b. The step size is chosen to $\Delta t = 0.02$.

The procedure outlined above shows clearly the benefits of choosing rheological models to model dissipation. They can be augmented in a modeling driven way, such that they fit real world behavior. At the same time, the consistency properties are maintained. This represents a major argument for applying rheological models to design consistent

time stepping schemes for dissipative systems.

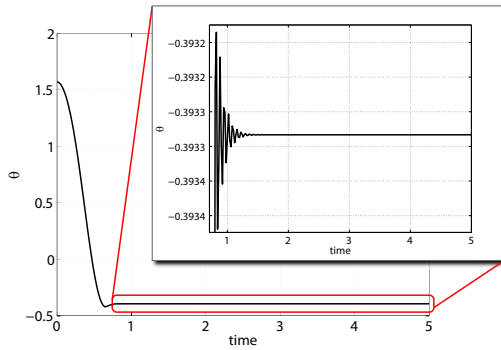


Figure 5.44.: Enhanced plasticity model: displacement of the physical pendulum (zoom shows the damped oscillations in the sticking state).

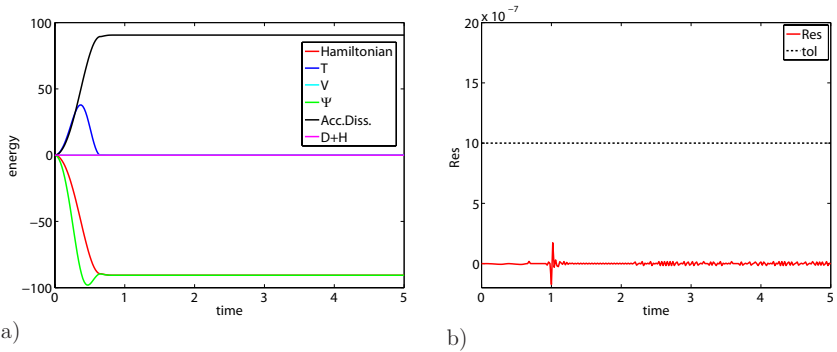


Figure 5.45.: Enhanced plasticity model: a) consistency of the augmented rheological model, b) fulfillment of the residual.

5.4.10. Planar parallel manipulator with joint friction

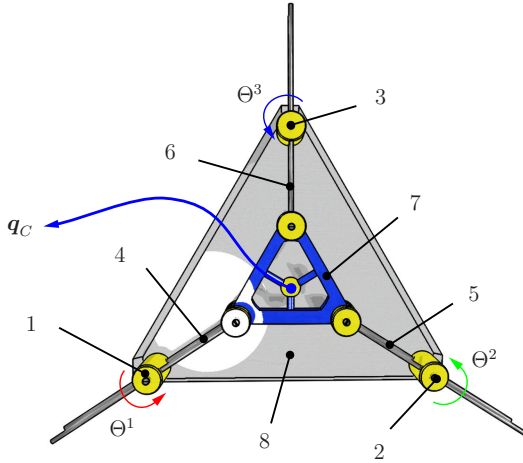


Figure 5.46.: Schematics of the RPR-manipulator.

This example studies an underactuated motion of a planar manipulator of RPR-type. In contrast to the mechanism investigated in Section 5.2.5, three of the revolute joints are being replaced by translatic joints, justifying the name (**R**evolute-**P**rismatic-**R**evolute). The idea is to prescribe the motion of the seventh body, namely the inner small triangle, while actuating the joint angles Θ^1 , Θ^2 and Θ^3 . Since the structure is equivalent to the example of the RRR-manipulator outlined in detail before, we now focus on the implementation of joint friction acting on the actuated coordinates (Θ^1 , Θ^2 and Θ^3). Here we choose the augmented plasticity model and want to investigate the influence of joint friction on the necessary driving torques (inputs) for a prescribed motion. This example was studied for the conservative case in detail in [149]. We recapitulate here the control constraints and outline the corresponding control Jacobian as well as the geometric and inertial properties. The system we want to investigate is depicted in Fig. 5.46.

As mentioned before, our intention is to let body number 7 move upon a prescribed trajectory and calculate the necessary driving torques (input values) acting in the revolute joints. The desired trajectory shall follow a figure-8 pattern as similarly proposed by

McPhee and Redmond [105]

$$\Phi_{\text{traj}}(\mathbf{q}) = \begin{bmatrix} q_x^7(t_0) + \frac{1}{12} \sin(\omega(t)) \\ q_y^7(t_0) + \frac{1}{16} \sin(2\omega(t)) \end{bmatrix} \quad (5.207)$$

while $\omega(t)$ describes the angular velocity which for this example is defined as a 9th order polynomial. The polynomial was proposed in [30] and is well suited for control problems due to its continuous and steady character. In this example it is defined as follows

$$\theta(t) = \begin{cases} s_1(t) & \text{for } 0 \leq t \leq t_1 \\ s_2(t) & \text{for } t_1 \leq t \leq t_2 \\ s_3(t) & \text{for } t_2 \leq t \leq t_3 \end{cases} \quad (5.208)$$

where

$$\begin{aligned} s_1(t) &= \left[\frac{126}{6} t_1 \left(\frac{t}{t_1} \right)^6 - \frac{420}{7} t_1 \left(\frac{t}{t_1} \right)^7 + \frac{540}{8} t_1 \left(\frac{t}{t_1} \right)^8 - \frac{315}{9} t_1 \left(\frac{t}{t_1} \right)^9 + \frac{70}{10} t_1 \left(\frac{t}{t_1} \right)^{10} \right] \omega_0 \\ s_2(t) &= s_1(t_1) + \omega_0(t - t_1) \\ s_3(t) &= s_2(t) - (t_3 - t_2) \left[\frac{126}{6} \left(\frac{t-t_2}{t_3-t_2} \right)^6 - \frac{420}{7} \left(\frac{t-t_2}{t_3-t_2} \right)^7 + \frac{540}{8} \left(\frac{t-t_2}{t_3-t_2} \right)^8 \right. \\ &\quad \left. - \frac{315}{9} \left(\frac{t-t_2}{t_3-t_2} \right)^9 + \frac{70}{10} \left(\frac{t-t_2}{t_3-t_2} \right)^{10} \right] \omega_0 \end{aligned} \quad (5.209)$$

Specifically we choose here

$$t_1 = 1, \quad t_2 = 2, \quad t_3 = 3 \quad \text{and} \quad \omega_0 = \pi \quad (5.210)$$

Since during this motion the inner triangle (body 7) shall not rotate we also have to implement another constraint suppressing the rotation

$$\Phi^3(\mathbf{q}) = \mathbf{e}_2 \cdot \mathbf{d}_1^7 \quad (5.211)$$

The whole control constraint for the desired motion can then be written as

$$\Phi_C(\mathbf{q}) = \begin{bmatrix} \Phi_{\text{traj}}(\mathbf{q}) \\ \Phi^3(\mathbf{q}_0) \end{bmatrix} \quad (5.212)$$

The corresponding constraint Jacobian for the new control constraints yields

$$\mathbf{B} = [\mathbf{0}_{3 \times 48} \quad \mathbf{I}_{3 \times 3}] \quad (5.213)$$

Since there are no external forces acting on the system, the center of mass does not have to move, just as with the example of the RRR-structure. Moreover, since no external torques act on the system, the total angular momentum shall again represent a conserved quantity. Now we also activate our joint friction model according to Section 5.4.9. Therefore we choose the following parameters for the model: $E = 350$, a breakaway force of $F_{\text{max}} = 50$ and a damping value for the parallel dashpot unit of $d = 10$.

body	\mathcal{M}	\mathcal{E}_1	\mathcal{E}_2	length	width
1	3	0.0125	0.0275	0.25	0.05
2	3	0.0125	0.0275	0.25	0.05
3	3	0.0125	0.0275	0.25	0.05
4	4	0.04	0.08	0.35	0.05
5	4	0.04	0.08	0.35	0.05
6	4	0.04	0.08	0.35	0.05

Table 5.13.: Inertial and geometric properties pertaining to the six legs of the manipulator.

body	\mathcal{M}	\mathcal{E}_1	\mathcal{E}_2	L
7	3	0.0408	0.0408	0.4
8	8	0.1	0.1	1.0

Table 5.14.: Inertial and geometric properties pertaining to the two platforms of the manipulator.

Inertial and geometric properties of the rigid bodies constituting the parallel manipulator are summarized in Tables 5.13 and 5.14.

The initial configuration of the closed-loop system can be completely specified by its generalized coordinates, accordingly (see Section 5.2.5)

$$\mathbf{u}_0 = \begin{bmatrix} \varphi^8(0) \cdot \mathbf{e}_1 \\ \varphi^8(0) \cdot \mathbf{e}_2 \\ \theta^8(0) \\ \Theta^1(0) \\ \Theta^2(0) \\ \Theta^3(0) \\ \Theta^4(0) \\ \Theta^5(0) \\ \Theta^6(0) \\ \Theta^7(0) \end{bmatrix} = \begin{bmatrix} 0 \\ 0.2887 \\ 0 \\ \frac{\pi}{6} \\ \frac{2}{3}\pi \\ -\frac{\pi}{2} \\ \frac{\pi}{6} \\ \frac{2}{3}\pi \\ -\frac{\pi}{2} \\ 0 \end{bmatrix} \tag{5.214}$$

Figure 5.47 depicts the consistency properties, decomposed into the energy components in the upper diagram and the conservation properties in the two lower diagrams. Since the system is actuated, there is no conservation of energy. But due to no action of gravity, the conservation of the angular momentum is guaranteed. Fig. 5.48b shows the evolution of the augmented angles Θ^I , $I = 1, 2, 3$, while Fig. 5.48a shows the comparison of the necessary driving torques, once with activated joint friction (nc) and once for the conservative case (c). It is obvious how immense the influence of joint friction for control

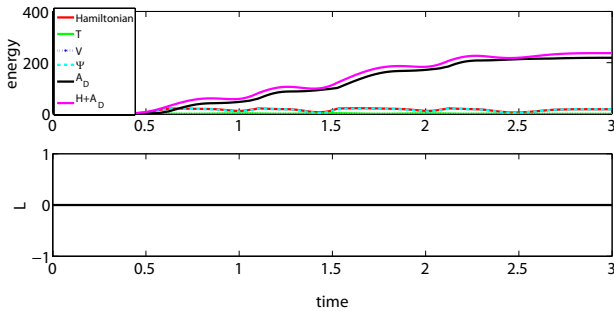


Figure 5.47.: Consistency for RPR ($\Delta t = 0.01$).

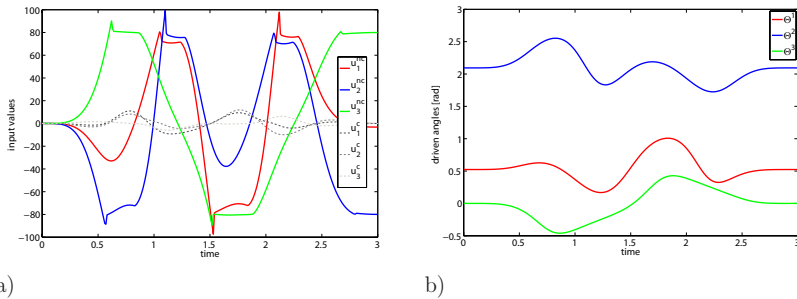
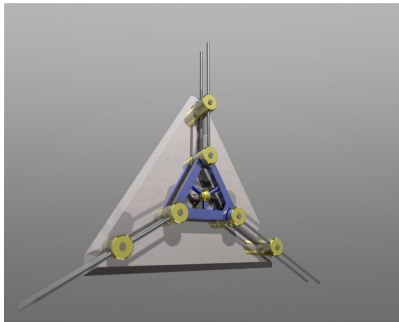
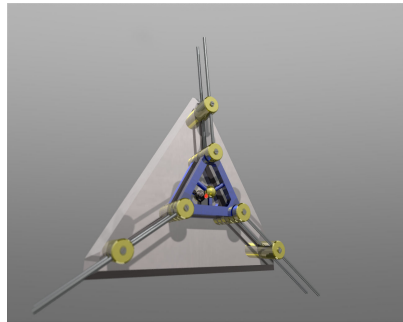


Figure 5.48.: Controlled RPR-structure: a) comparison of necessary inputs for the non-conservative^{nc} and conservative^c case, b) evolution of the driven angles.

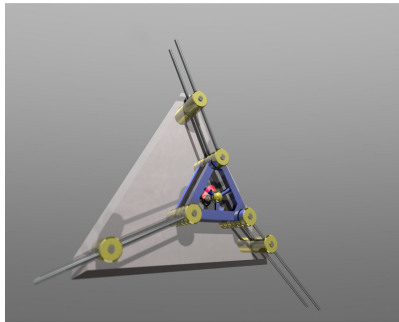
problems is. Depending on the values chosen for the friction model, the driving torques exceed notably the values for the conservative case. Therefore it is essential for these applications to model friction adequately in order to capture real world behavior. Since one typically has to adjust the electric motors driving the system, numerical dissipation would result in higher driving inputs than necessary, inefficient for practical applications. Some snapshots of the motion are depicted in Fig. 5.49. We choose a time step size of $\Delta t = 0.01$.



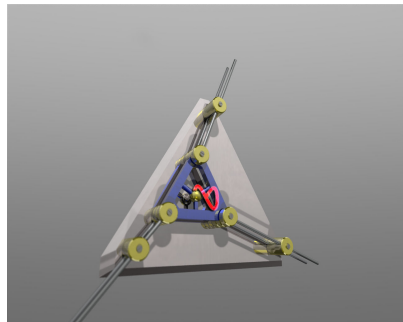
$t = 0$



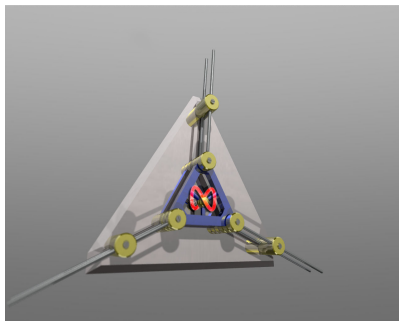
$t = 0.5$



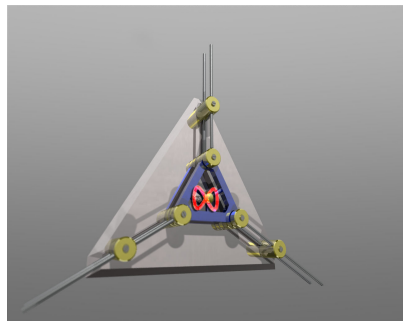
$t = 1$



$t = 2$



$t = 2.5$



$t = 3$

Figure 5.49.: Snapshots of the driven motion of the free floating planar manipulator.

5.5. Nonholonomic Constraints

We focus in this section on the incorporation of nonholonomic constraints. As already mentioned in Chapter 3, nonholonomic constraints represent non-integrable constraints. Typically they arise under the assumption of rolling without slipping. In this connection they can be viewed as a simplified contact model, which is always restricted by the non slipping assumption mentioned above. In multibody dynamics these kind of constraints are not that widely spread, but yet there are some applications in robotics which rely on rolling elements (see e.g. [43]). The analysis of nonholonomic systems from a mathematical point of view has been of great interest, mainly in the field of analytical mechanics (see e.g. [113, 114]). Here the ideas and academic examples were established, based upon d'Alembert's principle and Lagrangian mechanics. Recent publications in the field of numerical mechanics combine control issues with nonholonomic problems, refer e.g. to [32, 126, 44].

We will outline how these new constraints can again be appended to the original scheme outlined in Section 3.2.1. Similarly to the incorporation of control constraints we will present a basic energy-momentum scheme for nonholonomic constraints and again perform a size reduction by the new appended constraints, leading to a minimized set of equations. To demonstrate the performance of the new scheme, we will present an academic example of a rolling ball on a turntable. The advantage is that for this special case, there are analytical solutions available, hence we can verify the numerical results. The last, more practical, example will render the fully actuated motion of a two wheeled robot.

5.5.1. Systems with mixed geometric and kinematic constraints

According to [16, 148] we will now extend the basic set of DAEs (see Equation (3.1)) by the new nonholonomic constraints. Again this makes possible the beneficial structure of the DAE-type as mentioned in Section 3.3. For the continuous set of governing equations we obtain

$$\dot{\mathbf{q}} - \mathbf{v} = \mathbf{0} \quad (5.215a)$$

$$\mathbf{M}\dot{\mathbf{v}} - \nabla V(\mathbf{q}) + \mathbf{G}^T \boldsymbol{\lambda} + \mathbf{A}^T \boldsymbol{\mu} = \mathbf{0} \quad (5.215b)$$

$$\boldsymbol{\Phi}(\mathbf{q}) = \mathbf{0} \quad (5.215c)$$

$$\mathbf{A}(\mathbf{q})\dot{\mathbf{q}} = \mathbf{0} \quad (5.215d)$$

In the equations above the last expression is characterizing the m_n nonintegrable relationships. Along with the geometric constraints in Equation (5.215c) the new kinematic constraints define a $2n - m$ dimensional smooth submanifold

$$\mathbf{M} = \{(\mathbf{q}, \dot{\mathbf{q}}) \in \mathbb{R}^n \times \mathbb{R}^n \mid \boldsymbol{\Phi}(\mathbf{q}) = \mathbf{0}, \mathbf{A}(\mathbf{q})\dot{\mathbf{q}} = \mathbf{0}\} \quad (5.216)$$

of the phase space. In the following we once again seek an energy-momentum time integration of Equations (5.215), deriving a mechanical time integration scheme for non-holonomic systems.

5.5.2. Conserving integration of the mixed set of DAEs

'Currently there appear to be no reliable general-purpose algorithms available on which production-level software may be based for solving DAEs... arising as models of problems involving kinematic or mixed kinematic and geometric constraints' Rabier and Rheinboldt [125, page 97]

In the following we will present an energy-momentum conserving time stepping scheme, by again performing a direct discretization of Equations (5.215). We obtain the following one-step integration scheme

$$\mathbf{q}_{n+1} - \mathbf{q}_n = \frac{\Delta t}{2} (\mathbf{v}_n + \mathbf{v}_{n+1}) \quad (5.217a)$$

$$\mathbf{M} (\mathbf{v}_{n+1} - \mathbf{v}_n) = \Delta t [\nabla V(\mathbf{q}_n, \mathbf{q}_{n+1}) - \mathbf{G}(\mathbf{q}_n, \mathbf{q}_{n+1})^T \boldsymbol{\lambda} - \mathbf{A}(\mathbf{q}_n, \mathbf{q}_{n+1})^T \boldsymbol{\mu}] \quad (5.217b)$$

$$\boldsymbol{\Phi}(\mathbf{q}_{n+1}) = \mathbf{0} \quad (5.217c)$$

$$\mathbf{A}(\mathbf{q}_n, \mathbf{q}_{n+1}) (\mathbf{q}_{n+1} - \mathbf{q}_n) = \mathbf{0} \quad (5.217d)$$

The scheme above represents a slight modification of the scheme proposed in [16], concerning the expression (5.217d). Instead of a mid-point evaluation of $\mathbf{A}(\mathbf{q})$ as proposed in the reference cited above, we will devise the specific form with the following examples. The fundamental difference is, that a simple mid-point evaluation of the constraint Jacobian for the nonholonomic constraints does not yield a momentum conserving scheme. This effect also influences the obtained results as shall be proofed with the example given in Section 5.5.3.

As already outlined in Section 3.2.1, due to the appended constraint equations the system becomes more and more ill conditioned by lowering the time step size. Accordingly the reduction procedures outlined before can be applied once more. In this case we will shortly summarize the necessary steps to eliminate the newly introduced Jacobian for the nonholonomic part along with the holonomic contribution. Therefore we proceed along the lines given in [16]. The complete constraint Jacobian concerning both geometric and kinematics constraints can be written as

$$\boldsymbol{\Gamma}^T = [\mathbf{G}(\mathbf{q}_n, \mathbf{q}_{n+1})^T \quad \mathbf{A}(\mathbf{q}_n, \mathbf{q}_{n+1})^T] \quad (5.218)$$

The elimination now again relies on the construction of a matrix \mathbf{P} which spans the null space of $\boldsymbol{\Gamma}$. A premultiplication of the Equations (5.217) with \mathbf{P}^T and a substitution of

\mathbf{v}_{n+1} via Equation (5.217a) leads to the following set of DAEs

$$\mathbf{P}^T \left[\frac{2}{\Delta t} \mathbf{M} \mathbf{q}_{n+1} + \Delta t \nabla V(\mathbf{q}_n, \mathbf{q}_{n+1}) - 2\mathbf{M} \left(\mathbf{v}_n + \frac{\mathbf{q}_n}{\Delta t} \right) \right] = \mathbf{0} \quad (5.219a)$$

$$\Phi(\mathbf{q}_{n+1}) = \mathbf{0} \quad (5.219b)$$

$$\mathbf{A}(\mathbf{q}_n, \mathbf{q}_{n+1}) (\mathbf{q}_{n+1} - \mathbf{q}_n) = \mathbf{0} \quad (5.219c)$$

Again a second size reduction can be achieved by a reparametrization of unknowns according to Section 3.2.2. In the following we will present examples rendering the performance of the presented scheme and revealing the specific shape of $\mathbf{A}(\mathbf{q}_{n+1}, \mathbf{q}_n)$.

5.5.3. Ball on a rotating plate

The present example represents a typical nonholonomic problem. Describing the motion of a ball with a given initial angular velocity moving on a turntable, which is rotating with a constant frequency. The problem was approached analytically e.g. in [161], comparable investigations were also carried out in [156].

The system we want to investigate is depicted in Fig. 5.50. In this connection we again

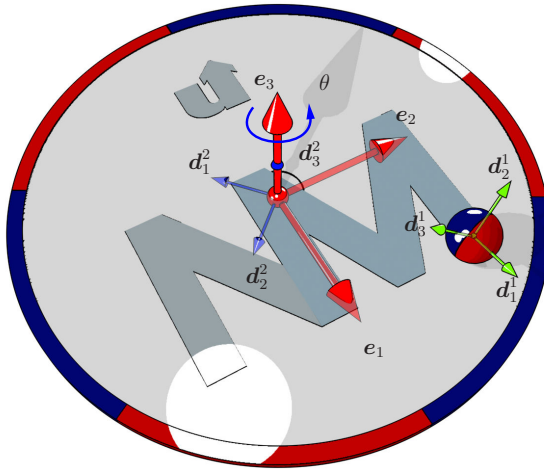


Figure 5.50.: Ball on a rotating plate.

apply the rotationless formulation for the modeling, thereby we obtain the following vector of redundant coordinates for the present 2-body system

$$\mathbf{q}_{\text{ori}} = \begin{bmatrix} \mathbf{q}^1 \\ \mathbf{q}^2 \end{bmatrix}_{24 \times 1} \quad (5.220)$$

To control the rotational motion of the plate we first perform a coordinate augmentation by introducing the rotation angle θ about the \mathbf{e}_3 -axis of the plate

$$\mathbf{q} = \begin{bmatrix} \mathbf{q}_{\text{ori}} \\ \theta \end{bmatrix}_{25 \times 1} \quad (5.221)$$

The additional constraint which needs to be fulfilled due to the augmentation yields

$$\Phi(\mathbf{q}) = \mathbf{d}_1^2 \cdot \mathbf{e}_1 + \mathbf{d}_1^2 \cdot \mathbf{e}_2 - \sin \theta + \cos \theta \quad (5.222)$$

In addition to constraint (5.222), the following geometric constraints have to be imposed on the system: Six internal constraints of the form (4.3) for each of the two rigid bodies plus five external constraints for the rotating plate given by

$$\Phi_{\text{ext}}(\mathbf{q}) = \begin{bmatrix} \varphi^2 + L\mathbf{d}_3^2 \\ \mathbf{d}_1^2 \cdot \mathbf{e}_3 \\ \mathbf{d}_2^2 \cdot \mathbf{e}_3 \end{bmatrix} \quad (5.223)$$

where L denotes the thickness of the plate. To summarize, we have $m_g = 18$ independent geometric constraints. On the other hand, the number of redundant coordinates amounts to $n = 25$. Due to the assumption of rolling without slipping, three additional kinematic constraints ($m_k = 3$), have to be accounted for. In this connection, the point of contact between the ball and the plate needs to be identified. Starting with the ball, the velocity of the contact point is given by

$$\mathbf{v}_c^1 = \mathbf{v}_\varphi^1 + \sum_{I=1}^3 \bar{X}_I^1 \mathbf{d}_I^1 \quad (5.224)$$

where \mathbf{v}_φ^1 is the velocity of the center of mass and \bar{X}_I^1 specifies the material coordinates of the contact point with respect to the body-fixed director frame. To detect these coordinates, the following geometric contact condition needs to be satisfied

$$\sum_{I=1}^3 \bar{X}_I^1 \mathbf{d}_I^1 = -R\mathbf{e}_3 \quad (5.225)$$

where R is the radius of the ball. Accordingly,

$$\bar{X}_I^1 = -R\mathbf{e}_3 \cdot \mathbf{d}_I^1 \quad (5.226)$$

5. Modeling Techniques

for $I = 1, 2, 3$. Similarly, the material coordinates \bar{X}_I^2 characterizing the contact point on the plate are given by

$$\bar{X}_I^2 = \mathbf{r}_c^2 \cdot \mathbf{d}_I^2 \quad (5.227)$$

with

$$\mathbf{r}_c^2 = \begin{bmatrix} \varphi_1^1 \\ \varphi_2^1 \\ L/2 \end{bmatrix} \quad (5.228)$$

The corresponding velocity of the contact point on the plate reads

$$\mathbf{v}_c^2 = \mathbf{v}_\varphi^2 + \sum_{I=1}^3 \bar{X}_I^2 \mathbf{d}_I^2 \quad (5.229)$$

The kinematic constraint $\mathbf{v}_c^1 = \mathbf{v}_c^2$ can now be written in the form

$$\mathbf{A}(\mathbf{q})\mathbf{v} = \mathbf{0} \quad (5.230)$$

with

$$\mathbf{A}(\mathbf{q}) = [\mathbf{I} \quad -R\mathbf{e}_3 \cdot \mathbf{d}_1^1 \quad -R\mathbf{e}_3 \cdot \mathbf{d}_2^1 \quad -R\mathbf{e}_3 \cdot \mathbf{d}_3^1 \quad -\mathbf{I} \quad \mathbf{r}_c^2 \cdot \mathbf{d}_1^2 \quad \mathbf{r}_c^2 \cdot \mathbf{d}_2^2 \quad \mathbf{r}_c^2 \cdot \mathbf{d}_3^2 \quad \mathbf{0}_{3 \times 1}] \quad (5.231)$$

Note that only two of the three kinematic constraints (5.230) are to be labeled non-holonomic. The third equation may be integrated to yield a holonomic constraint which characterizes the constant distance between the ball center and the plate. However, in the present approach there is no need for reassignment, since the proposed numerical scheme still satisfies the associated holonomic constraint exactly, see [16] for further details.

Discrete formulation

In contrast to the original design of an energy conserving scheme in [16], we next propose a modification which, in addition to algorithmic energy conservation, facilitates algorithmic conservation of the relevant component of the total angular momentum. To this end we next devise algorithmic counterparts of (5.226) and (5.227). In particular, the discrete versions are defined by

$$\tilde{\mathbf{X}}^1(\mathbf{q}_{n+1}, \mathbf{q}_n) = \begin{bmatrix} \tilde{X}_1^1 \\ \tilde{X}_2^1 \\ \tilde{X}_3^1 \end{bmatrix} = -R\Lambda^1(\mathbf{q}_{n+1/2})^{-1} \mathbf{e}_3 \quad (5.232)$$

with

$$\Lambda^1(\mathbf{q}_{n+1/2}) = [\mathbf{d}_1^1 \quad \mathbf{d}_2^1 \quad \mathbf{d}_3^1]_{n+1/2} \quad (5.233)$$

Furthermore,

$$\tilde{\mathbf{X}}^2(\mathbf{q}_{n+1}, \mathbf{q}_n) = \begin{bmatrix} \tilde{X}_1^2 \\ \tilde{X}_2^2 \\ \tilde{X}_3^2 \end{bmatrix} = \mathbf{\Lambda}^2(\mathbf{q}_{n+1/2})^{-1} \begin{bmatrix} \varphi_1^1 \\ \varphi_2^1 \\ L/2 \end{bmatrix}_{n+1/2} \quad (5.234)$$

with

$$\mathbf{\Lambda}^2(\mathbf{q}_{n+1/2}) = [\mathbf{d}_1^2 \quad \mathbf{d}_2^2 \quad \mathbf{d}_3^2]_{n+1/2} \quad (5.235)$$

Now, the discrete counterpart of (5.231) is given by

$$\mathbf{A}(\mathbf{q}_{n+1}, \mathbf{q}_n) = [\mathbf{I} \quad \tilde{X}_1^1 \mathbf{I} \quad \tilde{X}_2^1 \mathbf{I} \quad \tilde{X}_3^1 \mathbf{I} \quad -\mathbf{I} \quad \tilde{X}_1^2 \mathbf{I} \quad \tilde{X}_2^2 \mathbf{I} \quad \tilde{X}_3^2 \mathbf{I}] \quad (5.236)$$

Incorporation of a control constraint

To evaluate the numerical performance of the present energy-momentum scheme, we compare the numerical results with an analytical reference solution. The analytical solution – see Yang [161] – relies on the assumption that the plate is rotating with constant angular velocity. Therefore, we incorporate into our scheme a control constraint of the form

$$b = \theta \quad \text{and} \quad \gamma(t) = Ct \quad (5.237)$$

where C denotes the constant angular velocity. This constraint is being appended to the DAEs according to Section 5.3. The corresponding actuating torque is given by $\mathbf{B}^T \bar{\mathbf{u}}$ (see Section 5.3), with

$$\mathbf{B}^T = \begin{bmatrix} \mathbf{0}_{24 \times 1} \\ 1 \end{bmatrix} \quad (5.238)$$

Results

The analytical solution yields circular trajectories of the ball center. In particular, according to Yang [161], the coordinates of the contact point with respect to the spatially fixed reference frame are given by

$$x(t) = \frac{\dot{y}_0}{l} \cos(lt) + \frac{\dot{x}_0}{l} \sin(lt) - \frac{\dot{y}_0}{l} + x_0 \quad (5.239a)$$

$$y(t) = \frac{\dot{x}_0}{l} \cos(lt) + \frac{\dot{y}_0}{l} \sin(lt) - \frac{\dot{x}_0}{l} + y_0 \quad (5.239b)$$

Here, $l = \frac{Ck^2}{a^2+k^2}$ and x_0, y_0, \dot{x}_0 and \dot{y}_0 are the initial positions and velocities of the ball. Moreover, a is the radius of the ball, k is the radius of gyration which in the present case is given by $k = a\sqrt{2/5}$ and, as before, C is the constant angular velocity of the

rotating plate.

For the numerical simulation we choose $a = 0.5$, $x_0 = 0$, $y_0 = 0$, $\dot{x}_0 = 1$, $\dot{y}_0 = 0$ and $C = 2$. The simulated motion is illustrated with some snapshots in Fig. 5.52. In addition to that, Fig. 5.51 corroborates convergence of the numerical solution towards the analytical one. In this connection, the original energy conserving scheme [16] (this scheme relies on the mid-point evaluation $\mathbf{A}(\mathbf{q}_{n+1/2})$, which is in contrast to (5.236)) is compared with the present energy-momentum scheme. It can be observed that the additional algorithmic conservation property of the present scheme yields a significant improvement of the numerical results (although, of course, in the present example the angular momentum is not conserved). The improved numerical behavior is also reflected by the fact that the new scheme in general requires less Newton iterations than the original scheme¹⁰.

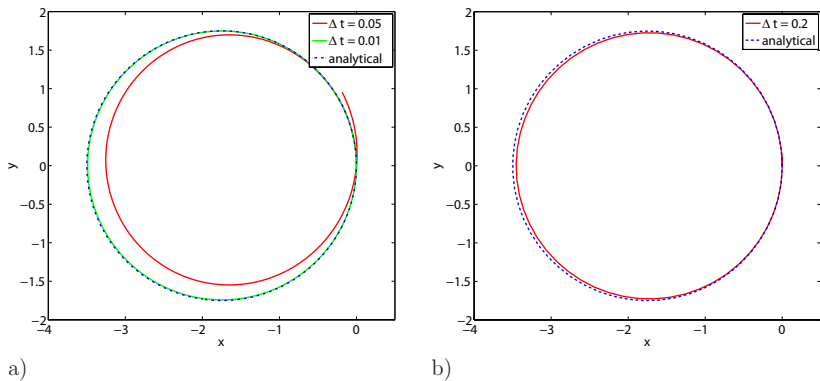


Figure 5.51.: Ball on rotating plate: comparison of the results for the case of constant angular velocity of the plate. a) original energy conserving scheme [16], b) newly proposed energy-momentum scheme.

5.5.4. Two wheeled robot

This example shall present a practical application of the features outlined before. It deals with the fully actuated motion of a two wheeled robot (see e.g. [139]). Here we will combine three modeling features presented within this chapter: (i) the coordinate

¹⁰An additional example of a free spinning plate, proving the conservation of energy and angular momentum can be found in [148].

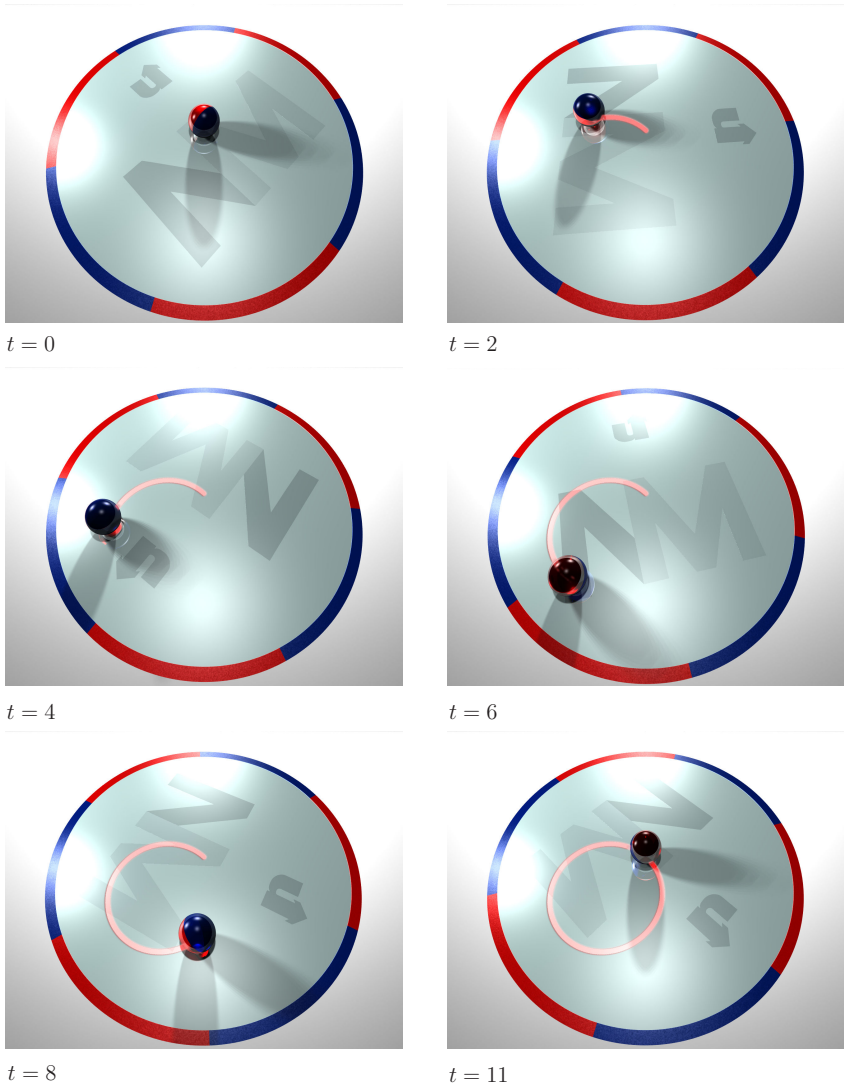


Figure 5.52.: Simulation results for the case of constant angular velocity of the plate.

augmentation which again facilitates the actuation, leading to (ii) the incorporation of control constraints and finally (iii) constraining the robots motion kinematically. The mechanical model of the robot is depicted in Fig. 5.53. The application of the rotation-

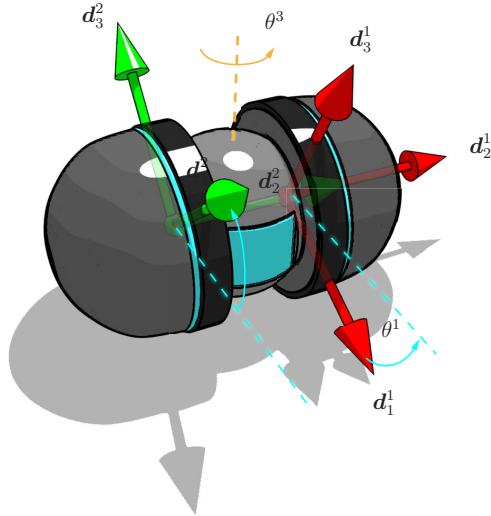


Figure 5.53.: Schematics of the two wheeled robot.

less formulation leads to the following vector of redundant coordinates

$$\mathbf{q}_{\text{ori}} = \begin{bmatrix} \mathbf{q}^1 \\ \mathbf{q}^2 \end{bmatrix}_{24 \times 1} \quad (5.240)$$

According to Fig. 5.53 we will augment the two angles measuring the rotation of the wheels (θ^1 and θ^2) and finally a third angle (θ^3) accounting for the rotation of the whole robot about its vertical axis. Hence the global configuration vector reads

$$\mathbf{q} = \begin{bmatrix} \mathbf{q}_{\text{ori}} \\ \theta^1 \\ \theta^2 \\ \theta^3 \end{bmatrix}_{27 \times 1} \quad (5.241)$$

The wheel rotation is captured by the following augmented constraint equations

$$\phi_{\text{aug}}^i = \mathbf{d}_3^i \cdot \mathbf{e}_3 + \mathbf{d}_3^i \cdot (\mathbf{d}_2^i \times \mathbf{e}_3) + \sin \theta^i - \cos \theta^i \quad \text{with } i = 1, 2 \quad (5.242)$$

The rotation of the whole robot unit about its vertical axis can be expressed as

$$\Phi_{\text{aug}}^3 = \mathbf{d}_2^2 \cdot \mathbf{e}_1 + \mathbf{d}_2^2 \cdot \mathbf{e}_2 + \sin \theta^2 - \cos \theta^2 \quad (5.243)$$

To sum up, we have $n = 27$ redundant coordinates, along with three augmented values $m_{\text{aug}} = 3$, $m_{\text{int}} = 12$ internal constraint equations, $m_h = 4$ holonomic constraints (realizing a revolute connection between the wheels) as well as $m_k = 6$ kinematic constraints. This finally leads to $n - m_{\text{aug}} - m_{\text{int}} - m_h - m_k = 2$ DOF. Comparable to Section 5.5.3, we can formulate the nonholonomic constraints. Again we have to find the contact points of the wheels with the plane. The procedure equals the steps of stating the velocity of the contact point of the ball in Section 5.5.3, therefore we similarly obtain

$$\mathbf{v}_c^i = \mathbf{v}_\varphi^i + \sum_{I=1}^3 \bar{X}_I^i \mathbf{d}_I^i \quad \text{for both wheels } i = 1, 2 \quad (5.244)$$

where \bar{X}_I^i relies on the same expression as stated in the foregoing example

$$\sum_{I=1}^3 \bar{X}_I^i \mathbf{d}_I^i = -R\mathbf{e}_3 \quad (5.245)$$

here R is the radius of the wheels. Accordingly,

$$\bar{X}_I^i = -R\mathbf{e}_3 \cdot \mathbf{d}_I^i \quad (5.246)$$

for $I = 1, 2, 3$ and $i = 1, 2$. We enforce the velocity at the contact point of both wheels to be zero, hence these kinematic constraints can again be written as

$$\mathbf{A}(\mathbf{q})\mathbf{v} = \mathbf{0} \quad (5.247)$$

The global constraint Jacobian for the nonholonomic constraints yields for this example

$$\mathbf{A}(\mathbf{q}) = \begin{bmatrix} \mathbf{I} & -R\mathbf{e}_3 \cdot \mathbf{d}_1^1 & -R\mathbf{e}_3 \cdot \mathbf{d}_2^1 & -R\mathbf{e}_3 \cdot \mathbf{d}_3^1 & \mathbf{0}_{3 \times 12} & \mathbf{0}_{3 \times 3} \\ \mathbf{0}_{3 \times 12} & \mathbf{I} & -R\mathbf{e}_3 \cdot \mathbf{d}_1^2 & -R\mathbf{e}_3 \cdot \mathbf{d}_2^2 & -R\mathbf{e}_3 \cdot \mathbf{d}_3^2 & \mathbf{0}_{3 \times 3} \end{bmatrix} \quad (5.248)$$

Discrete formulation

In complete analogy to Section 5.5.3 we obtain the discrete counterparts of the expressions above. First we express the material coordinates of the contact point

$$\tilde{\mathbf{X}}^i(\mathbf{q}_{n+1}, \mathbf{q}_n) = \begin{bmatrix} \tilde{X}_1^i \\ \tilde{X}_2^i \\ \tilde{X}_3^i \end{bmatrix} = -R\mathbf{\Lambda}^i(\mathbf{q}_{n+1/2})^{-1}\mathbf{e}_3 \quad (5.249)$$

where we state

$$\mathbf{\Lambda}^i(\mathbf{q}_{n+1/2}) = [\mathbf{d}_1^i \quad \mathbf{d}_2^i \quad \mathbf{d}_3^i]_{n+1/2} \quad (5.250)$$

for both wheels $i = 1, 2$. The discrete constraint Jacobian of the kinematic constraints can be written as

$$\mathbf{A}(\mathbf{q}_{n+1}, \mathbf{q}_n) = \begin{bmatrix} \mathbf{I}_{3 \times 3} & \tilde{\mathbf{X}}_1^1 \mathbf{I}_{3 \times 3} & \tilde{\mathbf{X}}_2^1 \mathbf{I}_{3 \times 3} & \tilde{\mathbf{X}}_3^1 \mathbf{I}_{3 \times 3} & \mathbf{0}_{3 \times 12} & \mathbf{0}_{3 \times 3} \\ \mathbf{0}_{3 \times 12} & \mathbf{I}_{3 \times 3} & \tilde{\mathbf{X}}_1^2 \mathbf{I}_{3 \times 3} & \tilde{\mathbf{X}}_2^2 \mathbf{I}_{3 \times 3} & \tilde{\mathbf{X}}_3^2 \mathbf{I}_{3 \times 3} & \mathbf{0}_{3 \times 3} \end{bmatrix} \quad (5.251)$$

Control of the two wheeled robot

The task is to let the robot follow a certain path. In this case we want the robot to follow the contour of our institute logo (NM). Since the system at hand has two degrees of freedom, we prescribe the motion of the two wheels (θ^1 and θ^2), while the third angle is only measuring the turning of the system. The imposed control constraints according to Section 5.3 read

$$\gamma(t) = \begin{bmatrix} s^1(t) \\ s^2(t) \end{bmatrix} \quad (5.252)$$

where we use again a smooth 9th order polynomial proposed by Blajer [30] to prescribe the segmented motion. This polynomial in general yields

$$s^i(t) = s_0 + \left[126 \left(\frac{t}{t_f - t_0} \right)^5 - 420 \left(\frac{t}{t_f - t_0} \right)^6 + 540 \left(\frac{t}{t_f - t_0} \right)^7 - 315 \left(\frac{t}{t_f - t_0} \right)^8 + 70 \left(\frac{t}{t_f - t_0} \right)^9 \right] (s_f - s_0) \quad (5.253)$$

here s_0 marks the initial value at the initial time t_0 , accordingly s_f and t_f label the final values. In this connection we can let the robot move in eleven segments in time in order to draw the desired contour. The complete control constraints can be written as

$$\mathbf{0} = \begin{bmatrix} \theta^1 \\ \theta^2 \end{bmatrix} - \gamma(t) \quad (5.254)$$

The corresponding control Jacobian is again of Boolean type

$$\mathbf{B} = \begin{bmatrix} \mathbf{0}_{1 \times 24} & 1 & 0 & 0 \\ \mathbf{0}_{1 \times 24} & 0 & 1 & 0 \end{bmatrix} \quad (5.255)$$

Results

For drawing the contour of the logo, the robot needs eleven segments, comprised of driving forward and turning maneuvers. All segments are driven in time along the prescribed polynomial function. Inertial properties are summarized in Table 5.15. The initial configuration is specified by

$$\varphi^1 = \begin{bmatrix} 0 \\ 0.358 \\ 0 \end{bmatrix} \quad \text{and} \quad \varphi^2 = -\varphi^1 \quad (5.256)$$

body	\mathcal{M}	\mathcal{E}_1	\mathcal{E}_2	\mathcal{E}_3
1	0.2	0.0151	0.0151	0.0156
2	0.2	0.0151	0.0151	0.0156

Table 5.15.: Inertial properties of the two wheeled robot.

The directors \mathbf{d}_i^j of both wheels coincide with the inertial cartesian basis $\{\mathbf{e}_i\}$. The radius of the wheels is chosen to $R = 0.55$.

In the following figure we find summarized the results. Choosing a time step size of $\Delta t = 0.01$, the evolution of the prescribed angles is depicted in Fig. 5.54a. The necessary driving torques which are commonly placed in the wheels are obtained within the same simulation and are displayed in Fig. 5.54b. Finally Fig. 5.55 displays some snapshots of the motion. This example for the trajectory planning of mobile robots demonstrated the superior performance of the integration scheme along with all implemented features.

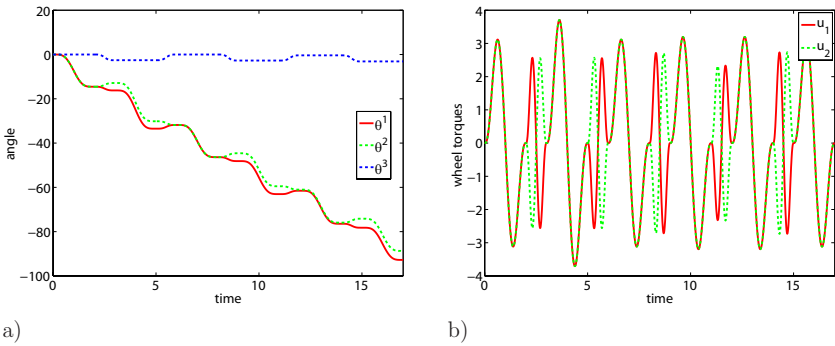


Figure 5.54.: Two wheeled robot: a) prescribed angles for the wheels, b) necessary driving torques for the desired motion.

5. Modeling Techniques



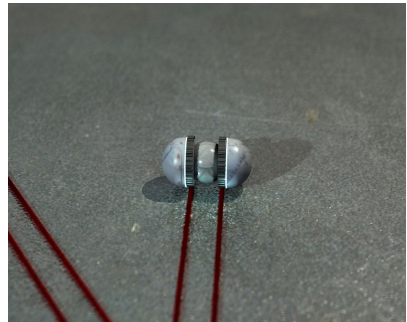
$t = 0$



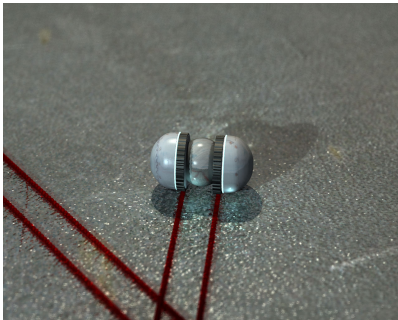
$t = 2$



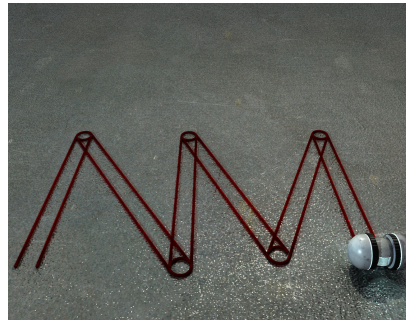
$t = 5$



$t = 8$



$t = 13$



$t = 17$

Figure 5.55.: Simulation results for the trajectory planning of the two wheeled robot.

6. Hybrid Multibody Systems

In this chapter we will deal with the coupling of rigid and flexible bodies. This will lead to a unified description for hybrid multibody systems. Modern modeling techniques demand the combination of both rigid and flexible components, in order to replicate real world behavior. Typically in up to date commercial multibody codes (e.g. MSC.ADAMS), flexibility is only captured on a linear level. That is, accounting only for small deformation and linear material behavior (modal reduction). For many practical issues, where parts undergo large deformations and where the assumption of linear elastic material behavior is not valid, one has to rely on fully discretized systems. Since for dynamic simulations, large scale finite element models of complete constructions are computationally inefficient, and since not all parts within a construction undergo the same deformation, it is common to rely on hybrid models. This procedure offers to exploit all benefits from the rigid body modeling features presented in Chapter 5. Once again for the time discretization of the flexible components we will rely on energy-momentum schemes as proposed in the rigid body sections before. These schemes perform especially well in non-linear structural dynamics (see e.g. Kuhl and Crisfield or Simo and Tarnow [89, 141]). In this connection we will recapitulate the procedure of designing a mechanical time integration scheme for non-linear structural dynamics along the lines of Betsch and Steinmann [24]. Then we will outline the coupling of rigid and flexible bodies similar to the procedure already given in [26, 98]. The new contribution of this work will be the introduction of null space matrices, which will eliminate the coupling constraints. Our examples will combine all of the modeling features outlined in Chapter 5 for rigid bodies, with flexible bodies, leading to a unified approach for hybrid multibody systems by applying a consistent time integration scheme.

The distinguishing difference of our current approach to other coupling approaches in the literature (see e.g. [54, 138, 1]) is that any arbitrary material model can be implemented in the energy-momentum framework. For this purpose thermo-visco-elastic material behavior as presented by Gross and Betsch [70, 68] could be employed. Likewise elasto-plastic material can be accommodated as well, as proposed by Mohr et al. [108, 109, 110]. In this connection Mohr et al. [111] already presented a coupling of rigid and inelastic flexible components in a consistent time integration framework.

The outline of this chapter is as follows: First we will present the flexible body formula-

tion and derive a mechanical time integration scheme for the elastic bodies. Then we will outline the coupling of both rigid and flexible components, introducing a corresponding null space matrix for the reduction by the coupling constraint Jacobian. Then we will present a basic and a reduced consistent time stepping scheme for hybrid systems. The performance will be demonstrated with some representative numerical examples.

6.1. Flexible Body Dynamics

Here we will outline the description of flexible bodies with the intention of designing an energy-momentum conserving time stepping scheme. Hence we rely on the steps given in [24] and recapitulate briefly the basic notation.

We first perform a spatial discretization applying a standard finite element method (for further details see e.g. [160, 121, 79, 78]). In the first instance we will derive the semidiscrete equations of motion in Lagrangian form.

The deformation field $\varphi : \mathcal{B} \times \mathbb{I} \mapsto \mathbb{R}^{n_{dim}}$ of a time interval $\mathbb{I} = [0, T]$ can be written in the form

$$\varphi(\mathbf{X}, t) = \sum_{A=1}^{n_{node}} N_A(\mathbf{X}) \mathbf{q}^A(t) \quad (6.1)$$

The equation above describes the motion of a material point \mathbf{X} of the body \mathcal{B} at the time t , n_{node} denotes the number of nodes. Thereby $N_A : \mathcal{B} \mapsto \mathbb{R}$ are global shape functions and \mathbf{q}^A denotes the position vector at the time $t \in \mathbb{I}$ of the nodal point A . Based on the definition (6.1) we obtain directly the discrete physical velocity

$$\mathbf{v}(\mathbf{X}, t) = \sum_{A=1}^{n_{node}} N_A(\mathbf{X}) \dot{\mathbf{q}}^A(t) \quad (6.2)$$

The deformation gradient, mapping the line elements from the reference tangent space $T\mathcal{B}_0$ to the spatial tangent space $T\mathcal{B}_t$ (see Fig. 6.1), can then be written in the form

$$\mathbf{F} = \nabla_{\mathbf{X}} \varphi(\mathbf{X}, t) = \sum_{A=1}^{n_{node}} \mathbf{q}^A \otimes \nabla N_A \quad (6.3)$$

The right Cauchy-Green tensor $\mathbf{C} = \mathbf{F}^T \mathbf{F}$ in the semi-discrete version can be expressed as

$$\mathbf{C} = \sum_{A,B=1}^{n_{node}} \mathbf{q}^A \cdot \mathbf{q}^B \nabla N_A \otimes \nabla N_B \quad (6.4)$$

We will model hyperelastic materials by using a scalar-valued strain energy function $W(\mathbf{C})$, whereby the second Piola-Kirchhoff stress tensor can be calculated via

$$\mathbf{S} = 2\nabla_{\mathbf{C}} W \quad (6.5)$$

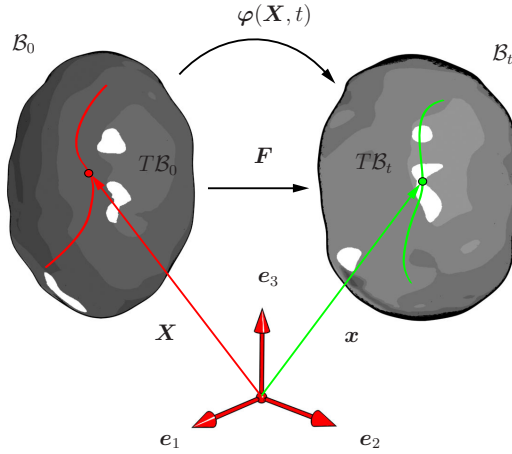


Figure 6.1.: Configurations of nonlinear continuum mechanics.

The strain energy function is then given by

$$V_{\text{int}} = \int_{\mathcal{B}} W(\mathbf{C}) dV \quad (6.6)$$

The kinetic energy of the flexible body system at a time t is governed by

$$T = \frac{1}{2} \int_{\mathcal{B}} \rho_R \mathbf{v} \cdot \mathbf{v} dV \quad (6.7)$$

Inserting Equation (6.2) into the expression above, yields the following statement

$$T = \frac{1}{2} \sum_{A,B=1}^{n_{\text{node}}} M_{AB} \dot{\mathbf{q}}^A \cdot \dot{\mathbf{q}}^B \quad \text{with} \quad M_{AB} = \int_{\mathcal{B}} \rho_R N_A N_B dV \quad (6.8)$$

Here M_{AB} are the coefficients of the mass matrix \mathbf{M} of the elastic body.

6.1.1. Semidiscrete equations of motion

Having the kinetic and potential energies at hand, we can express the Lagrangian function $L = T - V_{\text{int}}$ and thereby derive the continuous equations of motion according to

$$\dot{\mathbf{q}}^f - \mathbf{v}^f = \mathbf{0} \quad (6.9a)$$

$$\mathbf{M}^f \dot{\mathbf{v}}^f + \mathbf{F}_{\text{int}} = \mathbf{0} \quad (6.9b)$$

In this connection we mark all terms which are associated with the elastic bodies with an upper index f , this is in order to distinguish between rigid and flexible parts in the following sections.

The internal nodal forces \mathbf{F}_{int} follow directly from the potential according to

$$\mathbf{F}_{\text{int}} = \nabla_{\mathbf{q}^f} V_{\text{int}} = \int_B \frac{\partial W(\mathbf{C})}{\partial \mathbf{C}} : \frac{\partial \mathbf{C}}{\partial \mathbf{q}^f} dV \quad (6.10)$$

At this stage we omit the proof of the conservation properties, and only refer to [24] for a detailed discussion of these properties. Next, we want to present the discrete counterpart of the semidiscrete set of Equations (6.9). Thereby we aim again at the design of a mechanical time integration scheme. Similar to the equations of motion for rigid bodies, outlined in Chapter 3, the material law affects the internal force \mathbf{F}_{int} in the discrete setting and needs to be evaluated appropriately in order to obtain mechanical conservation properties.

6.1.2. Discrete equations of motion

In the first instance we apply the general mid-point rule to discretize the set of ODEs in (6.9), this leads to

$$\mathbf{q}_{n+1}^f - \mathbf{q}_n^f = \frac{\Delta t}{2} (\mathbf{v}_{n+1} + \mathbf{v}_n) \quad (6.11a)$$

$$\mathbf{M}^f \left(\mathbf{v}_{n+1}^f - \mathbf{v}_n^f \right) + \Delta t \bar{\mathbf{F}}_{\text{int}} = \mathbf{0} \quad (6.11b)$$

Similar to Section 5.4 a mid-point evaluation of \mathbf{F}_{int} does not yield conservation properties in general. To this end, following the lines of [24, 58, 61], in the most general case of an arbitrary material model (associated with a corresponding strain energy function) the time integration of \mathbf{F}_{int} will be done by applying the discrete gradient method (marked as \bullet) in the equations above). For this purpose we write the discrete internal load vector as

$$\bar{\mathbf{F}}_{\text{int}} = \int_B \bar{\nabla} W(\mathbf{C}_n, \mathbf{C}_{n+1}) : \frac{\partial \mathbf{C}(\mathbf{q}_{n+1/2}^f)}{\partial \mathbf{q}_{n+1/2}^f} dV \quad (6.12)$$

Here we need to replace $\nabla W(\mathbf{C})$ by its discrete version, guaranteeing the conservation of total energy and angular momentum (see also [24])

$$\bar{\nabla} W(\mathbf{C}_{n+1}, \mathbf{C}_n) = \nabla W \left(\mathbf{C} \left(\frac{1}{2} \right) \right) + \frac{W(\mathbf{C}_2) - W(\mathbf{C}_1) - \nabla W(\mathbf{C}(\frac{1}{2})) : [\mathbf{C}_2 - \mathbf{C}_1]}{\|\mathbf{C}_2 - \mathbf{C}_1\|^2} [\mathbf{C}_2 - \mathbf{C}_1] \quad (6.13)$$

The examples in the subsequent sections will rely on the St. Venant-Kirchhoff material model. Its strain energy density function is given by

$$W(\mathbf{C}) = \frac{1}{2} \mathbf{E} : \mathbb{D} : \mathbf{E} \quad \text{with} \quad \mathbf{E} = \frac{1}{2} [\mathbf{C} - \mathbf{I}] \quad (6.14)$$

Here \mathbf{E} denotes the Green-Lagrange strain tensor and \mathbb{D} the fourth-order elasticity tensor. The elasticity tensor is comprised of the Lamé parameters Λ and μ . These can be directly derived from the Young's modulus E and the Poisson's ratio ν according to

$$\Lambda = \frac{E\nu}{(1+\nu)(1-2\nu)} \quad \text{and} \quad \mu = \frac{E}{2+2\nu} \quad (6.15)$$

For the St. Venant-Kirchhoff material model, the augmented formulation in Equation (6.13) is equivalent to the energy-momentum difference method of Simo and Tarnow [141]. The time approximation of the internal force then yields

$$\bar{\mathbf{F}}_{\text{int}}^A = \sum_{B=1}^{n_{\text{node}}} \mathbf{q}^B \left(\frac{1}{2} \right) \int_B \nabla N_A \otimes \nabla N_B : \mathbb{D} : \frac{1}{2} [\mathbf{E}_1 + \mathbf{E}_2] \, dV \quad (6.16)$$

where $\mathbf{E}_I = [\mathbf{C}_I - \mathbf{I}] / 2$ with $I = 1, 2$. The St. Venant-Kirchhoff material model represents an exception and breaks down to the formulation above to obtain the desired conservation properties. For general material laws, such as the Ogden material, the enhanced evaluation of Equation (6.13) must be applied. In this work, we restrict ourselves to the St. Venant-Kirchhoff material. For further details concerning the implementation, by using e.g. higher order finite element methods in time we also refer to Gross [66, 71]. For a detailed proof of the conservation properties of the scheme proposed above we only refer to [24].

6.2. Coupling of Rigid and Flexible Components

In this section we will combine both the rigid body components with the flexible parts. This will be established by introducing so-called coupling constraints. To this end we

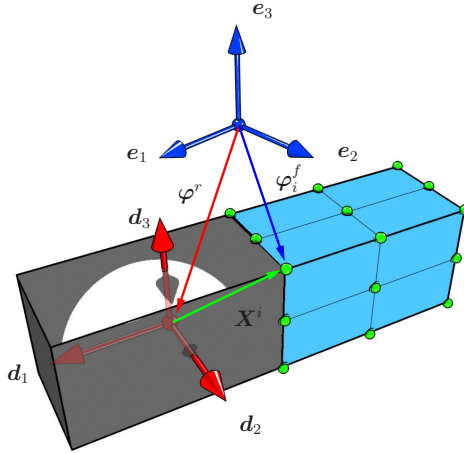


Figure 6.2.: Interpretation of coupling constraints.

close a vector loop according to Figure 6.2, connecting the rigid part \mathcal{B}^r with a representative node of the flexible component \mathcal{B}^f . In this connection we obtain a global configuration vector consisting of both rigid and flexible components

$$\mathbf{q} = \begin{bmatrix} \mathbf{q}^r \\ \mathbf{q}^f \end{bmatrix}_{(n^r+n_{dof}) \times 1} \quad (6.17)$$

Here we denote with an upper index r the rigid body presentation, n_{dof} accounts for the number of degrees of freedom of the flexible structure. Furthermore we need to extend the global mass matrix, accounting for both coupled parts

$$\mathbf{M} = \begin{bmatrix} \mathbf{M}^r & \mathbf{0} \\ \mathbf{0} & \mathbf{M}^f \end{bmatrix}_{(n^r+n_{dof}) \times (n^r+n_{dof})} \quad (6.18)$$

According to Fig. 6.2 we can formulate the following coupling constraint for an arbitrary node i by closing the vector loop

$$\Phi_{\text{coupl}}^i = \varphi^r + \sum_{I=1}^3 \mathbf{d}_I X_I^i - \varphi_i^f \quad (6.19)$$

The number of coupling constraints corresponds to the number of nodes which are situated at the connecting plane. Consequently the constraint Jacobian of the coupling

constraint above reads

$$\mathbf{G}_{\text{coupl}} = [\mathbf{I} \ X_1^i \mathbf{I} \ X_2^i \mathbf{I} \ X_3^i \mathbf{I} \ \mathbf{0} \ \dots \ -\mathbf{I} \ \dots \ \mathbf{0}]_{3 \times (n^r + n_{\text{def}})} \quad (6.20)$$

The constraint Jacobian above can be decomposed into a rigid body part and flexible body component.

$$\mathbf{G}_{\text{coupl}}^r = [\mathbf{I} \ X_1^i \mathbf{I} \ X_2^i \mathbf{I} \ X_3^i \mathbf{I}] \quad (6.21a)$$

$$\mathbf{G}_{\text{coupl}}^f = [\mathbf{0} \ \dots \ -\mathbf{I} \ \dots \ \mathbf{0}] \quad (6.21b)$$

These parts will be of interest in the subsequent section dealing with the dynamics of hybrid systems.

6.3. Dynamics of Hybrid Multibody Systems

Now, we will present the continuous and discrete equations of motion for hybrid multibody systems. Hence both components will be coupled via the coupling constraints outlined in the section before. This leads to a set of DAEs where the constraint Jacobian of the coupling constraints combines the rigid and elastic components. This leads to the following set of equations

$$\dot{\mathbf{q}} = \mathbf{v} \quad (6.22a)$$

$$\mathbf{M}^r \dot{\mathbf{v}}^r + \mathbf{f}^r + \mathbf{G}_r^T \boldsymbol{\lambda}_r + \mathbf{G}_{\text{coupl}}^r{}^T \boldsymbol{\lambda}_{\text{coupl}} = \mathbf{0} \quad (6.22b)$$

$$\boldsymbol{\Phi}_r(\mathbf{q}^r) = \mathbf{0} \quad (6.22c)$$

$$\boldsymbol{\Phi}_{\text{coupl}}(\mathbf{q}) = \mathbf{0} \quad (6.22d)$$

$$\mathbf{M}^f \dot{\mathbf{v}}^f + \mathbf{F}_{\text{int}} + \mathbf{G}_{\text{coupl}}^f{}^T \boldsymbol{\lambda}_{\text{coupl}} = \mathbf{0} \quad (6.22e)$$

Hereby $\boldsymbol{\Phi}_r(\mathbf{q}^r)$ and \mathbf{G}_r account in general for all modeling features outlined in Chapter 5. The coupling constraint Jacobians are associated with corresponding Lagrange multipliers, marked as $\boldsymbol{\lambda}_{\text{coupl}}$. The internal and external loads acting on the rigid body components are summarized in \mathbf{f}^r , similar to the expression given in Section 3.1.

In the following we will devise the discrete counterpart of the equations above. In this connection we will design an energy-momentum consistent time stepping scheme, relying on the steps presented for rigid bodies in Section 3.2 and for flexible components in

Section 6.1.2. The discrete set of DAEs yields

$$\mathbf{q}_{n+1} - \mathbf{q}_n = \frac{\Delta t}{2} (\mathbf{v}_{n+1} + \mathbf{v}_n) \quad (6.23a)$$

$$\mathbf{M}^r (\mathbf{v}_{n+1}^r - \mathbf{v}_n^r) + \Delta t [\bar{\mathbf{f}}^r + \mathbf{G}_r^T \boldsymbol{\lambda}_r + \mathbf{G}_{\text{coupl}}^{rT} \boldsymbol{\lambda}_{\text{coupl}}] = \mathbf{0} \quad (6.23b)$$

$$\boldsymbol{\Phi}_r(\mathbf{q}_{n+1}^r) = \mathbf{0} \quad (6.23c)$$

$$\boldsymbol{\Phi}_{\text{coupl}}(\mathbf{q}_{n+1}) = \mathbf{0} \quad (6.23d)$$

$$\mathbf{M}^f (\mathbf{v}_{n+1}^f - \mathbf{v}_n^f) + \Delta t [\bar{\mathbf{F}}_{\text{int}} + \mathbf{G}_{\text{coupl}}^{fT} \boldsymbol{\lambda}_{\text{coupl}}] = \mathbf{0} \quad (6.23e)$$

The formulation again relies on the discrete gradient evaluation of all terms marked with (\bullet) . Only this evaluation guarantees the construction of an energy-momentum consistent time stepping scheme. Keep in mind, that the incorporation of dissipative effects concerning the rigid body part is embedded in $\bar{\mathbf{f}}^r = \bar{\nabla}V(\mathbf{q}_{n+1}^r, \mathbf{q}_n^r) + \mathbf{Q}(\mathbf{q}_{n+1}^r, \mathbf{q}_n^r) + \mathbf{F}_{\text{int}}^{\text{alg}}$, the evaluation relies on the steps outlined in Section 5.4. The scheme above will be titled as the **Basic-Hybrid-Energy-Momentum-Consistent** scheme (**BHEMC**). In the following we will devise a reduction sequence, similar to the procedure in Section 4.1.1. In the following we will reduce the number of equations by the count of coupling constraints, rendering a reduced scheme for hybrid systems.

6.3.1. Reduction by coupling constraints

The reduction sequence for hybrid systems relies on the same steps as outlined in Section 4.1.1, based upon a velocity analysis according to [2, 18]. Therefore in the first instance we express the velocity of the connected FE-nodes as a function of the rigid body velocity. The global velocity vector of size $n \times 1$ of the complete system reads

$$\dot{\mathbf{q}} = \begin{bmatrix} \dot{\mathbf{q}}^r \\ \dot{\mathbf{q}}^f \end{bmatrix}_{(n^r+n_{\text{dof}}) \times 1} \quad (6.24)$$

The expression of the redundancy of the coupled nodes n_c in dependence of the rigid body velocity yields

$$\dot{\mathbf{q}} = \mathbb{C}_{n \times (n-n_c)} \cdot \underbrace{\begin{bmatrix} \dot{\mathbf{q}}_{n^r \times 1}^r \\ \dot{\mathbf{q}}_{(n_{\text{dof}}-n_c) \times 1}^f \end{bmatrix}}_{\mathbf{v}} \quad (6.25)$$

The upper step eliminates the coupling constraints. Additively we rely on the null space procedures presented in the rigid body section (see Chapter 4) and perform a second reduction, eliminating the constraint Jacobians associated with the rigid components.

This leads to a second null space matrix according to

$$\mathbf{v} = \mathbf{P}_{(n-n_c) \times (n-n_c-m)} \underbrace{\begin{bmatrix} \dot{\mathbf{q}}_r^{(n^r-m) \times 1} \\ \dot{\mathbf{q}}_f^{(n_{\text{dof}}-n_c) \times 1} \end{bmatrix}}_{\boldsymbol{\nu}} \quad (6.26)$$

Here m marks the number of rigid body constraints, accounting for both holonomic or nonholonomic constraints. The complete null space matrix eliminating the coupling constraints along with all rigid body constraints by following the velocity analysis reads

$$\dot{\mathbf{q}} = \underbrace{\mathbb{C} \cdot \mathbf{P}}_{\mathbb{P}_{n \times (n-n_c-m)}} \boldsymbol{\nu} \quad (6.27)$$

The discrete counterpart of the matrix above can be directly derived. Since the null space eliminating the coupling constraints is in general constant, a numerical treatment is straightforward. Concerning \mathbf{P} we refer to Chapters 4 and 5 for their discrete counterparts. So in general the complete null space matrix can be written as

$$\mathbb{P}(\mathbf{q}_{n+1}, \mathbf{q}_n) = \mathbb{C} \cdot \mathbf{P}(\mathbf{q}_{n+1}, \mathbf{q}_n) \quad (6.28)$$

Reduced scheme

Having the complete null space matrix at hand, we can again reduce the **BHEMC**-scheme in complete analogy to the **REM**-scheme outlined in Section 3.2.2. Therefore we premultiply the set of equations in (6.29) with the discrete version given in Equation (6.28) leading to

$$\mathbf{q}_{n+1} - \mathbf{q}_n = \frac{\Delta t}{2} (\mathbf{v}_{n+1} + \mathbf{v}_n) \quad (6.29a)$$

$$\mathbb{P}^T \cdot \begin{bmatrix} \mathbf{M}^r (\mathbf{v}_{n+1}^r - \mathbf{v}_n^r) + \Delta t \bar{\mathbf{f}}^r \\ \mathbf{M}^f (\mathbf{v}_{n+1}^f - \mathbf{v}_n^f) + \Delta t \bar{\mathbf{F}}_{\text{int}} \end{bmatrix} = \mathbf{0} \quad (6.29b)$$

$$\bar{\boldsymbol{\Phi}}_r(\mathbf{q}_{n+1}^r) = \mathbf{0} \quad (6.29c)$$

$$\bar{\boldsymbol{\Phi}}_{\text{coupl}}(\mathbf{q}_{n+1}) = \mathbf{0} \quad (6.29d)$$

The scheme above will again be referred to as the **Reduced-Hybrid-Energy-Momentum-Consistent** scheme, in short: the **RHEMC**-scheme. As also outlined before, a second size reduction in form of a mapping $\mathbf{F} : \mathbb{R}^{n-m} \mapsto \mathbb{Q} \subset \mathbb{R}^n$ again eliminates the constraint equations.

6.4. Numerical Examples

In this section we will demonstrate the performance of the proposed hybrid scheme with some representative examples. The first example of a 3D-helicopter rotor will demonstrate the coupling of a rigid body, namely the hub to four elastic components, representing the blades. The second example deals with a medieval trebuchet, relying on nonholonomic constraints for the modeling of the wheel to ground connection. Thereby the swing arm of the trebuchet is fully discretized with finite elements. Finally the last example combines all modeling features for rigid bodies, presented in Chapter 5, with flexible components. The system concerns the underactuated motion of a nonholonomic robot presented by Ben Horin et al. [13].

6.4.1. 3D-Helicopter rotor

Here we will investigate the free rotatory motion of a helicopter rotor. According to Fig. 6.3b the blades are modeled elastically and are connected to the hub by respective coupling constraints. The global configuration vector of the hybrid system reads

$$\mathbf{q} = \begin{bmatrix} \mathbf{q}_{12 \times 1}^r \\ \mathbf{q}_{1920 \times 1}^f \end{bmatrix} \quad (6.30)$$

The hub is modeled as a rigid body which is connected to the ground via a revolute joint. We rely on the coordinate augmentation technique in order to apply an external torque acting on the rigid body. Now, we introduce the following constraint equation, measuring the rotation angle of the rotor according to

$$\bar{\phi}_{\text{aug}} = \mathbf{d}_2 \cdot \mathbf{e}_1 + \mathbf{d}_2 \cdot \mathbf{e}_2 + \sin \theta - \cos \theta \quad (6.31)$$

With this example we would like to outline the conservation properties of the **BHEMC**-scheme. Therefore we neglect the gravitational force by setting $g = 0$ and apply an external loading in the form of Fig. 6.4 acting on the rigid body. We choose a maximum torque value of $\bar{m} = 20000$. The mass and inertia properties of the hub are summarized in Table 6.1. For the elastic parts we choose a density of $\rho = 510$ and the Lamé parameters of $\Lambda = 1 \cdot 10^7$ and $\mu = 3 \cdot 10^6$. We use $n_{\text{el}} = 228$ elements to discretize the flexible body structure. After the load disappears, the total energy as well as the angular momentum shall represent conserved quantities. For the sake of completeness we also

\mathcal{M}	\mathcal{E}_1	\mathcal{E}_2	\mathcal{E}_3
250	187.5	187.5	187.5

Table 6.1.: Inertia data for 3D rotor.

present the shape of the null space matrix \mathbb{C} eliminating the coupling constraints. As

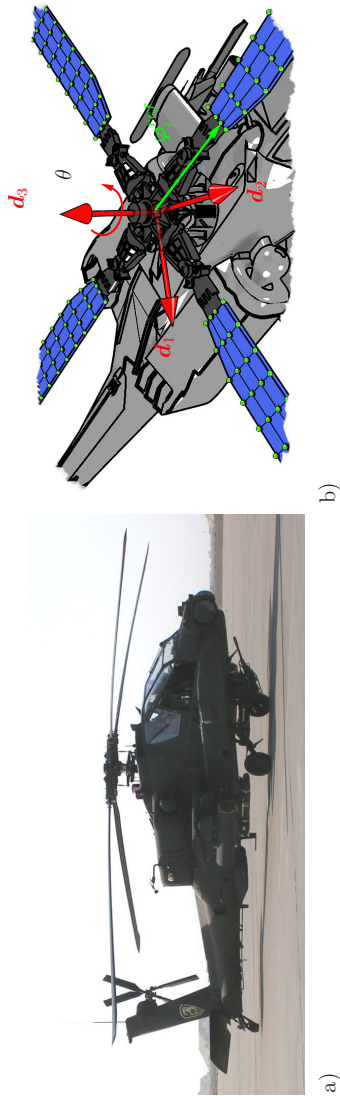


Figure 6.3: Helicopter rotor: a) real world model (www.wikipedia.org), b) mechanical model of the rotor.

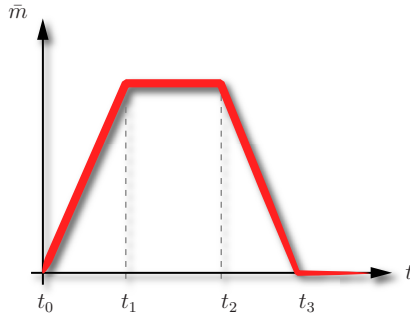


Figure 6.4.: Torque over time.

already mentioned above, the null space matrix is constant and gives the coherence of the coupled nodes $j = 1, \dots, n_{\text{node}}$ to the rigid body coordinates. At each node number, which is connected to the hub, we find the following expression embedded in the global \mathbb{C} matrix

$$\mathbb{C}^j = [\mathbf{I} \quad X_1^j \mathbf{I} \quad X_2^j \mathbf{I} \quad X_3^j \mathbf{I}] \quad (6.32)$$

The reduction matrix for the rigid body part, eliminating the internal, external and augmented constraints are given analogously, according to Chapter 5. In this connection we obtain the following external null space matrix

$$\mathbf{P}_{\text{ext}}^r = \begin{bmatrix} \mathbf{0}_{3 \times 1} \\ (\mathbf{d}_3^1)_{n+1/2} \end{bmatrix}_{6 \times 1} \quad (6.33)$$

For the elimination of the augmented constraint we obtain similar to the example of Section 5.2 the following expression

$$\mathbf{P}_{\text{aug}}^r = [\mathbf{0}_{1 \times 12} \quad \mathbb{C}] \quad (6.34)$$

with

$$\mathbb{C} = \frac{(\mathbf{e}_1^T + \mathbf{e}_2^T) \widehat{\mathbf{d}}_{2n+1/2}^1 \mathbf{d}_{3n+1/2}^1}{G_{\text{aug}}^{II}(\theta_n, \theta_{n+1})} \quad (6.35)$$

Hereby we make use of Equation (5.116) providing the expression for $G_{\text{aug}}^{II}(\theta_n, \theta_{n+1})$ in the equation above. With both reduction matrices above, we can now formulate the complete null space matrix for the rigid body component, which yields

$$\mathbf{P} = \begin{bmatrix} \mathbf{P}_{\text{int}}^r \cdot \mathbf{P}_{\text{ext}}^r \\ \mathbf{P}_{\text{aug}}^r \end{bmatrix}_{13 \times 1} \quad \text{and} \quad \mathbb{P}^r = \begin{bmatrix} \mathbf{P}_{13 \times 1} & \mathbf{0}_{13 \times 1824} \\ \mathbf{0}_{1824 \times 1} & \mathbf{I}_{1824 \times 1824} \end{bmatrix} \quad (6.36)$$

The global null space matrix, reducing the system by $n_c + m$ -equations can be formulated as

$$\mathbb{P} = \mathbb{C} \cdot \mathbb{P}^r \quad (6.37)$$

The simulation results are displayed in Figure 6.5. On the left hand side we see the conservation of the total energy. As already stated above, once the external load vanishes (after three time units), the total energy as well as the third component of the angular momentum (see Fig. 6.5b) represent conserved quantities. Also displayed in Fig. 6.5a the strain energy, reflecting the elasticity of the blades. Additionally Fig. 6.6a renders the evolution of the augmented angle and its time derivative, the angular velocity. In Fig. 6.6b find displayed the fulfillment of the coupling constraints. The time step size for the simulation was chosen to $\Delta t = 0.02$. Eventually Fig. 6.7 shows some snapshots of the motion at different times t , notice that the displayed helicopter is not part of the simulation, it only emphasizes the potential of the visualization, as will be outlined in Chapter 7.

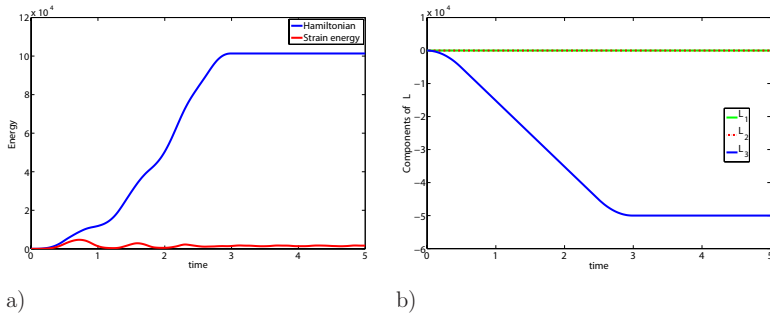


Figure 6.5.: Conservation properties of the rotor: a) total energy and strain energy, b) evolution of angular momentum.

6.4.2. Medieval trebuchet

The second example deals with a more practical application. We will now investigate the motion of a medieval trebuchet. The trebuchet as displayed in Fig. 6.8a was originally invented in China between the fifth and third centuries B.C. (see [42]) and reached the Mediterranean by the sixth century C.E.. The trebuchet is a war machine used mainly in sieges. It consists basically of six components. To be transportable the trebuchet is mounted on four wheels. The main part is the frame to which the swing arm is

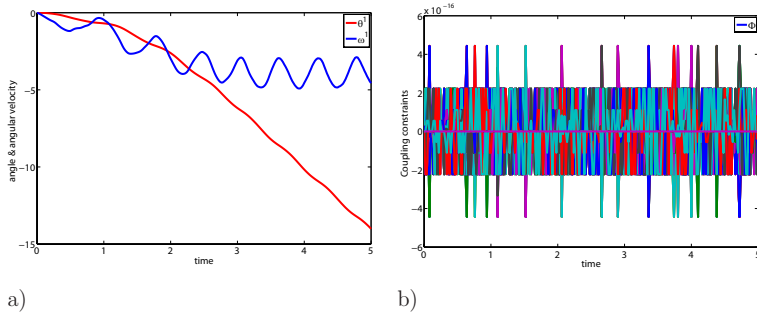


Figure 6.6.: 3D-helicopter rotor: a) evolution of the augmented coordinate, b) fulfillment of coupling constraints.

attached. The projectile which is commonly connected by a rope to the swing arm is being accelerated by a counter weight. In contrast to the catapult, which is basically a mechanization of the bow, the trebuchet relies on gravity or direct human power to be fired. Now, we will focus again on our hybrid energy momentum schemes and the rotationless formulation to generate a mechanical model of the trebuchet. For reasons of simplicity we will create a 2D-model of the war machine. Our mechanical model will consist of seven rigid bodies (see Fig. 6.8b), namely the two wheels (bodies 1 and 2), the frame (body 3), two parts of the swing arm (body 4 and 6), the counter weight (body 5) and finally the missile (body 7). A main part of the swing arm will be fully discretized, rendering the flexibility of this part, see Fig. 6.8b. In this connection we use $n_{\text{nel}} = 45$ four-node elements in two dimensional space to perform the discretization. This leads to the following configuration vector of the hybrid system

$$\mathbf{q} = \begin{bmatrix} \mathbf{q}_{42 \times 1}^r \\ \mathbf{q}_{128 \times 1}^f \end{bmatrix} \quad (6.38)$$

All rigid components of the model are combined via revolute joints. The wheels are connected to the ground by respective nonholonomic constraints¹. The nonholonomic constraints can be written as

$$\mathbf{A}(\mathbf{q}^r) \mathbf{v}^r = \mathbf{0} \quad \text{with} \quad \mathbf{A}(\mathbf{q}^r) = [\mathbf{I} \quad -r\mathbf{e}_2^T \mathbf{d}_1^i \mathbf{I} \quad -r\mathbf{e}_2^T \mathbf{d}_2^i \mathbf{I}] \quad (6.39)$$

where $i = 1, 2$ and r being the radius of the wheels. A discrete counterpart can be obtained by following the lines of Section 5.5.

¹In the 2D-case these constraints can be shown to be holonomic, however they can be treated as nonholonomic constraints and will also be implemented as kinematic constraints.

 $t = 0$  $t = 1$  $t = 2$  $t = 3$  $t = 4$  $t = 5$

Figure 6.7.: Snapshots of the 3D-rotor at different times.

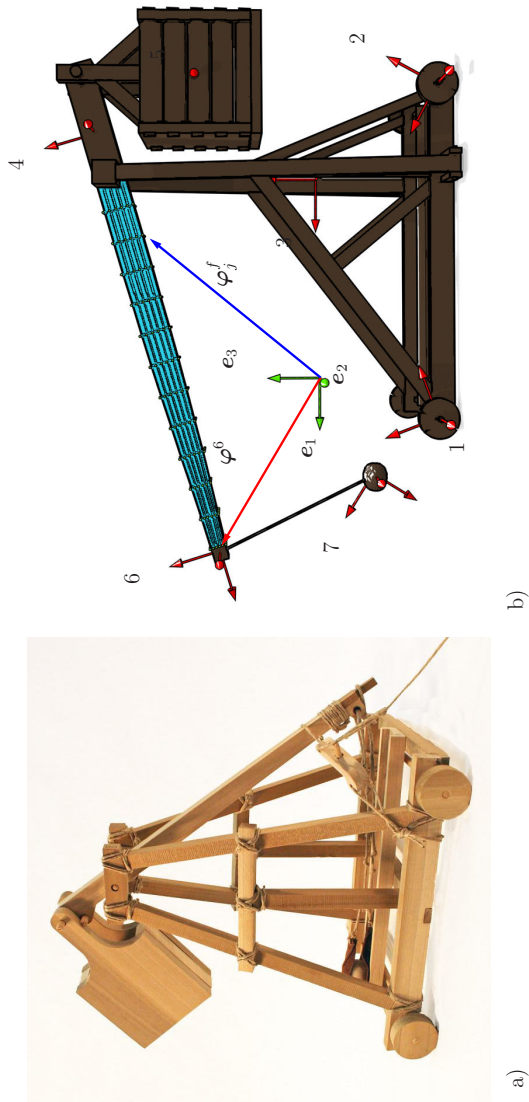


Figure 6.8.: Medieval trebuchet: a) real world model (www.trebuchet.com), b) mechanical model of the war machine.

The second point of interest is the modeling of the missile. According to Fig. 6.8 the mass first slides inside a guide, then it swings up and is finally released (typically this is performed via a sling) once a certain angle is reached (in this case we choose 45° , since it is well known to guarantee the longest distance). To realize this motion, we rely on position dependent constraints which are turned off once certain events occur:

- Sliding on the guide: $\Phi = \varphi_y^7$ if $\varphi_x^7 > \varphi_x^1$
- Release the projectile: if $\frac{\mathbf{v}^7}{\|\mathbf{v}^7\|} \cdot \begin{bmatrix} \cos \frac{\pi}{4} \\ \sin \frac{\pi}{4} \end{bmatrix} \geq 1$

Once the condition of the first statement is not met, the constraint is released, hence the constraint forces vanish. The second statement checks for the release of the projectile. Once the velocity vector of the missile and the \mathbf{e}_1 -axis comprise an angle of 45° , the connection is deactivated. In this sense the number of unknowns is decreasing.

For the rigid body components we choose the mass and inertia properties summarized in Table 6.2. The flexible body relies again on the St. Venant-Kirchhoff material model,

body	\mathcal{M}	\mathcal{E}_1	\mathcal{E}_2
1	173.65	10.85	10.85
2	173.65	10.85	10.85
3	1886.7	10062.5	157.22
4	737	9596.3	61.4
5	30000	22500	2500
6	400	51.2	51.2
7	58.96	0.78	4.9

Table 6.2.: Mass and inertia data for the trebuchet.

we choose the Lamé parameters to be $\Lambda = 2.88 \cdot 10^8$ and $\mu = 1.92 \cdot 10^8$ with a density of $\rho = 737$. For the simulation we choose a time step size of $\Delta t = 0.02$.

Starting from rest, the system is moving under the action of gravity. Hence the total system energy shall represent a conserved quantity. This is reproduced by the hybrid time stepping scheme as displayed in Fig. 6.9. The path of the missile is depicted in Fig. 6.10a while the fulfillment of the coupling constraints is again given in Fig. 6.10b. Obviously the hybrid energy momentum scheme yields a stable and robust performance.

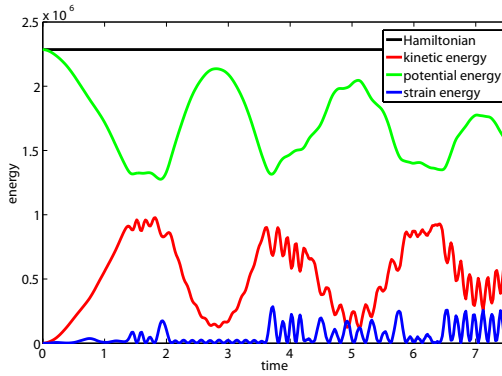
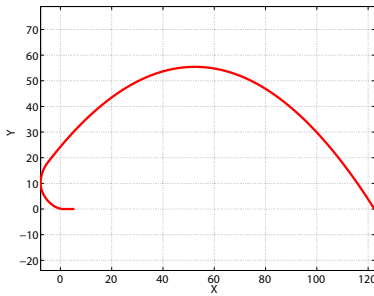
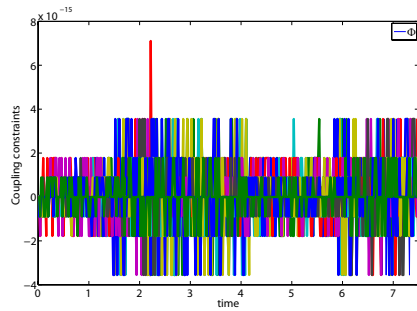


Figure 6.9.: Conservation properties of the trebuchet.



a)



b)

Figure 6.10.: Medieval trebuchet: a) path of the missile, b) fulfillment of coupling constraints.

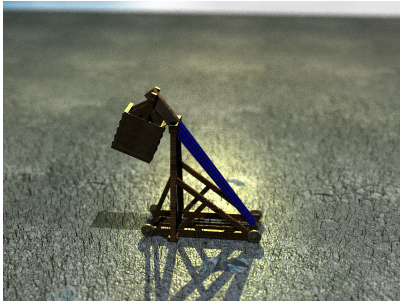
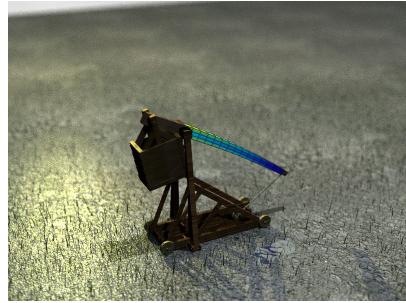
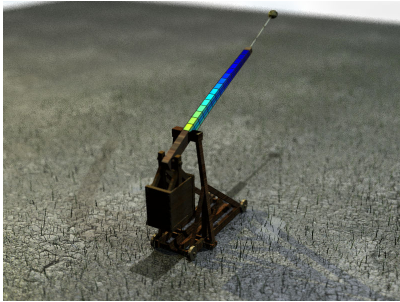
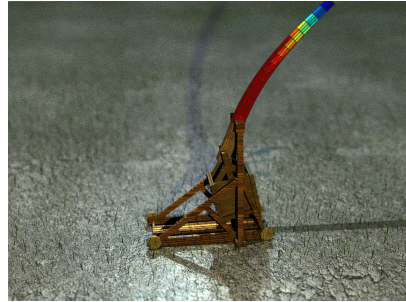
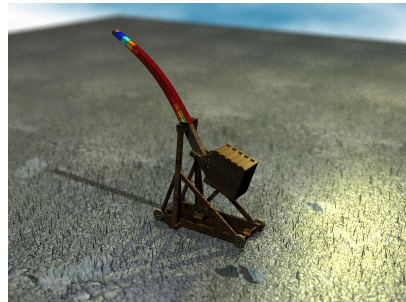
 $t = 0$  $t = 0.6$  $t = 1.2$  $t = 3.7$  $t = 4.5$  $t = 7.1$

Figure 6.11.: Medieval trebuchet: snapshots of the motion.

6.4.3. Nonholonomic manipulator

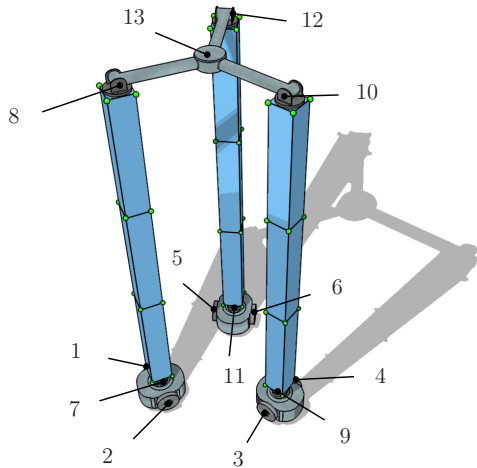


Figure 6.12.: Schematics of the nonholonomic manipulator.

The last example of this section will combine all of the modeling techniques for rigid bodies, outlined in Chapter 5, with flexible body dynamics, leading to a unified approach for hybrid multibody dynamics. The system of interest was proposed by Ben Horin et al. [13] and deals with the motion of a nonholonomic spatial robot as depicted in Fig. 6.12. Obviously the system at hand consists of 13 rigid bodies. The legs will be modeled as elastic parts, discretized via spatial 8-node finite elements. In this case we choose $n_{nel} = 9$. The purpose of the example at hand is to let the whole system perform an underactuated movement. Underactuated, because the number of inputs is less than the total number of DOF. In the real world application, as well as in our numerical example, we will actuate the wheels in order to steer the system. Commonly this is performed via electric motors which are situated in the wheel axis. For this purpose we again rely on the coordinate augmentation technique to incorporate the rotation angle of each wheel, similarly to the example in Section 5.5.4. Additionally we will also afflict some joints with friction, as outlined in Section 5.4. For this purpose we will rely on the enhanced joint plasticity model presented in Section 5.4.9. Hence we will apply all modeling techniques for rigid bodies, namely the coordinate augmentation, nonholonomic constraints to model the wheel connection to the ground, control constraints will be addressed to let the robot move upon a partially prescribed path and friction will be acting according

to the plasticity model in some of the joints.

First we start with the rotationless formulation for the example at hand concerning the rigid body parts. As mentioned above, the system consists of 13 rigid bodies, this leads to the following original configuration vector

$$\mathbf{q}_{\text{ori}}^r = \begin{bmatrix} \mathbf{q}^1 \\ \vdots \\ \mathbf{q}^{13} \end{bmatrix}_{156 \times 1} \quad (6.40)$$

For the control purpose we need to augment the rotation angle of each wheel, this leads to six additional values, accompanied with a corresponding constraint equation. Additionally we want joint friction to be acting in the revolute connection between bodies 8 and 13, 10 and 13 and finally 12 and 13. For this purpose we also augment the relative rotation of these joints. So finally concerning the rigid components we obtain the following configuration vector

$$\mathbf{q}^r = [\mathbf{q}_{\text{ori}}^{rT} \ \Theta^1 \ \Theta^2 \ \Theta^3 \ \Theta^4 \ \Theta^5 \ \Theta^6 \ \Theta^7 \ \Theta^8 \ \Theta^9]_{165 \times 1}^T \quad (6.41)$$

To summarize, Θ^j where $j = 1, \dots, 6$ are measuring the wheel rotation, while Θ^k with $k = 7, 8, 9$ concerns the relative joint angle of the friction afflicted revolute joints. For the sake of completeness we will now outline the constraint equations for the augmented coordinates. Starting with the wheel rotation, we refer to Section 5.5.4 and recapitulate

$$\phi_{\text{aug}}^i = \mathbf{d}_3^i \cdot \mathbf{e}_3 + \mathbf{d}_3^i \cdot (\mathbf{d}_2^i \times \mathbf{e}_3) + \sin \Theta^i - \cos \Theta^i \quad \text{with } i = 1, 2, 3, 4, 5, 6 \quad (6.42)$$

The augmented angles in the revolute connection of bodies 8, 10 and 12 with the platform 13 are measured via the following constraints

$$\phi_{\text{rev}}^1 = \mathbf{d}_3^8 \cdot \mathbf{d}_2^{13} + \mathbf{d}_3^8 \cdot \mathbf{d}_3^{13} + \sin \Theta^7 - \cos \Theta^7 \quad (6.43a)$$

$$\phi_{\text{rev}}^2 = \mathbf{d}_3^{10} \cdot \mathbf{d}_1^{13} \cos\left(\frac{\pi}{6}\right) + \mathbf{d}_3^{10} \cdot \mathbf{d}_2^{13} \sin\left(\frac{\pi}{6}\right) + \mathbf{d}_3^{10} \cdot \mathbf{d}_3^{13} + \sin \Theta^8 - \cos \Theta^8 \quad (6.43b)$$

$$\phi_{\text{rev}}^3 = \mathbf{d}_3^{12} \cdot \mathbf{d}_1^{13} \cos\left(\frac{\pi}{6}\right) - \mathbf{d}_3^{12} \cdot \mathbf{d}_2^{13} \sin\left(\frac{\pi}{6}\right) + \mathbf{d}_3^{12} \cdot \mathbf{d}_3^{13} + \sin \Theta^9 - \cos \Theta^9 \quad (6.43c)$$

Additionally we summarize the mass and inertia properties of the rigid components in Table 6.3. For the control problem we will actuate all six wheels and for this purpose prescribe the rotation of the wheels. In this connection we obtain the following control constraints

$$\Phi_c = \begin{bmatrix} \Theta^1 \\ \Theta^2 \\ \Theta^3 \\ \Theta^4 \\ \Theta^5 \\ \Theta^6 \end{bmatrix} - \gamma(t) \quad \text{with} \quad \gamma(t) = \begin{bmatrix} s^1(t) \\ s^2(t) \\ s^3(t) \\ s^4(t) \\ s^5(t) \\ s^6(t) \end{bmatrix} \quad (6.44)$$

body	\mathcal{M}	\mathcal{E}_1	\mathcal{E}_2	\mathcal{E}_3
1	2.25	0.0014	0.0014	0.0015
2	2.25	0.0014	0.0014	0.0015
3	2.25	0.0014	0.0014	0.0015
4	2.25	0.0014	0.0014	0.0015
5	2.25	0.0014	0.0014	0.0015
6	2.25	0.0014	0.0014	0.0015
7	0.2	0.0001	0.0001	0.0003
8	0.2	0.0001	0.0001	0.0002
9	0.2	0.0001	0.0001	0.0003
10	0.2	0.0001	0.0001	0.0002
11	0.2	0.0001	0.0001	0.0003
12	0.2	0.0001	0.0001	0.0002
13	1.7	0.038	0.038	0.038

Table 6.3.: Mass and inertia data for the nonholonomic manipulator.

Once again we rely on the 9th order polynomial (see Equation (5.253)) to impose the motion. In this case we specifically choose

$$s^i(t) = \begin{cases} s_1^i(t) & \text{if } t \leq 0.5 \\ s_2^i(t) & \text{else} \end{cases} \quad (6.45)$$

Here $s_j^i(t)$ is the polynomial proposed by Blajer [30]. Hereby we distinguish between the initial time and position values. These values are given by

$$\begin{aligned} t_0^1 &= 0, & s_0^1 &= 0, & t_f^1 &= 0.5, & s_f^1 &= \frac{\pi}{1.1} \\ t_0^2 &= 0.5 & s_0^2 &= s_f^1, & t_f^2 &= 2.5 & s_f^2 &= 24 & s_f^3 &= 27 \end{aligned}$$

For the second polynomial we have two final values for the rotation. This is due to the fact that the inner wheel ($i = 1, 3, 6$) performs a different number of rotations than the outer wheel ($i = 2, 4, 5$) of each cart. The prescribed motion above can be interpreted as follows: in the first 0.5 time units, all carts are turned by an angle. After this time, the carts move due to the different angles of rotation on a curve. The constraint Jacobian for the control constraints is again of Boolean type and yields

$$\mathbf{B} = [\mathbf{0}_{6 \times 156} \quad \mathbf{I}_{6 \times 6} \quad \mathbf{0}_{6 \times 3}] \quad (6.46)$$

Concerning the modeling of joint friction, we apply as already mentioned above the enhanced plasticity model to the augmented angles Θ^7 , Θ^8 and Θ^9 . For the example at hand we choose the following parameters for the friction model: $E = 20000$, $F_{\max} = 10$ and $d = 10$.

For the connection of the wheels to the ground we choose kinematic constraints. Since for the modeling the two wheeled robot of Section 5.5.4 serves as reference, we refer to this section for a recapitulation of the constraint equations and their numerical treatment.

The elastic parts are discretized in space using 8-node elements, in this case we use a comparatively coarse mesh with $n_{\text{nel}} = 9$ elements. Therefore the global configuration vector is again extended by

$$\mathbf{q} = \begin{bmatrix} \mathbf{q}_{165 \times 1}^r \\ \mathbf{q}_{144 \times 1}^f \end{bmatrix}_{309 \times 1} \quad (6.47)$$

We rely again on the St. Venant-Kirchhoff material model. The Lamé parameters are chosen to $\Lambda = 1.3 \cdot 10^6$ and $\mu = 32000$, with a material density of $\rho = 110$. For the simulation the step size is chosen to $\Delta t = 0.01$, keep in mind that gravity is also acting on the system.

In this simulation we are mainly interested in the necessary driving torques of the wheels

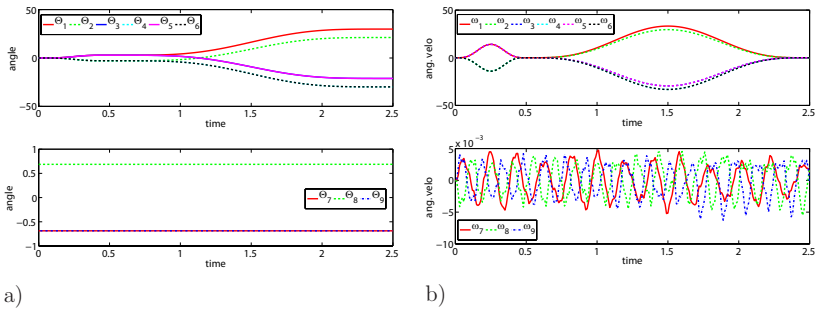


Figure 6.13.: Nonholonomic manipulator: a) evolution of the augmented angles, b) angular velocity of the augmented values.

which perform the desired motion, in this case also accounting for the flexibility of the links. Fig. 6.16 shows some snapshots of the motion, which is important in order to interpret the results. Obviously the manipulator is starting from its initial configuration, then in the first instance $t \leq 0.5$ the carts are turned. After this time the whole system is turning until it comes to rest, i.e. after $t = 2.5$.

Find displayed in Fig. 6.13a the evolution of the augmented angles. In the upper part of Fig. 6.13a we see the wheel angles, while the lower part displays the evolution of the angles of the revolute joints, where dissipation is acting. Obviously due to active joint friction, the relative angles seem to rest. Yet Fig. 6.13b reveals that these joints

are moving, thereby energy dissipates due to the chosen friction model. The figure displays the time derivative of the augmented coordinates, namely the angular velocity. We find summarized in Fig. 6.14a all energy components of the system at hand. Since we perform a controlled movement, the total energy does not represent a conserved quantity. We see additionally the evolution of the strain energy, reflecting the flexibility of the links. The driving torques which are necessary to let the system move upon the desired trajectory are depicted in Fig. 6.15. Obviously the flexibility of the links influences the characteristics of the torques, superposed we see some oscillations in the curves. Finally we find the evolution of the vertical displacement of the 13th body (Fig. 6.14b). This renders again the flexibility of the system, the platform is moving globally down, while being superposed by the flexible body oscillations.

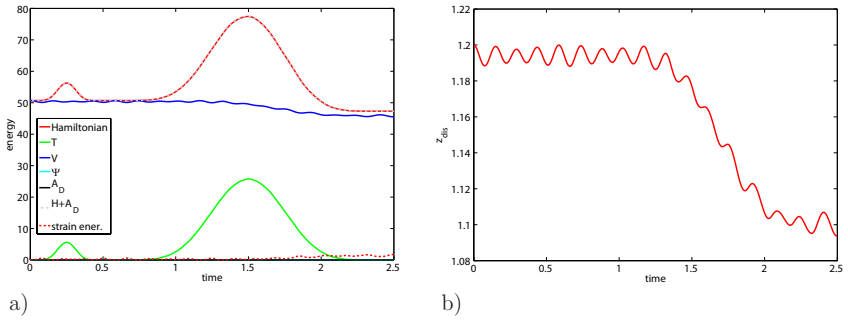


Figure 6.14.: Nonholonomic manipulator: a) energy components, b) vertical displacement of the platform (body 13).

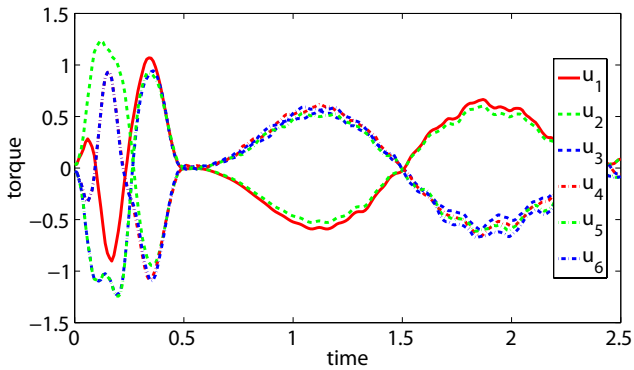
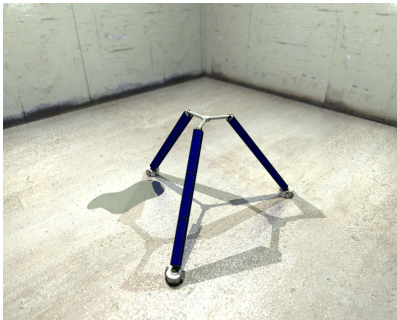
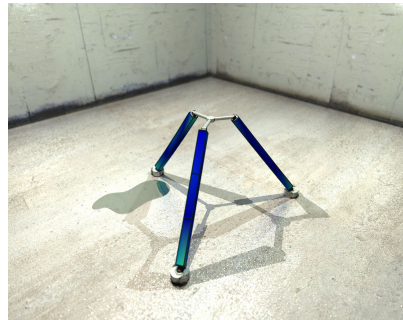


Figure 6.15.: Nonholonomic manipulator: Necessary driving torques of the wheels for the prescribed motion.

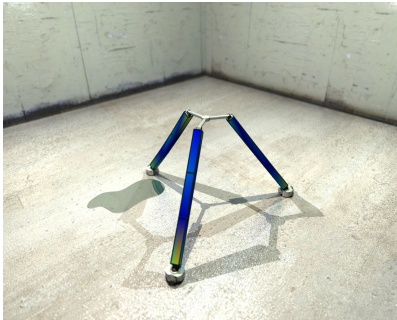
6. Hybrid Multibody Systems



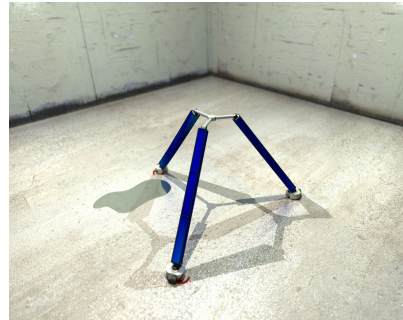
$t = 0$



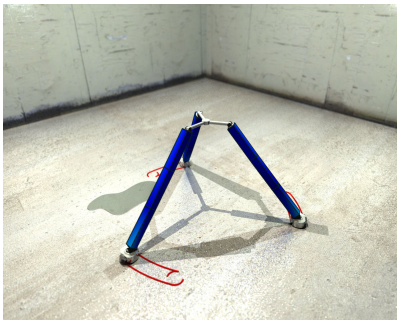
$t = 0.25$



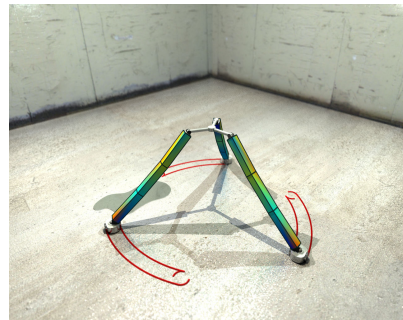
$t = 0.5$



$t = 1$



$t = 1.5$



$t = 2.5$

Figure 6.16.: Snapshots of the motion at different times t . The red traces mark the contact points of the wheels with the ground.

7. Visualization Approach for Hybrid Multibody Systems

This chapter is dedicated to the visualization process of hybrid multibody systems. In this connection we will present an approach of a photo-realistic representation of the results obtained in the chapters before.

In recent years the visualization of results in the field of computational mechanics has gained an increasing importance. Most of all in the field of computational fluid dynamics (CFD) modern visualization techniques have been developed to display computational data. For the understanding of a physical system, visualization plays a crucial role, it gives insight into the physical modeling and very often reveals implementation mistakes. In the past eight years the computer games industry has also made progress in the field of real time simulation. In these applications the process is inverted. Starting from a visualization (computer games) the implementation of so called physical engines (physics based computations) elevated in their importance. Nowadays the application of a physics engine has become a standard. Many companies are skilled in developing real time multibody codes which can be implemented in computer games (see e.g. Havok: www.havok.com, pixelux: www.pixeluxentertainment.com or Naturalmotion Ltd: www.naturalmotion.com).

Driven by these ideas, we will outline the visualization of the results obtained by our state of the art integration schemes for hybrid systems. Hence our visualization approach can be viewed as a pure post-processing step, since the implicit schemes outlined in Chapter 3 have not been implemented in a real time setting. Especially for presentation purpose, the procedure of obtaining computer generated images (CGI) is worth the effort, as presented with the examples within this thesis.

We will proceed as follows: first we will outline the description of rigid body rotations based upon quaternions, since in computer graphics this is the most common coordinate presentation (see e.g. [74]). In doing so, we will outline the connection of the rotationless formulation from Chapter 4 to the quaternion rotation. Then we will present some tools which will help to design rigid bodies and present the image generation with the open source renderer POV-Ray (see www.povray.org).

7.1. Visualization of Rigid Bodies

7.1.1. Direction Cosine vs. Quaternions

Since the rotation of rigid bodies in the rendering tools is performed via quaternion rotation, we need to transfer our data of the rotationless formulation to this specific kinematic. Therefore we will shortly outline the quaternion / Euler-parameter representation in the following.

Euler-Parameter, Quaternions

Quaternions firstly introduced by Lord Hamilton in 1843 [73], are especially well suited for the description of rotations and are widely spread in computer animation programs. Similarly to Section 4, the rigid body motion can be decomposed into a translational as well as a rotational part. The rotational part shall now be treated by Euler-parameters. All basic notation can also be found in [116, 117, 157, 22].

Obviously Euler-Parameters have the advantage of imposing only one constraint equation, since the rotation can be expressed by a vector \mathbf{u} , marking the axis of rotation and a corresponding angle of rotation Θ (see Figure 7.1). In order to describe the rotation,

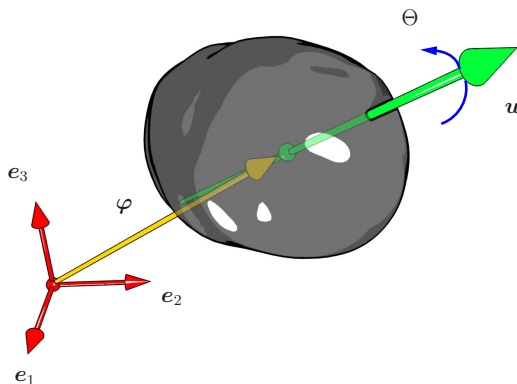


Figure 7.1.: Rigid body motion – Euler parameters.

we rely on the rotation tensor \mathbf{R} which can be derived, after performing some kinematic considerations, to (see also [2])

$$\mathbf{R}(\Theta, \mathbf{u}) = \mathbf{u} \otimes \mathbf{u} + \cos \Theta (\mathbf{I} - \mathbf{u} \otimes \mathbf{u}) + \sin \Theta \hat{\mathbf{u}} \quad (7.1)$$

with $\hat{\mathbf{u}}$ being the skew-symmetric cross-product matrix as outlined in Section 4.1.1. The rotation tensor \mathbf{R} is directly connected to the direction cosine formulation outlined in Chapter 4, via

$$\mathbf{d}_i(t) = \mathbf{R}(t)\mathbf{e}_i \quad (7.2)$$

The rotation tensor can be expressed as

$$\mathbf{R} = \mathbf{d}_i \otimes \mathbf{e}_i \quad (7.3)$$

By the introduction of the Euler-Rodrigues-Parameters

$$\mathbf{e} = \mathbf{u} \sin \frac{\Theta}{2} \quad (7.4a)$$

$$e_0 = \cos \frac{\Theta}{2} \quad (7.4b)$$

we can rewrite the expression in Equation (7.1) according to

$$\mathbf{R}(e_0, \mathbf{e}) = (e_0^2 - \mathbf{e} \cdot \mathbf{e})\mathbf{I} + 2\mathbf{e} \otimes \mathbf{e} + 2e_0\hat{\mathbf{e}} \quad (7.5)$$

Obviously the application of Euler-parameters yields four parameters to prescribe rigid body motion. This leads to an additive constraint equation. The vector of unknowns yields

$$\mathbf{p} = [e_0 \quad \mathbf{e}^T]^T \quad (7.6)$$

The constraint equation which has to be fulfilled yields

$$\cos^2 \Theta + \sin^2 \Theta - 1 = 0 \quad (7.7a)$$

$$e_0^2 + \mathbf{e} \cdot \mathbf{e} - 1 = 0 \quad (7.7b)$$

$$\mathbf{p} \cdot \mathbf{p} - 1 = \Phi_{\text{int}} \quad (7.7c)$$

Extraction of quaternions from the rotationless formulation

Since the rendering software, which we will use in the following to visualize the results, relies on quaternion rotation we need to convert our data from the rotationless formulation to Euler-parameters. In this connection we will follow the lines of Géradin and Cardona [54] and extract from the rotationless formulation the rotatory data for the visualization.

We obtain the rotation tensor from the rotationless formulation (see also Section 4.1)

$$\mathbf{R} = [\mathbf{d}_1 \quad \mathbf{d}_2 \quad \mathbf{d}_3] = \begin{bmatrix} r_{11} & r_{12} & r_{13} \\ r_{21} & r_{22} & r_{23} \\ r_{31} & r_{32} & r_{33} \end{bmatrix} \quad (7.8)$$

The extraction of the axis of rotation \mathbf{u} and the rotation angle Θ can be facilitated according to [144], proposing the following algorithm:

First construct a symmetric 4×4 matrix

$$\mathbf{S} = \begin{bmatrix} 1 + r_{11} + r_{22} + r_{33} & r_{32} - r_{23} & r_{13} - r_{31} & r_{21} - r_{12} \\ r_{32} - r_{23} & 1 + r_{11} - r_{22} - r_{33} & r_{12} + r_{21} & r_{13} + r_{31} \\ r_{13} - r_{31} & r_{21} + r_{12} & 1 - r_{11} + r_{22} - r_{33} & r_{23} + r_{32} \\ r_{21} - r_{12} & r_{13} + r_{31} & r_{23} + r_{32} & 1 - r_{11} - r_{22} + r_{33} \end{bmatrix} \quad (7.9)$$

Since \mathbf{S} is a quadratic expression of Euler parameters, we obtain these values according to

$$e_0 = \frac{1}{2}\sqrt{S_{11}} \quad e_1 = \frac{1}{2}\sqrt{S_{22}} \quad e_2 = \frac{1}{2}\sqrt{S_{33}} \quad e_3 = \frac{1}{2}\sqrt{S_{44}} \quad (7.10)$$

Having the Euler parameters at hand, we refer to Equations (7.4) and extract the rotation axis and angle

$$e_0 = \cos\left(\frac{\Theta}{2}\right) \quad \Rightarrow \quad \Theta = 2 \cos^{-1}(e_0) \quad (7.11a)$$

$$\mathbf{e} = \mathbf{u} \sin\left(\frac{\Theta}{2}\right) \quad \Rightarrow \quad \mathbf{u} = \mathbf{e} \sin^{-1}\left(\frac{\Theta}{2}\right) \quad (7.11b)$$

7.1.2. Modeling steps

In this section we will present the visualization of the motion of a free flying rigid body. Thereby we will outline how to import calculated data to the freeware renderer POV-Ray. The general procedure can be divided into the following phases

- Modeling of the rigid body¹
- Convert the geometry to the *.pov*-format²
- Load calculated data to POV-Ray
- Rotate object according to the quaternion rotation data
- Translate object according to data
- Render scene

¹Any commercial or non commercial tool can be used, e.g. 3Ds-Max, Maya, Solid-Works, Pro-Engineer, Moray etc..

²Depending on the modeling software used, one has to find suitable software to perform the conversion, e.g. 3D-Win (www.tb-software.com).

Since there are multiple possibilities to generate three dimensional objects, we restrict ourselves in this chapter to the generation of bodies embedded in POV-Ray. The program offers the modeling of basic objects such as spheres, cylinders, boxes etc. (for a complete overview of embedded objects, please consolidate the help files of POV-Ray). Hence we also do not emphasize the second item of the list above, since it also depends on the chosen modeling techniques. Therefore we will restrict ourselves on the process of importing calculated data into POV-Ray. For this purpose the data which will be extracted must have the following structure, according to the quaternion presentation

$$\mathbb{D}_i = [\boldsymbol{\varphi}_i^T \quad \mathbf{u}_i^T \quad \Theta_i]_{1 \times 7} \quad (7.12)$$

where $i = 1, \dots, n$ is counting the n time steps taken within the corresponding simulation. The global time data for one individual rigid body has the following shape

$$\mathbb{D}^{\text{rigid}} = \begin{bmatrix} \mathbb{D}_1 \\ \vdots \\ \mathbb{D}_n \end{bmatrix}_{n \times 7} \quad (7.13)$$

While generating the data for the angle of rotation Θ , it is important to keep in mind to rely on *deg* units, since POV-Ray works internally with degrees instead of radians. The conversion of the units can also be done in POV-Ray, since it supports mathematical operations. Having the array in Equation (7.13) at hand, we need to convert the data in a text file with the ending *.inc* according to the following format

```
#declare ARRAY_NAME=array[No. of columns][No. of rows]
{ {D[0][0], D[1][0], ..., D[6][0]},
  .,
  .,
  .,
  {D[0][n], D[1][n], ..., D[6][n]}
}
```

Here one must specify the name of the array \mathbb{D} along with its size, which is $n \times 7$. Note that the counting in POV-Ray starts always with 0. The upper array can then be directly imported in POV-Ray.

In order to load the extracted data in the format described above, we apply the following command of POV-Ray

```
#include "ARRAY_NAME.inc"
```

To access each individual entry inside the loaded array, we use the following syntax of POV-Ray:

```
#declare Var1_b1=ARRAY_NAME[clock] [0];
#declare Var2_b1=ARRAY_NAME[clock] [1];
#declare Var3_b1=ARRAY_NAME[clock] [2];
#declare Var4_b1=ARRAY_NAME[clock] [3];
#declare Var5_b1=ARRAY_NAME[clock] [4];
#declare Var6_b1=ARRAY_NAME[clock] [5];
#declare Var7_b1=ARRAY_NAME[clock] [6];
```

Thereby we have access to all parameters describing the rigid body motion. Here the variable *clock* is an internal counter of POV-Ray used for animations. In this case we use it to go through the data array, grabbing the information for different time steps. Notice again the internal counting which starts from zero. In the following, we can move any arbitrary object in POV-Ray according to the imported data-set. In order to have the quaternion rotation available in POV-Ray, we need to load a package called

```
#include "transforms.inc"
```

In this connection we first need to rotate the body about its center of mass (where the director triad is situated) and then perform a translation. Translated into the POV-Ray syntax, these operations read

```
object{ OBJECT_NAME
    Axis_Rotate_Trans(<Var4_b1,Var5_b1,Var6_b1>, Var7_b1)
    translate<Var1_b1,Var2_b1,Var3_b1>
}
```

Obviously we first address the object by calling its name, followed by the rotation command and finally placing the object translatorically.

According to the steps outlined above, we can load the data of complete rigid multibody systems. Keep in mind that during the modeling process, the global cartesian system of the modeling tool has to coincide with the director triad of the rigid body. This only guarantees a correct manipulation of the individual bodies once they are imported into the rendering software. In the following we will demonstrate the procedure with the example of a free flying rigid body.

Free flying rigid body

The numerical treatment of the free rigid body was already given in Chapter 4. The results will be captured in the data vector (Equation (7.13)). For the motion, which will be postprocessed, we choose the following parameters

$$m = 42.065, \quad \mathbf{J} = \begin{bmatrix} 8.443 & 0 & 0 \\ 0 & 0.057 & 0 \\ 0 & 0 & 8.443 \end{bmatrix}, \quad \mathbf{v} = [2 \ 0 \ 0]^T, \quad \boldsymbol{\omega} = [4 \ 2 \ 3]^T$$

Following the lines of the foregoing section we finally obtain the syntax displayed in the following

```
// LOAD PACKAGE FOR ROTATION
#include "transforms.inc"

// ADD LIGHT AND CAMERA
camera{ P_def_cam }
object{ P_def_light1 }

// LOADING DATA FROM MATLAB-----
#include "MyArray_b1.inc"
#declare Var1_b1=MyArray_b1[clock][0];
#declare Var2_b1=MyArray_b1[clock][1];
#declare Var3_b1=MyArray_b1[clock][2];
#declare Var4_b1=MyArray_b1[clock][3];
#declare Var5_b1=MyArray_b1[clock][4];
#declare Var6_b1=MyArray_b1[clock][5];
#declare Var7_b1=MyArray_b1[clock][6];
//-----

// RIGID BODY REPRESENTED BY A BOX
#declare RIGID_BODY=box{<-0.05,-0.4,-0.5>, <0.05,0.4,0.5>
                texture{
                    pigment{rgb<0.8,0.8,0.8>}
                }
            }
object{ RIGID_BODY
        Axis_Rotate_Trans(<Var4_b1,Var5_b1,Var6_b1>, Var7_b1)
        translate<Var1_b1,Var2_b1,Var3_b1>
    }
```

For the sake of simplicity, we neglected in the code above the definition of the camera and the lighting. Concerning these features, we only refer to the help manual of POV-Ray. The rendered result is displayed in Figure 7.2a.

The rendering software now allows to modify the scene arbitrarily. A background can be added, lights can be set to provide a realistic setting and textures to the objects can be attached for a more realistic presentation (for further features please visit www.povray.org or consult the manual). Figure 7.2b shows the same scene only with some features turned on. A background has been added, lighting has been adjusted and a focal blur of the camera is activated, providing the scene a more spatial impression. Bear in mind that most of the features making the scene appear photo realistic are computational

demanding.

Following the lines outlined above we can now set up whole multibody systems and provide an adequate presentation of the computational results. For the body generation in this thesis, we used a CAD-tool and a corresponding software to convert the data in POV-Ray format. Find in Section 7.3 some visualized results of examples which were not be provided in detail within the chapters before.

7.2. Visualization of Flexible Bodies

In this section we will outline the visualization of flexible bodies. In this connection we will present an approach for visualizing spatial eight node finite elements³. Thereby we will follow the procedure described in the section above and first prepare the calculated data. In a second step the data will again be transferred into POV-Ray, where we will construct the respective finite element based upon the embedded modeling features of POV-Ray.

In some applications, concerning finite element computation, the stress field also represents a sought quantity. We will also present a procedure of how to visualize the stress field in POV-Ray after the basic elements have been build.

7.2.1. Spatial 8-Node element

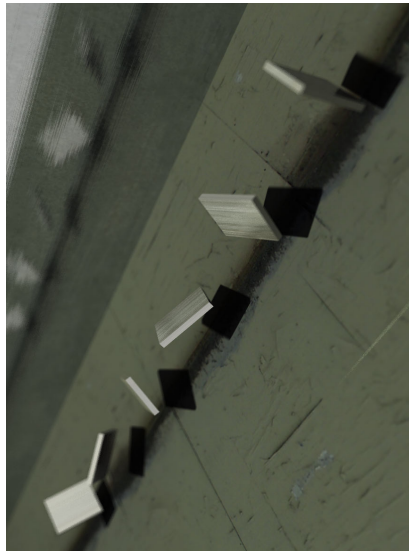
Similar to Section 7.1.2, we will need an array which extracts the necessary position data of each single node of the flexible body at all corresponding time steps. According to Fig. 7.3 we need to extract the spatial coordinates of eight nodes at all time steps. For one single element we obtain the following array in space

$$\mathbb{D}^i = [x_0^i \quad y_0^i \quad z_0^i \quad \cdots \quad x_7^i \quad y_7^i \quad z_7^i]_{1 \times 24} \quad (7.14)$$

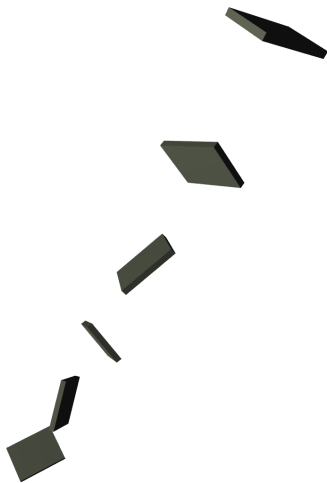
where $i \in \{1, 2, \dots, nel\}$ denotes the element number and x_j^i , y_j^i and z_j^i represent the coordinates of a node $j \in \{1, 2, \dots, 3 \cdot nel\}$. The position data of a system consisting of multiple finite elements at an arbitrary time t_i can be summarized in the following array

$$\mathbb{D}_{t_i} = \begin{bmatrix} \mathbb{D}^1 \\ \vdots \\ \mathbb{D}^{nel} \end{bmatrix}_{nel \times 24} \quad (7.15)$$

³We restrict ourselves to these elements, since we only use these type of elements throughout the thesis.



b)



a)

Figure 7.2.: Visualization of a free flying rigid body: a) standard presentation, b) more sophisticated presentation of the scene.

7. Visualization Approach for Hybrid Multibody Systems

The matrix we will import to POV-Ray for visualizing the whole flexible body containing a number of nel -elements and t_n time steps can be assembled to

$$\mathbb{D}^{\text{flex}} = \begin{bmatrix} \mathbb{D}_{t_1} \\ \vdots \\ \mathbb{D}_{t_n} \end{bmatrix}_{(nel \cdot t_n) \times 24} \quad (7.16)$$

The array above will be translated into the POV-Ray input language according to the procedure outlined in Section 7.1.2 for the extraction of the position data of the rigid body. For the visualization we need to access the position data of each single node at a

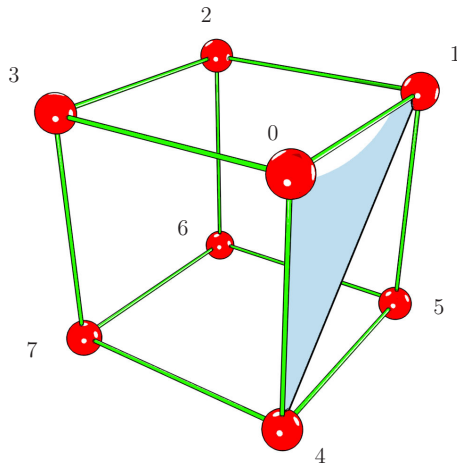


Figure 7.3.: Building an eight node spatial finite element in POV-Ray.

certain time. Therefore we declare the following variables containing the node data in POV-Ray.

```
#declare N_1 = <ARRAY_NAME[k] [0], ARRAY_NAME[k] [1], ARRAY_NAME[k] [2]>;
#declare N_2 = <ARRAY_NAME[k] [3], ARRAY_NAME[k] [4], ARRAY_NAME[k] [5]>;
#declare N_3 = <ARRAY_NAME[k] [6], ARRAY_NAME[k] [7], ARRAY_NAME[k] [8]>;
#declare N_4 = <ARRAY_NAME[k] [9], ARRAY_NAME[k] [10], ARRAY_NAME[k] [11]>;
#declare N_5 = <ARRAY_NAME[k] [12], ARRAY_NAME[k] [13], ARRAY_NAME[k] [14]>;
#declare N_6 = <ARRAY_NAME[k] [15], ARRAY_NAME[k] [16], ARRAY_NAME[k] [17]>;
#declare N_7 = <ARRAY_NAME[k] [18], ARRAY_NAME[k] [19], ARRAY_NAME[k] [20]>;
#declare N_8 = <ARRAY_NAME[k] [21], ARRAY_NAME[k] [22], ARRAY_NAME[k] [23]>;
```

Here k represents a loop index and is used to access the coordinates at all time steps. The FE-mesh will be modeled by using the *mesh2*-command of POV-Ray. According to Fig. 7.3 the mesh of a single 8-node element consists of 12 triangles. These triangles are drawn in POV-Ray by applying the *mesh2*-command, along with the definition of the corresponding vertices of each triangle. The following POV-Ray code renders a single finite element

```
// DEFINING NODES
mesh2 {vertex_vectors {8, N_1, N_2, N_3, N_4, N_5, N_6, N_7, N_8}

// BUILDING FACES
face_indices { 12,
<0,1,4>, <1,5,4>,
<0,1,4>, <1,5,4>,
<0,1,4>, <1,5,4>,
<0,1,4>, <1,5,4>,
<0,1,4>, <1,5,4>,
<0,1,4>, <1,5,4>,
<0,1,4>, <1,5,4>}

// ADDING TEXTURE TO FE-MESH
texture{pigment
  {
    color rgb <80/255, 80/255, 80/255>
  }
}
```

In addition we now want to emphasize the mesh, therefore we will draw the contours of the mesh according to the following POV-Ray command

```
# declare d=0.02
// upper side
cylinder{N_1, N_2, d, TEXTURE}
cylinder{N_1, N_4, d, TEXTURE}
cylinder{N_3, N_2, d, TEXTURE}
cylinder{N_4, N_3, d, TEXTURE}
// lower side
cylinder{N_5, N_6, d, TEXTURE}
cylinder{N_5, N_8, d, TEXTURE}
cylinder{N_7, N_6, d, TEXTURE}
cylinder{N_8, N_7, d, TEXTURE}
// right side
cylinder{N_5, N_1, d, TEXTURE}
cylinder{N_2, N_6, d, TEXTURE}
```

```
// left side
cylinder{N_3, N_7, d, TEXTURE}
cylinder{N_8, N_4, d, TEXTURE}
```

Here we draw a cylinder with a certain thickness d representing the mesh, by connecting the nodes among each other. The final result is displayed in Fig. 7.4a. Note that the procedure outlined above was presented for one single finite element with 8-nodes. For a complete FE-mesh, we need to execute the commands given above in a loop for the whole number of elements. Note that the mesh texture can be adjusted arbitrarily to present real world materials (see Fig. 7.4b).

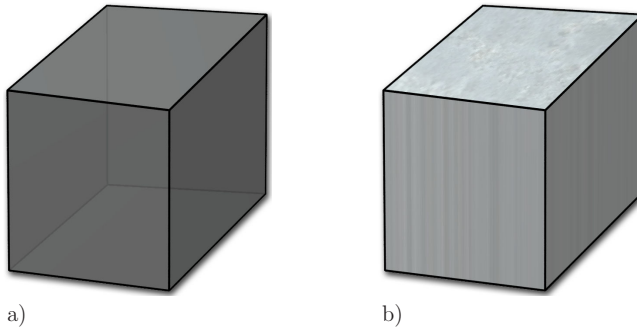


Figure 7.4.: 8-node finite element in POV-Ray: a) standard presentation, b) textured version.

7.2.2. Plotting the stress field

In some applications the stress field is also of interest. In this section we will outline a procedure in POV-Ray how to visualize the color-coded stress field of a finite element mesh. In this connection the required data is captured with the stress values at each node. The data will again be stored in an array, in this case

$$\mathbb{S}^i = [s_0^i \quad s_1^i \quad \cdots \quad s_7^i]_{1 \times 8} \quad (7.17)$$

where s_j^i represents the corresponding stress value at node j of element i . For a given number of elements nel at a time t_n obtain the array

$$\mathbb{S}_{t_n} = \begin{bmatrix} \mathbb{S}^1 \\ \vdots \\ \mathbb{S}^{nel} \end{bmatrix}_{nel \times 8} \quad (7.18)$$

The global array containing all information for each time step and for all elements yields

$$\mathbb{S} = \begin{bmatrix} \mathbb{S}_{t_1} \\ \vdots \\ \mathbb{S}_{t_n} \end{bmatrix}_{t_n \times nel \times 8} \quad (7.19)$$

The data will be included into POV-Ray in the same way as done with the rigid body and flexible body coordinates. Additively we need to load a colormap which serves as an interpreter, assigning each stress value a certain color. The colormap (labeled as CM in the code below) itself is an array containing the rgb-values of different colors in rows, while the columns provide the color-gradient. POV-Ray offers the possibility to assign each vertex of the FE-mesh a certain color. This can be done in POV-Ray by adding the following line to the code for generating the FE-mesh

```
texture_list{ 8,
texture{pigment{rgb<CM[index_1][0],CM[index_1][1],CM[index_1][2]>}}
texture{pigment{rgb<CM[index_2][0],CM[index_2][1],CM[index_2][2]>}}
texture{pigment{rgb<CM[index_3][0],CM[index_3][1],CM[index_3][2]>}}
texture{pigment{rgb<CM[index_4][0],CM[index_4][1],CM[index_4][2]>}}
texture{pigment{rgb<CM[index_5][0],CM[index_5][1],CM[index_5][2]>}}
texture{pigment{rgb<CM[index_6][0],CM[index_6][1],CM[index_6][2]>}}
texture{pigment{rgb<CM[index_7][0],CM[index_7][1],CM[index_7][2]>}}
texture{pigment{rgb<CM[index_8][0],CM[index_8][1],CM[index_8][2]>}}
}
```

The code above can be translated as follows: The colormap is accessed according to the stress value of a certain node at time t_n . Thereby `index_i` calculates, according to the following expression, the index of the colormap, hence the corresponding color

```
#if ((abs(S[k][i]))>cmax)
#declare c_i=cmax;
#else
#declare c_i=abs(STRESS[k][i]);
#end

#declare index_i=int((c_i-cmin)/(cmax-cmin)*m);
```

We make use of a linear interpolation of the color. Thereby `cmax` is a specified maximum value of the stress and `cmin` the counterpart where `m` marks the number of columns of the colormap. If the stress value exceeds `cmax`, the color for the maximal value will be addressed. Otherwise a corresponding color code will be estimated according to the linear interpolation.

Using the stress field representation, a texturing of the FE-mesh becomes dispensable. In Fig. 7.5 find a color coded representation of the stress-field applied to the single 8-node finite element.

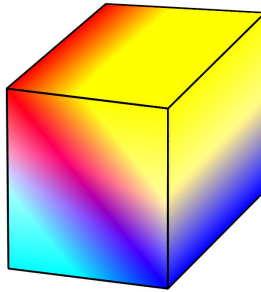


Figure 7.5.: Contour of the stress field of a 8-node finite element.

7.3. Visualization of other results obtained with EM-schemes

This section only shows some snapshots of results which were not presented in detail within the thesis. Their visualization was also performed by following the steps outlined in this chapter. The examples cover all modeling techniques and topics outlined in the thesis.

Ball inside a Cylinder

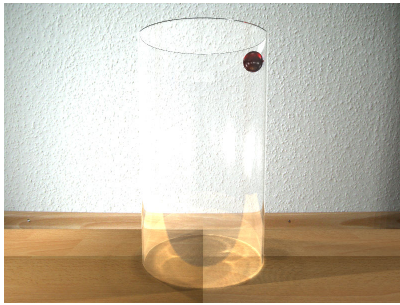
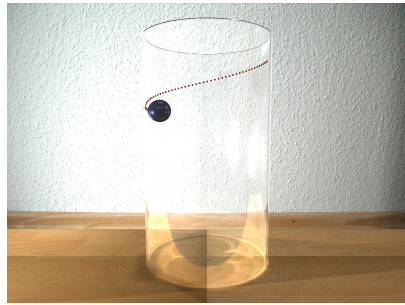
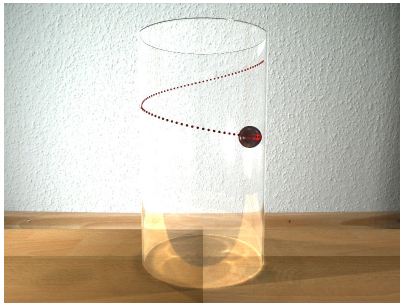
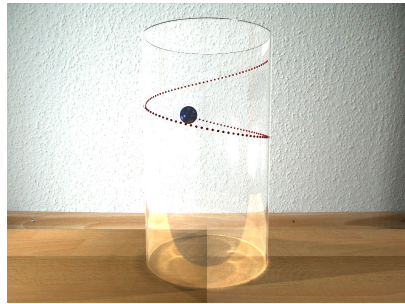
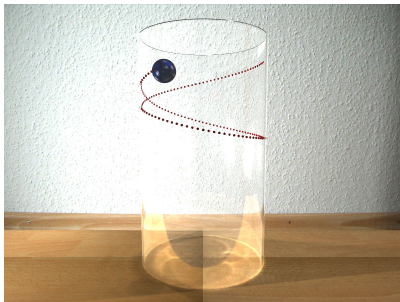
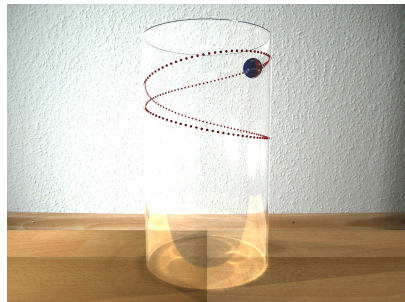
 $t = 0$  $t = 0.5$  $t = 0.8$  $t = 1.1$  $t = 1.4$  $t = 1.8$

Figure 7.6.: Ball rolling inside a cylinder, prototypical example of a nonholonomic system. The ball is moving up and down with a specific frequency.

Golfer's Dilemma



$t = 0$



$t = 0.1$



$t = 0.2$



$t = 0.3$



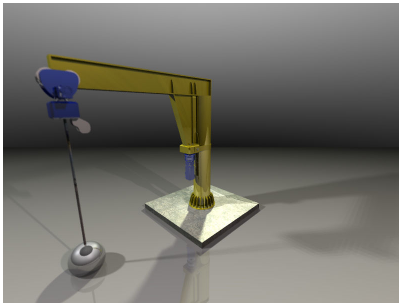
$t = 0.5$



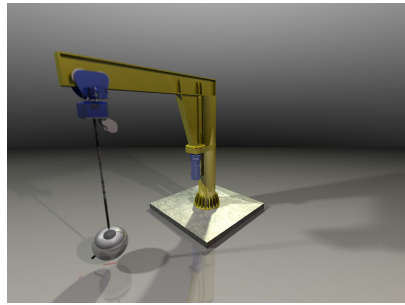
$t = 0.7$

Figure 7.7.: Golfer's dilemma, the ball leaves the hole. Application of the ball inside a cylinder phenomenon [72].

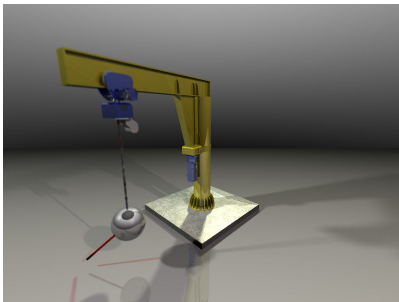
Rotary Crane



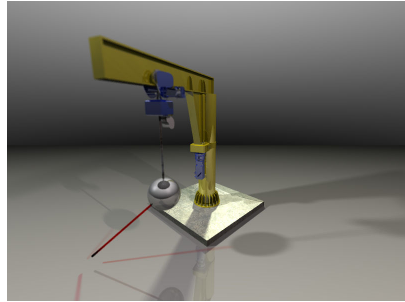
$t = 0$



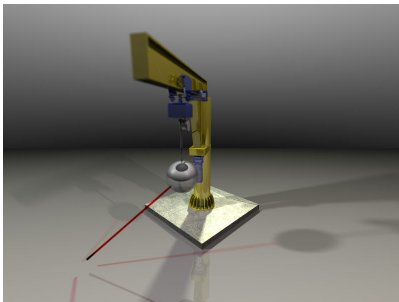
$t = 5$



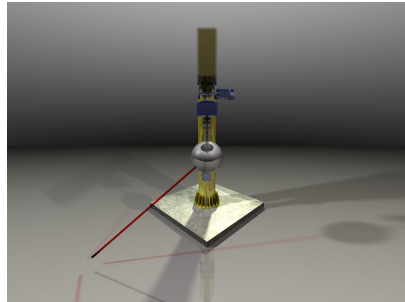
$t = 8$



$t = 12$



$t = 15$



$t = 20$

Figure 7.8.: Underactuated motion of a rotary crane also investigated in [31].

Robotic Manipulator



$t = 0$



$t = 1$



$t = 4.1$



$t = 6$



$t = 8.4$



$t = 10$

Figure 7.9.: Motion of a fully actuated robotic manipulator. Big thanks to my father for providing the 2D CAD-data and Frank Hanses for generating the corresponding 3D-model.

Wind Turbine

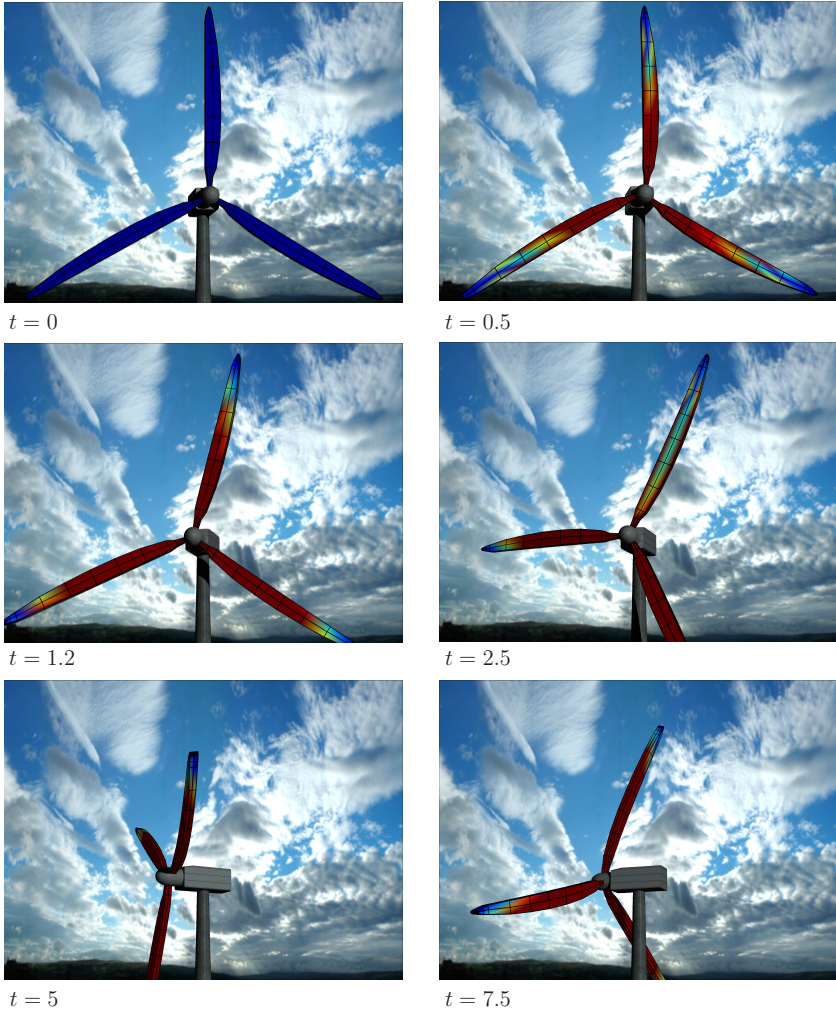


Figure 7.10.: Hybrid system of a wind turbine with elastic blades. Many thanks to Denis Anders, who obtained these results in his master thesis.

Molecular Dynamics Simulation

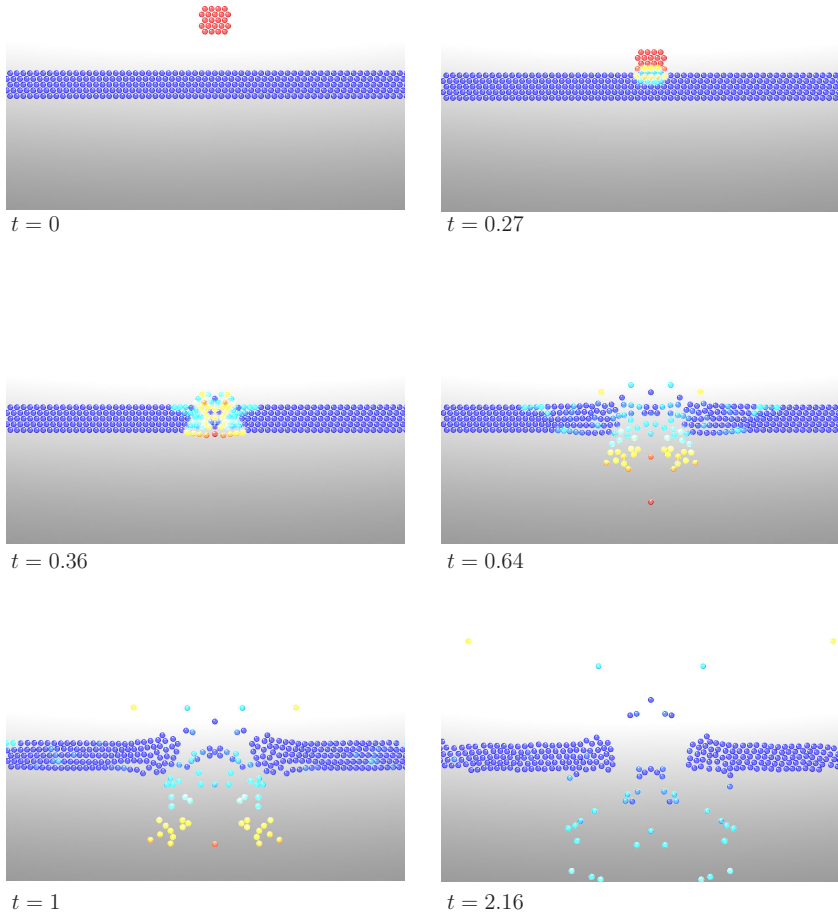


Figure 7.11.: Molecular dynamics simulation of an impact, applying an energy-momentum time integration scheme.

Celestial Mechanics

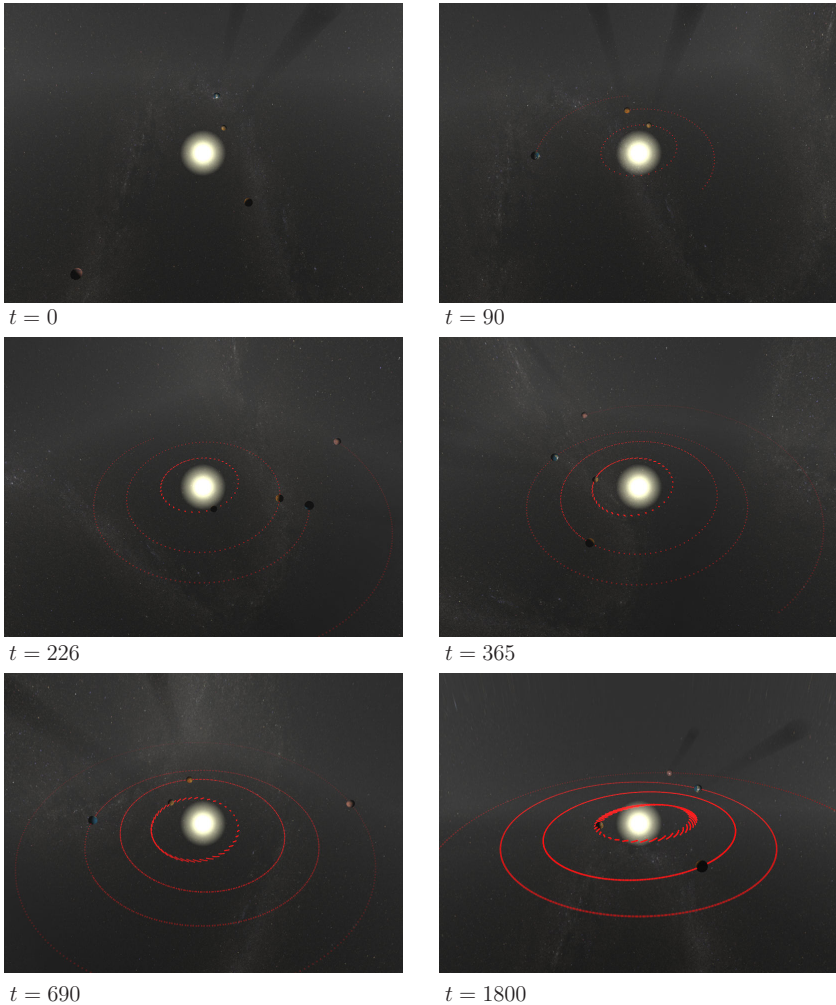
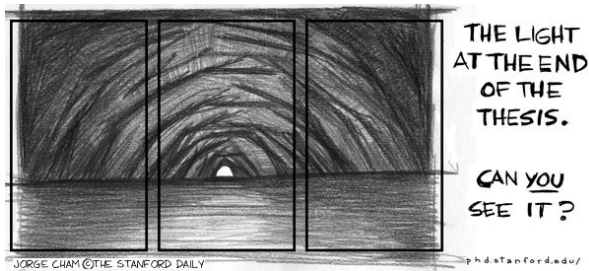


Figure 7.12.: Simulation of the motion of the first four planets of our solar system for ten years, again applying an energy-momentum consistent scheme.

8. Epilog – Conclusions



"Piled Higher and Deeper" by Jorge Cham www.phdcomics.com

The main goal of this thesis was the extension of our energy-momentum scheme for rigid bodies by specific modeling features and a final coupling with flexible structures. In this connection we will briefly summarize each modeling feature and address some future perspectives.

Rotationless Formulation: We have shown that the proposed kinematics is well-suited for the energy-momentum conserving integration of both open-loop and closed-loop multibody systems. Although the use of rotations has been completely circumvented throughout the whole discretization, torques can still be applied to a specific multibody system by resorting to the proposed coordinate augmentation technique.

Coordinate Augmentation: The augmentation technique introduced rotational DOF into the rotationless formulation mentioned above. This made possible the modeling of joint torques. Simultaneously the coordinate augmentation technique can be used to introduce any arbitrary coordinate which is needed in the modeling process. Furthermore it is worth mentioning that similar augmentation techniques are often applied in the context of multibody dynamics, see, for example, Gérardin and Cardona [54, Section 7.6.1] and Bottasso and Croce [37, Section 3.3] and the references cited in these works.

Discrete Null Space Matrices: Some numerical examples presented herein verify that

the computational effort can be significantly reduced by applying the discrete null space method [15]. This method entails a size-reduction of the discrete system and preserves the advantageous algorithmic conservation properties. The size-reduction of the algebraic system to be solved relies on (i) a properly designed discrete null space matrix and, (ii) a reparametrization of the unknowns. We have shown in Section 5.2 that explicit representations of the discrete null space matrix pertaining to closed-loop systems can be systematically designed. Moreover, we have extended the discrete null space method to accommodate the newly-proposed coordinate augmentation technique.

Control Problems: The incorporation of control constraints makes possible the treatment of inverse dynamics problems within the present simulation approach. Moreover, joint-torques associated with relative rotations can be applied with the augmentation technique, even though the present description of multibody systems does not rely on rotational parameters. Concerning the use of control constraints in the present work attention has been confined to the standard case of rheonomic holonomic constraints. This case corresponds to the orthogonal realization of control constraints in the sense of Blajer and Kołodziejczyk [30].

Dissipative Effects: Within this contribution we presented three different approaches of how to model dissipation in an energy-consistent framework. First we started with an ad hoc approach which relied on a linear viscous joint friction, and outlined all necessary considerations to design a consistent integration scheme. More sophisticated models for joint friction were derived by relying on rheological models. In this context we presented a viscoelastic model and a plasticity-based model. We showed that these models are especially well suited for the design of consistent time stepping schemes, since they rely on thermodynamic consistent models. The second advantage is, that these models can be augmented and modified in such a way, that via parameter identification, one can adjust them according to obtained experimental data of real dissipative elements.

In this sense we obtained an energy-momentum consistent time integration scheme, which does not suffer from numerical dissipation and yields a stable and robust performance.

Nonholonomic Constraints: The rolling without slipping condition was modeled by the incorporation of kinematic constraints. We outlined a modified energy-momentum scheme which in contrast to [16] preserved the angular momentum and led to an enhanced accuracy.

Hybrid Multibody Systems: The coupling of both rigid and flexible structures was made possible by the introduction of so called coupling constraints. Due to the beneficial structure of the DAE-set the accommodation of the new constraints could be performed straightforwardly. A specific size reduction by the new coupling constraints was done by applying a discrete null space matrix. For the modeling of flexible bodies we again relied on energy-momentum consistent time stepping schemes and outlined within this thesis the basic St. Venant-Kirchhoff material model.

Future Perspectives

In this thesis we focused on second order accurate time stepping schemes. The design of higher order schemes can be carried out by following the lines of Betsch and Gross [26, 71]. In this context it would be worthwhile to check the computational costs by comparing a time step reduction with a higher index of accuracy.

The control problems which arose in this thesis could be dealt with by applying the presented **BEM-C** scheme. Yet it is known that some underactuated systems which generally consist of mixed orthogonal-tangent realizations of control constraints, demand further numerical treatment. These cases should be addressed in detail in further investigations, following the ideas of Blajer, Ast, Seifried and Betsch et al. [30, 31, 7, 136, 19, 29].

Concerning the modeling of dissipation we could only provide an introduction to rheological models which are known to be thermodynamic consistent. It would be of great interest to adjust these rheological models in such a way, that they match ‘real world’ behavior. In this connection one could think of a one dimensional rheological model of a generalized Maxwell model to capture the behavior of a car suspension, while all necessary data could be estimated via parameter identification.

We focused in this thesis on the coupling of rigid and flexible bodies. In this connection we restricted ourselves to the St. Venant-Kirchhoff material model. To obtain better results especially for modeling hyperelastic materials, one could think of an extension to Neo-Hooke or Ogden type models. Concerning material modeling, one can implement any arbitrary material model and formulate its energy-consistent time stepping scheme to fit the global framework. In this connection first works combining rigid and inelastic bodies in an energy consistent context were presented in Mohr et al. [108, 111]. Also an extension to the coupling of beam and shell-elements is conceivable as already given by Betsch and co-workers in [21, 20, 96].

Another main issue to deal with are problems of optimal control. Analogue to the works of Bottasso et al. [38, 37, 36] or Leyendecker et al. [101, 99, 100] one could think of the implementation of optimal control cost functions into our multibody scheme.

A more technical point of interest would be to set up systematically the equations of motion for complex multibody systems applying our EM-scheme. In this connection one would have to design a simulation environment where rigid bodies could be coupled by arbitrary joints, while the developed algorithm would systematically construct the constraint equations in the background. This step would represent a first approach towards a commercialization of the presented features.

Finally thinking of visualization, nowadays the computer games industry uses so called ‘physical’ engines which in real time take care of a physically meaningful motion of characters, bodies or objects in general. Typically due to the demand of being real time capable, explicit schemes dominate this field. In this connection numerical position er-

8. Epilog – Conclusions

rors are unavoidable. Since energy-momentum schemes turned out to be very robust, handling coarse step sizes while maintaining physically meaningful results, it would be worthwhile to check its application to this fashionable field.

A. Conservation Properties

This Appendix contains a verification of the conservation properties outlined in Remark 3.2.1.

A.1. Conservation of energy

If the external forces can be derived from a potential energy function and if the constraint forces are ideal, then the total energy $E = T + V$ is conserved. To verify this, scalar multiplication of (3.11)₂ by $\mathbf{v} \in T_{\mathbf{q}}\mathbf{Q}$ yields

$$\begin{aligned}
 \mathbf{v} \cdot [\mathbf{M}\dot{\mathbf{v}} - \mathbf{f} + \mathbf{G}^T\boldsymbol{\lambda}] &= 0 \\
 \mathbf{v} \cdot \mathbf{M}\dot{\mathbf{v}} - (\mathbf{Q} - \nabla V(\mathbf{q})) \cdot \mathbf{v} + \boldsymbol{\nu} \cdot (\mathbf{G}\mathbf{P})^T\boldsymbol{\lambda} &= 0 \\
 \frac{d}{dt} \left(\frac{1}{2} \mathbf{v} \cdot \mathbf{M}\mathbf{v} \right) + \nabla V(\mathbf{q}) \cdot \dot{\mathbf{q}} - \mathbf{Q} \cdot \mathbf{v} &= 0 \\
 \frac{d}{dt}(T + V) &= \mathbf{Q} \cdot \mathbf{v}
 \end{aligned} \tag{A.1}$$

where use has been made of (3.12), (3.16), (3.15), (3.28a), (3.9) and the symmetry of the mass matrix. Accordingly, in the conservative case ($\mathbf{Q} = \mathbf{0}$), the total energy is a first integral of the motion or

$$E(\mathbf{q}, \mathbf{v}) = \text{const} \tag{A.2}$$

Similarly, algorithmic conservation of energy can be shown by scalar multiplying (3.21b) by $\mathbf{v}_{n+\frac{1}{2}} = (\mathbf{v}_n + \mathbf{v}_{n+1})/2$, to get

$$\begin{aligned}
 \mathbf{v}_{n+\frac{1}{2}} \cdot [\mathbf{M}(\mathbf{v}_{n+1} - \mathbf{v}_n) - \Delta t \mathbf{f}(\mathbf{q}_n, \mathbf{q}_{n+1}) + \Delta t \mathbf{G}(\mathbf{q}_n, \mathbf{q}_{n+1})^T \bar{\boldsymbol{\lambda}}] &= 0 \\
 \frac{1}{2}(\mathbf{v}_n + \mathbf{v}_{n+1}) \cdot \mathbf{M}(\mathbf{v}_{n+1} - \mathbf{v}_n) - \Delta t (\mathbf{Q}(\mathbf{q}_n, \mathbf{q}_{n+1}) - \bar{\nabla} V(\mathbf{q}_n, \mathbf{q}_{n+1})) \cdot \mathbf{v}_{n+\frac{1}{2}} &+ \Delta t \bar{\boldsymbol{\lambda}} \cdot \mathbf{G}(\mathbf{q}_n, \mathbf{q}_{n+1}) \mathbf{v}_{n+\frac{1}{2}} = 0
 \end{aligned} \tag{A.3}$$

where use has been made of (3.22). The mid-point velocities can be written in the form

$$\mathbf{v}_{n+\frac{1}{2}} = \mathbf{P}(\mathbf{q}_n, \mathbf{q}_{n+1})\mathbf{w} \tag{A.4}$$

for some $\mathbf{w} \in \mathbb{R}^{n-m}$ (cf. [16, 18]). Inserting the last equation into (A.3) and taking into account (3.21a) along with the symmetry of the mass matrix yields

$$\frac{1}{2}(\mathbf{v}_{n+1} \cdot \mathbf{M}\mathbf{v}_{n+1} - \mathbf{v}_n \cdot \mathbf{M}\mathbf{v}_n) + \bar{\nabla}V(\mathbf{q}_n, \mathbf{q}_{n+1}) \cdot (\mathbf{q}_{n+1} - \mathbf{q}_n) + \Delta t \bar{\boldsymbol{\lambda}} \cdot \mathbf{G}(\mathbf{q}_n, \mathbf{q}_{n+1}) \mathbf{P}(\mathbf{q}_n, \mathbf{q}_{n+1}) \mathbf{w} = \mathbf{Q}(\mathbf{q}_n, \mathbf{q}_{n+1}) \cdot (\mathbf{q}_{n+1} - \mathbf{q}_n) \quad (\text{A.5})$$

or

$$T(\mathbf{v}_{n+1}) - T(\mathbf{v}_n) + V(\mathbf{q}_{n+1}) - V(\mathbf{q}_n) = \mathbf{Q}(\mathbf{q}_n, \mathbf{q}_{n+1}) \cdot (\mathbf{q}_{n+1} - \mathbf{q}_n) \quad (\text{A.6})$$

where use has been made of (3.25) and the directionality property of the discrete derivative (see Gonzalez [59]). Accordingly, in the conservative case ($\mathbf{Q} = \mathbf{0}$) the present algorithm conserves the total energy. That is

$$E(\mathbf{q}_{n+1}, \mathbf{v}_{n+1}) = E(\mathbf{q}_n, \mathbf{v}_n) \quad (\text{A.7})$$

A.2. Conservation of angular momentum

Suppose the planar multibody system under consideration consists of N bodies with associated index set $\eta_N = \{i_1, \dots, i_N\}$. Then the total angular momentum relative to the origin of the inertial frame reads (cf. [25])

$$L = \sum_{I \in \eta_N} \left(M^I \boldsymbol{\varphi}^I \cdot \mathbf{E}\mathbf{v}_{\varphi}^I + \sum_{\alpha=1}^2 E_{\alpha}^I \mathbf{d}_{\alpha}^I \cdot \mathbf{E}\mathbf{v}_{\alpha}^I \right) \quad (\text{A.8})$$

Obviously, the angular momentum is a quadratic function of the state space coordinates $(\mathbf{q}, \mathbf{v}) \in \mathbb{R}^n \times \mathbb{R}^n$. The last equation can alternatively be written as

$$L = \mathbf{P}_L^T \mathbf{P}^T \mathbf{M}\mathbf{v} \quad (\text{A.9})$$

where \mathbf{P} is the $n \times (n-m)$ null space matrix of the system and \mathbf{P}_L is an appropriate matrix of dimension $(n-m) \times 1$. For example, for the revolute pair dealt with in Section 5.1.1, we get the 4×1 matrix

$$\mathbf{P}_L = \begin{bmatrix} -\mathbf{E}\boldsymbol{\varphi}^1 \\ 1 \\ 0 \end{bmatrix} \quad (\text{A.10})$$

Similarly, for the system with tree structure treated in Section 5.2.2, we have

$$\mathbf{P}_L = \begin{bmatrix} -\mathbf{E}\boldsymbol{\varphi}^8 \\ 1 \\ 0 \\ \vdots \\ 0 \end{bmatrix} \quad (\text{A.11})$$

and for the closed-loop system with null space matrix as described in Example 5.2.1, we have

$$\mathbf{P}_L = \begin{bmatrix} -\mathbf{E}\boldsymbol{\varphi}^7 \\ 1 \\ -\mathbf{E}\boldsymbol{\varphi}^8 \\ 1 \end{bmatrix} \quad (\text{A.12})$$

Taking the derivative of (A.8) with respect to time yields

$$\dot{L} = \sum_{I \in \eta_N} \left(M^I \boldsymbol{\varphi}^I \cdot \mathbf{E} \dot{\mathbf{v}}_\varphi^I + \sum_{\alpha=1}^2 E_\alpha^I \mathbf{d}_\alpha^I \cdot \mathbf{E} \dot{\mathbf{v}}_\alpha^I \right) \quad (\text{A.13})$$

where the skew-symmetry of \mathbf{E} has been taken into account. Alternatively, the last equation can be written as

$$\begin{aligned} \dot{L} &= \mathbf{P}_L^T \mathbf{P}^T \mathbf{M} \dot{\mathbf{v}} \\ \dot{L} &= \mathbf{P}_L^T \mathbf{P}^T (\mathbf{f} - \mathbf{G}^T \boldsymbol{\lambda}) \\ \dot{L} &= \mathbf{P}_L^T \mathbf{P}^T \mathbf{f} \end{aligned} \quad (\text{A.14})$$

where use has been made of (3.11) and (3.15). Thus in the case of vanishing external loads the total angular momentum is a first integral of the motion. Similarly, in the discrete setting we get

$$\begin{aligned} L_{n+1} - L_n &= \sum_{I \in \eta_N} M^I (\boldsymbol{\varphi}_{n+1}^I \cdot \mathbf{E}(\mathbf{v}_\varphi^I)_{n+1} - \boldsymbol{\varphi}_n^I \cdot \mathbf{E}(\mathbf{v}_\varphi^I)_n) \\ &\quad + \sum_{I \in \eta_N} \sum_{\alpha=1}^2 E_\alpha^I ((\mathbf{d}_\alpha^I)_{n+1} \cdot \mathbf{E}(\mathbf{v}_\alpha^I)_{n+1} - (\mathbf{d}_\alpha^I)_n \cdot \mathbf{E}(\mathbf{v}_\alpha^I)_n) \\ L_{n+1} - L_n &= \sum_{I \in \eta_N} M^I \left(\boldsymbol{\varphi}_{n+\frac{1}{2}}^I \cdot \mathbf{E}[(\mathbf{v}_\varphi^I)_{n+1} - (\mathbf{v}_\varphi^I)_n] + [\boldsymbol{\varphi}_{n+1}^I - \boldsymbol{\varphi}_n^I] \cdot \mathbf{E}(\mathbf{v}_\varphi^I)_{n+\frac{1}{2}} \right) \\ &\quad + \sum_{I \in \eta_N} \sum_{\alpha=1}^2 E_\alpha^I \left((\mathbf{d}_\alpha^I)_{n+\frac{1}{2}} \cdot \mathbf{E}[(\mathbf{v}_\alpha^I)_{n+1} - (\mathbf{v}_\alpha^I)_n] + [(\mathbf{d}_\alpha^I)_{n+1} - (\mathbf{d}_\alpha^I)_n] \cdot \mathbf{E}(\mathbf{v}_\alpha^I)_{n+\frac{1}{2}} \right) \\ L_{n+1} - L_n &= \sum_{I \in \eta_N} \left(M^I \boldsymbol{\varphi}_{n+\frac{1}{2}}^I \cdot \mathbf{E}[(\mathbf{v}_\varphi^I)_{n+1} - (\mathbf{v}_\varphi^I)_n] + \sum_{\alpha=1}^2 E_\alpha^I (\mathbf{d}_\alpha^I)_{n+\frac{1}{2}} \cdot \mathbf{E}[(\mathbf{v}_\alpha^I)_{n+1} - (\mathbf{v}_\alpha^I)_n] \right) \end{aligned} \quad (\text{A.15})$$

where use has been made of (3.21a) and the skew-symmetry of \mathbf{E} . The last equation can also be written as

$$L_{n+1} - L_n = \mathbf{P}_L^T (\mathbf{q}_{n+\frac{1}{2}}) \mathbf{P}(\mathbf{q}_n, \mathbf{q}_{n+1})^T \mathbf{M} [\mathbf{v}_{n+1} - \mathbf{v}_n] \quad (\text{A.16})$$

With regard to (3.21b) we get

$$\begin{aligned} L_{n+1} - L_n &= \Delta t \mathbf{P}_L^T(\mathbf{q}_{n+\frac{1}{2}}) \mathbf{P}(\mathbf{q}_n, \mathbf{q}_{n+1})^T (\mathbf{f}(\mathbf{q}_n, \mathbf{q}_{n+1}) - \mathbf{G}(\mathbf{q}_n, \mathbf{q}_{n+1})^T \bar{\boldsymbol{\lambda}}) \\ L_{n+1} - L_n &= \Delta t \mathbf{P}_L^T(\mathbf{q}_{n+\frac{1}{2}}) \mathbf{P}(\mathbf{q}_n, \mathbf{q}_{n+1})^T \mathbf{f}(\mathbf{q}_n, \mathbf{q}_{n+1}) \end{aligned} \quad (\text{A.17})$$

The last equation corroborates algorithmic conservation of the total angular momentum in the absence of external loads.

A.3. Algorithmic force of a viscoelastic model with linear spring characteristic

Here we want to show that the algorithmic force of Section 5.4.3 breaks down to the common mid-point evaluation once we assume a linear spring characteristic. In this case the free energy function yields

$$\Psi(q, \alpha) = \frac{1}{2} E_\infty q^2 + \frac{1}{2} E_d (q - \alpha)^2 \quad (\text{A.18})$$

The internal force is the derivative of the free energy function with respect to q , we obtain

$$F = \partial_q \Psi = E_\infty q + E_d (q - \alpha) \quad (\text{A.19})$$

by inserting the equation above into (5.180) and simplifying we obtain

$$F_{\text{int}}^{\text{alg}}(1/2) = \frac{1}{2} E_\infty \frac{(q_2 - q_1)(q_2 + q_1)}{q_2 - q_1} + \frac{1}{2} E_d \frac{(q_2 - \alpha_2)^2 - (q_1 - \alpha_1)^2}{q_2 - q_1} + \frac{\Delta \mathcal{D}}{q_2 - q_1} \quad (\text{A.20})$$

where we replace $\Delta \mathcal{D}$ by its mid-point evaluation, leading to

$$\Delta \mathcal{D} = E_d (q_{12} - \alpha_{12}) (\alpha_2 - \alpha_1) \quad (\text{A.21})$$

inserting back into the upper equation with a few reformulations we obtain¹

$$F_{\text{int}}^{\text{alg}} = E_\infty q_{12} + E_d q_{12} + \frac{1}{2} E_d \frac{q_1 (\alpha_1 + \alpha_2) - q_2 (\alpha_1 + \alpha_2)}{q_2 - q_1} \quad (\text{A.22})$$

which finally results in

$$F_{\text{int}}^{\text{alg}} = E_\infty q_{12} + E_d q_{12} - E_d \alpha_{12} \quad (\text{A.23})$$

being identical to the classical mid-point evaluation. This means that for linear spring characteristics, the algorithmic internal force coincides with the mid-point rule.

¹Note that $(\bullet)_{12}$ marks the mid-point evaluation, while $(\bullet)_1$ and $(\bullet)_2$ stand for the evaluation at times t_{n+1} and t_n , respectively.

Bibliography

- [1] F.M.L. Amirouche. *Fundamentals of Multibody Dynamics*. Birkhäuser, 2006.
- [2] J. Angeles. *Fundamentals of robotic mechanical systems*. Springer-Verlag, 2nd edition, 2003.
- [3] F. Armero. Energy-dissipative momentum-conserving time-stepping algorithms for finite strain multiplicative plasticity. *Comput. Methods Appl. Mech. Engrg.*, 195:4862–4889, 2006.
- [4] F. Armero. Assumed strain finite element methods for conserving temporal integrations in non-linear solid dynamics. *Int. J. Numer. Methods Eng.*, 74:1795–1847, 2008.
- [5] F. Armero and I. Romero. Dissipative integration algorithms for nonlinear elastodynamics. Proceedings of the European Conference on Computational Mechanics (ECCM'99), Munich, ed. W. Wunderlich, 1999.
- [6] F. Armero and I. Romero. On the formulation of high-frequency dissipative time-stepping algorithms for nonlinear dynamics. Part II: Second-order methods. *Comput. Methods Appl. Mech. Engrg.*, 190:6783–6824, 2001.
- [7] A. Ast and P. Eberhard. Flatness-based control of parallel kinematics using multi-body systems simulation and experimental results. *Archive of Applied Mechanics*, 76(3-4):181–197, 2006.
- [8] F. Avanzini, S. Serafin, and D. Rocchesso. Modeling interactions between rubbed dry surfaces using an elasto-plastic friction model. In *Proceedings of the 5th International Conference on Digital Audio Effects*, Hamburg, Germany, September 26-28 2002.
- [9] O. Bauchau and C. Ju. Modeling friction phenomena in flexible multibody dynamics. *Comp. Meth. Appl. Mech. Engrg.*, 195:6909–6924, 2006.
- [10] O.A. Bauchau. Computational schemes for flexible nonlinear multi-body systems. *Multibody System Dynamics*, 2:169–225, 1998.
- [11] O.A. Bauchau and C.L. Bottasso. On the design of energy preserving and decaying schemes for flexible, nonlinear multi-body systems. *Comput. Methods Appl. Mech. Engrg.*, 169:61–79, 1999.

- [12] O.A. Bauchau, C.L. Bottasso, and L. Trainelli. Robust integration schemes for flexible multibody systems. *Comput. Methods Appl. Mech. Engrg.*, 192:295–420, 2003.
- [13] P. Ben Horin, S. Djerassi, M. Shoham, and R. Ben Horin. Dynamics of a six degrees-of-freedom parallel robot actuated by three two-wheel carts. *Multibody System Dynamics*, 16(2):105–121, 2006.
- [14] M. Benzi, G.H. Golub, and J. Liesen. Numerical solution of saddle point problems. *Acta Numerica*, 14:1–137, 2005.
- [15] P. Betsch. The discrete null space method for the energy consistent integration of constrained mechanical systems. Part I: Holonomic constraints. *Comput. Methods Appl. Mech. Engrg.*, 194(50-52):5159–5190, 2005.
- [16] P. Betsch. Energy-consistent numerical integration of mechanical systems with mixed holonomic and nonholonomic constraints. *Comput. Methods Appl. Mech. Engrg.*, 195:7020–7035, 2006.
- [17] P. Betsch, C. Hesch, N. Sanger, and S. Uhlar. Variational integrators and energy-momentum schemes for flexible multibody dynamics. Manuscript submitted for publication in ASME Journal of Computational and Nonlinear Dynamics, March 2009.
- [18] P. Betsch and S. Leyendecker. The discrete null space method for the energy consistent integration of constrained mechanical systems. Part II: Multibody dynamics. *Int. J. Numer. Methods Eng.*, 67(4):499–552, 2006.
- [19] P. Betsch, M. Quasem, and S. Uhlar. Numerical integration of discrete mechanical systems with mixed holonomic and control constraints. *The Journal of Mechanical Science and Technology*, vol. 23, no. 4, pp.1012-1018, 2009 volume = 23, pages = 1012-1018, year = 2009.
- [20] P. Betsch and N. Sanger. A nonlinear finite element framework for flexible multibody dynamics: Rotationless formulation and energy-momentum conserving discretization. In Carlo L. Bottasso, editor, *Multibody Dynamics: Computational Methods and Applications*, volume 12 of *Computational Methods in Applied Sciences*, pages 119–141. Springer-Verlag, 2009.
- [21] P. Betsch and N. Sanger. On the use of geometrically exact shells in a conserving framework for flexible multibody dynamics. *Accepted for publication in Comput. Methods Appl. Mech. Engrg.*, 2009, doi: 10.1016/j.cma.2009.01.016.
- [22] P. Betsch and R. Siebert. Rigid body dynamics in terms of quaternions: Hamiltonian formulation and conserving numerical integration. *Int. J. Numer. Methods Eng.*, DOI: 10.1002/nme.2586, 2009.

-
- [23] P. Betsch and P. Steinmann. Conservation properties of a time FE method. Part I: Time-stepping schemes for N-body problems. *Int. J. Numer. Methods Eng.*, 49:599–638, 2000.
- [24] P. Betsch and P. Steinmann. Conservation properties of a time FE method. Part II: Time-stepping schemes for nonlinear elastodynamics. *Int. J. Numer. Methods Eng.*, 50:1931–1955, 2001.
- [25] P. Betsch and P. Steinmann. Constrained integration of rigid body dynamics. *Comput. Methods Appl. Mech. Engrg.*, 191:467–488, 2001.
- [26] P. Betsch and P. Steinmann. Conservation properties of a time FE method. Part III: Mechanical systems with holonomic constraints. *Int. J. Numer. Methods Eng.*, 53:2271–2304, 2002.
- [27] P. Betsch and P. Steinmann. A DAE approach to flexible multibody dynamics. *Multibody System Dynamics*, 8:367–391, 2002.
- [28] P. Betsch and S. Uhlar. Energy-momentum conserving integration of multibody dynamics. *Multibody System Dynamics*, 17(4):243–289, 2007.
- [29] P. Betsch, S. Uhlar, and M. Quasem. On the incorporation of servo constraints into a rotationless formulation of flexible multibody dynamics. In C.L. Bottasso, P. Masarati, and L. Trainelli, editors, *Proceedings of the ECCOMAS Thematic Conference on Multibody Dynamics*, Politecnico di Milano, Milano, Italy, 25-28 June 2007.
- [30] W. Blajer and K. Kołodziejczyk. A geometric approach to solving problems of control constraints: Theory and a DAE framework. *Multibody System Dynamics*, 11(4):343–364, 2004.
- [31] W. Blajer and K. Kołodziejczyk. A computational framework for control design of rotary cranes. In J.M. Goicolea, J. Cuadrado, and J.C. Garcia Orden, editors, *Proceedings of ECCOMAS Thematic Conference on Advances in Computational Multibody Dynamics (CD-ROM)*, Madrid, Spain, June 21-24 2005.
- [32] A.M. Bloch. *Nonholonomic mechanics and control*. Springer-Verlag, 2003.
- [33] J. Bonet and R.D. Wood. *Nonlinear Continuum Mechanics for Finite Element Analysis*. Cambridge University Press, 1997.
- [34] M. Borri, C.L. Bottasso, and L. Trainelli. Integration of elastic multibody systems by invariant conserving/dissipating algorithms. I. Formulation. *Comput. Methods Appl. Mech. Engrg.*, 190:3669–3699, 2001.

- [35] C.L. Bottasso, M. Borri, and L. Trainelli. Integration of elastic multibody systems by invariant conserving/dissipating algorithms. II. Numerical schemes and applications. *Comput. Methods Appl. Mech. Engrg.*, 190:3701–3733, 2001.
- [36] C.L. Bottasso, C.-S. Chang, A. Croce, D. Leonello, and L. Riviello. Adaptive planning and tracking of trajectories for the simulation of maneuvers with multibody models. *Comput. Methods Appl. Mech. Engrg.*, 195:7052–7072, 2006.
- [37] C.L. Bottasso and A. Croce. Optimal control of multibody systems using an energy preserving direct transcription method. *Multibody System Dynamics*, 12(1):17–45, 2004.
- [38] C.L. Bottasso, A. Croce, L. Ghezzi, and P. Faure. On the solution of inverse dynamics and trajectory optimization problems for multibody systems. *Multibody System Dynamics*, 11(1):1–22, 2004.
- [39] B. Brank, L. Briseghella, N. Tonello, and F.B. Damjanic. On non-linear dynamics of shells: Implementation of energy-momentum conserving algorithm for a finite rotation shell model. *Int. J. Numer. Methods Eng.*, 42:409–442, 1998.
- [40] K.E. Brenan, S.L. Campbell, and L.R. Petzold. *Numerical Solution of Initial-Value Problems in Differential-Algebraic Equations*. SIAM, 2nd edition, 1996.
- [41] C. Canudas de Wit, H. Olsson, K.J. Aström, and P. Lischinsky. A new model for control of systems with friction. *IEEE Transactions on automatic control*, 40(3):419–425, 1995.
- [42] P. Chevedden, L. Eigenbrod, V. Foley, and W. Soedel. The trebuchet. *Scientific American Special Online Issue*, February, 2002.
- [43] W. Chung. *Nonholonomic Manipulators*, volume 13 of *Springer Tracts in Advanced Robotics*. Springer-Verlag, 2004.
- [44] J. Cortés. *Geometric, Control and Numerical Aspects of Nonholonomic Systems*, volume 1793 of *Lecture Notes in Mathematics*. Springer-Verlag, 2002.
- [45] M.A. Crisfield and G. Jelenić. Energy/momentum conserving time integration procedures with finite elements and large rotations. In J. Ambrósio and M. Kleiber, editors, *NATO-ARW on Comp. Aspects of Nonlin. Struct. Sys. with Large Rigid Body Motion*, pages 181–200, Pultusk, Poland, July 2-7, 2000.
- [46] N. Do, A. Ferri, and A. Bauchau. Efficient simulation of a dynamic system with LuGre friction. In *Proceedings of IDETC'05*, Long Beach, CA, USA, September 24-28 2005.
- [47] R. Featherstone. *Rigid body dynamics algorithms*. Springer-Verlag, 2008.

-
- [48] M. Fliess and S.T. Glad. An algebraic approach to linear and nonlinear control. In H.L. Trentelman and J.C. Willems, editors, *Essays on Control: Perspectives in the Theory and its Applications*, pages 223–267. Birkhäuser, Boston, 1993.
- [49] M. Fliess, J. Lévine, P. Martin, and P. Rouchon. Flatness and defect of non-linear systems: Introductory theory and examples. *Int. J. Control*, 61(6):1327–1361, 1995.
- [50] J. García de Jalón. Twenty-five years of natural coordinates. *Multibody System Dynamics*, 18(1):15–33, 2007.
- [51] J. García de Jalón and E. Bayo. *Kinematic and Dynamic Simulation of Multibody Systems: The Real-Time Challenge*. Springer-Verlag, 1994.
- [52] J. García de Jalón, J. Unda, and A. Avello. Natural coordinates for the computer analysis of multibody systems. *Comput. Methods Appl. Mech. Engrg.*, 56:309–327, 1986.
- [53] T. Geike and J. McPhee. Inverse dynamic analysis of parallel manipulators with full mobility. *Mechanism and Machine Theory*, 38:549–562, 2003.
- [54] M. Géradin and A. Cardona. *Flexible multibody dynamics: A finite element approach*. John Wiley & Sons, 2001.
- [55] P.E. Gill, W. Murray, and M.H. Wright. *Practical optimization*. Academic Press, 1981.
- [56] J.M. Goicolea and J.C. Garcia Orden. Dynamic analysis of rigid and deformable multibody systems with penalty methods and energy-momentum schemes. *Comput. Methods Appl. Mech. Engrg.*, 188:789–804, 2000.
- [57] H. Goldstein. *Klassische Mechanik*. AULA-Verlag, Wiesbaden, 11th edition, 1991.
- [58] O. Gonzalez. *Design and analysis of conserving integrators for nonlinear Hamiltonian systems with symmetry*. Phd-thesis, Stanford University, 1996.
- [59] O. Gonzalez. Time integration and discrete Hamiltonian systems. *J. Nonlinear Sci.*, 6:449–467, 1996.
- [60] O. Gonzalez. Mechanical systems subject to holonomic constraints: Differential-algebraic formulations and conservative integration. *Physica D*, 132:165–174, 1999.
- [61] O. Gonzalez. Exact energy and momentum conserving algorithms for general models in nonlinear elasticity. *Comput. Methods Appl. Mech. Engrg.*, 190:1763–1783, 2000.

- [62] O. Gonzalez and J.C. Simo. On the stability of symplectic and energy-momentum algorithms for non-linear Hamiltonian systems with symmetry. *Comput. Methods Appl. Mech. Engrg.*, 134:197–222, 1996.
- [63] B. Göttlicher and K. Schweizerhof. Analysis of flexible structures with occasionally rigid parts under transient loading. *Computers and Structures*, 83(25-26):2035–2051, 2005.
- [64] D. Greenspan. Conservative numerical methods for $\ddot{x} = f(x)$. *Journal of Computational Physics*, 56:28–41, 1984.
- [65] M. Griebel, S. Knapek, and G. Zumbusch. *Numerical Simulation in Molecular Dynamics*. Springer-Verlag, 2007.
- [66] M. Groß. *Conserving Time Integrators for Nonlinear Elastodynamics*. Phd, University of Kaiserslautern, 2004.
- [67] M. Groß. *Higher-order accurate and energy-momentum consistent discretisation of dynamic finite deformation thermo-viscoelasticity*. Habilitation thesis, University of Siegen, 2009.
- [68] M. Groß and P. Betsch. Energy-momentum consistent finite element discretisation of dynamic finite deformation isothermal viscoelasticity. Submitted for publication.
- [69] M. Groß and P. Betsch. An energy consistent hybrid space-time finite element method for nonlinear thermo-viscoelastodynamics. In M. Papadrakakis, E. Oñate, and B. Schrefler, editors, *Computational Methods for Coupled Problems in Science and Engineering II*, pages 413–416. CIMNE, Barcelona, Spain, 2007.
- [70] M. Groß and P. Betsch. On deriving higher-order and energy-momentum-consistent time-stepping-schemes for thermo-viscoelastodynamics from a new hybrid space-time Galerkin method. In C.L. Bottasso, P. Masarati, and L. Trainelli, editors, *Proceedings of the ECCOMAS Thematic Conference on Multibody Dynamics*, Politecnico di Milano, Milano, Italy, 25–28 June 2007.
- [71] M. Groß, P. Betsch, and P. Steinmann. Conservation properties of a time FE method. Part IV: Higher order energy and momentum conserving schemes. *Int. J. Numer. Methods Eng.*, 63:1849–1897, 2005.
- [72] M. Gualtieri. Golfers dilemma. *Am. J. Phys.*, 74(6), 2006.
- [73] W.R Hamilton. Lectures on quaternions. *Royal Irish academy*, 1848.
- [74] A.J. Hanson. Visualizing quaternions. In *SIGGRAPH '05: ACM SIGGRAPH 2005 Courses*, page 1, New York, NY, USA, 2005. ACM Press.

-
- [75] V. Hayward and F. Altpeter. Discrete-time elasto-plastic friction estimation. *IEEE transactions on control systems technology*, 17:DOI:10.1109/TCST.2008.2001710, 2009.
- [76] H.M. Hilber, T.J.R. Hughes, and R.L. Taylor. Improved numerical dissipation for time integration algorithms in structural dynamics. *Earthquake Engineering and Structural Dynamics*, 5:283–292, 1977.
- [77] G.A. Holzapfel. *Nonlinear solid mechanics*. John Wiley & Sons, 2000.
- [78] T.J.R. Hughes. Stability, convergence and growth and decay of energy of the average acceleration method in nonlinear structural dynamics. *Computers & Structures*, 6:313–324, 1976.
- [79] T.J.R. Hughes. *The Finite Element Method*. Prentice–Hall, New Jersey, 1987.
- [80] A. Ibrahimbegović, S. Mamouri, R.L. Taylor, and A.J. Chen. Finite element method in dynamics of flexible multibody systems: Modeling of holonomic constraints and energy conserving integration schemes. *Multibody System Dynamics*, 4(2-3):195–223, 2000.
- [81] A. Ibrahimbegović, R.L. Taylor, and H. Lim. Non-linear dynamics of flexible multibody systems. *Computers and Structures*, 81:1113–1132, 2003.
- [82] L. O. Jay and D. Negrut. Extensions of the HHT-method to differential-algebraic equations in mechanics. *Electronic Transactions on Numerical Analysis*, 26:190–208, 2007.
- [83] L. O. Jay and D. Negrut. A second order extension of the generalized-alpha method for constrained systems in mechanics. *Springer-Verlag ‘Computational Methods in Applied Sciences’ series*, 2008.
- [84] C. Kane, J.E. Marsden, and M. Ortiz. Symplectic-energy-momentum preserving variational integrators. *J. Math. Phys.*, 40:3353–3371, 1999.
- [85] C. Kane, J.E. Marsden, M. Ortiz, and M. West. Variational integrators and the newmark algorithm for conservative and dissipative mechanical systems. *Int. J. Numer. Methods Eng.*, 49:1295–1325, 2000.
- [86] W.A. Khan, V.N. Krovi, S.K. Saha, and J. Angeles. Modular and recursive kinematics and dynamics for parallel manipulators. *Multibody System Dynamics*, 14(3-4):419–455, 2005.
- [87] B. Kleuter. *Generalized Parameter Identification for Finite Viscoelasticity*. Phd-thesis, University of Kaiserslautern, 2007.

- [88] L. Kübler, P. Eberhard, and J. Geisler. Flexible multibody systems with large deformations and nonlinear structural damping using absolute nodal coordinates. *Nonlinear Dynamics*, 34:31–52.
- [89] D. Kuhl and M.A. Crisfield. Energy-conserving and decaying algorithms in nonlinear structural mechanics. *Int. J. Numer. Methods Eng.*, 45:569–599, 1999.
- [90] P. Kunkel and V. Mehrmann. *Differential-Algebraic Equations*. European Mathematical Society, 2006.
- [91] F. Kuypers. *Klassische Mechanik*. Wiley, 2003.
- [92] T.A. Laursen and G.R. Love. Improved implicit integrators for transient impact problems—geometric admissibility withing the conserving framework. *Int. J. Numer. Methods Eng.*, 53:245–274, 2002.
- [93] B. Leimkuhler and S. Reich. *Simulating Hamiltonian Dynamics*. Cambridge University Press, 2004.
- [94] A. Lew, Marsden J.E., M. Ortiz, and M. West. Variational time integrators. *Int. J. Numer. Methods Eng.*, 60:153–212, 2004.
- [95] S. Leyendecker. *Mechanical integrators for constrained dynamical systems in flexible multibody dynamics*. Phd, University of Kaiserslautern, 2006.
- [96] S. Leyendecker, P. Betsch, and P. Steinmann. The discrete null space method for the energy consistent integration of constrained mechanical systems. Part III: Flexible multibody dynamics. Accepted for publication in *Multibody System Dynamics*.
- [97] S. Leyendecker, P. Betsch, and P. Steinmann. Energy-conserving integration of constrained Hamiltonian systems - a comparison of approaches. *Computational Mechanics*, 33(3):174–185, 2004.
- [98] S. Leyendecker, P. Betsch, and P. Steinmann. The discrete null space method for the energy consistent integration of constrained mechanical systems. Part III: Flexible multibody dynamics. *Multibody System Dynamics*, 19(1-2):45–72, 2008.
- [99] S. Leyendecker, J.E. Marsden, and M. Ortiz. Variational integrators for constrained dynamical systems. *Z. Angew. Math. Mech. (ZAMM)*, 88:677–708, 2008.
- [100] S. Leyendecker, S. Ober-Blöbaum, J.E. Marsden, and M. Ortiz. Discrete mechanics and optimal control for constrained systems. *Submitted*.

-
- [101] S. Leyendecker, S. Ober-Blöbaum, J.E. Marsden, and M. Ortiz. Discrete mechanics and optimal control for constrained multibody dynamics. In *Proceedings of the 6th International Conference on Multibody Systems, Nonlinear Dynamics, and Control, ASME International Design Engineering Technical Conferences (IDETC)*, Las Vegas, Nevada, USA, September 5-7 2007.
- [102] R. Mahnken and E. Stein. Concepts and computational methods for parameter identification of inelastic material models. COMPUTATIONAL PLASTICITY, Fundamentals and Applications, D.R.J. Owen, E. Onate and E. Hinton (Eds.), CIMNE, Barcelona 1997.
- [103] J.E. Marsden and T.S. Ratiu. *Introduction to Mechanics and Symmetry*. Springer-Verlag, 1994.
- [104] J.E. Marsden and M. West. Discrete mechanics and variational integrators. *Acta Numerica*, 10:357–514, 2001.
- [105] J.J. McPhee and S.M. Redmond. Modelling multibody systems with indirect coordinates. *Comput. Methods Appl. Mech. Engrg.*, 195:6942–6957, 2006.
- [106] X.N. Meng and T.A. Laursen. Energy consistent algorithms for dynamic finite deformation plasticity. *Comput. Methods Appl. Mech. Engrg.*, 191:1639–1675, 2002.
- [107] H.R. Mohammadi Daniali, P.J. Zsombor-Murray, and J. Angeles. Singularity analysis of planar parallel manipulators. *Mechanism and Machine Theory*, 30(5):665–678, 1995.
- [108] R. Mohr. *Consistent Time-Integration of Finite Elasto-Plasto-Dynamics*. Phd-thesis, University of Kaiserslautern, 2008.
- [109] R. Mohr, A. Menzel, and P. Steinmann. A consistent time fe-method for large strain elasto-plasto-dynamics. *Comput. Methods Appl. Mech. Engrg.*, 197:3024–3044, 2008.
- [110] R. Mohr, A. Menzel, and P. Steinmann. Galerkin-based mechanical integrators for finite elastodynamics formulated in principal stretches - pitfalls and remedies. *Comput. Methods Appl. Mech. Engrg.*, 197:4444–4466, 2008.
- [111] R. Mohr, S. Uhlar, A. Menzel, and P. Steinmann. Time-fe methods for the non-linear dynamics of constrained inelastic systems. *IUTAM Bookseries*, In IUTAM Symposium on Theoretical, Modelling and Computational Aspects of Inelastic Media:275–285, 2008.
- [112] D. Negrut, R. Rampalli, G. Ottarsson, and A. Sajdak. On an implementation of the HHT method in the context of index 3 differential algebraic equations of

- multibody dynamics. *ASME Journal of Computational and Nonlinear Dynamics*, 2:73–85, 2007.
- [113] J.I. Neimark and N.A. Fufaev. On stability of stationary motions of holonomic and nonholonomic systems. *PMM*, 30(2):293–300, 1966.
- [114] J.I. Neimark and N.A. Fufaev. *Dynamics of nonholonomic systems*. American Math. Soc., 1972.
- [115] N.M. Newmark. A method of computation for structural dynamics. *J. Eng. Mech. Div. ASCE*, 85:67–94, 1959.
- [116] P.E. Nikravesh. Spatial kinematic and dynamic analysis with Euler parameters. In E.J. Haug, editor, *Computer aided analysis and optimization of mechanical system dynamics*, pages 261–281. Springer-Verlag, 1984.
- [117] P.E. Nikravesh. *Computer-aided analysis of mechanical systems*. Prentice-Hall, 1988.
- [118] L. Noels, L. Stainier, and J.-P. Ponthot. An energy momentum conserving algorithm using the variational formulation of visco-plastic updates. *Int. J. Numer. Methods Eng.*, 65:904–942, 2006.
- [119] L. Noels, L. Stainier, and J.P. Ponthot. An energy-momentum conserving algorithm for non-linear hypoelastic constitutive models. *Int. J. Numer. Methods Eng.*, 59:83–114, 2004.
- [120] W. Nolting. *Grundkurs: Theoretische Physik, 2. Analytische Mechanik*. Verlag Zimmermann-Neufang, Ulmen, 1990.
- [121] R.W. Ogden. *Non-Linear Elastic Deformations*. Ellis Horwood, Chichester, 1984.
- [122] N. Ottosen and M. Ristinmaa. *The Mechanics of constitutive modeling*. Elsevier, 2005.
- [123] L.R. Petzold and P. Lötstedt. Numerical solution of nonlinear differential equations with algebraic constraints. II: Practical implications. *SIAM J. Sci. Stat. Comput.*, 7(3):720–733, 1986.
- [124] M.A. Puso. An energy and momentum conserving method for rigid-flexible body dynamics. *Int. J. Numer. Methods Eng.*, 53:1393–1414, 2002.
- [125] P.J. Rabier and W.C. Rheinboldt. *Nonholonomic motion of rigid mechanical systems from a DAE viewpoint*. SIAM, Philadelphia, PA, 2000.

-
- [126] M. Reyhanoglu, N.H. McClamroch, and A.M. Bloch. Motion planning for non-holonomic dynamic systems. In Z. Li and J. Canny, editors, *Nonholonomic motion planning*, pages 201–234. Kluwer Academic Publishers, 1993.
- [127] I. Romero and F. Armero. An objective finite element approximation of the kinematics of geometrically exact rods and its use in the formulation of an energy-momentum conserving scheme in dynamics. *Int. J. Numer. Methods Eng.*, 54:1683–1716, 2002.
- [128] R.M. Rosenberg. *Analytical dynamics of discrete systems*. Plenum Press, 1977.
- [129] H. Rubin and P. Ungar. Motion under a strong constraining force. *Commun. Pure Appl. Math.*, 10(1):65–87, 1957.
- [130] H. Sagan. *Introduction to the Calculus of Variations*. McGraw-Hill Book Company, New York, 1969.
- [131] S.K. Saha. Dynamics of serial multi-body systems using the decoupled natural orthogonal complement matrices. *ASME J. Appl. Mech.*, 66:986–996, 1999.
- [132] S.K. Saha and W.O. Schiehlen. Recursive kinematics and dynamics for parallel structured closed loop multibody systems. *Mech. Struct. & Mach.*, 29(2):143–175, 2001.
- [133] B. Schweizer. Numerical Approach for Solving Reynolds equation with JFO boundary conditions incorporating ALE techniques. *ASME Journal of Tribology*, 131(1), 2009.
- [134] B. Schweizer. Vibrations and bifurcations of turbocharger rotors. In *SIRM 2009 - 8th International Conference on Vibrations in Rotating Machines*, Vienna, Austria, February 23-25 2009.
- [135] B. Schweizer and M. Sievert. Nonlinear oscillations of automotive turbocharger turbines. *Journal of Sound and Vibration*, Doi:10.1016/j.jsv.2008.10.013, 2008.
- [136] R. Seifried and P. Eberhard. Design of feed-forward control for underactuated multibody systems with kinematic redundancy. *Motion and Vibration Control, H. Ulbrich and L. Ginzinger (Eds.), Heidelberg: Springer*, pages 275 – 284, 2009.
- [137] S. Serafin, F. Avanzini, and D. Rocchesso. Bowed string simulation using an elastoplastic friction model. In *Proceedings of the Stockholm Acoustics Conference*, 2003.
- [138] A.A. Shabana. *Dynamics of multibody systems*. Cambridge University Press, 2nd edition, 1998.
- [139] B. Siciliano and O. Khatib, editors. *Handbook of Robotics*. Springer-Verlag, 2008.

- [140] J.C. Simo and T.J.R. Hughes. *Computational Inelasticity*. Springer-Verlag, New York, 1998.
- [141] J.C. Simo and N. Tarnow. The discrete energy-momentum method. Conserving algorithms for nonlinear elastodynamics. *Z. angew. Math. Phys. (ZAMP)*, 43:757–792, 1992.
- [142] J.C. Simo, N. Tarnow, and K.K. Wong. Exact energy-momentum conserving algorithms and symplectic schemes for nonlinear dynamics. *Comput. Methods Appl. Mech. Engrg.*, 100:63–116, 1992.
- [143] J.C. Simo and K.K. Wong. Unconditionally stable algorithms for rigid body dynamics that exactly preserve energy and momentum. *Int. J. Numer. Methods Eng.*, 31:19–52, 1991.
- [144] R.A. Spurrier. Comment on ‘singularity-free extraction of a quaternionian from a discrete cosine matrix’. *J. Spacecraft*, 15(4):255, 1978.
- [145] G. Strang. *Linear Algebra*. Springer-Verlag, 2003.
- [146] J. Swewers, F. Al-Bender, C.G. Ganseman, and T. Prajogo. An integrated friction model structure with improved presliding behavior for accurate friction compensation. *IEEE Transactions on automatic control*, 45(4):675–686, 2000.
- [147] J.S. Török. *Analytical Mechanics with an Introduction to Dynamical Systems*. John Wiley & Sons, 2000.
- [148] S. Uhlar and P. Betsch. On the rotationless formulation of multibody dynamics and its conserving numerical integration. In C.L. Bottasso, P. Masarati, and L. Trainelli, editors, *Proceedings of the ECCOMAS Thematic Conference on Multibody Dynamics*, Politecnico di Milano, Milano, Italy, 25-28 June 2007.
- [149] S. Uhlar and P. Betsch. Conserving integrators for parallel manipulators. In J.-H. Ryu, editor, *Parallel Manipulators*, chapter 5, pages 75–108. I-Tech Education and Publishing, www.books.i-techonline.com, Vienna, Austria, 2008.
- [150] S. Uhlar and P. Betsch. Energy-consistent integration of multibody systems with friction. *The Journal of Mechanical Science and Technology*, 23:901–909, 2009.
- [151] S. Uhlar and P. Betsch. Energy consistent time integration of non-conservative hybrid multibody systems. In *Proceedings of the 7th International Conference on Multibody Systems, Nonlinear Dynamics, and Control, ASME International Design Engineering Technical Conferences (IDETC)*, San Diego, CA, 30 - 2 Aug. - Sep. 2009.

-
- [152] S. Uhlar and P. Betsch. Mechanical integrators for the inverse dynamics of dissipative multibody systems. In Gosselin C., Lange C., and Carretero J.A., editors, *Proceedings of the 2009 CCToMM Symposium on Mechanisms, Machines, and Mechatronics*, Université Laval, Québec, Québec, Canada, 28 - 29 May 2009.
- [153] S. Uhlar and P. Betsch. A rotationless formulation of multibody dynamics: Modeling of screw joints and incorporation of control constraints. *Multibody System Dynamics*, DOI:10.1007/s11044-009-9149-3, 2009.
- [154] S. Uhlar and P. Betsch. A unified modeling approach for hybrid multibody systems applying energy-momentum consistent time integration. In M. Wojtyra K. Arzczewski, J. Fraczek, editor, *Proceedings of the ECCOMAS Thematic Conference on Multibody Dynamics*, Warsaw University of Technology, Warsaw, Poland, 29 June - 2 July 2009.
- [155] R. Waiboer, R. Aarts, and B. Jonker. Velocity dependence of joint friction in robotic manipulators with gear transmissions. In J.M. Goicolea, J. Cuadrado, and J.C. Garcia Orden, editors, *Proceedings of ECCOMAS Thematic Conference on Advances in Computational Multibody Dynamics (CD-ROM)*, Madrid, Spain, June 21-24 2005.
- [156] W. Weckesser. A ball rolling on a freely spinning turntable. *Am. J. Phys.*, 65(8):736–738, 1997.
- [157] J.M. Wendlandt and J.E. Marsden. Mechanical integrators derived from a discrete variational principle. *Physica D*, 106:223–246, 1997.
- [158] M. West. *Variational Integrators*. Phd-thesis, California Institute of Technology, 2004.
- [159] W.L. Wood. *Practical Time-stepping Schemes*. Oxford University Press, 1990.
- [160] P. Wriggers. *Nonlinear Finite Element Methods*. Springer-Verlag, 2008.
- [161] R. Yang. *Nonholonomic Geometry, Mechanics and Control*. Phd-thesis, University of Maryland, 1992.

THE AUTHOR LIST: GIVING CREDIT WHERE CREDIT IS DUE

The first author
Senior grad student on the project. Made the figures.

The third author
First year student who actually did the experiments, performed the analysis and wrote the whole paper. Thinks being third author is "fair".

The second-to-last author
Ambitious assistant professor or post-doc who instigated the paper.

Michaels, C., Lee, E. F., Sap, P. S., Nichols, S. T., Oliveira, L., Smith, B. S.

JORGE CHAM © 2005

The second author
Grad student in the lab that has nothing to do with this project, but was included because he/she hung around the group meetings (usually for the food).

The middle authors
Author names nobody really reads. Reserved for undergrads and technical staff.

The last author
The head honcho. Hasn't even read the paper but, hey, he got the funding, and his famous name will get the paper accepted.

www.phdcomics.com

"Piled Higher and Deeper" by Jorge Cham www.phdcomics.com

Schriftenreihe des Lehrstuhls für Numerische Mechanik

Bisher in dieser Reihe erschienen:

Band I

Mechanische Integratoren für Kontaktvorgänge deformierbarer Körper unter großen Verzerrungen,

C. Hesch, Dissertation, 2007, urn:nbn:de:hbz:467-3156

Band II

Higher-order accurate and energy-momentum consistent discretisation of dynamic finite deformation thermo-viscoelasticity,

M. Groß, Habilitationsschrift, 2009, urn:nbn:de:hbz:467-3890

Band III

Energy Consistent Time-Integration of Hybrid Multibody Systems,

S. Uhlar, Dissertation, 2009, urn:nbn:de:hbz:467-4086